Université de Lille – Sciences et Technologies

Mémoire de titres et travaux en vue de l'obtention de
l'Habilitation à Diriger des Recherches

Functional conformational protein dynamics studied by solution- and solid-state NMR spectroscopy

Dynamique conformationnelle fonctionnelle chez les protéines étudiée par résonance magnétique nucléaire en solution et en état solide

---

Robert Schneider

Jury

Dr. Fabien Ferrage
Dr. Malene Ringkjøbing Jensen
Dr. Guido Pintacuda
Dr. Françoise Jacob-Dubuisson
Prof. Olivier Lafon
Dr. Isabelle Landrieu

Acknowledgements

Instead of an exceedingly long list of acknowledgements to the many people I am grateful and indebted to, I simply wish to express my gratitude to all my current and former colleagues and collaborators in Munich, Cambridge, Göttingen, Grenoble, Lille and in many other places, to my family in Germany, and to my friends all over the world.

—*R.S.*

Contents

Acknowledgements **iii**

Contents **v**

Curriculum vitae **1**

Publications **5**

Introduction **13**

I Previous projects **15**

1 Gating and inactivation in KcsA-Kv1.3 **17**

1.1 Introduction 17

1.2 Assignment and structural characterization of KcsA-Kv1.3 20

1.3 Open-inactivated KcsA-Kv1.3 25

1.4 Gate coupling in KcsA-Kv1.3 31

1.5 Conclusions 39

2 Molecular mobility by double-quantum NMR **43**

2.1 Introduction 43

2.2 Methodology and verification on TEE 44

2.3 ^{13}C-^{13}C order parameters in microcrystalline ubiquitin 47

2.4 Conclusions 55

3 The VDAC channel: N-terminal conformation and gating **57**

3.1 Introduction 57

3.2 The native conformation of the hVDAC1 N-terminus 59

3.3 β-barrel mobility underlies hVDAC1 closure . . . 62
3.4 Conclusions . . . 70

4 IDP folding and binding by relaxation dispersion 73
4.1 Introduction . . . 73
4.2 Experiments and analysis in terms of a two-state binding model . . . 77
4.3 A three-state binding model for the $\mathrm{N_{TAIL}}$:PX interaction . . . 78
4.4 Binding mechanism and structure of bound $\mathrm{N_{TAIL}}$ . . . 82
4.5 Discussion . . . 84

II Current work 89

5 Functional dynamics of the FhaC transporter 91
5.1 Introduction . . . 91
5.2 Methodology . . . 94
5.3 Resonance assignments . . . 97
5.4 Through-space correlations . . . 99
5.5 Open-state mutants and substrate addition . . . 101
5.6 Dynamics by $\mathrm{R}_{1\rho}$ relaxation dispersion . . . 104
5.7 Outlook . . . 107

III Future plans 111

6 Project: The closed state of voltage-gated ion channels 113
6.1 Introduction . . . 113
6.2 Methodology . . . 117
6.3 Application to voltage-gated ion channels . . . 119
6.4 Expected results, potential pitfalls and solutions . . . 121
6.5 Outlook . . . 122

7 Project: Disordered regions of membrane proteins 125
7.1 Introduction . . . 125
7.2 Systems of study . . . 128
7.3 Membrane protein IDRs in isolation and in the full-length proteins . . . 129
7.4 Interplay of membrane protein IDRs and transmembrane regions . . . 131

7.5 Outlook 132

IV Appendix **133**

List of Symbols and Abbreviations **135**

A Mollica et al., Front. Mol. Biosci. 2016 **137**

Bibliography **157**

Curriculum vitae

Robert Schneider

NMR & Molecular Interactions
UMR CNRS 8576, Université Lille 1
Parc scientifique de la Haute Borne - IRI
50 Avenue du Halley
59650 Villeneuve d'Ascq, France

Phone +33 (0)3 62 53 17 05
E-mail robert.schneider@univ-lille1.fr
ORCID ID: 0000-0003-3279-5365
ResearcherID: C-1868-2013

Born 09/21/1974, Munich, Germany

Research and Education

Since 09/2014	Maître de conférences (Assistant Professor), NMR and Molecular Interactions / Unité de Glycobiologie Structurale et Fonctionnelle, Université Lille 1, Villeneuve d'Ascq, France
05/2010 – 08/2014	Postdoctoral research associate, Institut de Biologie Structurale, Grenoble, France *Conformational sampling and interactions of intrinsically disordered proteins studied by solution NMR*
03/2009 – 05/2010	Postdoctoral research associate, Max Planck Institute for Biophysical Chemistry, Göttingen, Germany *Solid-state NMR study of the mitochondrial membrane protein VDAC*
02/2005 – 01/2009	Ph. D. in biophysics, Max Planck Institute for Biophysical Chemistry, Göttingen, Germany • *Structure and function of the chimeric potassium channel KcsA-Kv1.3 in lipid bilayers* • *Solid-state NMR measurement of protein dynamics using double-quantum spectroscopy* • *Structural investigation of polyglutamine fibrils*

10/2001 – 08/2002	Master's thesis research in neuroscience at the Massachusetts Institute of Technology, Cambridge, USA *Computational studies on object recognition and attention in visual cortex*
11/1996 – 08/2002	Diplom (Master's) studies in biology and physics, University of Munich, Germany Major subjects: neuroscience, physics, genetics, biochemistry
10/1995 – 07/1996	Studium generale, Leibniz College, Tübingen, Germany
09/1985 – 08/1994	Gymnasium (high school), Rosenheim, Germany

Other work experience

04/2003 – 10/2004	Work as rickshaw driver, Rikscha-Mobil GmbH, Munich, Germany
08/1994 – 09/1995	Alternative civilian service Vogtareuth Hospital, Rosenheim, Germany, and Friedrich Baur Institute, University of Munich, Germany

Fellowships, third-party funding, awards

Starting 10/2017	Partner in three-year collaborative ANR research grant "OpenBar" coordinated by Françoise Jacob-Dubuisson, Institut Pasteur de Lille
2016 – 2017	One-year research grant "Projets exploratoires premier soutien", University of Lille / CNRS
09/2011 – 08/2014	Postdoctoral fellowship, Human Frontier Science Program
09/2008	Ernst Award, Division of Magnetic Resonance Spectroscopy of the German Chemical Society (shared with Christian Ader)
10/2005 – 09/2008	Ph. D. scholarship, Graduate School "Spectroscopy and Dynamics of Molecular Coils and Aggregates" of the German Research Foundation (DFG)
4/2002 – 5/2002	Short-term fellowship for thesis work abroad, German Academic Exchange Service (DAAD)
11/1996 – 08/2002	Fellow of the German National Academic Foundation (Studienstiftung des deutschen Volkes) and study scholarship from the State of Bavaria

Scientific supervision

2017	Linn Karen Haase – Master II student project (Solid-state NMR analysis of a bacterial membrane protein)
Since 2015	Luiza Mamigonian Bessa – Ph. D. thesis co-supervision (Investigation of the Hepatitis C virus polymerase NS5B by NMR)
2014	Nicolas Chanet – Master II student project (Assignment and diffusion properties of a disordered protein)

Teaching experience

2015, 2016	Participation in a massive open online course (MOOC) “Nuclear Magnetic Resonance, a Compass to Nanoworld” (https://www.fun-mooc.fr/courses/lille1/54002S02/session02/about)
Since 2014	Lectures and practical courses at bachelor’s and master’s levels in biochemistry, molecular biology, and NMR spectroscopy (128 credit hours 2014/2015, >192 credit hours per academic year since 2015/2016)
2012 – 2013	Master II lecture on the study of intrinsically disordered proteins by NMR (2 × 1.5 credit hours)
2009 – 2010	Lecture (1 × 1.5 credit hours) and practical course (1 × 20 credit hours) on solid-state NMR spectroscopy

Academic service

10/2005 – 09/2007	Student speaker of the Graduate School “Spectroscopy and Dynamics of Molecular Coils and Aggregates” of the German Research Foundation (DFG), Göttingen, Germany
10/1998 – 09/2000	Chairman or vice chairman of the student council, member of the faculty council, and tutor for first-year students, University of Munich, Germany

Publications

Original research articles

Most important publications are starred.

23. Luiza M. Bessa, Hélène Launay, Marie Dujardin, François-Xavier Cantrelle, Guy Lippens, Isabelle Landrieu, **Robert Schneider**[1], and Xavier Hanoulle[1].
NMR reveals the intrinsically disordered domain 2 of NS5A protein as an allosteric regulator of the hepatitis C virus RNA polymerase NS5B.
Journal of Biological Chemistry 2017, advance online publication. DOI 10.1074/jbc.M117.813766. ([1]Corresponding authors.)

22. Danielle C. Desravines[1], Itziar Serna Martin[1], **Robert Schneider**[1,2], Philippe J. Mas, Nataliia Aleksandrova, Malene Ringkjøbing Jensen, Martin Blackledge, Darren J.Hart[2] (2017).
Structural characterization of the SMRT corepressor interacting with histone deacetylase 7.
Scientific Reports 7, 3678. DOI 10.1038/s41598-017-03718-5. ([1]Equally contributing authors; [2]corresponding authors.)

21. Juan Lopez, **Robert Schneider**, François-Xavier Cantrelle, Isabelle Huvent, Guy Lippens (2016).
Studying intrinsically disordered proteins under true in vivo conditions by combined cross polarization and carbonyl detection NMR.
Angewandte Chemie International Edition 55, 7418–7422. DOI 10.1002/anie.201601850.

20. Clément Danis, Clément Despres, Luiza M. Bessa, Idir Malki, Hamida Merzougui, Isabelle Huvent, Haoling Qi, Guy Lippens, François-Xavier Cantrelle, **Robert Schneider**, Xavier Hanoulle, Caroline Smet-Nocca, Isabelle Landrieu (2016).
Nuclear magnetic resonance spectroscopy for the identification of multiple phosphorylations of intrinsically disordered proteins.
Journal of Visualized Experiments 118, e55001. DOI 10.3791/55001.

19. Anton Abyzov, Nicola Salvi, **Robert Schneider**, Damien Maurin, Rob W. H. Ruigrok, Malene Ringkjøbing Jensen, Martin Blackledge (2016).
Identification of dynamic modes in an intrinsically disordered protein using temperature-dependent NMR relaxation.
Journal of the American Chemical Society, 138, 6240–6251. DOI 10.1021/jacs.6b02424.

18. * **Robert Schneider**, Damien Maurin, Guillaume Communie, Jaka Kragelj, D. Flemming Hansen, Rob W. H. Ruigrok, Malene Ringkjøbing Jensen, Martin Blackledge (2015).
Visualizing the molecular recognition trajectory of an intrinsically disordered protein using

multinuclear relaxation dispersion NMR.
Journal of the American Chemical Society 137, 1220–1229. DOI 10.1021/ja511066q.

17. Zrinka Gattin, **Robert Schneider**, Yvonne Laukat, Karin Giller, Elke Maier, Markus Zweckstetter, Christian Griesinger, Roland Benz, Stefan Becker, Adam Lange (2015).
Solid-state NMR, electrophysiology and molecular dynamics characterization of human VDAC2.
Journal of Biomolecular NMR 61, 311–320.DOI 10.1007/s10858-014-9876-5.

16. Emeline Barbet-Massin, Michele Felletti, **Robert Schneider**, Stefan Jehle, Guillaume Communie, Nicolas Martinez, Malene Ringkjøbing Jensen, Rob W.H. Ruigrok, Lyndon Emsley, Anne Lesage, Martin Blackledge, Guido Pintacuda (2014).
Insights into the structure and dynamics of measles virus nucleocapsids by 1H-detected solid-state NMR.
Biophysical Journal 107, 941–946. DOI 10.1016/j.bpj.2014.05.048.

15. Guillaume Communie, Johnny Habchi, Filip Yabukarski, David Blocquel, **Robert Schneider**, Nicolas Tarbouriech, Nicolas Papageorgiou, Rob W. H. Ruigrok, Marc Jamin, Malene Ringkjøbing Jensen, Sonia Longhi, Martin Blackledge (2013).
Atomic resolution description of the interaction between the nucleoprotein and phosphoprotein of Hendra virus.
PLoS Pathogens 9, e1003631. DOI 10.1371/journal.ppat.1003631.

14. **Robert Schneider**[1], Florian Odronitz[1], Björn Hammesfahr[1], Marcel Hellkamp, Martin Kollmar (2013).
Peakr: Simulating solid-state NMR spectra of proteins.
Bioinformatics 29, 1134–1140. DOI 10.1093/bioinformatics/btt125. ([1]Equally contributing authors.)

13. * Ulrich Zachariae[1], **Robert Schneider**[1], Rodolfo Briones, Zrinka Gattin, Jean-Philippe Demers, Karin Giller, Elke Maier, Markus Zweckstetter, Christian Griesinger, Stefan Becker, Roland Benz, Bert L. de Groot, Adam Lange (2012).
β-barrel mobility underlies closure of the voltage-dependent anion channel.
Structure 20, 1540–1549. DOI 10.1016/j.str.2012.06.015. ([1]Equally contributing authors.)

12. Valéry Ozenne, **Robert Schneider**, Mingxi Yao, Jie-rong Huang, Loïc Salmon, Markus Zweckstetter, Malene Ringkjøbing Jensen, Martin Blackledge (2012).
Mapping the potential energy landscape of intrinsically disordered proteins at amino acid resolution.
Journal of the American Chemical Society 134, 15138–15148. DOI 10.1021/ja306905s.

11. Cédric Leyrat, **Robert Schneider**, Euripedes A. Ribeiro Jr., Filip Yabukarski, Mingxi Yao, Francine G. A. Gérard, Malene Ringkjøbing Jensen, Rob W. H. Ruigrok, Martin Blackledge, Marc Jamin (2012).
Ensemble structure of the modular and flexible full-length vesicular stomatitis virus phosphoprotein.
Journal of Molecular Biology 423, 182–197. DOI 10.1016/j.jmb.2012.07.003.

10. **Robert Schneider**, Miria Schumacher, Henrik Müller, Deepak Nand, Volker Klaukien, Henrike Heise, Dietmar Riedel, Gerhard Wolf, Elmar Behrmann, Stefan Raunser, Ralf Seidel, Martin Engelhard, Marc Baldus (2011).

Structural characterization of polyglutamine fibrils by solid-state NMR spectroscopy.
Journal of Molecular Biology 412, 121–136. DOI 10.1016/j.jmb.2011.06.045.

9. * **Robert Schneider**, Manuel Etzkorn, Karin Giller, Venita Daebel, Jörg Eisfeld, Markus Zweckstetter, Christian Griesinger, Stefan Becker, Adam Lange (2010).
The native conformation of the human VDAC1 N terminus.
Angewandte Chemie International Edition 49, 1882–1885. DOI 10.1002/anie.200906241.

8. **Robert Schneider**, Karsten Seidel, Manuel Etzkorn, Adam Lange, Stefan Becker, Marc Baldus (2010).
Probing molecular motion by double-quantum (^{13}C,^{13}C) solid-state NMR spectroscopy: Application to ubiquitin.
Journal of the American Chemical Society 132, 223–233. DOI 10.1021/ja906283h.

7. * Christian Ader[1], **Robert Schneider**[1], Sönke Hornig, Phanindra Velisetty, Vitya Vardanyan, Karin Giller, Iris Ohmert, Stefan Becker, Olaf Pongs, Marc Baldus (2009).
Coupling of activation and inactivation gate in a K$^+$ channel: potassium and ligand sensitivity.
EMBO Journal 28, 2825–2834. DOI 10.1038/emboj.2009.218. ([1]Equally contributing authors.)

6. Christian Ader, **Robert Schneider**, Karsten Seidel, Manuel Etzkorn, Stefan Becker, Marc Baldus (2009).
Structural rearrangements of membrane proteins probed by water-edited solid-state NMR spectroscopy.
Journal of the American Chemical Society 131, 170–176. DOI 10.1021/ja806306e.

5. Karsten Seidel, Manuel Etzkorn, **Robert Schneider**, Christian Ader, Marc Baldus (2009).
Comparative analysis of NMR chemical shift predictions for proteins in the solid phase.
Solid State Nuclear Magnetic Resonance 35, 235–242. DOI 10.1016/j.ssnmr.2008.12.008.

4. * Christian Ader[1], **Robert Schneider**[1], Sönke Hornig, Phanindra Velisetty, Erica M. Wilson, Adam Lange, Karin Giller, Iris Ohmert, Marie-France Martin-Eauclaire, Dirk Trauner, Stefan Becker, Olaf Pongs, Marc Baldus (2008).
A structural link between inactivation and block of a K$^+$ channel.
Nature Structural and Molecular Biology 15, 605–612. DOI 10.1038/nsmb.1430.
(Faculty of 1000 Recommended Article (http://f1000.com/1113127). [1]Equally contributing authors.)

3. * **Robert Schneider**, Christian Ader, Adam Lange, Karin Giller, Sönke Hornig, Olaf Pongs, Stefan Becker, Marc Baldus (2008).
Solid-state NMR spectroscopy applied to a chimeric potassium channel in lipid bilayers.
Journal of the American Chemical Society 130, 7427–7435. DOI 10.1021/ja800190c.

2. Ulrich Zachariae, **Robert Schneider**, Phanindra Velisetty, Adam Lange, Daniel Seeliger, Sören Wacker, Yasmin Karimi-Nejad, Gert Vriend, Stefan Becker, Olaf Pongs, Marc Baldus, Bert L. de Groot (2008).
The molecular mechanism of toxin-induced conformational changes in a potassium channel: relation to C-type inactivation.
Structure 16, 747–754. DOI 10.1016/j.str.2008.01.018.

1. Jegannath Korukottu, **Robert Schneider**, Vinesh Vijayan, Adam Lange, Olaf Pongs, Stefan Becker, Marc Baldus, Markus Zweckstetter (2008).
   High-resolution 3D structure determination of kaliotoxin by solid-state NMR spectroscopy.
   PLoS ONE 3, e2359. DOI 10.1371/journal.pone.0002359.

Review articles

4. Jérémy Guérin, Sarah Bigot, **Robert Schneider**, Susan K. Buchanan, Françoise Jacob-Dubuisson (2017).
   Two-partner secretion: combining efficiency and simplicity in the secretion of large proteins for bacteria-host and bacteria-bacteria interactions.
   Frontiers in Cellular and Infection Microbiology 7, 148. DOI 10.3389/fcimb.2017.00148.
3. Luca Mollica, Luiza M. Bessa, Xavier Hanoulle, Malene Ringkjøbing Jensen, Martin Blackledge, **Robert Schneider** (2016).
   Binding mechanisms of intrinsically disordered proteins: theory, simulation, and experiment.
   Frontiers in Molecular Biosciences 3, 52. DOI 10.3389/fmolb.2016.00052.
2. **Robert Schneider**, Jie-rong Huang, Mingxi Yao, Guillaume Communie, Valéry Ozenne, Luca Mollica, Loïc Salmon, Malene Ringkjøbing Jensen, Martin Blackledge (2012).
   Towards a robust description of intrinsic protein disorder using nuclear magnetic resonance spectroscopy.
   Molecular BioSystems 8, 58–68. DOI 10.1039/c1mb05291h.
1. Christian Ader, **Robert Schneider**, Karsten Seidel, Manuel Etzkorn, Marc Baldus (2007).
   Magic-angle-spinning NMR spectroscopy applied to small molecules and peptides in lipid bilayers.
   Biochemical Society Transactions 35, 991–995. DOI 10.1042/BST0350991.

Other publications

3. **Robert Schneider** (2009).
   Crystalline, membrane-embedded, and fibrillar proteins investigated by solid-state NMR spectroscopy.
   Ph. D. thesis, University of Göttingen, Germany.
   (http://webdoc.sub.gwdg.de/diss/2009/schneider_r/)
2. **Robert Schneider** and Maximilian Riesenhuber (2004).
   On the difficulty of feature-based attentional modulations in visual object recognition: A modeling study.
   AI Memo 2004-004, CBCL Memo 235, MIT AI Lab and CBCL, Cambridge, MA.
   (http://publications.csail.mit.edu/ai/)
1. **Robert Schneider** and Maximilian Riesenhuber (2002).
   A detailed look at scale and translation invariance in a hierarchical neural model of visual object recognition.
   AI Memo 2002-011, CBCL Memo 218, MIT AI Lab and CBCL, Cambridge, MA.
   (http://publications.csail.mit.edu/ai/)

Oral presentations at conferences

6. Studying intrinsically disordered proteins under true in vivo conditions by combined cross polarization and carbonyl detection NMR.
   Discussion Meeting of the Magnetic Resonance Divison of the German Chemical Society (Gesellschaft Deutscher Chemiker, GDCh), Düsseldorf, Germany, 12–15/9/2016.

5. Visualizing the molecular recognition trajectory of an intrinsically disordered protein using multinuclear relaxation dispersion NMR.
   Euromar 2015, Prague, Czech Republic, 5–10/7/2015.

4. Folding and binding of the disordered tail of Sendai virus nucleoprotein studied by relaxation dispersion spectroscopy.
   25th International Conference on Magnetic Resonance in Biological Systems, Lyon, France, 19–24/8/2012.

3. Folding and binding of the disordered tail of Sendai virus nucleoprotein to its partner studied by CPMG relaxation dispersion spectroscopy.
   2nd Bio-NMR Annual User Meeting, Portorož, Slovenia, 8–11/5/2012.

2. A structural link between activation and block of a K+ channel (presented together with Christian Ader).
   Discussion Meeting of the Magnetic Resonance Divison of the German Chemical Society (Gesellschaft Deutscher Chemiker, GDCh), Regensburg, Germany, 22–25/9/2008.

1. Solid-state NMR applied to the full-length KcsA-Kv1.3 potassium channel in lipid bilayers.
   5th Alpine Conference on Solid-State NMR, Chamonix, France, 9–13/9/2007.

Poster presentations at conferences

16. **Robert Schneider**, Xavier Hanoulle, Jérémy Guérin, Maëlenn Païline Delcourt, Françoise Jacob-Dubuisson.
    Conformational dynamics in the beta-barrel transporter FhaC investigated by solid-state NMR.
    Conference “NMR: a tool for biology”, Institut Pasteur, Paris, France, 30/1–1/2/2017.

15. **Robert Schneider**, Xavier Hanoulle, Jérémy Guérin, Maëlenn Païline Delcourt, Françoise Jacob-Dubuisson.
    Conformational dynamics in the beta-barrel transporter FhaC investigated by solid-state NMR.
    Discussion Meeting of the Magnetic Resonance Divison of the German Chemical Society (Gesellschaft Deutscher Chemiker, GDCh), Düsseldorf, Germany, 12–15/9/2016.

14. **Robert Schneider**, Emeline Barbet-Massin, Guillaume Communie, Michele Felletti, Malene Ringkjøbing Jensen, Rob Ruigrok, Lyndon Emsley, Anne Lesage, Guido Pintacuda, Martin Blackledge.
    Measles virus nucleocapsid assemblies studied by ^{1}H-detected solid-state NMR.
    Euromar 2014, Zurich, Switzerland, 29/6–3/7/2014.

13. **Robert Schneider**, Emeline Barbet-Massin, Guillaume Communie, Michele Felletti, Anne Lesage, Lyndon Emsley, Malene Ringkjøbing Jensen, Rob Ruigrok, Martin Blackledge, Guido Pintacuda.
Measles virus nucleocapsid assemblies studied by ^{1}H-detected solid-state NMR.
8th Alpine Conference on Solid-State NMR, Chamonix, France, 8–12/9/2013.

12. **Robert Schneider**, Malene Ringkjøbing Jensen, Damien Maurin, Guillaume Communie, D. Flemming Hansen, Rob Ruigrok, Martin Blackledge.
Folding and binding of the disordered tail of Sendai virus nucleoprotein studied by NMR relaxation dispersion spectroscopy.
13th Human Frontier Science Program Awardees Meeting, Strasbourg, France, 7–10/7/2013.

11. **Robert Schneider**, Malene Ringkjøbing Jensen, Damien Maurin, Guillaume Communie, D. Flemming Hansen, Rob Ruigrok, Martin Blackledge.
Folding and binding of the disordered tail of Sendai virus nucleoprotein studied by relaxation dispersion spectroscopy.
54th Experimental NMR Conference, Asilomar, USA, 14–19/4/2013.

10. **Robert Schneider**, Florian Odronitz, Björn Hammesfahr, Marcel Hellkamp, Martin Kollmar.
Peakr: Simulating solid-state NMR spectra of proteins.
54th Experimental NMR Conference, Asilomar, USA, 14–19/4/2013.

9. **Robert Schneider**, Danielle Desravines, Nataliia Aleksandrova, Eva Maria Geenen, Malene Ringkjøbing Jensen, Darren Hart, Martin Blackledge.
NMR study of a disordered segment of the nuclear receptor corepressor SMRT.
Gordon Research Conference on Computational Aspects of Biomolecular NMR, Il Ciocco, Italy, 22–27/5/2011.

8. Malene Ringkjøbing Jensen, Cedric Leyrat, **Robert Schneider**, Filip Yabukarski, Nicolas Tarbouriech, Euripedes de Almeida Ribeiro Jr., Francine C. A. Gerard, Ivan Ivanov, Rob W. H. Ruigrok, Marc Jamin, Martin Blackledge.
Intrinsic disorder and transient structure in the vesicular stomatitis virus phosphoprotein.
Biophysical Society 55th Annual Meeting, Baltimore, USA, 5–9/3/2011.

7. **Robert Schneider**, Manuel Etzkorn, Venita Daebel, Karin Giller, Stefan Becker, Christian Griesinger, Adam Lange.
Conformation of human VDAC1 in lipid bilayers investigated by solid-state NMR.
6th Alpine Conference on Solid-State NMR, Chamonix, France, 13–17/9/2009.

6. **Robert Schneider**, Christian Ader, Sönke Hornig, Phanindra Velisetty, Vitya Vardanyan, Karin Giller, Iris Ohmert, Stefan Becker, Olaf Pongs, Marc Baldus.
Coupling between activation and inactivation gates of a potassium channel revealed by solid-state NMR.
8th European Symposium of the Protein Society, Zurich, Switzerland, 14–18/6/2009.

5. **Robert Schneider**, Christian Ader, Sönke Hornig, Karin Giller, Adam Lange, Olaf Pongs, Stefan Becker, Marc Baldus.
Studying potassium channel structure and inactivation in lipid bilayers by solid-state NMR.
49th Experimental NMR Conference, Asilomar, USA, 11–14/3/2008.

4. **Robert Schneider**, Christian Ader, Adam Lange, Karin Giller, Stefan Becker, Marc Baldus.
   Solid-state NMR spectroscopy applied to the full-length KcsA-Kv1.3 potassium channel in lipid bilayers.
   Discussion Meeting of the Magnetic Resonance Divison of the German Chemical Society (Gesellschaft Deutscher Chemiker, GDCh), Göttingen, Germany, 26–29/9/2007.
3. **Robert Schneider**, Karsten Seidel, Manuel Etzkorn, Marc Baldus.
   Chemical-shift variations correlate with structural differences in microcrystalline ubiquitin.
   19th International Conference on Magnetic Resonance in Biological Systems, Göttingen, Germany, 20–25/8/2006.
2. **Robert Schneider**, Karsten Seidel, Manuel Etzkorn, Marc Baldus.
   Chemical-shift variations correlate with structural differences in microcrystalline ubiquitin.
   Euromar 2006, York, England, 16–21/7/2006.
1. **Robert Schneider**, Adam Lange, Marc Baldus.
   Refinement of MAS-based molecular structures using chemical-shift selective transfer methods.
   Discussion Meeting of the Magnetic Resonance Divison of the German Chemical Society (Gesellschaft Deutscher Chemiker, GDCh), Mainz, Germany, 09/2005.

Metrics

Total citations	702
h-index	16

(Source: Thomson Reuters, 17/10/2017)

Introduction

'A protein that doesn't move is dead.'

—Rob Ruigrok

Proteins are dynamic entities, moving on a wide range of timescales and within an environment that is itself highly dynamic and complex. Knowledge of their three-dimensional structure at atomic resolution is essential for understanding their function, similar as the structure of the DNA double helix directly suggested a mechanism for its replication [1]. While all three principal high-resolution structure elucidation techniques of structural biology – X-ray crystallography, nuclear magnetic resonance (NMR) spectroscopy, and cryo-electron microscopy (cryo-EM) – are, in principle, affected by and sensitive to protein dynamics, the three-dimensional protein structures they yield are principally static snapshots of a dynamic ensemble, reflecting the most populated state (or an average over such states). Moreover, the crystalline environment and/or cryogenic temperatures in which proteins are normally visualized by crystallography and cryo-EM are very different from the native conditions in which proteins function, affecting protein dynamics and accessible conformations. Nevertheless, in the vast majority of cases, the conformations proteins assume under such conditions, usually their low-energy "ground states", are perfectly and highly relevant. Still, complementary information under more native-like conditions is necessary for a more complete understanding of protein structure and function. This is all the more true for the class of intrinsically disordered proteins (IDPs) which are functional in the absence of stable three-dimensional or even secondary structure [2]; for such proteins, a structurally well-defined ground state that could be studied by crystallography or electron microscopy does not even exist.

For all its shortcomings, most notably low sensitivity, certain limitations with respect to molecular size, and a still rather tedious path to resonance assignment and structure determination, NMR spectroscopy has the unique benefit of being the one technique in structural biology that can yield multisite atomic-resolution information on biological macromolecules, even highly dynamic ones, in native or near-native conditions – *i.e.* in solution, in lipid membranes, or even in living cells [3], and at physiological temperatures – , as well as being able to provide direct, quantitative measures of dynamics on a wide range of time scales [4]. Despite the major advances that have been made in recent years in crystallography and cryo-EM, notably in structure elucidation of membrane proteins and supramolecular assemblies [5, 6] – systems for which NMR spectroscopy, especially in the solid state, was thought to be uniquely, if not exclusively well-placed not long ago – , NMR thus keeps its place in today's world of integrative structural biology. In any case, to address a biological question, it is rarely helpful to insist that a single technique provide all the answers; a combination of methods, where each can play out its strengths and its weaknesses can be compensated, is usually much better suited.

In my research up to now, I have attempted to follow this principle, using NMR spectroscopy, both in solution and in the solid state, to investigate biological systems for whose study it has unique advantages, while employing collaborations and existing data from other methods to obtain a more complete picture. A focus of my work has been on functional dynamics and conformational transitions in membrane and disordered proteins. In this research habilitation, I will retrace some of my previous projects in this direction, before discussing current work and future research plans. Part I, on the one hand, deals with projects from my doctoral thesis and first postdoctoral period in Göttingen, where I investigated structure and gating in the potassium ion channel KcsA-Kv1.3 and the mitochondrial ion channel VDAC, as well as developed and applied a method to measure protein dynamics via double-quantum spectroscopy in the solid state. On the other hand, I summarize work performed during my postdoctoral stay in Grenoble, where I used relaxation dispersion experiments to elucidate the binding mechanism of an intrinsically disordered protein to its partner. In Part II, current work aiming at a description of the transport mechanism of the bacterial outer membrane protein FhaC is discussed. Finally, Part III outlines plans to investigate the resting state of voltage-gated ion channels and disordered intracellular regions of membrane proteins.

Part I

Previous projects

Chapter 1

Gating and inactivation in the potassium channel KcsA-Kv1.3 in lipid bilayers

1.1 Introduction

Ion channels are membrane proteins which are involved in regulating transmembrane flow of ions. As such, they are responsible for transmembrane voltage and propagation of electrical signals such as action potentials in neurons [7], as well as for a multitude of other functions, including muscle excitation and regulation of blood pressure [8]. A variety of ion channel architectures exist, the most common of which being the "pore-loop" architecture where a region of the protein loops back into the membrane without traversing it, forming the ion selectivity filter [9]. These channels are tetramers or monomers containing four similar domains, where each monomer or domain, respectively, contains two to seven transmembrane helices [9]. Voltage-gated potassium, sodium and calcium channels, but also ionotropic glutamate receptors belong to this class. The ion permeation pore in these channels is formed by two transmembrane helices, linked by the pore loop, which are contributed by each monomer or domain.

To exert their functions, ion channels can exist in different states. Apart from open and closed states of the ion-conducting pore, so-called inactivated states exist which are distinct from the normal closed state ready for activation (*i.e.* opening and ion conduction). Two different inactivation processes, fast and slow inactivation, have been described for K^+, Na^+ and Ca^{2+} channels. Fast inactivation is functionally related to decay of the current carried by the permeant ion on the low millisecond timescale; slow inactivation on the millisecond to second timescale leads to refractory periods of transmembrane voltage which limit the rate of action potentials that can be produced by an excitable cell [10, 11].

Ion channel function has been intensely studied for a long time, notably by electrophysiology [7, 12]. The first atomic structure of an ion channel was resolved by X-ray crystallography in 1998 [13], and since, a multitude of further ion channel structures have been described, more recently also by cryo-electron microscopy [14–21]). These studies have enabled an understanding of the mechanistic basis of ion selectivity [13, 17] and shown that fast (or N-type, in K^+ channels) inactivation is due to binding of an intracellular channel segment to the pore [22, 23]. At the time of my thesis, however, slow or C-type inactivation had remained elusive in structural terms. Moreover, there was, and still is, a lack of high-resolution structural information on ion channels embedded in their native environment, *i.e.* the lipid bilayer.

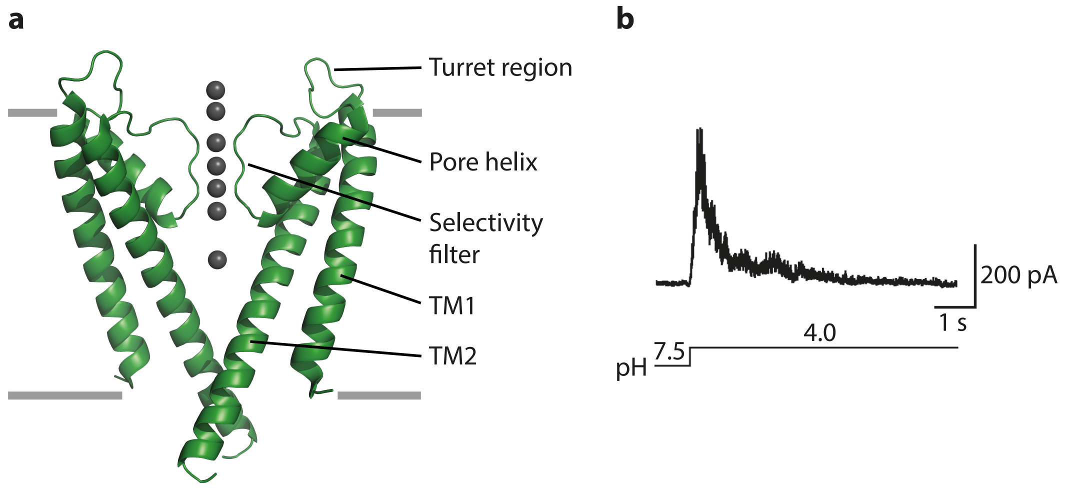

Figure 1.1: **(a)** Transmembrane region of the KcsA potassium channel (PDB: 1K4C) [24]. Two of its four subunits are shown in cartoon representation, with structural motifs indicated. K^+ ions are shown as gray spheres. Approximate membrane boundaries are indicated by gray bars. **(b)** KcsA-Kv1.3 current recorded from inside-out patches of proteoliposomes after a pH jump from 7.5 to 4.0 at +100 mV in asymmetrical K^+ solutions (intracellular side 200 mM KCl, extracellular side 8 mM KCl; from ref. [25]).

In the group of Marc Baldus where I performed my thesis work, a variant of the prokaryotic potassium channel KcsA called KcsA-Kv1.3 had already been investigated by solid-state NMR in liposomes [26]. KcsA, a tetramer of 4 × 160 residues from the soil bacterium *Streptomyces lividans* [27], is the ion channel whose three-dimensional structure was first determined [13] (see Fig. 1.1 a). Its variant KcsA-Kv1.3 differs from KcsA in 11 amino acids between residues 52 and 64 in the extracellular turret loop and pore helix regions of the channel, which were replaced by the corresponding residues 368 to 380 from the human voltage-gated K^+ channel Kv1.3. This makes KcsA-Kv1.3 a high-affinity receptor for scorpion toxins, similar to Kv1.3 itself [28, 29]. Otherwise, it is essentially indistinguishable from KcsA, exhibiting the same exquisite selectivity for potassium over the smaller sodium ions while allowing for high K^+ throughput rates, mediated by the conserved Thr-Val-Gly-Tyr-Gly signature sequence of the selectivity filter [13, 30]. Notably, as KcsA itself, *in vitro*, KcsA-Kv1.3 can be gated, *i.e.* its ion conduction pathway opened and closed, by a change in pH [31], and it exhibits an inactivation process comparable to C-type inactivation of voltage-gated channels (Fig. 1.1 b) [10, 12, 32].

Previously, the binding of kaliotoxin (KTX) to KcsA-Kv1.3 had been studied in the group by solid-state NMR in lipid bilayers, and resonance assignments for 19 residues in the turret and selectivity filter regions of the channel had been reported [26]. In my work, I first extended resonance assignments to all regions of the channel, notably the intracellular N- and C-termini that were truncated or disordered in the original KcsA crystal structures [13, 24], and investigated its secondary structure when embedded in lipid bilayers [33]. In collaboration with my colleague Christian Ader, I then studied the open-inactivated conformation KcsA-Kv1.3 assumes at pH 4.0. We were able to provide the first direct structural insight into this channel state. We described the opening of the transmembrane activation gate, *i.e.* the channel region which opens up to initiate ion flux, and found a nonconductive selectivity filter conformation similar to that seen in crystal structures obtained at low potassium concentration [25]. This result confirmed that the region of KcsA-Kv1.3 responsible for inactivation (the inactivation gate) is indeed the selectivity filter. Notably, the same selectivity filter conformation was also found in the presence of a porphyrin channel blocker [25]. Finally, we observed an influence of potassium concentration on transmembrane activation gate opening which we could trace to a steric coupling between selectivity filter and transmembrane gate, suggesting that coordinated conformational transitions in both channel gates mediate its ion conduction cycle [34].

1.2 Assignment and structural characterization of KcsA-Kv1.3 in lipid bilayers

(Schneider et al., J. Am. Chem. Soc. 2008 [33])

For resonance assignment, (^{13}C,^{15}N)-uniformly labeled full-length KcsA-Kv1.3 and a sample reverse-labeled for leucine, valine, tryptophan, and tyrosine, *i.e.* containing these amino acid types in natural abundance [35, 36], were used, as well as a sample truncated after residue 125 by chymotrypsin digestion to assist in identification of C-terminal residues. Channel samples were reconstituted into soybean asolectin liposomes at a 100:1 lipid:protein molar ratio, in a buffer containing 50 mM sodium phosphate at pH 7.4 and 50 mM NaCl. Solid-state NMR experiments were conducted on 600 and 800 MHz spectrometers at MAS speeds of typically 10 to 12.5 kHz and sample temperatures corresponding to liquid crystalline (+2 to +12°C) and gel phase (-5 to -20°C) states of the lipid bilayer. Cross-polarization (CP) [37] based (^{13}C,^{13}C) and (^{15}N,^{13}C) two- and three-dimensional correlation experiments of type CC, NCACX, and NCOCX (see, e.g., ref. [38]) were recorded.

With these experiments, sequential assignments could be obtained for 94 of all 160 residues of KcsA-Kv1.3. Together with the assignments for Glu118 and Glu120 obtained via pH titrations (see Section 1.4), this accounts for 60% of its sequence. It should be noted that assignments were grouped in three categories based on estimated reliability. While usually several sequential correlations from different spectra were available for category 1 assignments, category 3 assignments were generally characterized by one sequential correlation peak, weaker signal intensity, or spectral overlap (see the Supporting Information of ref. [33]). Notably, very reliable assignments were obtained throughout the regions of functional importance (*i.e.* selectivity filter and transmembrane gating hinge, see Section 1.3). 75 assigned residues are within the parts of the protein seen in KcsA crystals [24] (PDB ID 1K4C, residues 22–124), while 21 additional residues from the intracellular N- and C-termini were identified. Assigned residues are indicated in Figure 1.2.

Using the well-established correlation between ^{13}C secondary chemical shifts and secondary structure [39, 40], we identified helical stretches of KcsA-Kv1.3 in lipid bilayers and compared them with those found in crystalline and micellar preparations of KcsA (Fig. 1.3). In transmembrane and extracellular regions, secondary structure derived from solid-state NMR chemical shifts corresponds closely to that found in the KcsA crystal

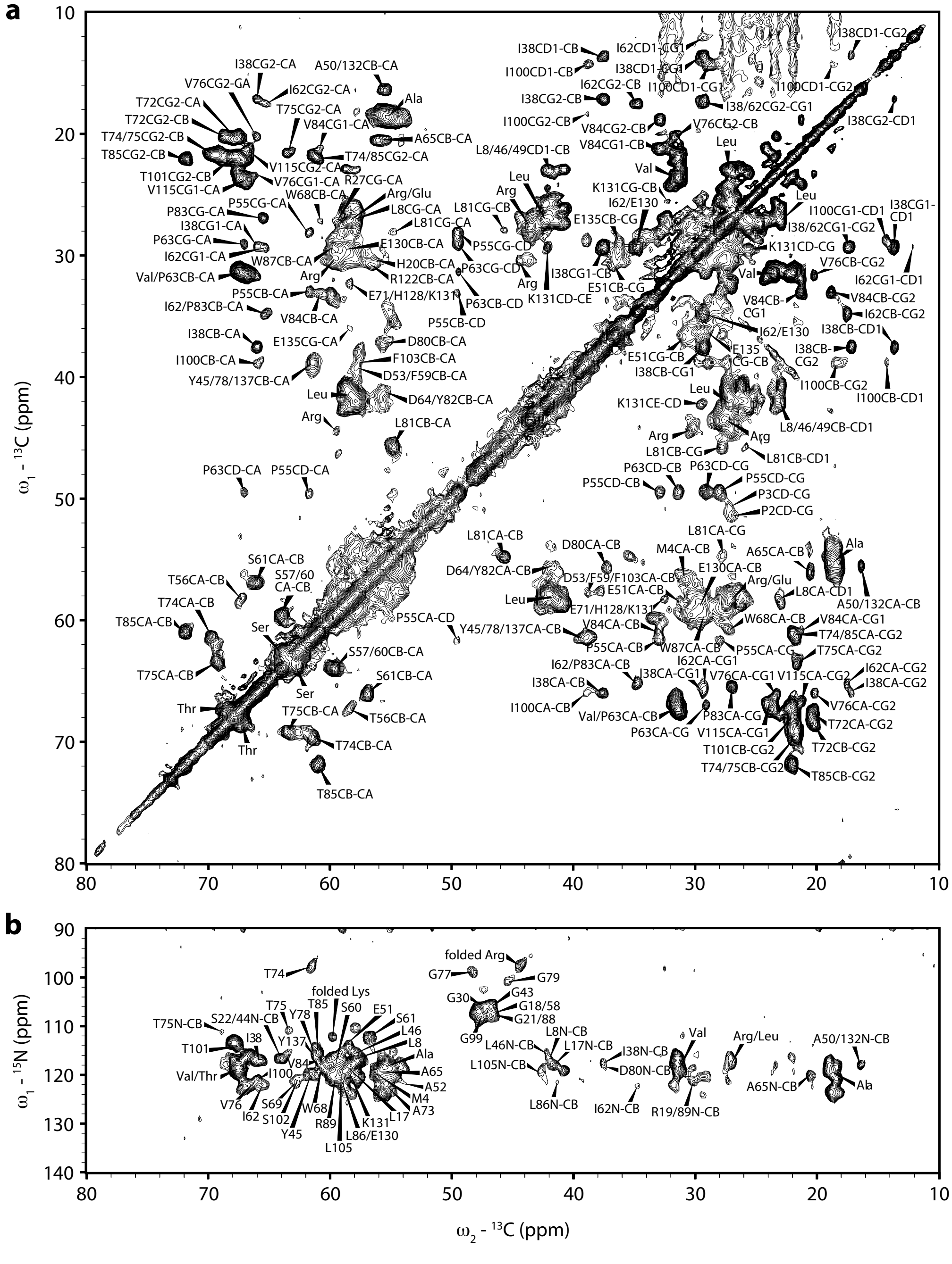

Figure 1.2: 2D ssNMR correlation spectra on KcsA-Kv1.3 in liposomes recorded at 800 MHz ^{1}H Larmor frequency, 12.5 kHz MAS and with lipid bilayers in the liquid crystalline state. **(a)** Proton-driven (^{13}C,^{13}C) spin diffusion spectrum (mixing time 20 ms). **(b)** NCACB correlation spectrum. Assigned residues as well as regions of significant overlap for certain residue types are indicated in both spectra. In the NCACB spectrum, peaks marked only with residue type and number represent (^{15}N,^{13}C$^{\alpha}$) correlations.

structure. Solid-state NMR data suggest that transmembrane helix 1 (TM1) is about 2 residues longer both at its N- and C-termini than in crystals, which may be explained by the presence of the lipid bilayer, the Kv1.3 mutations in the turret region, and the absence of an antibody binding to the turret as in the crystal structure [24]. We also obtained evidence for helical structure in the intracellular N- and C-termini of the channel, in agreement with previous data from electron paramagnetic resonance (EPR) and solution-state NMR [41–43].

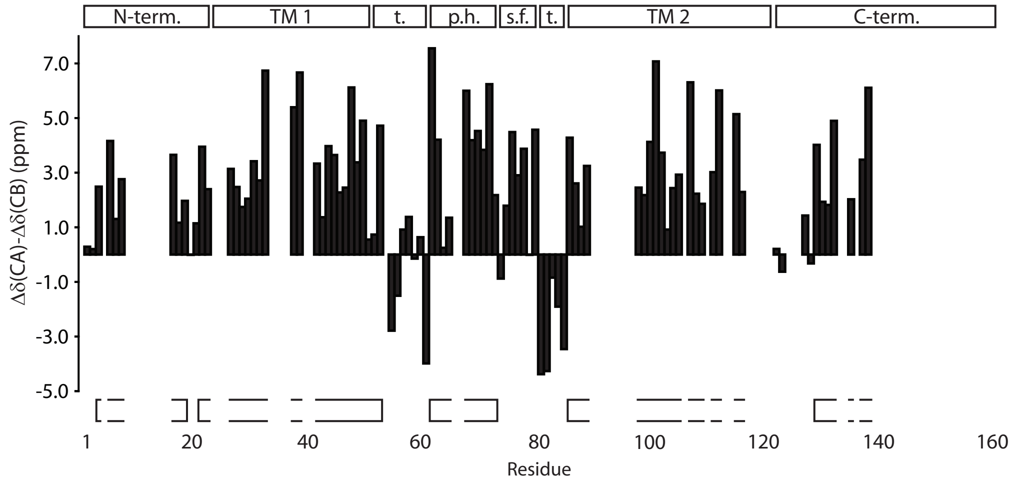

Figure 1.3: Secondary chemical shifts (calculated as $[\delta(C^{\alpha})-\delta(C^{\alpha}_{\mathrm{ref}})]-[\delta(C^{\beta})-\delta(C^{\beta}_{\mathrm{ref}})]$) of KcsA-Kv1.3, using average chemical shift values from the Biological Magnetic Resonance Data Bank (BMRB; http://www.bmrb.wisc.edu) as reference values $\delta(C^{\alpha}_{\mathrm{ref}})$, $\delta(C^{\beta}_{\mathrm{ref}})$. Positive values indicate helical structure. Secondary structure elements of the KcsA crystal structure (PDB 1K4C) are given as horizontal bars at the top (TM: transmembrane helix; t.: turret loop; p.h.: pore helix; s.f.: selectivity filter), as well as N- and C-terminal regions not covered by the crystal structure. Horizontal bars at the bottom show helical segments as seen by ssNMR.

A comparison of secondary chemical shifts with those obtained in solution-state NMR studies of KcsA in dodecylphosphocholine (foscholine) [43] and sodium dodecyl sulfate (SDS) [42] micelles is instructive, even though caution has to be exercised due to lacking assignments in the solid state (Figure 1.4). In the intracellular C-terminus, helical structure appears to be more pronounced and to begin earlier in the sequence (residue 129) in lipid bilayers than in micelles. Also, solid-state NMR data indicate pronounced helical sec-

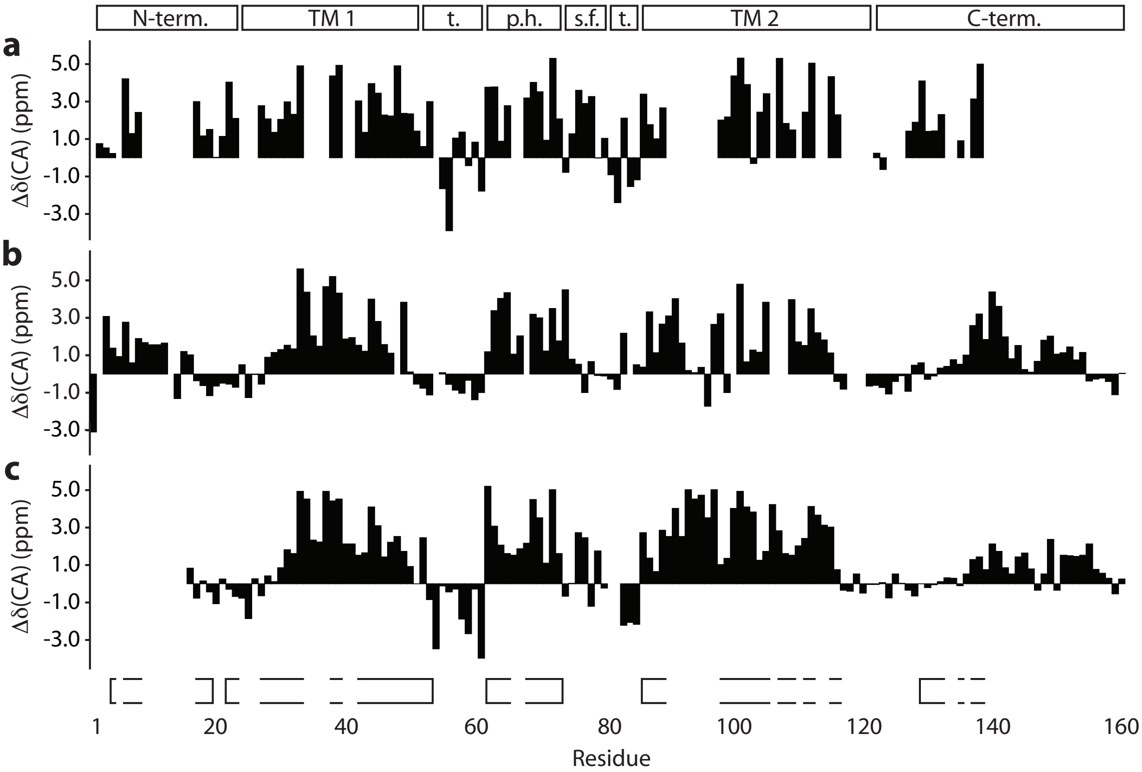

Figure 1.4: Comparison of C^{α} secondary chemical shifts. **(a)** KcsA-Kv1.3 in liposomes as seen by solid-state NMR. **(b)** Full-length KcsA studied by solution-state NMR in foscholine micelles [43]. **(c)** KcsA(16-160) measured by solution-state NMR in SDS micelles [42]. Positive values indicate helical structure. Secondary structure elements are given as in Figure 1.3.

ondary structure for all assigned residues between Ser22 and Gly30, while the TM1 helix only begins at residue 30 in micelles. These differences may be functionally relevant given the roles of the C-terminus in tetramer assembly and of His25 in gating [44, 45]. Interestingly, solid-state NMR C^{α} secondary chemical shifts measured for two crucial channel regions controlling ion conduction, *i.e.* the selectivity filter and the transmembrane gating hinge (see Section 1.3), fit better to SHIFTX [46] chemical shift predictions based on the KcsA crystal structure than do solution-state NMR values found for KcsA in micelles (Figure 1.5). These results thus underline the importance of studying transmembrane proteins in a lipid bilayer environment. They also indicate that, under the experimental conditions we used, KcsA-Kv1.3 exhibits a conductive selectivity filter conformation and a closed ion conduction pathway, as does KcsA in the crystal structure [24]. Notably, a crystal structure of full-length KcsA that was obtained later confirmed the organization of the C-terminus as a helical bundle, with helical secondary structure essentially continuous from the TM2 helix [47].

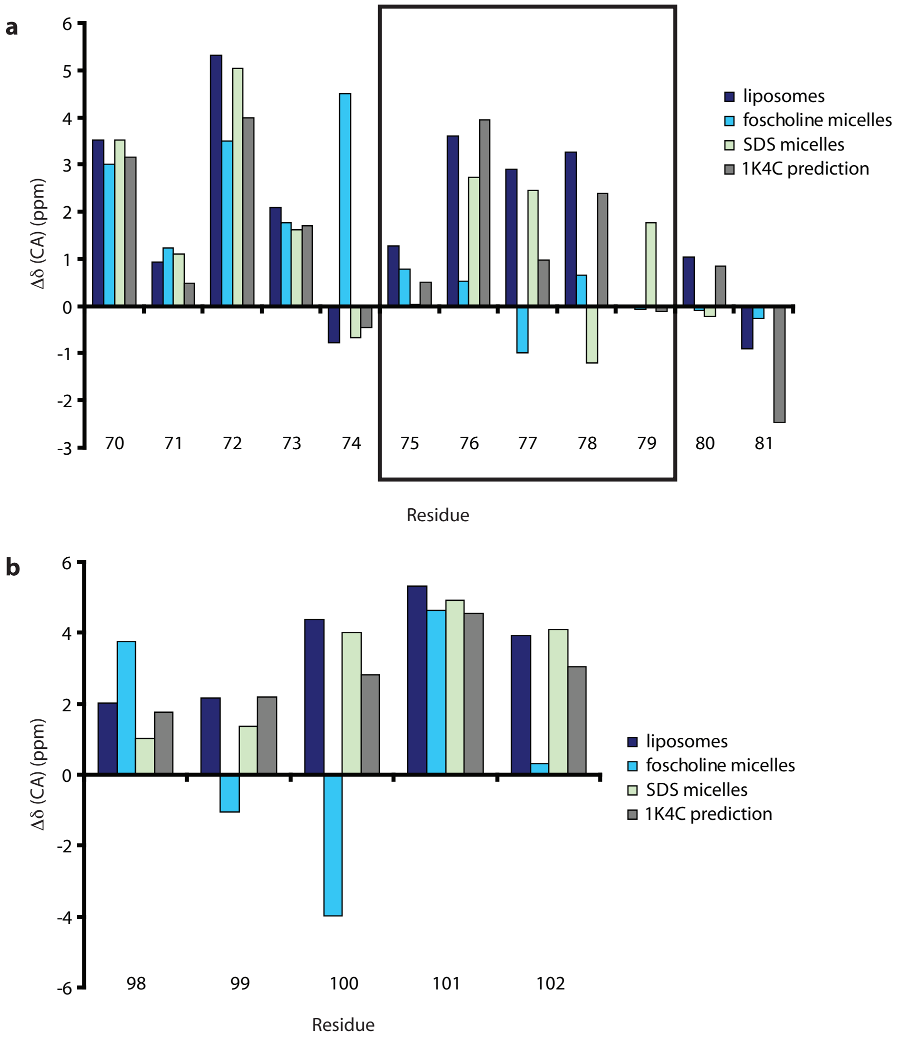

Figure 1.5: Comparison of C^{α} secondary chemical shifts in the selectivity filter region **(a)** and the putative TM2 gate **(b)** between solid-state NMR data measured on KcsA-Kv1.3 in liposomes (dark blue), solution-state NMR data measured on KcsA in foscholine micelles [43] (light blue) and SDS micelles [42] (light green), and SHIFTX [46] predictions for the KcsA crystal structure [24] (gray).

It is worth mentioning that all residues of the selectivity filter (residues 75–79) and almost all residues of the extracellular turret loops (residues 54–61 and 80–85) were clearly identifiable with sizable signal-to-noise in dipolar-based correlation spectra. This finding argues against large-amplitude mobility of these residues on the sub-ms timescale, which had been suggested for the selectivity filter as a means to conduct ions [48]. It thus seems that the selectivity filter does accomplish ion selectivity via a defined structure providing a “snug fit” to dehydrated potassium ions [13, 49]. However, our results were obtained in the absence of ion conduction (without a transmembrane concentration gradient and with a closed activation gate, see Section 1.3), so any – likely – mobility associated with the passage of ions would most probably not have occurred in our experimental setup.

1.3 The open-inactivated conformation of KcsA-Kv1.3 at pH 4.0 (Ader, Schneider et al., Nat. Struct. Mol. Biol. 2008 [25])

Electrophysiological experiments in lipid bilayers by our collaborators, Olaf Pongs and coworkers, had shown that, like the parent KcsA channel, KcsA-Kv1.3 is closed at pH 7.5 and activated by an increase in H^+ concentration on the intracellular side, leading to a measurable current [31, 32, 50]. However, both KcsA and KcsA-Kv1.3 rapidly enter into an inactivated state during a prolonged pH stimulus and thus exhibit a low open probability of about 6% in the steady state at pH 4.0 [31, 50] (Fig. 1.1 b). While other ion channels had been crystallized with the ion conduction pore in an open conformation [16, 51], no structural information on this state was available at the time on KcsA; and despite a wealth of functional and simulation data on K^+ channel inactivation [12, 32, 52, 53], the structure of an inactivated K^+ channel was still elusive.

Our solid-state NMR resonance assignments of KcsA-Kv1.3 in lipid bilayers at pH 7.5 indicated that, in these conditions, the channel is found in a conformation similar to that of KcsA in the crystal structure (PDB 1K4C [24]) with a conductive selectivity filter and a closed ion conduction pathway (see Section 1.2). Based on our resonance assignments, we set out to determine the conformation of KcsA-Kv1.3 at pH 4.0 which, according to electrophysiology, was expected to correspond to an open-inactivated state. To titrate KcsA-Kv1.3 proteoliposome samples to pH 4.0, we removed them from solid-state NMR rotors, resuspended them in 100 mM citrate buffer at pH 4.0, and pelleted them again by ultracentrifugation before back-transfer to solid-state NMR rotors. This procedure could be repeated multiple times for a single sample without evident degradation, which was useful for further such titrations reported in Section 1.4. We recorded the same types of (^{13}C,^{13}C) and (^{15}N,^{13}C) solid-state NMR experiments as detailed in Section 1.2.

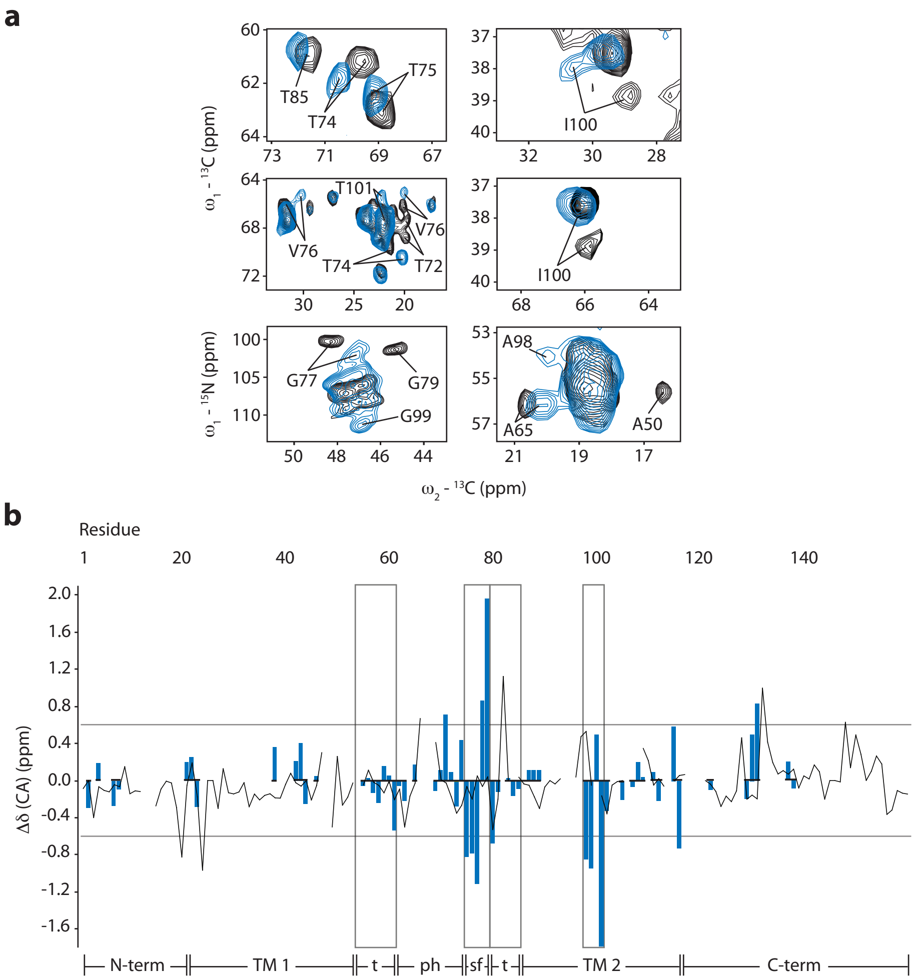

Figure 1.6: Comparison of ssNMR data for KcsA-Kv1.3 at pH 7.5 and pH 4.0. **(a)** Sections of (^{13}C,^{13}C) and (^{15}N,^{13}C) ssNMR correlation spectra at pH 7.5 (black) and pH 4.0 (blue). Resonances assigned to residues within the selectivity filter, pore helix, TM2 helix and turret regions are labeled. **(b)** Summary of C$^{\alpha}$ chemical shift changes observed for KcsA-Kv1.3 at pH 4.0 (blue bars) compared to pH 7.5. Horizontal lines at ±0.6 ppm indicate the threshold chosen for substantial chemical shift changes. Lines below (N-term, N-terminus; TM1, transmembrane helix 1; t, extracellular turret; ph, pore helix; sf, selectivity filter; TM2, transmembrane helix 2; C-term, C-terminus) schematically show secondary structure along the sequence as seen in ssNMR. Rectangular frames highlight the selectivity filter, TM2 gating hinge and turrets. For comparison, chemical shift changes between pH 7.0 and pH 4.0 described for KcsA in foscholine micelles [43] are shown as a solid black line.

Globally, the spectra obtained at pH 4.0 were very similar to those at pH 7.5, indicating that channel integrity was preserved. However, distinct spectral changes were observed in defined regions of the channel, mostly in the selectivity filter and in a region around a conserved glycine residue (Gly99) in transmembrane helix 2 (TM2; Fig. 1.6). In the related MthK channel that had been crystallized with the ion conduction pore in an open conformation, the TM2 helices bend at the corresponding glycine "hinge" residue, opening an internal cavity large enough to allow for the passage of ions [51], while in the KcsA crystal structure, the TM2 helices form a narrow bundle crossing below the hinge preventing ion conduction [24]. Our data thus imply that pH-dependent gating in KcsA-Kv1.3 is associated with defined local conformational changes in functionally important regions, *i.e.* gating hinge and selectivity filter. Notably, the chemical shift changes we observed differ considerably from those reported for KcsA in foscholine micelles upon a pH change from 7.0 to 4.0 ([43], see black line in Fig. 1.6 b), again pointing to the importance of a membranous environment for the study of ion channel structure and function.

Unfortunately, N/CHHC through-space correlation experiments [54] did not yield meaningful information on the conformation of KcsA-Kv1.3 at pH 4.0. We thus resorted to an analysis of chemical shifts, attempting to derive a set of backbone dihedral angles that could reasonably account for the chemical shifts we observed in the selectivity filter and the gating hinge region at pH 4.0. To do so, we systematically varied the backbone (ϕ,ψ) dihedral angles of these residues individually in PDB models of the KcsA crystal structure (PDB 1K4C [24]) and calculated their corresponding expected chemical shifts using SHIFTX [46]. Dihedral angle pairs yielding best agreement of calculated and experimental C^α, C^β secondary chemical shifts [40] and requiring the smallest angular change with respect to the KcsA crystal structure (taken as the conformation of KcsA-Kv1.3 at pH 7.5) were then selected. For residues Gly77 and Gly79 with their large accessible conformational space, this procedure did not yield an unambiguous result. Consequently, we performed simulated annealing of the selectivity filter region in CNS [55], allowing Gly77 and Gly79 to adjust freely while restraining neighboring residues to dihedral angles as found in the chemical shift analysis. This procedure yielded probable dihedral angles for these residues as well, with SHIFTX-predicted chemical shifts in close agreement with experimental values. Results are shown in Figure 1.7.

In structural terms, results of this procedure for the selectivity filter are shown in Figure 1.8. A hallmark of the conductive conformation of the K^+ channel selectivity filter (PDB 1K4C) is a regular, in-line arrangement of backbone carbonyls (Fig. 1.8 a). Observed

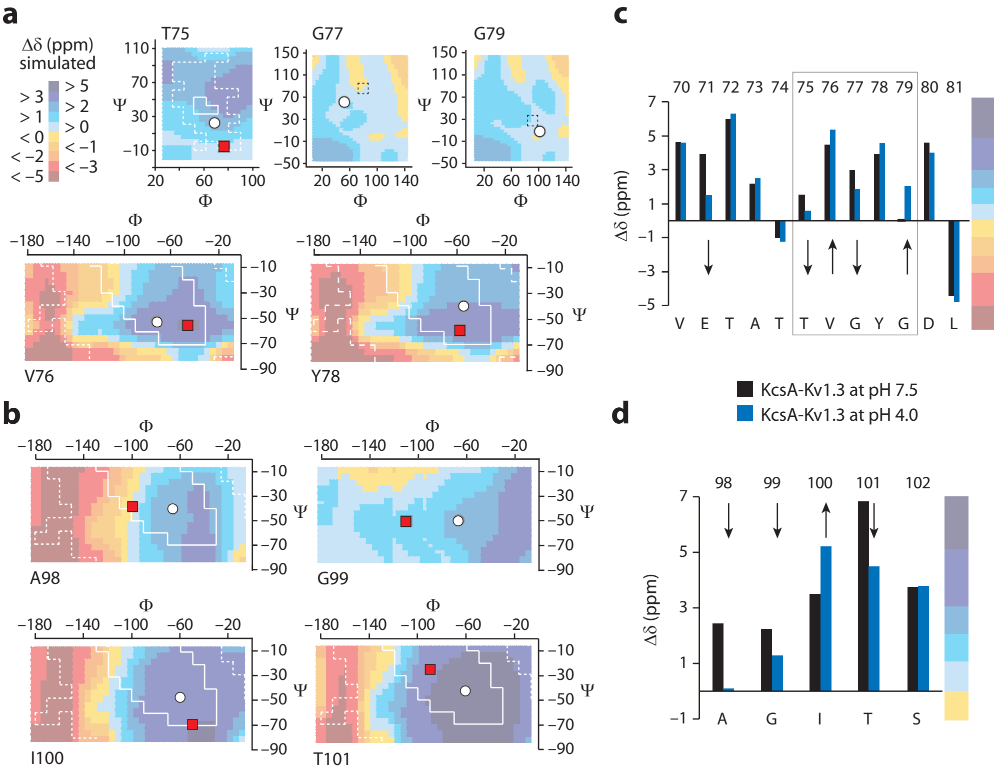

Figure 1.7: Analysis of changes in KcsA-Kv1.3 backbone conformation associated with pH-dependent gating. **(a, b)** Surfaces representing SHIFTX-calculated secondary chemical shifts ($[\delta(C^{\alpha})-\delta(C^{\alpha}_{\text{ref}})]-[\delta(C^{\beta})-\delta(C^{\beta}_{\text{ref}})]$) as a function of dihedral angles ϕ and ψ, for residues composing the selectivity filter (a) and the TM2 gating hinge (b), are shown as a color code. White circles indicate dihedral angles for the crystal structure of KcsA (PDB 1K4C). Red or broken squares indicate dihedral angle pairs for which the best agreement between SHIFTX-calculated secondary chemical shifts and their experimental values at pH 4.0 is found (for details, see text). Core (white, solid line) and allowed (white, dashed line) regions of Ramachandran space are given according to ref. [56]. **(c, d)** Experimental secondary chemical shifts (in ppm) for KcsA-Kv1.3 at pH 7.5 (black) and pH 4.0 (blue) are given for residues Val70 to Leu81 (c) and residues Ala98 to Ser102 (d). The black frame in (c) indicates the selectivity filter. Arrows show directions of changes in secondary chemical shift from pH 7.5 to pH 4.0. For direct comparison to panels (a) and (b), the color gradient on the right illustrates the same color code for secondary chemical shifts as used for plotting SHIFTX-calculated secondary chemical shift surfaces in (a) and (b).

chemical shift changes for the selectivity filter at pH 4.0 thus likely reflect a movement out of line of these carbonyls. This is indeed what is suggested by the set of dihedral angles we derived for these residues (Fig. 1.8 b). Notably, the conformation derived from solid-state NMR data is similar to the one described for the KcsA selectivity filter in low concentrations of potassium, which is presumably nonconductive to potassium ions (PDB 1K4D [24], Fig. 1.8 c). Conversely, secondary chemical shifts predicted by SHIFTX for this nonconductive KcsA conformation found in different crystal structures [24, 57, 58] agree well with those measured for KcsA-Kv1.3 at pH 4.0 (Fig. 1.8 d). It thus appears that inactivation of the KcsA-Kv1.3 K$^+$ channel is associated with a change in selectivity filter

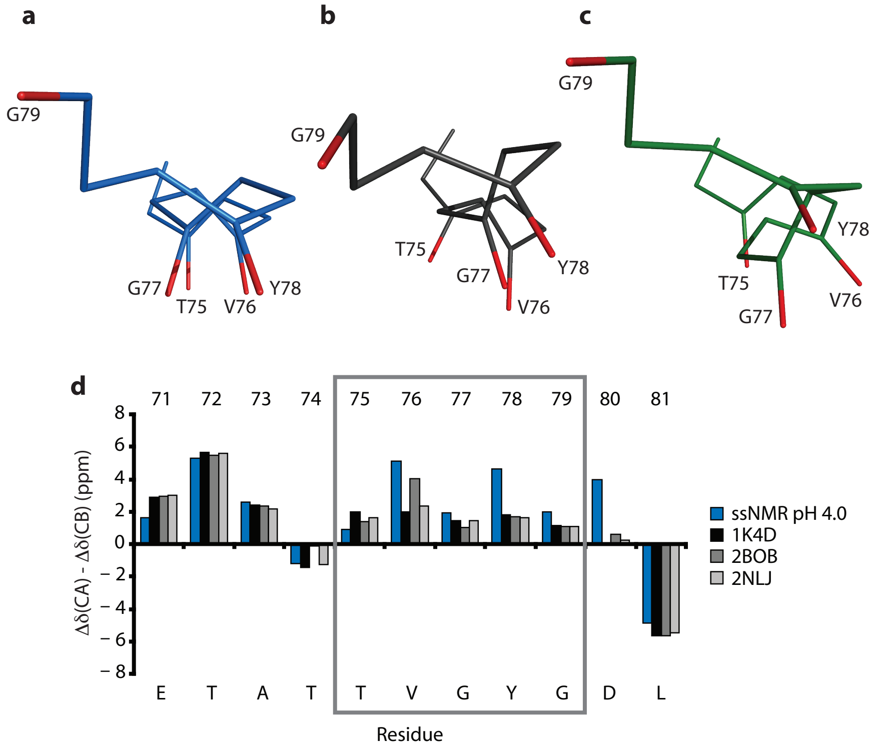

Figure 1.8: View on the selectivity filter backbone of one channel subunit from the extracellular side, down the ion conduction pore. **(a)** Conductive conformation of the selectivity filter as seen in KcsA at high potassium concentrations (PDB ID 1K4C) [24]. **(b)** Model of the selectivity filter of KcsA-Kv1.3 at pH 4.0 determined from ssNMR data as described in the text. **(c)** Collapsed KcsA selectivity filter as seen in low potassium concentrations (PDB 1K4D) [24]. **(d)** Comparison of experimental secondary chemical shifts ($\Delta\delta$(CA)-$\Delta\delta$(CB)) in the selectivity filter region at pH 4.0 (blue) with SHIFTX [46] predictions of secondary chemical shifts for crystal structures of KcsA with the selectivity filter in a collapsed conformation (PDB 1K4D [24], 2BOB [57], and 2NLJ [58]).

conformation that resembles the switch to the nonconductive low-potassium conformation of the KcsA K^+ channel.

Strikingly, in our study, my colleague Christian Ader found that binding of a tetraphenylporphyrin channel blocker [59] to KcsA-Kv1.3 at neutral pH results in chemical shifts in selectivity filter residues identical to those observed for free KcsA-Kv1.3 at pH 4.0. Available data suggests that the porphyrin inserts one of its four arms into the selectivity filter [25]. The underlying common principle thus seems to be that both inactivation and channel block by the porphyrin generate a low K^+ occupancy in the selectivity filter.

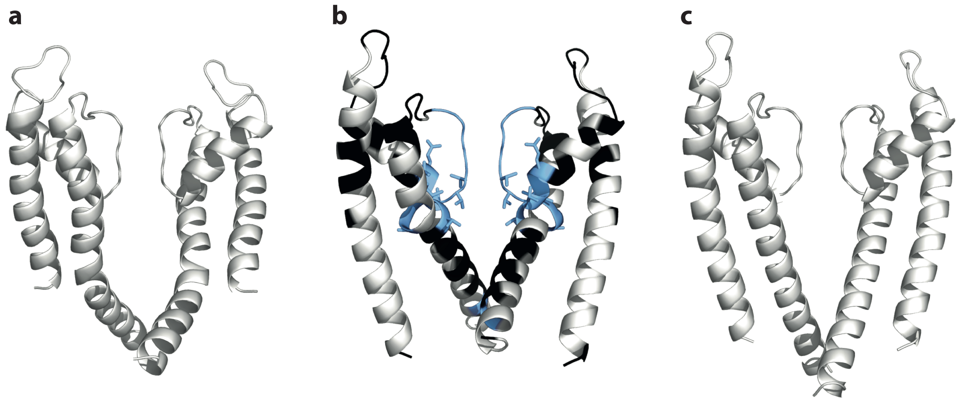

Figure 1.9: **(a)** Crystal structure of the pore domain of Kv1.2 crystallized in an open conformation (PDB 2A79 [16]). Note that the gating hinge in this eukaryotic channel is constituted by a Pro-Val-Pro motif situated further below in the TM2 helix than the glycine residue serving as gating hinge in KcsA. **(b)** Structural model of KcsA-Kv1.3 at pH 4.0, with dihedral angles in selectivity filter and TM2 gate as obtained by chemical shift analysis and restrained simulated annealing as described in the text. Residues assigned both at pH 4.0 and 7.5 are colored blue if C^α chemical shift changes above 0.6 ppm were observed between the two states and black otherwise; unassigned residues are grey. Sidechains are indicated for residues with considerable sidechain chemical shift changes. **(c)** KcsA-Kv1.3 structural model at pH 7.5 (corresponding to the KcsA crystal structure (PDB 1K4C [24]) with introduced Kv1.3 mutations).

For the gating hinge region around Gly99 in TM2, which forms a straight helix in the KcsA crystal structure and, according to our chemical shifts, also in KcsA-Kv1.3 at neutral pH, our analysis indicates changes in backbone dihedral angles at pH 4.0 suggesting a break in helical structure. Indeed, the dihedral angles extracted from our analysis, when entered into a PDB model of KcsA, lead to a bend in the TM2 helix and, consequently, opening of the inner TM2 helix bundle of the channel, corresponding to opening of the activation gate for the passage of ions [51]. The resultant model resembles structures of K^+ channels crystallized in an open conformation [15, 16, 51] (Fig. 1.9).

Overall, our data imply that, at pH 4.0, the KcsA-Kv1.3 channel exhibits an opened activation gate and a collapsed selectivity filter corresponding to a closed inactivation gate, in agreement with a large body of K^+ channel data [12, 32, 53]. Notably, these results were obtained in buffers without potassium. The permeant ion of K^+ channels does however influence their gating, as detailed in the next section.

1.4 Coupling of activation and inactivation gates in KcsA-Kv1.3 (Ader, Schneider et al., EMBO J. 2009 [34])

Section 1.3 described two gates controlling ion flow in the KcsA-Kv1.3 channel, namely activation and inactivation gate associated with transmembrane helix 2 (TM2) and selectivity filter, respectively [12, 32, 60]. Both gates may be open and closed, leading to a (possibly simplified) description of channel gating in terms of four states, closed state C,

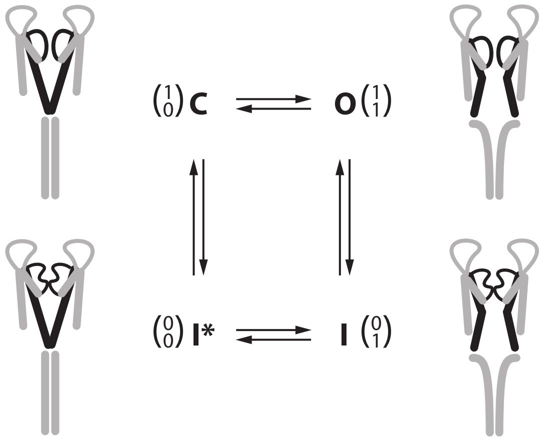

Figure 1.10: A four-state minimal gating model with an upper (inactivation) and a lower (activation) gate in the conduction pathway of the KcsA-Kv1.3 channel. Gate positions (0 for closed and 1 for opened) are diagrammed in one-column matrices with upper gate in upper and lower gate in lower row. C – closed channel in resting state; O – opened channel; I and I* – inactivated states. Pictograms of two KcsA-Kv1.3 subunits sketch corresponding conformational states of selectivity filter and TM2 helix (black). TM1 and pore helices, turret loop and C-terminus are also indicated (grey). The N-terminus is omitted for clarity.

opened state O, and inactivated states I and I* (Fig. 1.10) [60]. In these terms, states C and I of KcsA-Kv1.3 were characterized in the previous sections.

To coordinate conformational transitions in the gating cycle, coupling between activation and inactivation gates may be expected, as has indeed been described for voltage-gated K^+ channels [60–63]. However, at the time of my thesis, it was not well understood how such a coupling could be implemented in structural terms.

Using solid-state NMR, we indeed found evidence for gate coupling, starting from the rather fortuitous observation that opening of the activation gate in KcsA-Kv1.3 at pH 4.0 depends on potassium concentration. As mentioned, data reported on in previous sections were obtained in buffers without added potassium (see Section 1.2). Under these conditions, a change of pH to 4.0 leads to activation gate opening and selectivity filter collapse, as described in Section 1.3 (Fig. 1.11 a, blue spectrum). However, in the presence of millimolar concentrations of K^+ ($\geq$ 10 mM, keeping total ionic strength constant), the spectral signature of KcsA-Kv1.3 at pH 4.0 remains essentially identical to that seen at pH 7.5 (Fig. 1.11 b, red spectrum), suggesting that the activation gate remains closed and the selectivity filter conductive. For the transmembrane activation gate, this result was confirmed by independent experiments probing the water-accessible surface of KcsA-Kv1.3 at pH 7.5 and 4.0 [64–66]. Without added potassium, the water-accessible surface of KcsA-Kv1.3 increases significantly at pH 4.0 as expected for an opening of the TM2 helix bundle, while in the presence of 50 mM potassium, the water-accessible surface remains close to its value at pH 7.5 [34].

These data demonstrate that gating of KcsA-Kv1.3 is sensitive to potassium and that, in the presence of millimolar K^+ concentrations, the closed-conductive conformation representing a KcsA-Kv1.3 channel at rest prevails in liposomes even at pH 4.0. (In hindsight, we were thus lucky to have used a buffer without potassium for the previous parts of this study, since otherwise we would probably never have observed the open-inactivated conformation at pH 4.0.) This result was unexpected, given that a transition to acidic pH in the presence of millimolar K^+ concentrations clearly opens KcsA-Kv1.3 in electrophysiology experiments, reflected in a measurable ionic current, before leading to inactivation (Fig. 1.1 b). However, solid-state NMR experiments were obviously conducted in the absence of a transmembrane potential that would drive K^+ ions through the channel, which may well account for these differing observations.

A further reporter for the state of activation gate and selectivity filter was found in the chemical shift of sidechain δ carbon atoms of glutamate residues, known to be correlated

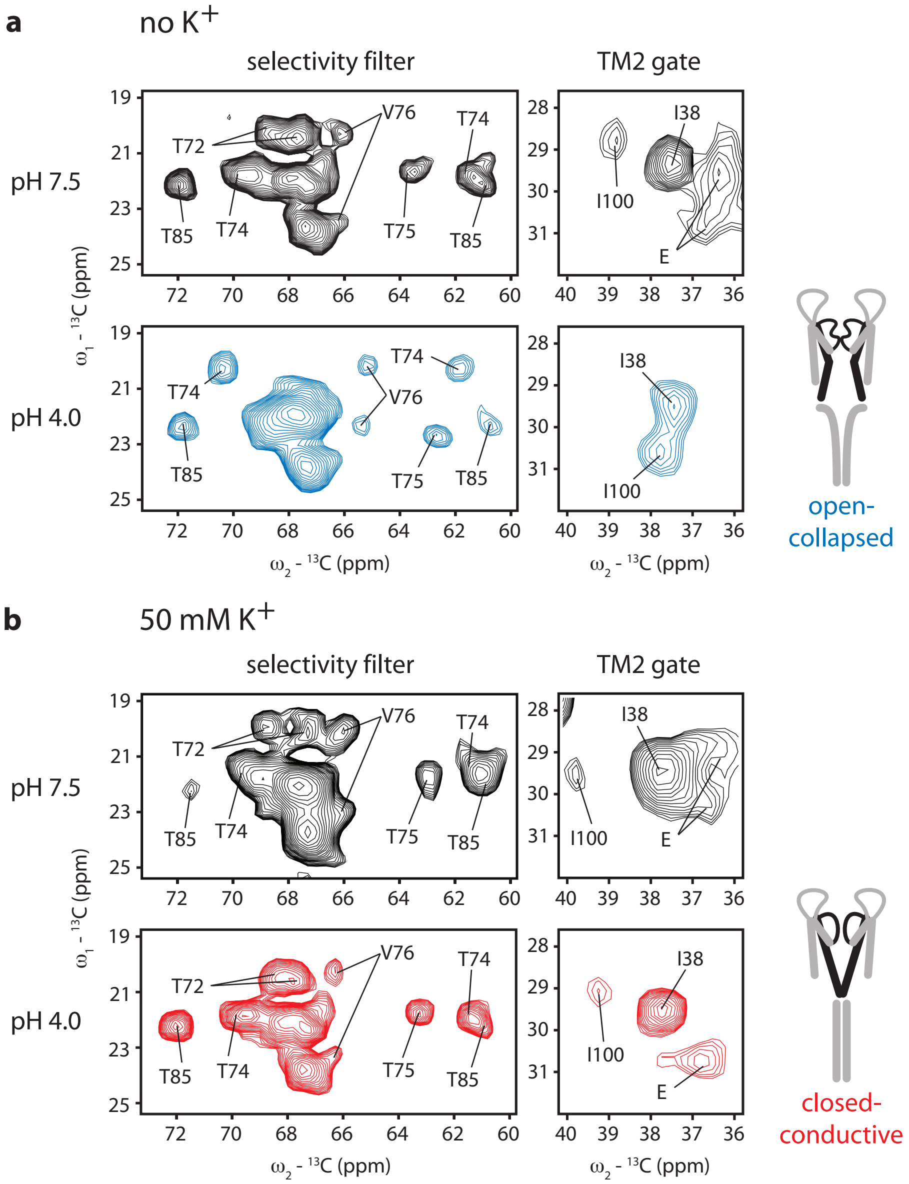

Figure 1.11: Regions of PDSD (^{13}C,^{13}C) correlation spectra of KcsA-Kv1.3 in the absence **(a)** and presence **(b)** of potassium (50 mM) at pH 7.5 (black spectra) and pH 4.0 (blue/red spectra). Pictograms as in Figure 1.10 indicate the conformational state of KcsA-Kv1.3 at pH 4.0 with and without potassium. The open-collapsed conformation of KcsA-Kv1.3 is induced stably at pH 4.0 in the absence of potassium **(a)**, but not in the presence of millimolar concentrations of potassium **(b)** as seen from chemical shift analysis.

with the protonation state of the carboxylic group [67, 68]. Mutational studies on KcsA had suggested that activation gate opening at acidic pH is associated with protonation of glutamate side chains, notably Glu118 and Glu120 at the lower end of the inner TM2 helix [69]. On the other hand, Glu71 behind the selectivity filter had been shown to

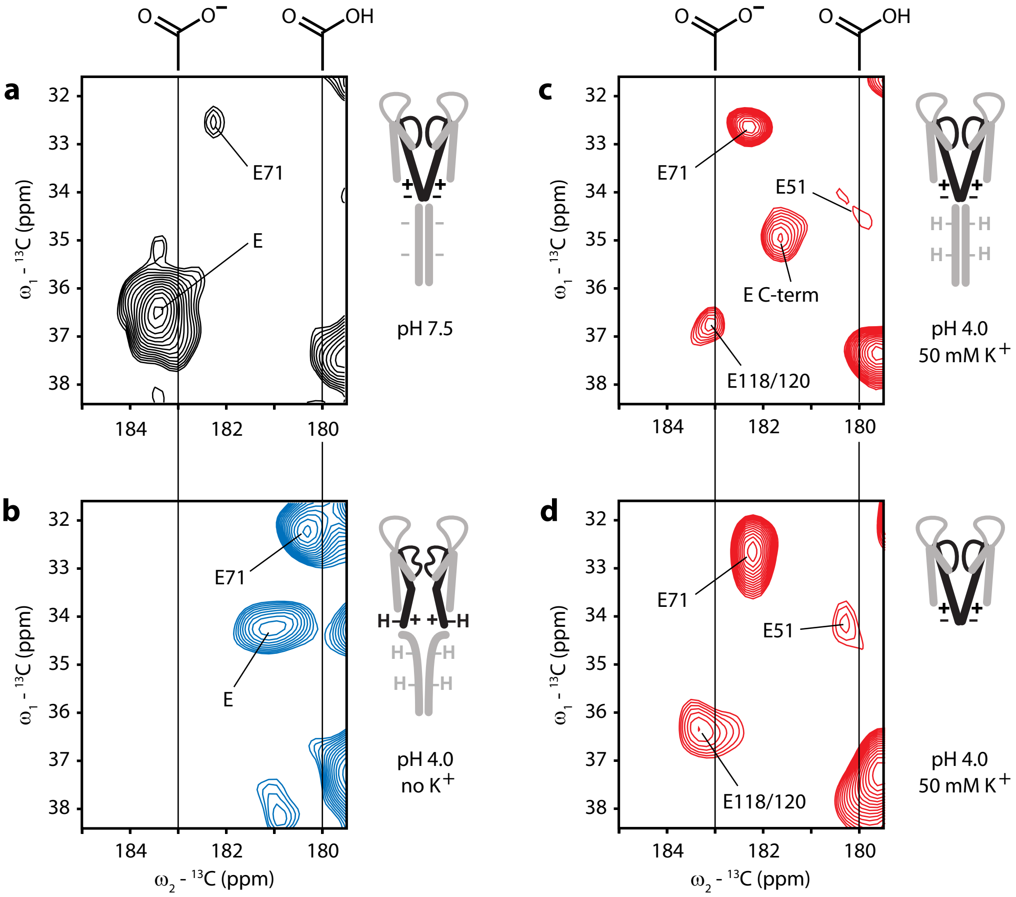

Figure 1.12: Protonation or hydrogen bonding state of glutamate sidechain carboxyls depends on pH and [K$^+$]. **(a-d)** Regions from (^{13}C,^{13}C) correlation spectra showing glutamate C$^\gamma$–C$^\delta$ cross-peaks for different pH and [K$^+$] conditions, as indicated below the pictograms. Literature values for protonated and deprotonated glutamate C$^\delta$ chemical shifts are indicated by vertical lines in the spectra. Charge and protonation states in lower TM2 helix and C-terminus are shown schematically in the pictograms. (d) shows a spectrum from C-terminally truncated KcsA-Kv1.3.

play an important role in inactivation gating in KcsA [32, 53]. We found chemical shifts of glutamate C$^\delta$ resonances suggesting that, at pH 7.5, all glutamates except Glu71 are deprotonated. At pH 4.0, in the absence of K$^+$, their more upfield chemical shifts indicate a (more) protonated state (Fig. 1.12 a, b). Notably, later explicit determination of the Glu71 sidechain protonation state via measurement of the C^{δ} chemical shift tensor has shown that it has an unusually high pK_a and is protonated already at pH 7.5. Its chemical shift change associated with the transition to acidic pH was interpreted by the loss of a hydrogen bond to the amide proton of Tyr78 observed in the transition from a conductive to a collapsed selectivity filter structure [70].

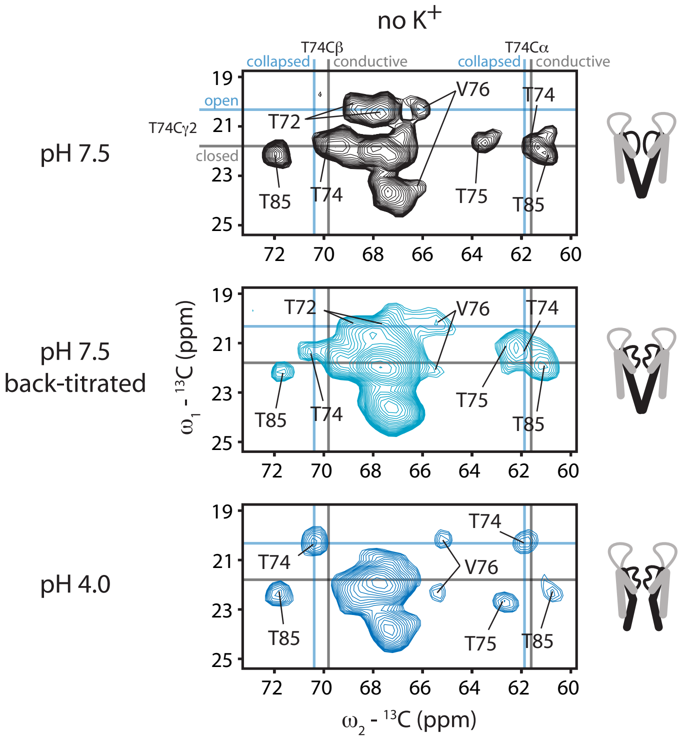

Figure 1.13: Regions from (^{13}C,^{13}C) PDSD spectra illustrating the conformation of the selectivity filter of KcsA-Kv1.3 at pH 7.5 (top, closed-conductive channel), at pH 7.5 after back-titration from pH 4.0 (center, closed-inactivated channel), and at pH 4.0 (bottom, open-inactivated channel), all in the absence of added potassium in the buffer. Pictograms on the right illustrate the overall conformations of selectivity filter and TM2 helix in the respective states. For Thr74, vertical lines indicate positions of C^{α} and C^{β} shifts indicative of selectivity filter conformation, while horizontal lines indicate positions of the sidechain $C^{\gamma 2}$ shift indicative of the state of the TM2 helix. In the closed-inactivated channel (center panel), sidechain $C^{\gamma 2}$ shifts of lower pore helix and lower selectivity filter threonines (Thr72, Thr74, Thr75) have shifted back to values seen at neutral pH before the titration, while C^{α} and C^{β} shifts of Thr74 and Thr75 as well as those of the other selectivity filter residues still correspond to the collapsed conformation as seen at pH 4.0.

Strikingly, at pH 4.0 in the presence of > 10mM potassium, only the solvent-exposed glutamates in turret (Glu51) and C-terminus (identified via disappearance of their resonance signal in C-terminally truncated KcsA-Kv1.3, Fig. 1.12 d) become protonated. The other two glutamate C^{γ}–C^{δ} crosspeaks, whose positions remain unchanged with respect to pH 7.5, correspond to Glu71 and the previously unassigned Glu118 and Glu120 in the TM2 helix. That is, for these glutamate residues, protonation or hydrogen bonding state appears to depend on the conformational state of selectivity filter and TM2 gate, which in turn depends on potassium concentration as well as on pH. The upfield-chemical-shift state of these glutamates is thus associated both with a stably opened activation gate (Glu118, Glu120) and with collapse of the selectivity filter (Glu71).

Notably, by back-titration of a KcsA-Kv1.3 sample from pH 4.0 to pH 7.5 in the absence of potassium, we could prepare a closed-inactivated state of the channel, corresponding to state I* in Figure 1.10 (Fig. 1.13). In this state, chemical shifts of residues in gating hinge, lower pore helix, and turret regions return to their values originally observed at neutral pH, as do all glutamate C^{γ}–C^{δ} sidechain peaks except that of Glu71, which remains at its position observed at pH 4.0, *i.e.* reporting on a still collapsed selectivity filter. Similarly, backbone resonances of selectivity filter residues remain at values corresponding to the collapsed selectivity filter. However, sidechain resonances of residues in the lower selectivity filter (Thr72–Thr75) move back to their values observed at pH 7.5. In fact, these sidechain resonances are always seen to shift together with resonances originating from the TM2 gate, rather than from the selectivity filter. This suggests that they are part of an interaction surface coupling inactivation gate to activation gate. Importantly, the closed-conductive conformation of the K^+ channel at pH 7.5 could be fully restored by adding 50 mM potassium to the buffer.

Previous reports had already indicated that activation gate and inactivation gate are coupled in potassium channels. In C-type inactivation, opening of the activation gate induces closure of the inactivation gate [10, 71]; on the other hand, inactivation gate closure can promote activation gate opening [60, 72]. Our observations that activation and inactivation gates are coupled in KcsA-Kv1.3 and that activation gate opening is influenced by the potassium concentration suggest that the selectivity filter, *i.e.* the inactivation gate, being the obvious potassium binding site of the channel, can influence the state of the TM2 helix, *i.e.* the activation gate. To test this hypothesis, we employed two ligands which bind to the selectivity filter and affect its conformation differently. The first one was the porphyrin ligand already mentioned in Section 1.3 [59] whose binding induces a collapsed

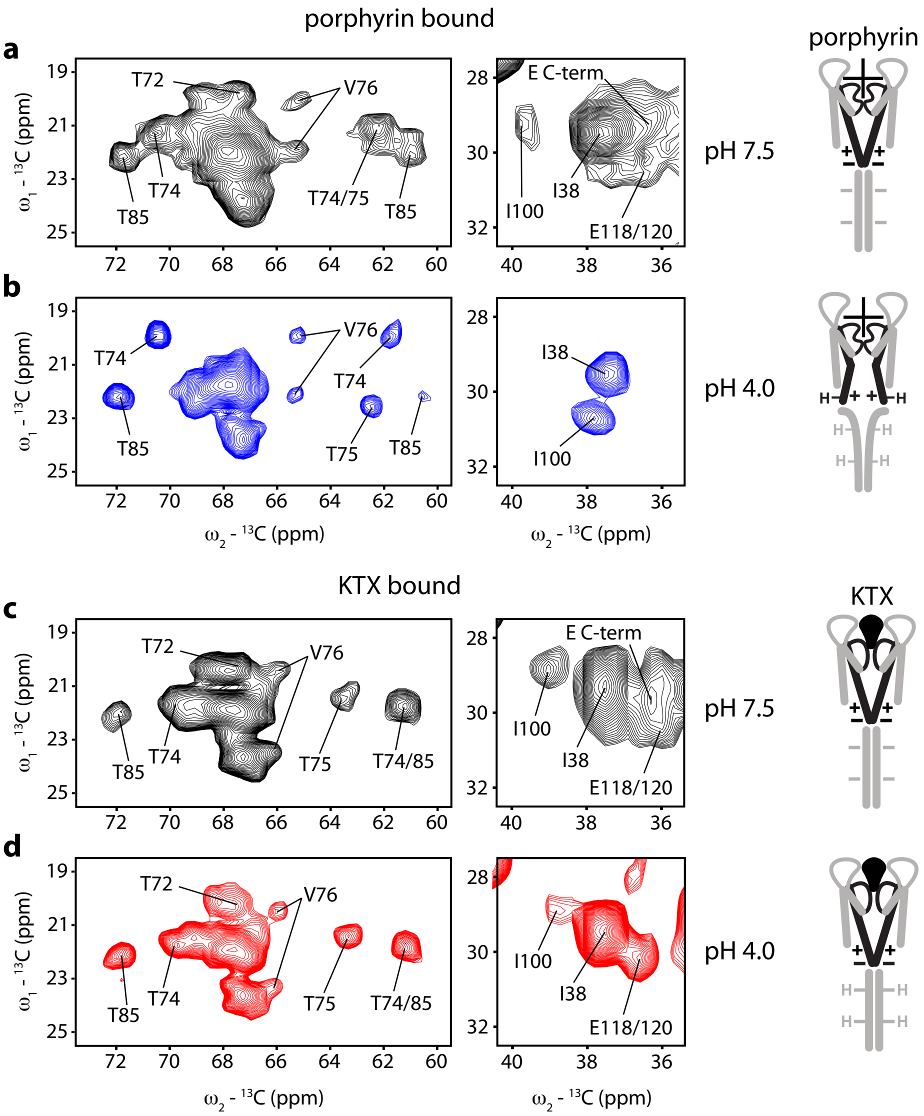

Figure 1.14: Spectral regions covering resonances of selectivity filter, gating hinge, and glutamate residues from turret, TM2 helix and C-terminus for KcsA-Kv1.3 bound to porphyrin **(a, b)** and KTX **(c, d)** in the absence of potassium at pH 7.5 (a, c) and pH 4.0 (b, d). Cartoons on the right illustrate the state of KcsA-Kv1.3 under the respective conditions in terms of selectivity filter and TM2 gate conformations as well as glutamate protonation and charge distribution in the lower TM2 helix linked to activation gating.

selectivity filter conformation at pH 7.5. Spectra of the KcsA-Kv1.3-porphyrin complex at pH 4.0 in the absence of K^+ are similar to those obtained for the unliganded channel, *i.e.* they report on an opened activation gate and a collapsed, nonconductive selectivity filter (Fig. 1.14 a, b). The second ligand we used was kaliotoxin (KTX), whose binding has been described to only affect upper selectivity filter residues [26] and to stabilize a conductive conformation in the selectivity filter [73]. Strikingly, spectra from the KTX-bound channel reveal that, in this state, the lower activation gate remains closed at pH 4.0 even if no potassium is added to the buffer solution (Fig. 1.14 c, d).

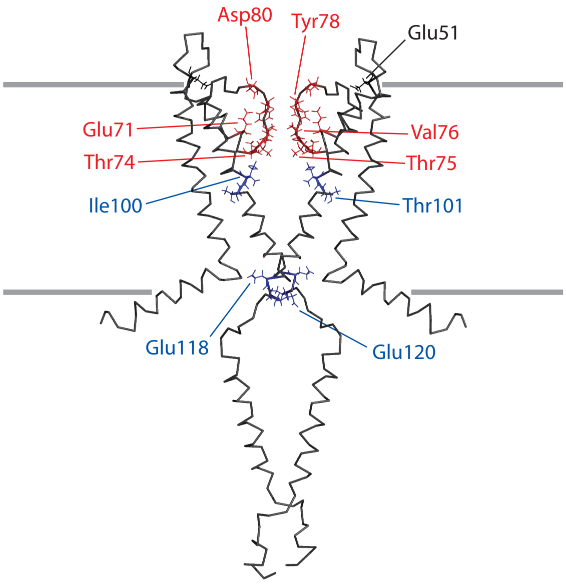

Figure 1.15: Structural model of KcsA-Kv1.3 (see [33]). Residues in activation and inactivation gates used as probes for channel conformation throughout the ssNMR experiments are indicated in blue and red, respectively. Only two channel subunits are shown for clarity. The approximate extent of the lipid bilayer is indicated by grey lines.

The important implication of these findings is that activation and inactivation gates in KcsA-Kv1.3 are indeed coupled, *i.e.* the conformation of the selectivity filter influences that of the TM2 helix and vice versa. A closed inactivation gate (collapsed selectivity filter) promotes a stably opened transmembrane activation gate, and conversely, opening of the transmembrane activation gate induces the collapsed conformation of the selectivity filter. On the other hand, an open inactivation gate (conductive selectivity filter) favors the closed conformation of the activation gate. The coupling appears to be implemented by sidechain interactions between residues in lower selectivity filter and TM2 gate including Thr74, Thr75, Ile100, and Thr101 which are close in space (Fig. 1.15). Our data imply that K^+, the permeant ion itself, modulates activation as well as inactivation gating, providing a scenario for coordinated, consecutive gating transitions involving opening, inactivation, and closing.

1.5 Conclusions

We have characterized structure and function of the chimeric potassium channel KcsA-Kv1.3 in lipid bilayers by solid-state NMR, in close reference to electrophysiological experiments. A large amount of initial work consisted in obtaining extensive resonance assignments of the channel, which served as a basis for the remainder of this study. Secondary structure analysis based on solid-state NMR chemical shifts showed close agreement with the crystal structure of the parent KcsA channel in the pore region and hinted at the presence of helical structure in the intracellular N- and C-termini. Our data also highlighted differences in helical content, as well as in secondary structure in functionally important regions, with respect to solution-state NMR data obtained in detergent micelles. Analysis of solid-state NMR data at pH 4.0 allowed for the generation of the first detailed structural model of the open-inactivated state of a potassium channel. Chemical shift analysis showed that the transmembrane activation gate opens by bending the TM2 transmembrane helix at a conserved glycine residue, as observed in the crystal structure of a related bacterial channel. Our analysis also indicated a collapsed selectivity filter conformation, similar to the one seen in low-potassium crystal structures of KcsA, as corresponding to the closed inactivation gate. Finally, we found that not only inactivation, but also activation gating is potassium-dependent. By stabilizing different selectivity filter conformations using two different ligands, we showed that it is the conformation of the selectivity filter that exerts an influence on the transmembrane activation gate via a steric coupling implemented by sidechains of the lower selectivity filter and the TM2 gating hinge.

In the years that followed publication of our results, activation and inactivation gating in KcsA were studied in further detail in a series of studies. The group of Ann McDermott published four studies that, while adding interesting aspects such as the hydration dependence of the KcsA selectivity filter collapse and the protonation state of the Glu71 sidechain, essentially reproduced and confirmed our results – obtained on KcsA-Kv1.3 –

for the parent KcsA channel [70, 74–76]. Notably, in these studies, as opposed to ours, opening of the transmembrane gate was also observed in low potassium concentration at neutral pH, as well as in the presence of (limited) amounts of potassium in acidic pH. Differences between KcsA and KcsA-Kv1.3 as well as the different lipid systems used may account for these differing observations.

Like our work, the studies by Ann McDermott and coworkers also concluded that the inactivated state of the channel most likely consists in the low-potassium collapsed conformation of the selectivity filter, as did a solution-state NMR study of KcsA in dodecyl maltoside micelles by Ichio Shimada's group [77]. These scientists also managed to observe the open-activated channel state, which had remained elusive in liposomes.

In a string of high-profile publications, the group of Eduardo Perozo finally achieved crystallization of full-length KcsA in its closed state [47] and then in different states of opening and inactivation [78–80]. Their data showed the channel C-terminus to indeed be nearly fully helical and to form a four-helix bundle. Our results on opening, incativation and gate coupling are in close agreement with their findings. Opening of the transmembrane gate is seen to occur by bending of the TM2 helices. The hinge of this motion, showing strongest deviation from helical structure, is however seen in residue Gly104 in the crystal structures, not in Gly99 as deduced from our chemical shifts. We could not observe Phe103 or Gly104 in our data at pH 4.0, so a conformational change in KcsA-Kv1.3 in these residues may have escaped us. However, the chemical shift changes we observed clearly indicated a structural change in residues Ala98–Thr101, while Ser102 did not exhibit a change in its chemical shift. Given that this region of the TM2 helix disposes of two glycine residues, both may in principle act as gating hinges, and the difference may be related to the presence or absence of a lipid bilayer. On the other hand, the structure of the TM2 helix in the open KcsA crystal structure (PDB 3F5W [79]) is seen to begin to deviate from that of its counterpart in closed KcsA (PDB 1K4C [24]) at residue Ala98, which may reconcile these observations.

In the crystal structures of open KcsA, it is observed that, the further the TM2 helix bends, the more the sidechains of residues near the gating hinge (notably Ile100 and Phe103) exert steric strain on the selectivity filter (via Thr74 and Thr75), leading to a conformational change in the selectivity filter for the most open structures, in full agreement with our results [78]. The limited resolution of these crystal structures did not allow to conclusively establish the exact conformation of the selectivity filter, but the electron density corresponds closely to the collapsed conformation seen in the low-potassium crystal structure [79], as also indicated by our data.

A recent publication from the laboratory of Francis Valiyaveetil has however again cast doubt on what appeared to be the resolution of the long-standing mystery of potassium channel C-type inactivation [81]. Using semisynthetic channels, these researchers introduced the unnatural amino acid D-alanine into the selectivity filter of KcsA and KvAP channels, replacing Gly77 in the selectivity filter. With this substitution, the selectivity filter cannot assume the low-potassium collapsed conformation due to steric hindrance. However, functional experiments clearly showed that these channels can undergo classical C-type inactivation like wild-type channels. It was suggested that the collapsed selectivity filter conformation may not correspond to the C-type inactivated state, but rather to a different, long-lived deeply inactivated or “defunct” state, which has been described for some potassium channels upon K^+ removal [82]. However, very recently, a molecular dynamics simulation study reinforced the notion that collapsed and C-type inactivated conformations of the selectivity filter are identical and indicated that D-alanine in position 77 actually does not inhibit the KcsA selectivity filter from assuming an asymmetric collapsed-like conformation [83]. Hence, while the debate about the true C-type inactivated conformation of potassium channels still does not appear to be fully settled, our and others’ finding that a collapsed selectivity filter conformation plays a role in potassium channel gating certainly remains relevant.

Chapter 2

Molecular mobility by double-quantum solid-state NMR spectroscopy (Schneider et al., J. Am. Chem. Soc. 2010 [84])

2.1 Introduction

NMR spectroscopy can provide information on dynamics in biomolecules on a wide range of time scales. In solution, relaxation approaches have long been used to probe fast motion on the pico- to nanosecond time scale, up to the rotational correlation time of the molecule [85]. Motion on such time scales has been shown to be relevant, e.g., for conformational entropy and thus the free energy of complex association [86, 87]. On the other hand, rotating-frame ($R_{1\rho}$) and Carr-Purcell-Meiboom-Gill (CPMG) relaxation dispersion, chemical exchange saturation transfer (CEST) and ZZ-exchange methodologies allow to probe the time scale from microseconds to the second, where important dynamic processes such as allostery, enzyme catalysis, ligand binding, and fast folding processes occur [88–90]. The gap between these time scales has in recent years been closed by exploiting the dynamic information in residual dipolar couplings (RDCs) which are sensitive to dynamics on all time scales up to the millisecond [91, 92].

Solid-state NMR also offers a wide range of techniques to measure molecular dynamics. In some respects, access to dynamic information is more direct in the solid state than in solution. Due to the absence of overall molecular tumbling, relaxation measurements are sensitive to motions up to the millisecond [93]. In addition, anisotropic parameters which provide information on dynamic amplitudes, such as the dipolar coupling, are not averaged out by molecular motion, but directly present in the coherent Hamiltonian (or can be reintroduced by appropriate recoupling pulse sequences) [93]. However, other challenges arise, such as the difficulties of separating motionally induced incoherent relaxation from coherent dephasing effects [94] and of precisely measuring anisotropic parameters [95]. Nevertheless, the rich dynamic information content of solid-state NMR data has been more and more exploited in recent years [93, 96].

For obtaining site-specific information on dynamics from dipolar couplings in the solid state, typically, one-bond heteronuclear ^{1}H-^{15}N or ^{1}H-^{13}C couplings are measured [97, 98]. In the study described in this chapter, I developed an approach to detect complementary modes of motion, measuring ^{13}C-^{13}C couplings in uniformly (^{13}C,^{15}N)-labeled proteins via recording the build-up of double-quantum coherence. The method was developed on a small model molecule, L-tyrosine-ethylester (TEE, Fig. 2.1), and applied to the protein ubiquitin to find out whether chemical shift differences observed between different solid-phase ubiquitin preparations could be related to differences in local dynamics. Later, I applied this method to study dynamics in the mitochondrial membrane protein VDAC (see Chapter 3).

2.2 Methodology and verification on TEE

In solids, molecular motion leads to (partial) averaging of rank 2 components of anisotropic interactions such as the dipolar coupling, as long as the motion is faster than the inverse coupling strength in frequency units. This manifests itself as a reduced effective coupling, reflected for example in a delayed time course of build-up of a coherence that relies on this coupling. The effective coupling can be extracted by recording such a build-up – *via* different mixing times of an appropriate recoupling sequence – and fitting it to numerical simulations of the spin system of interest under the pulse sequence used, applying different simulated coupling strengths. For the one-bond dipolar coupling of two spins i, j, the rigid limit value is given by $d_{ij,\mathrm{rigid}} = \frac{\mu_0}{4\pi}\hbar\frac{\gamma_i\gamma_j}{r_{ij}^3}$ (in units of rad·s^{-1}) with μ_0 the vacuum permeability, $\hbar$ the reduced Planck's constant, γ_i, γ_j the spins' gyromagnetic ratios and an internuclear distance r_{ij}. An order parameter S ($0 \leq S \leq 1$) quantifying the amplitude of the motion can then be defined as the ratio of the fitted effective coupling and its rigid-limit value, $S = d_{\mathrm{exp}}/d_{\mathrm{rigid}}$, where $S = 0$ indicates fully isotropic motion and $S = 1$ the rigid limit.

To measure the ^{13}C-^{13}C coupling, we chose to use the symmetry-based SPC5 recoupling sequence [101] in the context of 2D double quantum–single quantum (2Q,1Q) correlation

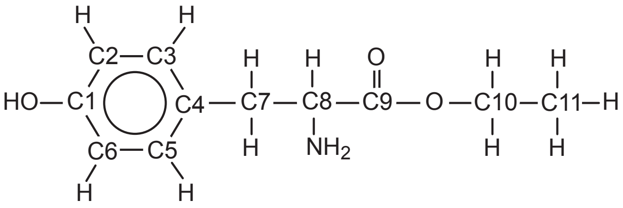

Figure 2.1: Schematic representation of L-tyrosine-ethylester (TEE) [99, 100].

experiments. In order to relate experimental data to local mobility, we first examined the polarization transfer dynamics for a dipolar coupled ^{13}C spin network in detail. For spin system simulations, we used the GAMMA software package [102], considering spin system geometry and isotropic chemical shifts. These simulations revealed that, to adequately capture the fastest buildup characteristics observed experimentally in uniformly ^{13}C-labeled TEE, the ^{13}C spins directly bonded to the two ^{13}C spins contributing to the 2Q coherence of interest have to be included in the simulations, leading to 4-spin simulations in most cases (e.g. containing C_4, C_7, C_8, and C_9 spins for the double-quantum coherence of the TEE C_7-C_8 spin system). Motion was represented by uniformly scaling all (one-bond) dipolar couplings in the spin system by an order parameter S between 0 and 1. Results for 2- and 4-spin systems are shown in Figure 2.2 a.

(2Q,1Q) spectra were recorded on microcrystalline TEE at a sample temperature of about -2°C on a 400 MHz spectrometer at a MAS speed of 7.8 kHz. Double-quantum excitation and reconversion times using the SPC5 pulse sequence were varied between 154 and 1436 μs. Spectra were imported into MATLAB (The MathWorks, Natick, MA, USA) using the MatNMR package [103]. Extraction of cross-peak intensities and least-squares fitting to GAMMA simulations was performed using custom-written MATLAB scripts. A cut-out from an example spectrum is shown in Figure 2.2 b.

Experimental and best-fitting simulated build-ups for carbons C_8 and C_{10} are depicted in Figure 2.2 c. Note that build-ups of the two cross-peaks reporting on the same 2Q coherence should yield identical S_{CC} values; within the S_{CC} uncertainty usually determined to be ±0.05, this is always the case. Within experimental accuracy, all spin pairs in TEE except for the (C_{10},C_{11}) moiety are described by ^{13}C-^{13}C order parameters (S_{CC}) close to 1, in agreement with previous ssNMR studies of (^{1}H,^{13}C) one-bond couplings [99] (Fig. 2.3). The (C_{10},C_{11}) spin pair is best described by an order parameter of 0.80. This value is larger than the average value (0.62) of the ^{1}H-^{13}C order parameters (S_{HC}) determined for C_{10}

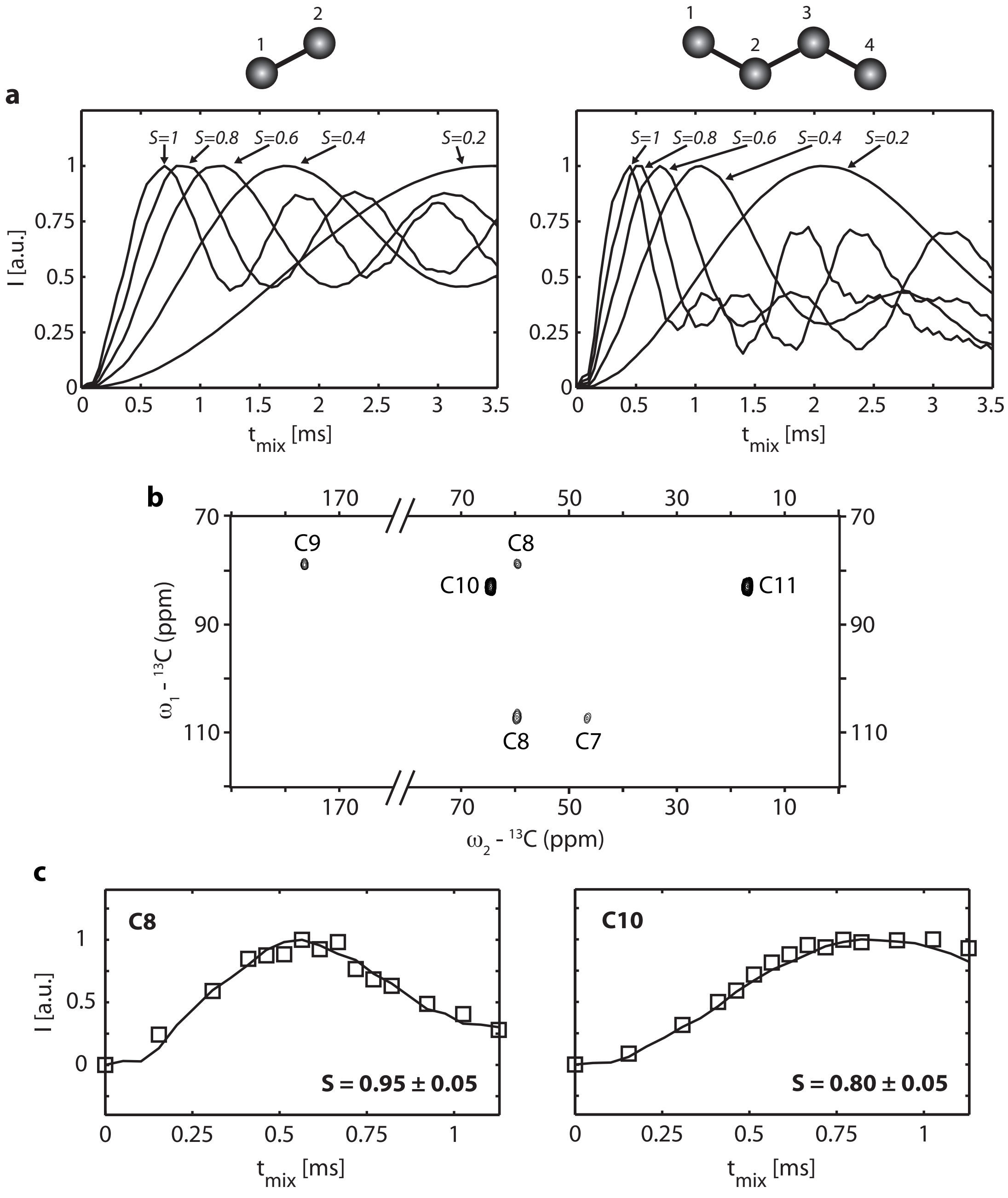

Figure 2.2: **(a)** Theoretical signal evolution for spin 1 (2-spin system, left) and spin 2 (4-spin system, right) in a 2D (2Q,1Q) correlation experiment for variable order parameters S. Intensities shown are calculated for double-quantum coherences between spins 1 and 2 (a) and between spins 2 and 3 (b), respectively, and are normalized to the maximum. Double-quantum excitation and reconversion times of length t_{mix} each were simulated for the SPC5 sequence [101]. **(b)** Cut-out of a 2D (2Q,1Q) correlation experiment on TEE for t_{mix} = 923 μs. **(c)** Experimental 2Q cross-peak signal evolution (squares) and best-fitting numerical simulations (lines) for the TEE ^{13}C spins indicated in the panels. Order parameters S of best-fitting simulations are given. Error bars of experimental data determined from spectral noise are smaller than the data points.

and C_{11} [99]. This can be expected since S_{HC} should also be sensitive to rotations around the C_{10}–C_{11} bond, which do not affect the effective (^{13}C,^{13}C) coupling between these two nuclei. S_{CC} and S_{HC} thus probe different modes of motion. Conversely, the fact that S_{CC} is significantly lower than 1 for (C_{10},C_{11}) indicates that the ester tail exhibits modes of motion in addition to such bond rotation, e.g. a nutation as suggested in ref. [100]. Our data thus confirm previous results that polycrystalline TEE is rigid at the temperatures investigated, except for the ethyl ester tail.

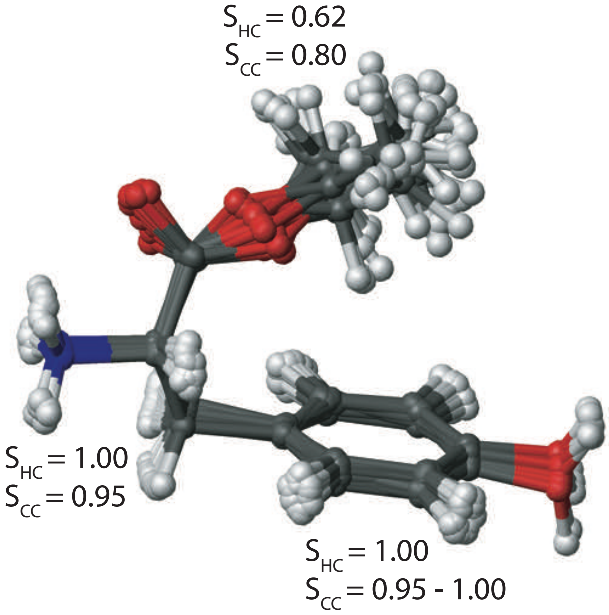

Figure 2.3: Comparison of dipolar (^{1}H,^{13}C) and DQ (^{13}C,^{13}C) order parameters for the (C2,C3), (C5,C6), (C7,C8), and (C10,C11) spin pairs of TEE. In both cases, values obtained from individual cross-peak buildups were averaged between the two nuclei involved. (^{1}H,^{13}C) order parameters and the molecular model of polycrystalline TEE are taken from ref. [99].

2.3 ^{13}C-^{13}C order parameters in microcrystalline ubiquitin

Microcrystalline preparations of (soluble) proteins have been shown to yield high quality solid-state NMR spectra while largely preserving native protein structure [104]. However, details of the preparation of protein microcrystals may influence NMR spectral parameters such as chemical shift, especially in regions known to exhibit increased dynamics in solution [104–106]. Such chemical shift differences between different solid-phase preparations and with respect to solution-state NMR chemical shifts had been reported for the 76-residue protein ubiquitin [106] (Fig. 2.4 a). This protein fulfils a wide variety of cellular functions, among the best known of which is the targeting of proteins for proteasomal degradation [107, 108], and has long been a classic model protein for studies of protein structure and dynamics by solution- and solid-state NMR [97, 109–111]. Here, two different solid-phase preparations – obtained by crystallization in poly(ethylene glycol) (PEG, "Ubi-P" [106]) and 2-methyl-2,4-pentanediol (MPD, "Ubi-M" [111]) – were considered.

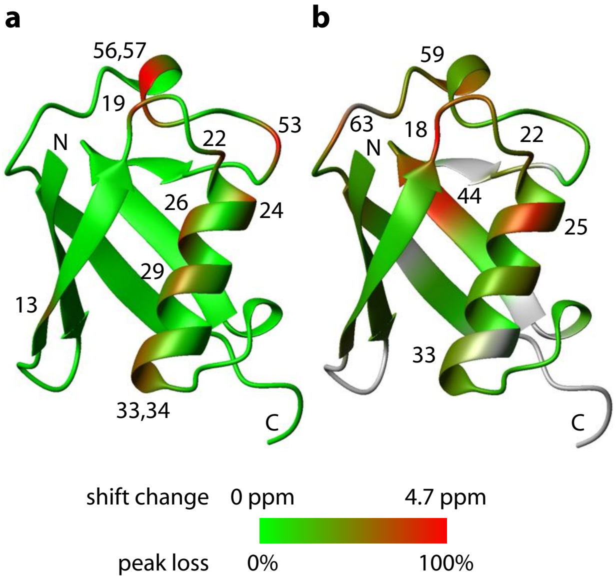

Figure 2.4: Color code on the ubiquitin crystal structure (PDB 1UBQ [112]) indicates the percentage of expected but absent non-methyl CHHC correlations per residue **(a)** and summed C', C^{α}, and C^{β} chemical shift differences between Ubi-P and Ubi-M as described in ref. [106] **(b)**. All residues with absent non-methyl CHHC correlations (a) and selected residues with large preparation-dependent chemical shift variations (b) are labeled, as well as the N- and C-terminus of the molecule.

Apart from chemical shift variations across ubiquitin preparations, we also observed that a number of inter-residue correlation peaks that would have been expected based on the ubiquitin crystal structure (PDB 1UBQ [112]) are absent in CHHC through-space correlation spectra that yield (^{13}C,^{13}C) correlations via their directly bound protons [54]. We recorded a series of CHHC spectra with different (^{1}H,^{1}H) mixing times on Ubi-P and looked for spectral intensity at positions where cross-peaks would be expected due to short (^{1}H,^{1}H) distances in the crystal structure, based on resonance assignments reported before

[106]. In a spectrum with 180 μs mixing time, we found intensity for 186 of 196 (95%) predicted non-methyl correlations with associated (^{1}H,^{1}H) distances below 3.5 Å, which were thus considered to be present. The missing correlations were found to occur in similar regions of the protein as the largest preparation-dependent chemical shift differences (Fig. 2.4 b). Consequently, the question arose whether structural differences, molecular mobility, or a combination of the two are responsible for these effects.

We thus conducted a comprehensive analysis of (^{13}C,^{13}C) bond dynamics in Ubi-P using the double-quantum technique described in Section 2.2. Spectra were recorded on an 800 MHz spectrometer at 8 kHz MAS frequency and a sample temperature of 17°C. The temperature was chosen to be identical to that used in a previous study of dynamics of (^{1}H,^{13}C) spin systems in Ubi-M [97], in order to be able to compare the results directly. One of the (2Q,1Q) spectra used in the analysis is shown in Figure 2.5 a. Several resonances which exhibit low (^{1}H,^{13}C) order parameters (S_{HC}) in Ubi-M or are absent from the Ubi-M dataset, indicating elevated mobility, are seen to be present in this spectrum, suggesting they are more rigid in Ubi-P. Examples of extracted build-ups with best fitting simulations are shown in Figure 2.5 b, including overlapping lysine sidechain signals representing the most mobile moieties detected.

The complete set of S_{CC} order parameters for (C$^\alpha$,C$^\beta$) pairs obtained on Ubi-P is shown in Figure 2.6 a. (C$^\alpha$,C$^\beta$) S_{CC} order parameters could be determined for 40 residues. In the most mobile 20% of these residues, the (C$^\alpha$,C$^\beta$) S_{CC} value is below 0.85 (indicated by a solid line in Figure 2.6 a). These residues occur at the N-terminus, in second and third β-strand, and in loop regions. This shows that, also in the PEG-precipitated state, parts of the ubiquitin sequence exhibit considerable dynamics on the sub-ms or faster time scales, comparable to the ester tail in TEE (see Section 2.2).

Figure 2.6 b compares Ubi-P S_{CC} order parameters with S_{HC} values measured on Ubi-M [97] (both S_{CC} and S_{HC} values are averaged over C$^\alpha$ and C$^\beta$ nuclei to facilitate comparison). The difference between average S_{HC} and S_{CC} order parameters thus obtained (0.72 and 0.91, respectively) is 0.19, well in line with our results on TEE (see Section 2.2), where the difference between S_{HC} and S_{CC} values for sites which are not fully rigid, *i.e.* the ester tail, amounts to 0.18. Apart from the overall offset, local differences in relative mobility between Ubi-P and Ubi-M datasets are apparent. Especially residues in the loop between the first two β-sheets (Leu8, Thr9), in the α-helix (Asn25), and near the 3-10 helix (Leu56) are more rigid in Ubi-P. Interestingly, residues near the short 3-10 helix (residues Ser57 – Tyr59), where several absent CHHC correlations and larger preparation-dependent chem-

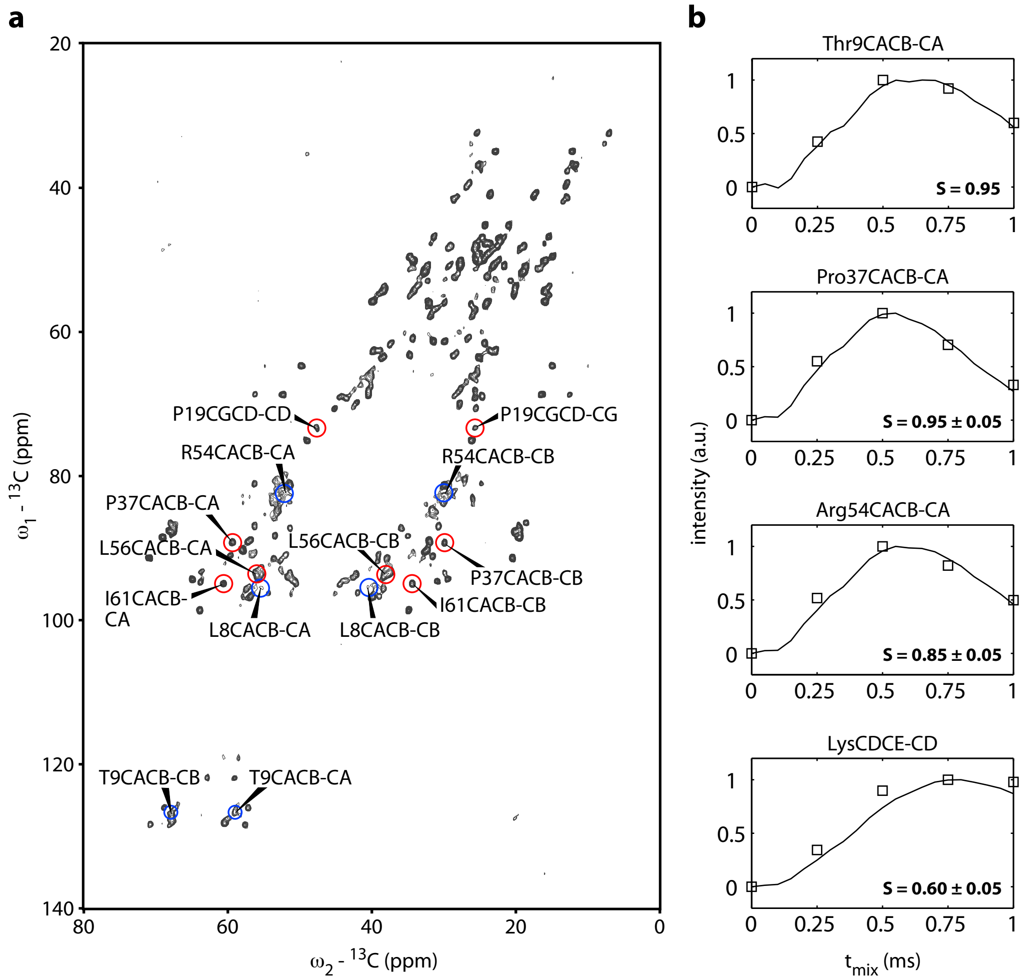

Figure 2.5: **(a)** (2Q,1Q) correlation spectrum of Ubi-P recorded at 800 MHz ^{1}H resonance frequency with a 2Q excitation time of 250 μs. Labeled and circled in red are selected resonances clearly present already at this short mixing time, even though they exhibit low order parameters in Ubi-M [97]. Resonances circled in blue are absent from the Ubi-M dataset, possibly due to even larger degrees of motion, but present in this spectrum, despite lower signal intensity. **(b)** Experimental 2Q cross-peak buildups (squares) and best-fitting simulations (lines) for (C$^{\alpha}$,C$^{\beta}$) nuclei in Thr9, Pro37 and Arg54 as well as overlapped signals of lysine (C$^{\delta}$,C$^{\varepsilon}$) sidechain nuclei. S_{CC} order parameters of best-fitting simulations are given with error values. For the Thr9 CACB–CA correlation, the error is smaller than 0.05. Error bars of experimental data, calculated based on spectral noise, are smaller than the data points.

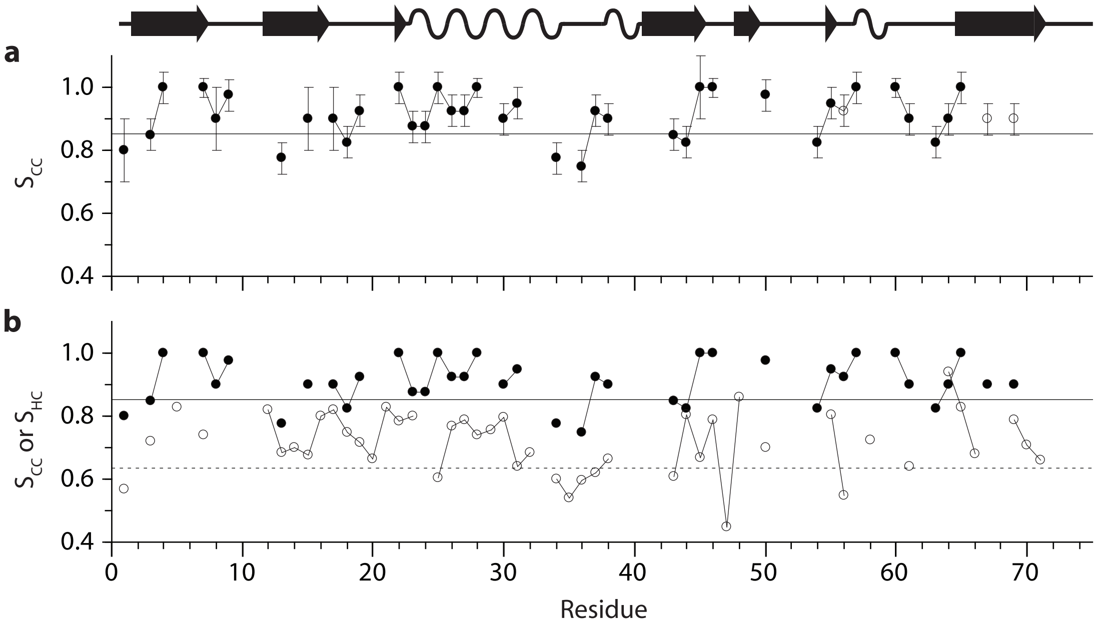

Figure 2.6: **(a)** Plot of Ubi-P (C$^\alpha$,C$^\beta$) S_{CC} order parameters. Open symbols indicate values obtained from signals overlapping with close sequence neighbors. Solid line indicates an S_{CC} value of 0.85 below which the most mobile 20% of determined S_{CC} values are found. Secondary structure of ubiquitin as found in the crystal structure (PDB 1UBQ) is sketched at the top. **(b)** Comparison of Ubi-P (C$^\alpha$,C$^\beta$) S_{CC} (filled symbols) and Ubi-M S_{HC} order parameters [97] (open symbols). S_{HC} values plotted are averaged over C$^\alpha$ and C$^\beta$ nuclei if both values are available. Solid line as in (a); dotted line denotes the upper limit ($S_{\mathrm{HC}} = 0.63$) for the most mobile 20% of residues detected in Ubi-M.

ical shift changes were found (Fig. 2.4), are nearly rigid in Ubi-P as seen by their S_{CC} values. Conversely, e.g. residues Ile13, Glu18, and Ile44 exhibit larger relative mobility in Ubi-P than in Ubi-M. On the other hand, some common regions of elevated dynamics can be found, most notably at the N-terminus of the molecule and at the end of the α-helix (residues Glu34 – Ile36). Globally, though, residue-specific dynamics does appear to be affected in ubiquitin by different solid-phase preparations.

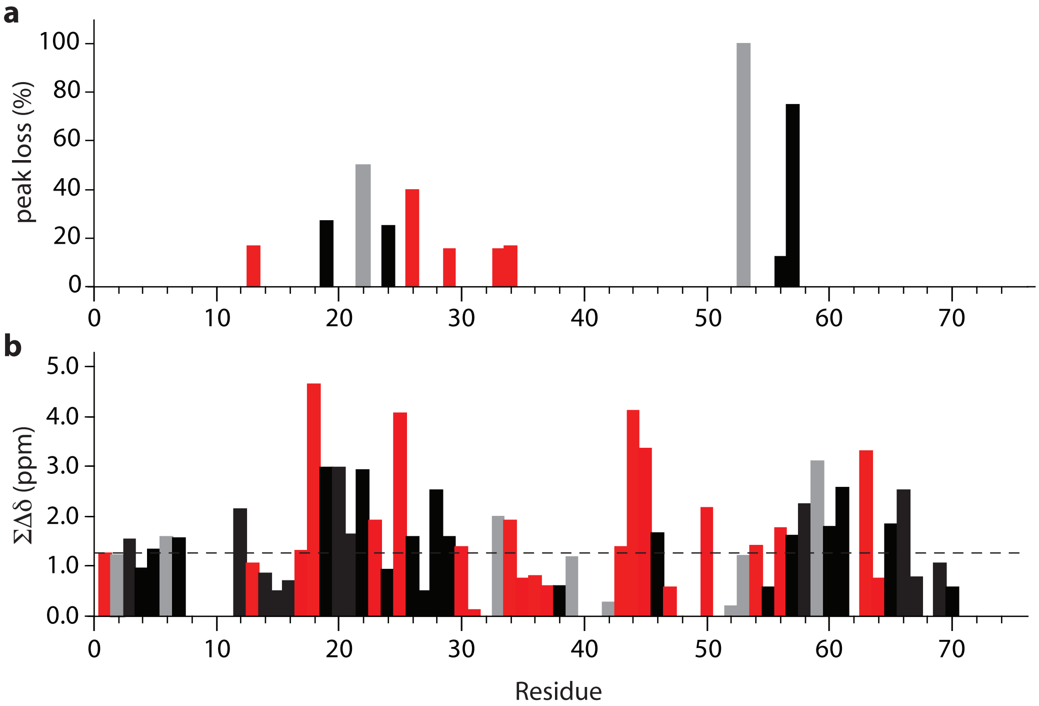

Figure 2.7: (a) Per-residue percentage of expected correlations ((^{1}H,^{1}H) distances up to 3.5 Å, only non-methyl ^{13}C nuclei) which are absent from the Ubi-P CHHC spectrum with 180 μs mixing time. Red bars denote residues where backbone or sidechain nuclei with elevated dynamics (S_{CC} values within the most mobile 20% of the dataset) are involved in absent CHHC correlations. Gray bars denote absent correlations involving residue Gly53 for which no (C$^\alpha$,C$^\beta$) S_{CC} order parameter can be determined. Other absent correlations are shown as black bars. **(b)** Sum of C', C$^\alpha$, and C$^\beta$ chemical shift differences between Ubi-P and Ubi-M as determined in ref. [106]. Red bars indicate residues with (C$^\alpha$,C$^\beta$) S_{CC} or S_{HC} order parameters within the most dynamic 20% of their respective dataset (below 0.85 or 0.63, respectively), or with an elevated normalized $S_{\mathrm{CC}} - S_{\mathrm{HC}}$ order parameter difference. Gray bars denote residues for which neither S_{CC} nor S_{HC} (C$^\alpha$,C$^\beta$) order parameters could be determined. Available data for residues with black bars do not indicate elevated mobility or large mobility differences.

With order parameters for a majority of Ubi-P residues at hand, it became possible to investigate the involvement of mobility in absent CHHC correlations and preparation-dependent chemical shift changes. Figure 2.7 a shows that, in several residues for which expected through-space correlations are absent, elevated levels of backbone or sidechain mobility are indeed found. For Gly53, involved in an absent CHHC correlation with Thr22, no (C^α,C^β) S_{CC} order parameter could be determined due to the absence of a C^β in glycine; mobility in this region may nevertheless play a role in the absence of this cross-peak, considering the lack of assignments for residues Glu51 – Asp52 from dipolar spectra [106] and the low S_{CC} order parameter of Arg54. Figure 2.7 b shows sums of C', C^α, and C^β chemical shift differences between Ubi-P and Ubi-M as determined in ref. [106]. Red bars indicate residues either belonging to the most mobile 20% of the S_{CC} or S_{HC} dataset or exhibiting above-average differences between S_{CC} and S_{HC} order parameters (using a metric independent of the overall offset between the datasets, see [84] for details). While obviously no 1:1 correlation is present, especially the largest chemical shift changes do occur in such residues. However, for a number of residues, most notably Pro19 – Thr22 and Asp58 – Ile61, elevated chemical-shift differences do not appear to correlate with dynamics. To investigate whether structural changes play a role instead, a structure calculation of Ubi-P based on the CHHC spectra also used for analyzing absent cross-peaks was carried out.

For structure calculation of Ubi-P, four CHHC spectra of the protein with (^{1}H,^{1}H) mixing times up to 250 μs recorded on a 600 MHz spectrometer were used as input for the automated assignment and structure calculation algorithm PASD implemented in Xplor-NIH [113–115]. Together with dihedral angle restraints obtained from chemical shift assignments using TALOS [116], distance restraints obtained in this manner were used for a final simulated annealing step in CNS [55]. Notably, the ubiquitin crystal structure (1UBQ) was used as a search model for CHHC crosspeak assignment by PASD since, at least at the time of this study, automated *de novo* assignment of through-space correlation spectra and structure calculation from solid-state NMR data were still, to say the least, challenging, despite one example to the contrary [117]. Resultant distance restraints thus always correspond to the conformation of the crystal structure, and deviations from it in the resultant structure can only be expected in regions lacking distance restraints and/or with dihedral angle restraints differing from the crystal structure.

The 10 lowest energy structures resulting from this procedure (Fig. 2.8 a) exhibit a backbone root-mean-square deviation (RMSD) of residues 1–70 to the mean of 0.49 Å and of

1.79 Å to the ubiquitin crystal structure. Inspection of the structure reveals that some regions for which restraints are available and which are rigid as judged by S_{CC} order parameters assume slightly different conformations in Ubi-P than in the crystal structure (Fig. 2.8 b), notably the 3-10 helix around Asp58. Thus, the preparation-dependent chemical shift changes and absent CHHC correlations occurring in this region appear to be related to a local conformational change. Around residue Leu50, the conformational differences observed in the calculated structure are difficult to interpret due to a lack of resonance assignments, and thus restraints. The lack of assignments hints itself at potential dynamics in this region; however, available data indicate that both structural differences and mobility may play a role. The flanking Arg54 residue is among the more mobile residues in the Ubi-P S_{CC} dataset, and its backbone ψ dihedral angle is predicted to be significantly different in Ubi-P (by about 160°) than in the crystal structure, based on chemical shifts. This suggests that the deviation of the calculated Ubi-P structural ensemble from the crystal structure around residue Gly53 indeed reflects a structural alteration of ubiquitin in PEG microcrystals and not only a lack of restraints. The conformational

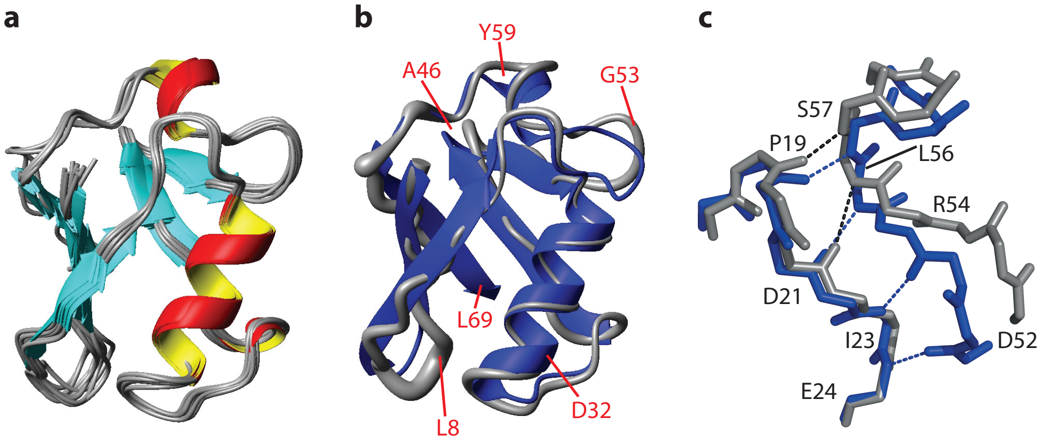

Figure 2.8: (a) Ensemble of 10 structures of Ubi-P with lowest overall energy calculated from solid-state NMR data. Structures were aligned along the backbone atoms of residues 1–70 using MOLMOL [118]. Only these residues are shown. **(b)** Sausage plot of residues 1–70 of the ensemble shown in (a) (gray) aligned with the ubiquitin crystal structure (PDB 1UBQ, blue). Residues in regions with largest local RMSD deviations between the two structures are labeled in red. **(c)** Close-up of residues 18-24 and 52-60 in the mean structure of the Ubi-P ensemble (gray) and in the crystal structure (1UBQ, blue). Backbone polar contacts as detected by PyMOL [119] are indicated by dashed lines (black for Ubi-P, blue for 1UBQ).

changes observed in the region of residues 50 – 60 likely also affect residues 19 – 25 in the loop between second β-strand and α-helix, which are close in space and linked by hydrogen bonds to residues in the 50 – 60 region in the crystal structure (Fig. 2.8 c). This may explain those preparation-dependent chemical shift changes and absent CHHC correlations in residues 19 – 24 which are not related to dynamics. Thus, in total, our results indicate that a majority of preparation-dependent chemical-shift differences and absent through-space correlations in ubiquitin are related either to elevated mobility (in either or both ubiquitin preparations) or to local structural changes.

2.4 Conclusions

We have established a novel method to measure residue-specific protein dynamics in the solid state via double-quantum experiments, yielding order parameters for (^{13}C,^{13}C) bonds. Simulations and fitting routines were developed to analyze experimental data quantitatively. The method was validated on the small molecule L-tyrosine-ethylester and applied to ubiquitin microcrystals prepared by poly(ethylene glycol) precipitation. We have found elevated dynamics on the sub-ms time scale in a number of residues in this ubiquitin preparation, notably in some key residues known to be involved in ubiquitin interactions with other proteins (Ile44, Arg54, Lys63) [120–122]. Finally, we have described differences in molecular mobility between different solid-phase preparations of ubiquitin, and we have shown that chemical-shift differences observed between these can be related to either elevated – or differential – mobility in the different sample states or to conformational changes.

Other types of dynamics may be present in Ubi-P; for example, peak doublings have been observed for a number of its residues (Thr9, Ile13, Ser20, Ile23, Val26, Pro37, and Ala46) [106]. Such doubling may indicate slow dynamics on a timescale above the millisecond, or simply the presence of multiple different (non-exchanging) conformations. On the other hand, fast intermediate exchange has long been known to affect ubiquitin residues in the "hotspot" regions also investigated in this study, *i.e.* Ile23, Asn25, and Thr55, in solution. For these residues, an exchange rate of around 25,000 s^{-1} has been measured using $R_{1\rho}$ experiments [121]. A later solid-state NMR study using CPMG relaxation dispersion experiments has found a much slower exchange rate around 2,000 s^{-1} for these residues in perdeuterated Ubi-M microcrystals [123]. That study, together with a crystal structure of Ubi-M published in 2011 (PDB 3ONS [124]), offered an explanation for this exchange.

The Ubi-M crystal structure exhibits a flip of the Asp52–Gly53 peptide plane, leading to a type II instead of type I β turn in this region, as well as a rearrangement of hydrogen bonding (notably to Glu24). Exchange between this conformation and the dominant one in solution, which is identical to the one in the 1UBQ crystal structure, likely accounts for the exchange event observed in solution- and solid-state NMR. In the latter case, it is likely the crystalline environment, notably the crystal contacts observed in that region of ubiquitin, which slows down the exchange [123, 124]. A lack of assignments for this region precludes elucidation of the exact conformation or dynamics of the Asp52–Gly53 peptide bond in Ubi-P. However, as mentioned, data from the neighboring Asp54 residue suggest that, also in Ubi-P, this region may be dynamic and exhibit a conformation different from the one in the 1UBQ crystal structure (see Fig. 2.8 c). Available data however show a change in the Arg54–Thr55 peptide bond in Ubi-P with respect to the 1UBQ structure, which is not observed in the Ubi-M crystal structure. It is not unconceivable that this region evidently characterized by enhanced plasticity is capable of assuming such a third state; however, in the absence of more data from the residues involved, this statement must remain hypothetical.

The technique developed here to measure protein dynamics via build-up of (^{13}C,^{13}C) double quantum coherence has shown its merit in the elucidation of the origin of preparation-dependent variations in solid-state NMR parameters in the protein ubiquitin. For all its relevance to structural and cell biology, ubiquitin is nevertheless a small and well-behaved model protein. In the following chapter, it will be shown that double-quantum (^{13}C,^{13}C) order parameters can also be measured in a larger membrane protein and provide important insight into its dynamics.

Chapter 3

The mitochondrial voltage-dependent anion channel: conformation of the N-terminus and a model for its gating

3.1 Introduction

The 30 kDa voltage-dependent anion channel (VDAC) is the most abundant protein in the outer mitochondrial membrane of eukaryotes, where it mediates permeation of ATP, ADP, and other metabolites [125, 126]. It is thus essential for energy production and cell growth. In addition, it is considered to be a key player in the mitochondrial pathway of apoptosis [127, 128]. After its discovery in 1975 [129], more than three decades of experimental study yielded numerous different structural models based on biochemical data [130]. All of these were based on a β-barrel framework as in bacterial porins, with 12 to 19 β strands and an N-terminal helical region that sometimes was suggested to be part of a hybrid barrel assembly [131].

In 2008, the three-dimensional structure of the VDAC1 isoform from mouse and human was revealed in three independent studies to be a novel 19-stranded β-barrel fold with a partly helical N-terminal region situated within the aqueous pore [132–134] (Fig. 3.1 a). Although all three structures are highly similar in the β barrel, they exhibit clear differences in the functionally important N-terminal region, and it was not clear which conformation this part of the molecule assumes in the lipid bilayer (Fig. 3.1 b). In addition, structural information on the voltage-dependent gating process that gave VDAC its name remained elusive from the structures. In electrophysiological experiments on VDAC in lipid bilayers, the molecule exhibits a dominant conductance of about 4 nS if transmembrane voltages below 30 mV are applied, as well as a slight selectivity for anions. At higher voltages, VDAC switches with increasing probability to one or more "closed" (or subconductance) states with conductances of around 2 nS (Fig. 3.1 c). These states are impermeable to ATP and ADP and, notably, slightly cation-selective [125, 126, 135]. The functional relevance of this gating process is not entirely clear since, classically, the permeable outer mitochondrial membrane should not be able to sustain a transmembrane potential. However, for example, Donnan potentials based on impermeable charged macromolecules have been suggested [126]. VDAC gating is affected by apoptotic and anti-apoptotic proteins, and closure of VDAC has been suggested to precede mitochondrial apoptosis [128, 136, 137]. The N-terminus has been shown to be involved in both gating and interaction with apoptosis-related proteins [128, 137–139]. It was thus of great interest to obtain further insight into the conformation of VDAC's N-terminus and its voltage-dependent gating.

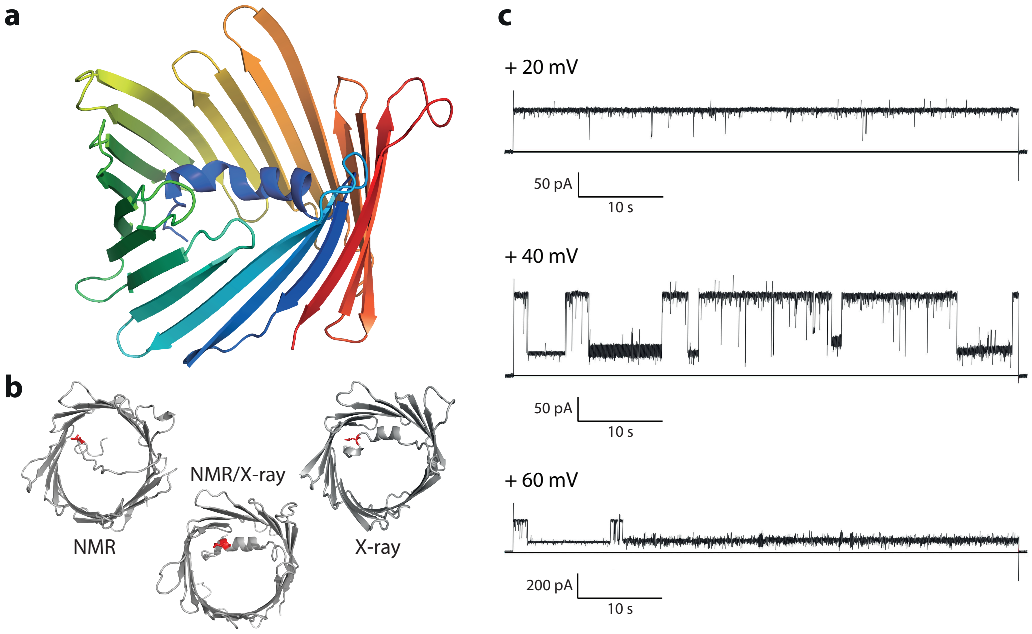

Figure 3.1: (a) Crystal structure of mouse VDAC1 (mVDAC1) (PDB 3EMN [134]) colored from the N terminus in blue to the C terminus in red. **(b)** Three published VDAC1 structures with residue Leu10 (red) in stick representation, illustrating the different conformations of the N-terminus. Left: hVDAC1 NMR structure (PDB: 2K4T [132]); center: hVDAC1 combined NMR/X-ray structure (PDB: 2JK4 [133]); right: mVDAC1 X-ray structure (PDB: 3EMN [134]). **(c)** Electrophysiological current traces measured with hVDAC1 in asolectin lipid bilayers at the indicated transmembrane voltages. Experiments were performed by Jörg Eisfeld (Ionovation GmbH, Osnabrück, Germany).

During my first postdoctoral period in the group of Adam Lange, I studied the human VDAC1 isoform (hVDAC1) in lipid bilayers using solid-state NMR. I was able to identify and assign the signals from the N-terminus and elucidate its native structure in the lipid membrane [140]. Functionality of the VDAC preparation used was assured by electrophysiology experiments. In addition, I found that the N-terminus stabilizes the hVDAC1 β barrel. In a collaborative second study, combining solid-state NMR with molecular dynamics (MD) simulations and electrophysiology, we further elaborated on these results. Based on our combined findings, we were able to propose a model for VDAC's voltage-dependent gating process and its closed channel state [141].

3.2 The native conformation of the hVDAC1 N-terminus (Schneider et al., Angew. Chem. Int. Ed. 2010 [140])

To elucidate the conformation of the hVDAC1 N-terminus in the lipid membrane, we performed solid-state NMR experiments on uniformly (^{15}N,^{13}C)-labeled hVDAC1 expressed in *E. coli* and refolded from inclusion bodies as described in [142] which was then reconstituted into dimyristoylphosphocholine (DMPC) liposomes at a protein:lipid ratio of 1:50 (mol/mol). To aid in resonance assignment, additional samples with amino acid type-specific labeling schemes ((Lys, Trp, Tyr, Val) reverse- and (Ala, Asp, Leu, Val) forward-labeling [35, 36]) were employed, as well as an N-terminally truncated variant (Δ(1-20)-hVDAC1). A large set of dipolar-based (^{13}C,^{13}C) and (^{15}N,^{13}C) correlation spectra was recorded on 800 and 850 MHz spectrometers at MAS speeds between 10 and 18 kHz and sample temperatures between -15 and +25°C.

Resultant spectra exhibit very good sensitivity and resolution (Fig. 3.2 a). Good agreement of a SHIFTX [46] prediction of C$^{\alpha}$ and C$^{\beta}$ chemical shifts, based on the mouse VDAC1 (mVDAC1) crystal structure, with the corresponding region of the intraresidue PDSD (^{13}C,^{13}C) correlation spectrum shown in Figure 3.2 a indicates preservation of the global fold of the protein. Based on our spectra of the different protein variants, we were able to obtain unambiguous de novo sequential resonance assignments for residues Ala2–Val17. These residues give rise to distinct well-resolved cross-peaks in experiments based on dipolar transfer schemes (see Fig. 3.2 a), demonstrating that the hVDAC1 N-terminus assumes a well-defined conformation in liposomes and does not exhibit sizable dynamics on the sub-millisecond time scale. Secondary chemical shifts in this region show that residues 7–8 and 12–17 are in helical conformation, whereas Asp9, Leu10, and Gly11 form a kink

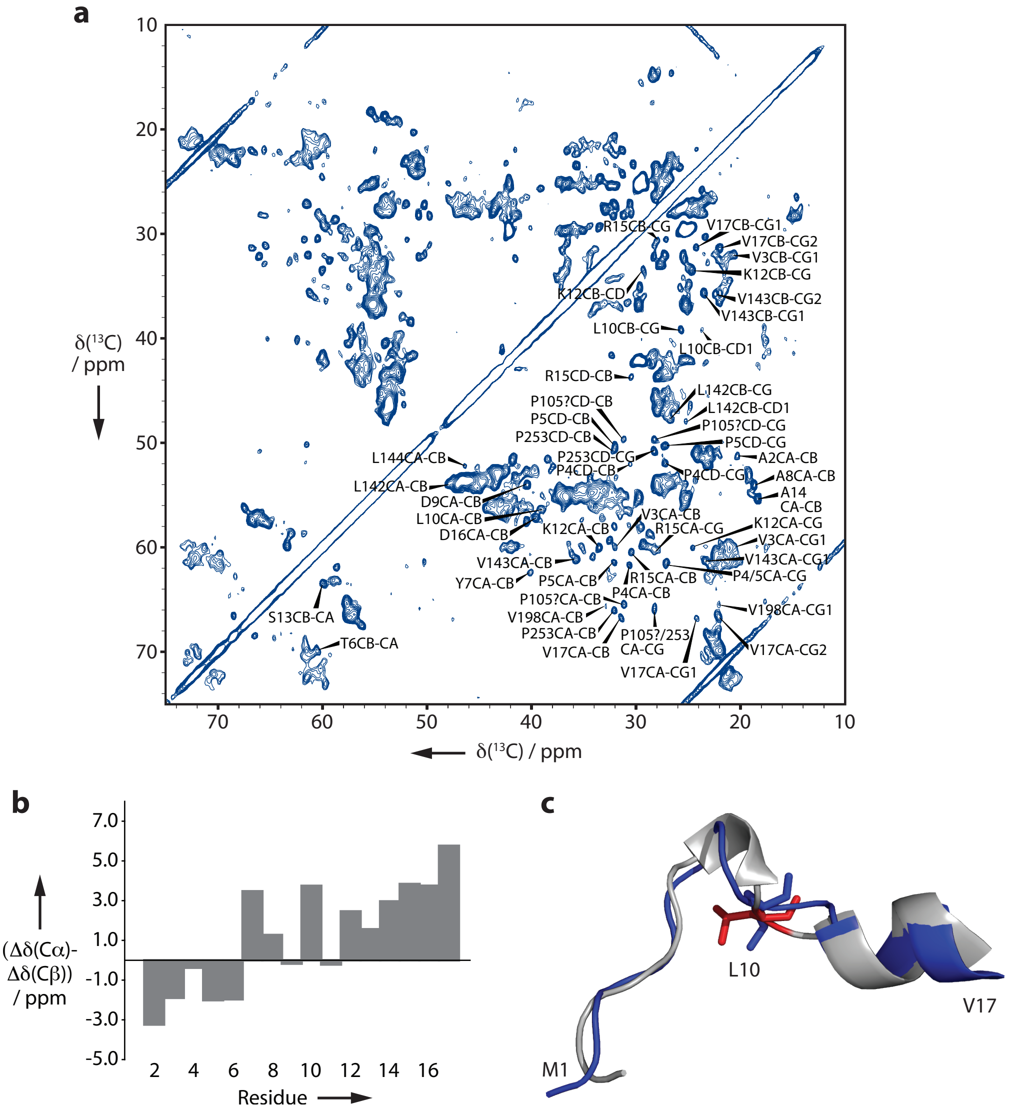

Figure 3.2: (a) (^{13}C,^{13}C) PDSD spectrum (15 ms mixing time) of full-length hVDAC1 in DMPC lipid bilayers recorded on an 850 MHz spectrometer. Resonance assignments are indicated. **(b)** (C$^{\alpha}$,C$^{\beta}$) secondary chemical shifts of hVDAC1 residues 2–17 in lipid bilayers. **(c)** Model of the hVDAC1 N-terminus in lipid bilayers as derived from solid-state NMR data (blue) aligned with the mVDAC1 crystal structure (PDB: 3EMN, gray/red), with Leu10 in stick representation.

and residues 2–6 are in an extended conformation (Fig. 3.2 b). A structural model of the N-terminus was calculated using CNS [55] based on backbone dihedral angles predicted from chemical shifts [116] and a distance restraint between residues Leu10 and Val143 (see below), while keeping the VDAC1 β-barrel frame fixed. The resultant conformation of the N-terminus closely agrees with the one found in the mVDAC1 crystal structure (PDB 3EMN [134], Fig. 3.2 c).

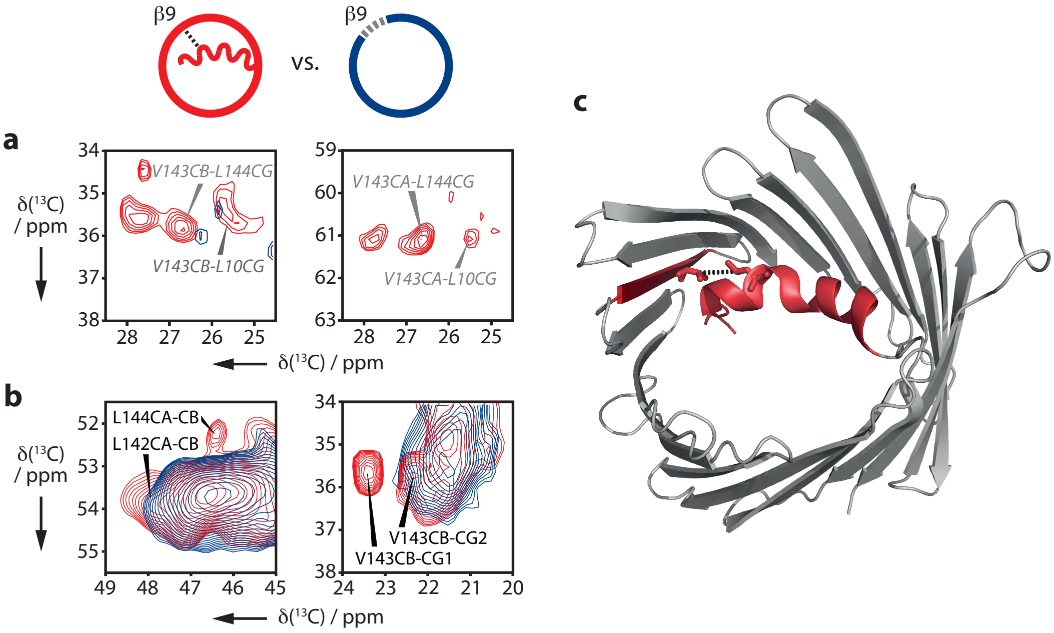

Figure 3.3: Comparison of spectra from wild-type (WT-)hVDAC1 (red) and N-terminally truncated (Δ(1-20)-) hVDAC1 (blue). **(a)** Overlaid regions from 300 ms (^{13}C,^{13}C) PDSD spectra on (Ala, Asp, Leu, Val) forward-labeled samples. Correlations consistent with Val143 sequential and long-range contacts are only visible in WT-hVDAC1. Labels in gray italics indicate ambiguous assignments. **(b)** Overlaid regions from (^{13}C,^{13}C) DREAM [143] (left) and 15 ms PDSD spectra (right) on uniformly (^{13}C,^{15}N)-labeled samples, showing intraresidue correlations from the hydrophobic patch around Val143 that vanish in Δ(1-20)-hVDAC1. **(c)** View of the mVDAC1 crystal structure (PDB: 3EMN) with N-terminus and β strand 9 shown in red. The hydrophobic contact between residues Leu10 and Val143 (in stick representation) is indicated by a dotted line.

Despite considerable signal overlap in the β-strand regions of the spectra, it was possible to obtain resonance assignments for some additional residues in β-strand and loop conformations, in particular for residues Leu142, Val143, and Leu144 in β strand 9, since they constitute the only Leu-Val sequential pairs in hVDAC1. Notably, Val143 and Leu150 form a hydrophobic patch that points into the water-filled interior of the barrel. Long-range correlations consistent with a contact between this Leu-Val-Leu motif and the N-terminal helix (Leu10–Val143) could be identified in PDSD spectra with long mixing times, although the corresponding cross-peaks could not be unambiguously assigned due to chemical shift ambiguity (Fig. 3.3 a). Such contacts were also observed in the hVDAC1 NMR structure [132] and are in line with the mVDAC1 crystal structure [134] (Fig. 3.3 c). Importantly, signals from the Leu-Val-Leu motif are strongly affected upon truncation of the N-terminus (Fig. 3.3 a, b). This result further confirms the contact between N-terminus and β strand 9 and suggests that the helix plays a role in maintaining β-barrel integrity. Our data indicate that signals from β strand 9 disappear rather than shift, pointing to a sizable increase in local dynamics (or structural disorder) upon removal of the N-terminus.

Changes in the β barrel upon truncation of the N-terminus as observed here may explain the long-standing, seemingly puzzling observation that N-terminally truncated VDAC1 exhibits lower conductance than the full-length channel, even though removal of the N-terminus situated within the channel pore would be expected to increase conductance [130, 144, 145]. Our observations suggest that removal of the N-terminus destabilizes the barrel – consistent with increased noise and instability in electrophysiological recordings of N-terminal truncation variants [144, 145] – and may lead to a reduced pore diameter. Such conformational changes may also play a role in VDAC1 voltage gating, as had already been postulated in earlier models [146, 147]. This hypothesis was investigated in the follow-up project described in the next section.

3.3 β-barrel mobility underlies closure of hVDAC1 (Zachariae, Schneider et al., Structure 2012 [141])

There is a general consensus that the structures of hVDAC1 and mVDAC1 solved in 2008 represent the open conformation of the channel [148]. Numerous different models have been proposed for the voltage-dependent gating process and the closed state of VDAC. Movement of the N-terminal helix within the pore has been suggested as a mechanism based on VDAC1 structures [132, 134]; however, it has been shown that such a movement alone could not explain the channel's voltage sensitivity and ion selectivity observed experimentally [148]. Alternatively, based on electron microscopy, electrophysiology and mutagenesis data, larger-scale rearrangements have been proposed, involving parts of the channel leaving the barrel [146, 147, 149]. In particular, it was found that gating is influenced by lateral pressure in the lipid bilayer [150] as well as osmotic pressure applied on the bilayer [146]. From the latter finding, a substantial internal volume change during gating was inferred, pointing to a large reconfiguration of channel geometry. In addition, molecular dynamics simulations have shown that the β-barrel frame of VDAC1 can exhibit extensive breathing motions [151].

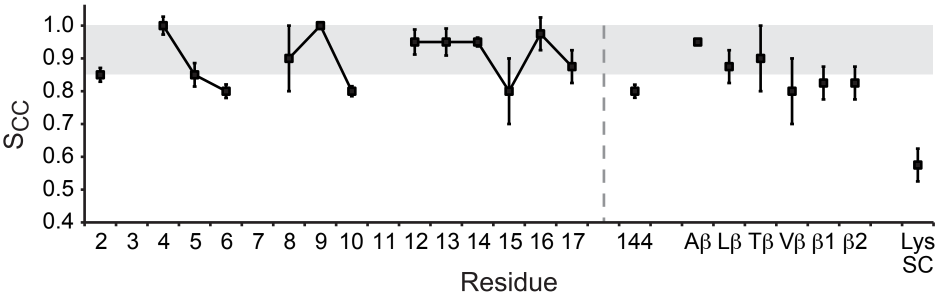

Figure 3.4: S_{CC} order parameters measured on hVDAC1 in lipid bilayers. All values refer to C$^{\alpha}$-C$^{\beta}$ correlations except "Lys SC" for lysine C$^{\delta}$-C$^{\epsilon}$ side chain correlations (as a reference for mobile moieties). Labels "Aβ," "Lβ," "Tβ," "Vβ" refer to average C$^{\alpha}$-C$^{\beta}$ order parameters of overlapping signals from alanine, leucine, threonine, and valine residues in β-strand conformation; labels "β1," "β2" represent other β-strand residue types whose resonances overlap in two broad spectral regions (C$^{\alpha}$ $\sim$55 ppm, C$^{\beta}$ $\sim$35 ppm). The order parameter range from 0.85 to 1 is indicated by gray shading. A vertical dashed line separates N-terminal residues (left) from residues in other parts of the molecule.

Based on our finding of a rather rigid N-terminus whose removal destabilizes the β barrel, we set out to investigate gating in hVDAC1 using a combination of solid-state NMR, molecular dynamics simulations, and electrophysiology, in collaboration with Ulrich Zachariae and Bert de Groot (MD simulations) and Roland Benz (electrophysiology). First, we sought to quantitatively underpin the qualitative finding of a relatively rigid N-terminus (Section 3.2). We measured (^{13}C,^{13}C) order parameters via build-ups of double-quantum coherence as introduced in Chapter 2 on hVDAC1 in DMPC bilayers (Fig. 3.4). SPC5 [101] (2Q,1Q) correlation spectra with six mixing times between 250 and 1000 μs were recorded at 8 kHz MAS on an 800 MHz spectrometer. We obtained residue-specific (C$^{\alpha}$,C$^{\beta}$) S_{CC} order parameters for a majority of N-terminal residues; however, due to spectral overlap, only values averaged over individual or even different residue types could be determined for residues in the β barrel, except for Leu144. These nevertheless allow for an estimation of global dynamics on the sub-ms time scale in the β barrel. Figure 3.4 shows that, while residues Thr6, Leu10 in the helix kink, and Arg15 exhibit elevated mobility, globally, backbone S_{CC} order parameters in the N terminus are in the same range as, or even somewhat higher than, average values found for residues in the β-barrel, confirming that the N-terminus is rather less mobile than the barrel on the sub-ms timescale.

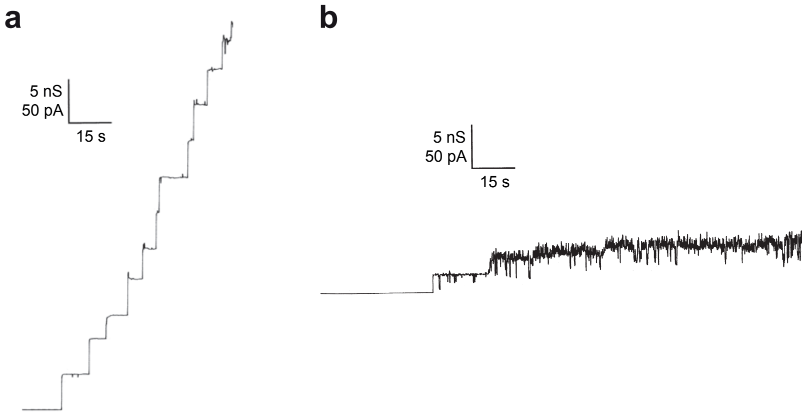

Figure 3.5: Lipid bilayer measurements on WT-hVDAC1 and on the deletion mutant Δ(1-20)-hVDAC1. Shown are single-channel recordings of insertions of WT-hVDAC1 **(a)** and of Δ(1-20)-hVDAC1 **(b)** into the lipid bilayer.

Removal of the N-terminus in the Δ(1-20)-hVDAC1 variant leads to disappearing resonance signals from the barrel, suggesting its destabilization (Section 3.2). It had long been known that deletion of most or all of the 20 N-terminal residues in VDAC leads to noisier recordings in electrophysiology, affects or abolishes voltage gating, and reduces channel conductance [130, 140, 144, 152]. This was also the case in our Δ(1-20)-hVDAC1 preparation. Conductances between 0.5 and 2.5 nS were mostly observed (instead of 4 nS for the full-length channel at low transmembrane voltages), without apparent voltage gating (Fig. 3.5).

To further investigate the apparent stabilizing effect of the N-terminus on the β barrel, we disrupted the hydrophobic contact of Leu10 in the N-terminus with the hydrophobic barrel patch around Val143 in β strand 9 (see Section 3.2) using a conservative mutation of Leu10 to Asn (L10N-hVDAC1). The pattern of resonances in solid-state NMR spectra of L10N-hVDAC1, including signals from the N-terminus, is very well preserved, indicating correct folding of the mutant. However, striking differences in intensity are visible in signals from the N-terminus (Fig. 3.6 a) and from β strand 9 (Fig. 3.6 b). Signals from

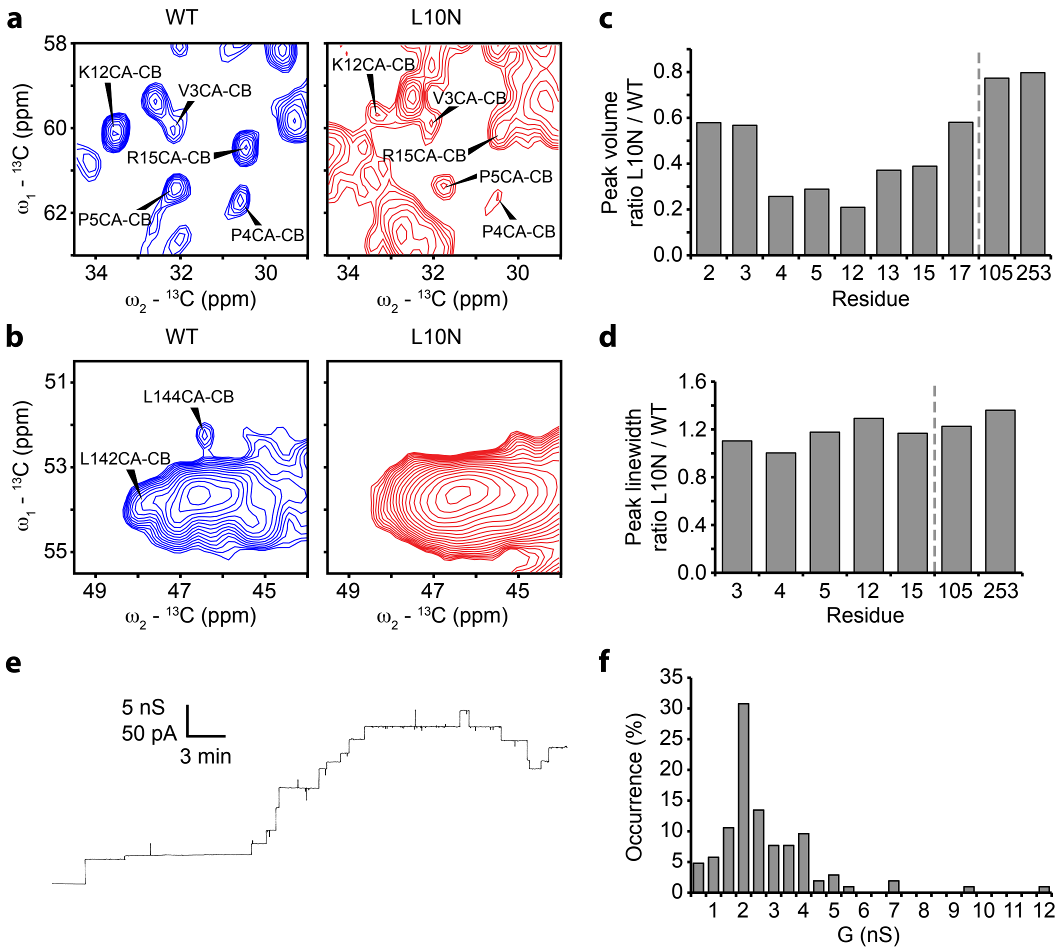

Figure 3.6: Solid-state NMR and electrophysiological data from L10N-hVDAC1. **(a)**, **(b)** Regions of (^{13}C,^{13}C) PDSD correlation spectra (15 ms mixing time) displaying resonances from N terminus (a) and β strand 9 (b). Blue, WT; red, L10N-hVDAC1. **(c)** Ratios of normalized C$^{\alpha}$-C$^{\beta}$ cross-peak volumes between (^{13}C,^{13}C) PDSD spectra (15 ms mixing time) recorded on L10N- and WT-hVDAC1. **(d)** Ratios of average C$^{\alpha}$-C$^{\beta}$ cross-peak linewidths between 15 ms (^{13}C,^{13}C) PDSD spectra of L10N- and WT-hVDAC1. **(e)** Single-channel recordings of L10N-hVDAC1 insertions into lipid bilayers. Applied voltage was 10 mV. **(f)** Histogram of conductance values (G) observed on L10N-hVDAC1 in lipid bilayers at a transmembrane voltage of 10 mV.

the N-terminus and β strand 9 are selectively and significantly attenuated compared to signals from other regions (Fig. 3.6 c), while their linewidths increase slightly, but in a similar manner throughout the protein (Fig. 3.6 d). These results suggest increased dynamics in the N-terminus of L10N-hVDAC1 or, more precisely, the presence of an increased population of molecules with a highly mobile N-terminus, invisible in solid-state NMR spectra, in slow exchange with the visible population. In electrophysiology, L10N-hVDAC1 forms stable, voltage-gated pores; however, already at a transmembrane voltage of 10 mV, where WT-hVDAC1 is predominantly open with a major conductance of about 4 nS, L10N-hVDAC1 exhibits a dominant conductance of 2 nS, a value resembling the closed state of WT-hVDAC1 and the observable conductance state of Δ(1-20)-hVDAC1 (Fig. 3.6 e, f). These data confirm the crucial role of the hydrophobic contact between Leu10 and the region around Val143 for attachment of the N-terminus to the β-barrel wall and suggest that disruption of this contact facilitates dynamical and/or conformational changes that allow entry of hVDAC1 into a closed state.

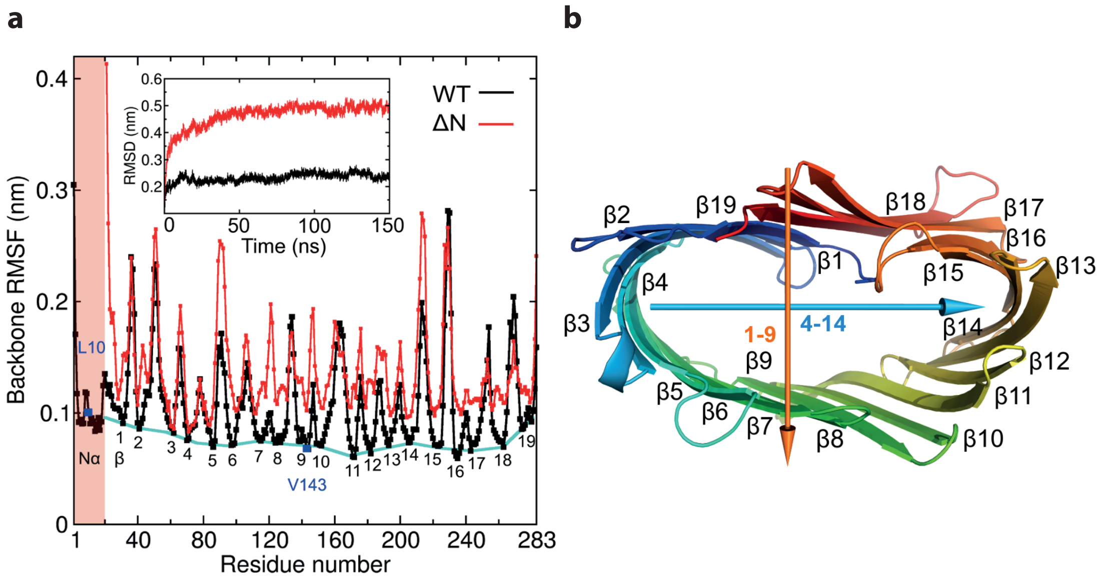

Figure 3.7: **(a)** Root-mean-square fluctuation (RMSF) distribution in WT- (black) and Δ(1-20)-mVDAC1 (red) over 300 ns equilibrium MD simulations. Cyan, baseline of minimal RMSF across the barrel. Inset: Root-mean-square deviation (RMSD) of WT- (black) and Δ(1-20)-mVDAC1 (red) with respect to the initial structure under a membrane surface tension of -45 mN/m. **(b)** Partial collapse of the Δ(1-20)-mVDAC1 barrel under low uniaxial membrane stress ($\sim$ -10 mN/m) occurs preferentially along an axis approximately running through β strands 1–9 rather than in the perpendicular direction. β strands 1 to 19 are color-coded from blue to red.

In an attempt to elucidate the origin of these observations, we performed MD simulations of mVDAC1 in DMPC lipid bilayers. Mouse VDAC1, which differs from hVDAC1 only in 4 residues, was chosen since its three-dimensional structure had been determined to higher resolution [134]. In equilibrium simulations, removal of the N-terminus leads to substantially higher fluctuations in the protein, especially in β strands 5 to 19 (Fig. 3.7 a). Inspection of the behavior of Δ(1-20)-mVDAC1 in the simulations revealed an increased tendency of the protein to adopt a more elliptic shape (Fig. 3.7 b). This was also observed when applying membrane surface tension in the simulations. Elliptic shapes are more easily adopted by Δ(1-20)-mVDAC1 than by the full-length protein. Notably, the β-barrel of Δ(1-20)-mVDAC1 was found to be more susceptible to deformation along an axis passing through β strands 1 and 9 than in the perpendicular direction (Fig. 3.7 b). That is, the N-terminal helix, running alongside of β strands 10 to 17, is located at a position where it maximally stabilizes the barrel structure. Under low surface stress of about -10 mN/m, a range relevant for mechanosensitive channels [153, 154], the ellipticity of the Δ(1-20)-mVDAC1 barrel (defined from the ellipsis axes as $\frac{b-a}{a}$) converges to a value of about 0.5 (referred to as a *semi-collapsed state* in the following). We also tested the stability of attachment of the N-terminus to the barrel via the hydrophobic Leu10-Val143 contact using force-probe MD simulations. The L10N-mutated helix was found to detach from the barrel at significantly lower forces than the WT N-terminus.

Using a computational electrophysiology scheme newly developed at the time [155], we performed atomistic simulations of ion flux through wild-type (WT-) and truncated Δ(1-20)-mVDAC1 at different barrel ellipticities (Fig. 3.8). Non-distorted WT-mVDAC1 exhibits a conductance of 4.2 nS and a selectivity for anions over cations of about 1.7, in good agreement with experimental values (about 4 nS and 2.2, respectively). The larger pore of non-distorted Δ(1-20)-mVDAC1 leads to an increased conductance of 6.7 nS. However, increasing barrel ellipticities progressively brings calculated conductances into the range of that of the experimentally observed closed state of around 2 nS. For Δ(1-20)-mVDAC1, this is the case for ellipticities of about 0.45 to 0.5 (Fig. 3.8). Notably, while such conductances could be obtained in WT-mVDAC1, *i.e.* in the presence of the N-terminal helix, the experimentally observed switch to slight cation selectivity was only found in simulations of Δ(1-20)-mVDAC1, for an ellipticity of 0.47, close to the convergence value of the deletion mutant under low membrane stress.

Overall, our observations suggest a scenario in which an ensemble of semi-collapsed, elliptic geometries of the VDAC1 β-barrel underlie the subconductance states observed experimentally under elevated transmembrane voltages. We found that VDAC1 is more prone to adopt these states if the N-terminal helix does not stabilize the β barrel, and that a switch to cation selectivity as observed experimentally occurs only if the N-terminus does not reside within the barrel. Hence, our data are consistent with a voltage-dependent motion of the – positively charged – N-terminal helix, partially or fully detaching it from the β-barrel, as a possible mechanism to control entry of VDAC1 into the closed state (Fig. 3.9).

Notably, previous studies had already shown that it is possible for the VDAC1 N-terminus to leave the barrel [156–158]. For example, dimerization of VDAC1 via a cysteine residue introduced into the N-terminus had been observed [158]. Our finding that large deformations of the VDAC1 β barrel are required to account for the reduction in conductance observed experimentally is in excellent agreement with the observation of a substantial volume reduction (in the order of 10^4 Å^3) during closure [146]. A gating mechanism by

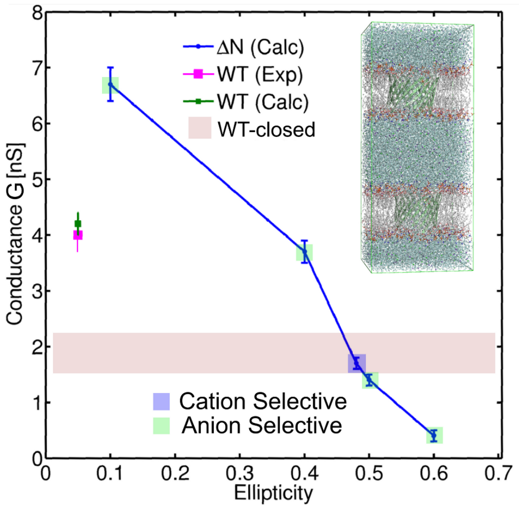

Figure 3.8: Conductance of WT- (green) and Δ(1-20)-mVDAC1 (blue) in relation to elliptic distortion of the β-barrel scaffold, calculated from computational electrophysiology simulations. Inset on the right shows the simulation setup with two mVDAC1-containing membranes with opposite orientation in the simulation box [155]. Background shading of the data points indicates the ion selectivity of the corresponding mVDAC1 states (light green, anion-selective; light blue, cation-selective). The magenta data point corresponds to the experimental conductance of open WT-hVDAC1, whereas the experimentally determined average conductance of the closed state of WT-hVDAC1 is indicated by a red shaded bar. Error bars reflect standard error of the mean (SEM).

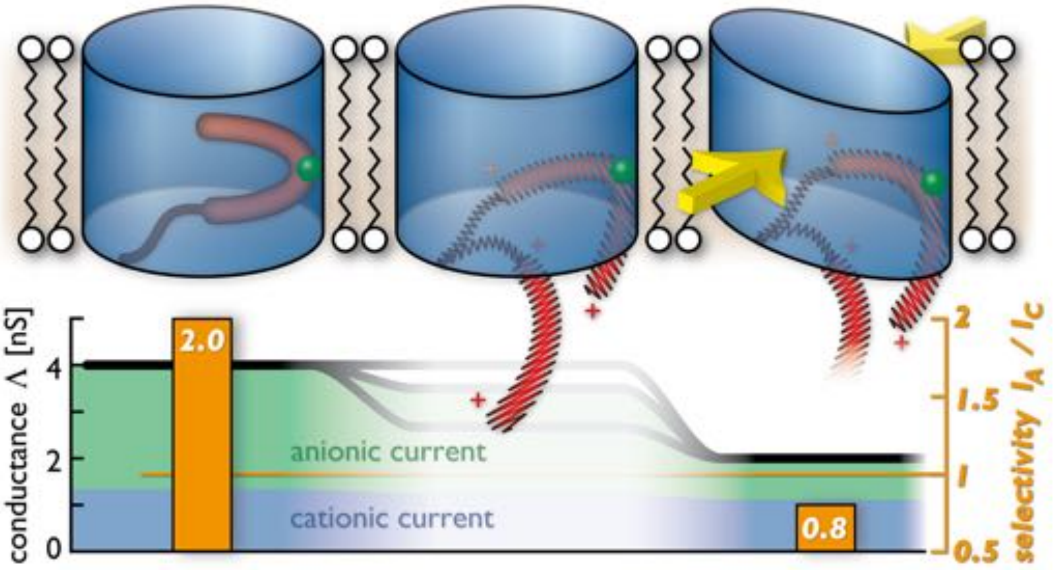

Figure 3.9: Suggested model of VDAC voltage-induced gating. At zero transmembrane potential, the VDAC pore (blue) is most likely to reside in the open state (upper left). Increasing the membrane voltage beyond ±30 mV (center) exerts a force on the N-terminal helix (red), which is attached to the barrel wall by the contact residue Leu10 (green). Detachment or removal of the N-terminal helix from the barrel wall at the Leu10-Val143 contact renders the pore more susceptible to (semi-) collapse under membrane stress (right). At an ellipticity of 0.47, the semi-collapsed barrel geometry displays the conductance and ion selectivity found experimentally for the wild-type closed state (lower right), whereas our calculations reproduce the wild-type open state values for noncollapsed structures containing the N-terminal helix (lower left). Hatching of the N-terminal region in the upper central and right panels indicates that the conformation of a possibly detached N-terminus is not known.

semi-collapse of the pore is also consistent with the observed dependence of gating on osmotic pressure [146] and on the presence of nonlamellar lipids, which increase lateral pressure, in the surrounding membrane [150]. Thus, a coherent mechanism of VDAC gating that explains a wide range of experimental data emerged from our study.

3.4 Conclusions

Using solid-state NMR, we were able to elucidate the conformation of the hVDAC1 N-terminus in lipid bilayers, which had remained controversial from previous three-dimensional structures of the protein. We found that the N-terminus forms a kinked helix, much as seen in the crystal structure of mVDAC1 [134]. The N-terminus assumes a defined, mostly rigid conformation and plays a stabilizing role for the β barrel, crucially involving a hydrophobic contact between Leu10 and a hydrophobic patch around Val143 on the inside of the barrel. Our combined NMR, electrophysiology and molecular dynamics simulation data suggest a model in which elevated transmembrane voltages induce a displacement of the N-terminus from its resting position within the barrel, leading to elliptic, semi-collapsed barrel shapes that can account for both conductance and ion selectivity of the closed state of VDAC1 observed experimentally.

In the wake of the resolution of the three-dimensional structure of VDAC1 and of our studies, some controversy remained as to whether the resolved structures represent an active form of the protein or an artifact due to refolding from inclusion bodies [159]. The alternative model proposed based on biochemical data, a hybrid barrel comprising 13 β strands and an α helix, has however no parallel in any known protein structure and would be unfavorable structurally and energetically, as well as unlikely to form channels of the size observed for VDAC1 in electron microscopy [160]. While we certainly did not resolve a full high-resolution structure of hVDAC1 in lipid bilayers, our results are in line with the published VDAC1 3D structures, notably with respect to the position of the N-terminus and its attachment to the barrel wall via the hydrophobic Leu10-Val143 contact. In addition, apart from the lipids used to form the bilayers employed, we used the same purification and reconstitution protocol for solid-state NMR and electrophysiological measurements and obtained functional pores exhibiting classical VDAC behavior in the latter. It is thus highly likely that the published 3D structures of VDAC1 indeed represent a functional state of the protein.

The question whether VDAC gating involves departure of the N-terminus from the β barrel has been further addressed in crosslinking studies. In one of these, residues Leu10 in the N-terminus and Ala170 in β strand 11 of mVDAC1 were mutated to cysteines and crosslinked chemically [161]. The resultant protein exhibited normal voltage-gating behavior, leading the authors to conclude that the N-terminus does not move independently from the barrel during voltage gating. However, while fixing residue 10 to the barrel wall, its contact to the hydrophobic patch in strands 10 and 11 was nevertheless perturbed in this mutant, which may still permit conformational changes involving these strands that might be occurring during gating. Moreover, as our MD simulations have shown, VDAC1 may well assume elliptic conformations with conductances characteristic of the closed state even if the N-terminus is present within the barrel; however, a switch to cation selectivity would not be expected in this case according to our data. Ion selectivity in the closed state was however not investigated in the L10C/A170C crosslinked mutant. Finally, this study employed a mVDAC1 construct with a His$_6$ tag at the very N-terminus of the protein, which might affect its gating properties.

On the other hand, another study investigated two different mVDAC1 variants with crosslinks of the N-terminus to the barrel, A14C/S193C and V3C/K119C [162]. Here, clear effects of crosslinking on gating were observed. The crosslinked V3C/K119C variant, interestingly, exhibited asymmetric gating behavior, where only one polarity of transmembrane voltage led to channel closure. A14C/S193C-mVDAC1 was found to be essentially locked in the open state. These results show that the effects of crosslinking the N-terminus to the barrel wall strongly depend on the exact amino acid positions chosen, and that certain crosslinking positions are indeed capable of abolishing voltage gating, as would be expected in a model of VDAC voltage gating as the one we have proposed. Crosslinks for which channel gating is still observed may thus permit sufficient residual flexibility of the N-terminal VDAC segment for gating to occur.

Ultimately, to resolve the question of VDAC voltage gating and the conformation of its closed state, methods will have to be devised to either stabilize or otherwise access this so far elusive state structurally. Development of such methods will be the subject of one of the projects in Part III.

Chapter 4

Folding and binding of an intrinsically disordered protein to its partner elucidated by relaxation dispersion NMR (Schneider et al., J. Am. Chem. Soc. 2015 [163])

4.1 Introduction

The discovery that proteins can be functional in the absence of stable three-dimensional or even secondary structure has revolutionized the field of structural biology over the last 20 years. Disorder in proteins was certainly not a new observation; however, previously, it had usually not been associated with function, rather, for example, with disordered loop regions in otherwise stably folded proteins that are at best an obstacle to crystallization. Observations of functional disorder had been made (reviewed for example in [164]), notably in regions of DNA-binding proteins that fold upon binding to DNA [165], but were not recognized as examples of a more general, novel phenomenon. This began to change with studies such as that of the cyclin-dependent kinase (Cdk) inhibitor p21, which inhibits Cdks via a disordered N-terminal segment that retains its function even after denaturing treatments [166]. Over the years, many more examples of such intrinsically disordered proteins (IDPs) or intrinsically disordered regions (IDRs) were found, experimentally as well as by bioinformatic prediction [2, 167]. According to some estimates, on the order of 30 to 40% of eukaryotic proteins contain disordered regions of 50 or more residues in length or are entirely disordered [168, 169].

Disordered proteins are implicated in a wide range of important cellular functions, notably signal transduction, scaffolding, regulation of transcription and translation, cell cycle regulation, or chaperoning [2, 170, 171]. More recently, exciting new discoveries have unveiled the role of intrinsic disorder in processes such as liquid-liquid phase separation and formation of membrane-less organelles [172, 173], emergence of novel traits that can be transmitted by protein-based inheritance [174], desiccation tolerance [175] or transport through the nuclear pore [176]. Disordered proteins also play roles in numerous diseases, such as various types of cancer and neurodegenerative disease [177], and first pharmacological studies have reported small molecules or antibodies that target disordered protein regions [178–180]. Thus, there is great interest in understanding intrinsically disordered proteins and their functions, both from a fundamental science perspective and with regard to medical applications.

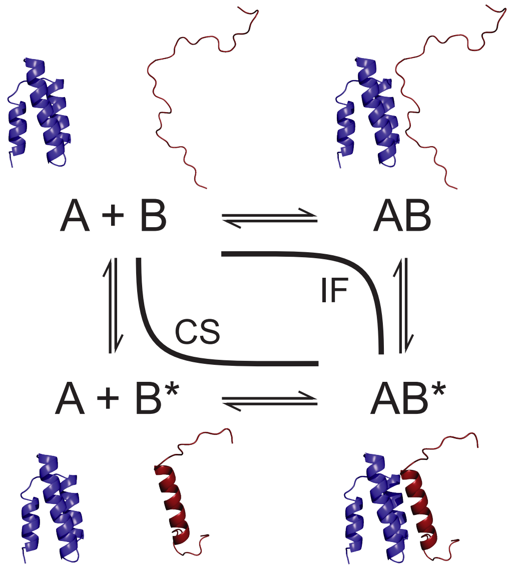

Figure 4.1: Schematic of conformational selection (CS) and induced fit (IF) as parallel pathways of a bimolecular folding and binding interaction. One of the partners, B, is an IDP that exists in different conformations, unfolded (B) and folded into its final bound state (B*).

In many cases, interactions with other proteins, small molecules, RNA or DNA are at the heart of IDP function. Questions thus arise as to how IDPs interact with their partners in the absence of well-structured binding sites, which mechanisms they employ to assure specific binding, and which advantages intrinsic disorder may confer for protein-protein interactions. IDPs often do not exhibit fully random statistical coil behavior, but can adopt transiently populated secondary structures and long-range tertiary interactions [181, 182]. Such structural preorganization has often been found relevant in intermolecular interactions undergone by IDPs. While so-called “fuzzy complexes” of IDPs have been described that retain a high degree of disorder even in the bound state [183], binding of IDPs to physiological partners often occurs via short linear motifs [184, 185] that become structured during the interaction, a phenomenon known as “folding upon binding” or “coupled folding and binding” [186]. How exactly this is accomplished mechanistically has been the subject of intense discussions. The debate has mostly focused on two mechanisms that can be considered as limiting cases: conformational selection (i.e., folding before binding; [187, 188]) and induced fit (i.e., folding after binding; [189]) (Fig. 4.1). More complex combined mechanisms have also been envisioned [190]. Other subjects of debate are, for example, whether IDPs exhibit enhanced binding specificity [191] or rather increased promiscuity [192]. Answering these questions is by no means trivial, and the number of experimental studies addressing them has thus remained comparatively limited.

Solution NMR spectroscopy is the only structural biology technique that can yield high-resolution site-specific information on highly dynamic entities such as IDPs. It is thus no surprise that NMR spectroscopy research groups have been among the pioneers in the field of “unstructural biology” [167, 193]. A large number of studies have been published [194] and approaches developed to characterize the conformational sampling of IDPs in solution from NMR (and other, complementary) data [195, 196]. IDPs rapidly sample a vast conformational space. Consequently, they cannot be described in terms of individual or small numbers of “average” conformers; rather, implicit or explicit ensemble descriptions have to be invoked [195, 197].

Apart from describing conformational ensembles of IDPs in solution, NMR spectroscopy can also be used to characterize IDP binding interactions structurally and mechanistically. However, NMR studies of interactions involving IDPs are frequently hampered by spectral line broadening, since exchange between free and bound conformations often occurs on timescales that give rise to intermediate exchange broadening (in the millisecond range), precluding direct detection of bound-state signals. In such cases, the origin of this line broadening can be investigated by detecting the free state of the IDP at low titration admixtures of the partner protein, where the resonances are only weakly broadened and the bound state represents a weakly populated minor state. Information on the minor state(s) can then be obtained via relaxation dispersion (RD) experiments [85, 198] which measure the dependence of the exchange line broadening of the visible resonances on an applied radiofrequency field. This dependence contains information on interconversion rates, populations, and chemical shifts of the molecular species in the exchange equilibrium [199].

During my postdoctoral stay in the group of Martin Blackledge in Grenoble, I used relaxation dispersion NMR experiments to investigate the folding-and-binding interaction of the disordered C-terminal tail region of the nucleoprotein N from Sendai virus (SeV $\mathrm{N_{TAIL}}$, residues 401–524) with its folded partner, the C-terminal PX domain (residues 474–568) of the phosphoprotein P. SeV, as its close relative, measles virus, belongs to the paramyxoviridae genus. In this virus family, the $\mathrm{N_{TAIL}}$:PX interaction is thought to play an essential role in replication by initiating the interaction between the viral polymerase and the genome [200]. Previously, it had been shown in the group that the PX molecular recognition element (MoRE) of $\mathrm{N_{TAIL}}$ (residues 472–493), in its unbound state, samples three distinct, differently populated helical substates, in rapid exchange with a completely unfolded population [201]. One of the questions about the $\mathrm{N_{TAIL}}$:PX interaction thus concerned the role of this pre-formed structure in the binding. My results allowed to propose

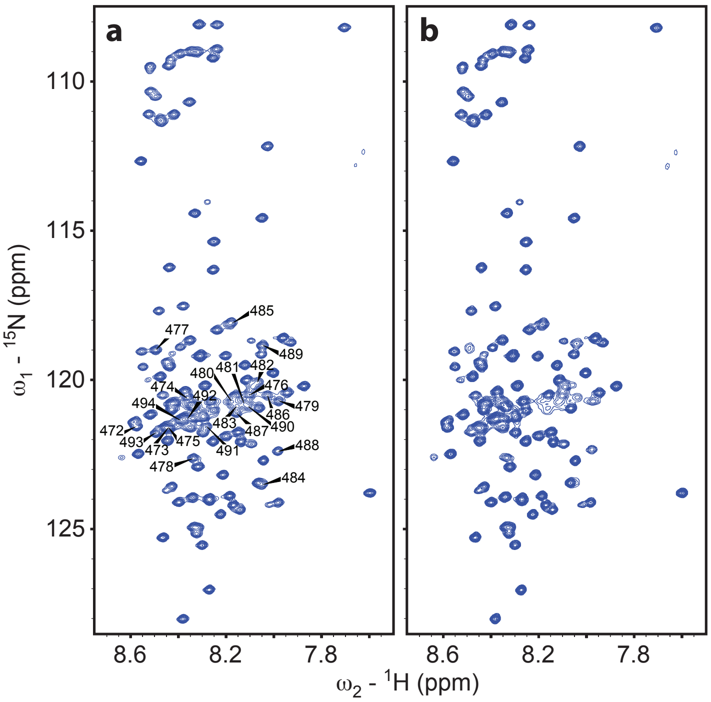

Figure 4.2: ^{15}N-^{1}H correlation spectra of $\mathrm{N_{TAIL}}$ taken from the reference planes (no CPMG pulse train applied) of amide ^{15}N RD experiments. **(a)** Free $\mathrm{N_{TAIL}}$, **(b)** $\mathrm{N_{TAIL}}$ with 8% PX. Labels in (a) indicate peaks originating from residues in the helical region of $\mathrm{N_{TAIL}}$ that interacts with PX.

a detailed binding mechanism in which one of the pre-formed helical N_{TAIL} conformers binds to PX in an initial encounter complex before moving into its final binding location within a groove on the surface of its partner.

4.2 Experiments and analysis in terms of a two-state binding model

N_{TAIL} resonances from throughout the interaction region experience strong line broadening already in the presence of substoichiometric amounts of PX (Fig. 4.2), and most of them are broadened beyond detection at PX:N_{TAIL} molar ratios higher than 0.20. To identify the molecular mechanisms giving rise to this broadening, Carr-Purcell-Meiboom-Gill (CPMG) RD experiments were performed on ^{15}N, ^{13}C', and ^{1}H^{N} nuclei [202–204] of N_{TAIL} at two magnetic fields (14.1 and 18.8 T), a sample temperature of 25°C and at admixtures

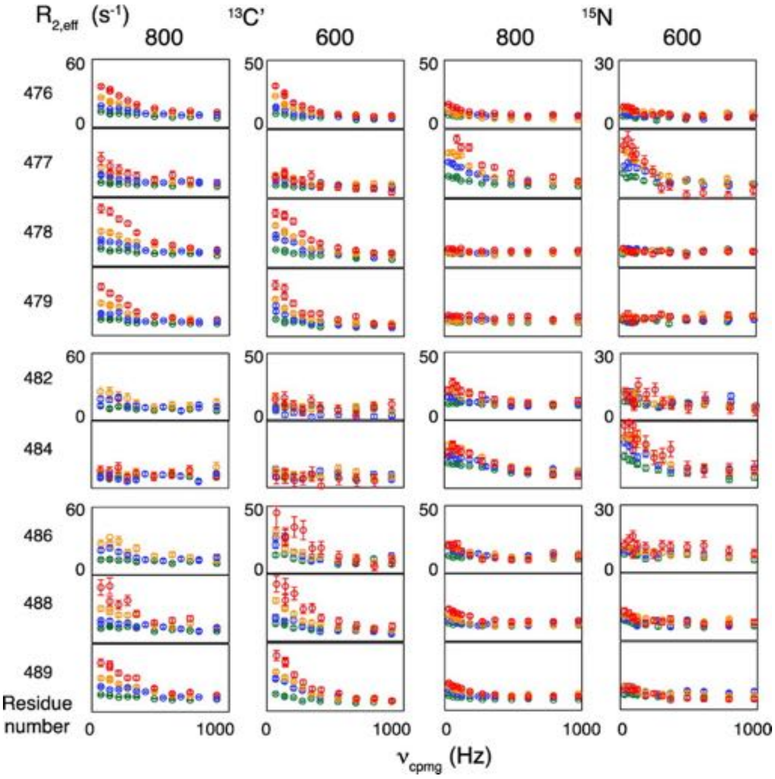

Figure 4.3: ^{13}C and ^{15}N RD curves for selected N_{TAIL} residues measured at 14.1 and 18.8 T (600 and 800 MHz ^{1}H Larmor frequency) for 2% (green), 3.5% (blue), 5% (orange), and 8% (red) molar ratio admixtures of PX:N_{TAIL}. Residue number i refers to the peptide plane containing the amide group of residue i and the carbonyl carbon of residue $i - 1$.

containing unlabeled PX and (^{13}C,^{15}N)-labeled $\mathrm{N_{TAIL}}$ in molar ratios ranging from 0 to 0.15. RD profiles ($R_{2,\mathrm{eff}}(\nu_{\mathrm{CPMG}})$) were calculated from peak heights. First, they were fit on a residue- and nucleus-specific basis using numerical integration of the Bloch-McConnell equations for a two-state system in CATIA [205] to identify datasets with significant dispersion (non-flat RD profiles). To obtain quantitative information on the exchange process, retained RD profiles were then fit using different approaches, residue-wise or combining all residues, at individual titration admixtures or across admixtures, to models of two- or three-state exchange, using numerical integration in CATIA or cpmg_fitd9 [206] or custom-written software using the analytical Carver-Richards equation [207].

In free $\mathrm{N_{TAIL}}$, no RD was detected, confirming the rapid nature of the exchange between the three helical substates and the unfolded state [201]. However, for all PX:$\mathrm{N_{TAIL}}$ molar ratios used, RD was measured throughout the molecular recognition element for all three types of nuclei (Fig. 4.3). The distribution of residues with sizable RD differs notably depending on the nucleus measured; the central section of the helical region (residues 480–484) exhibits weaker ^{13}C' dispersion and larger ^{15}N exchange contributions (Fig. 4.3). Given that the exchange detected by RD only occurs in a rather short stretch of neighboring residues in the MoRE of $\mathrm{N_{TAIL}}$ upon binding to PX, it seems likely that these residues would be affected by the same exchange process. However, exchange rates k_{ex} and minor state populations p_{B} resulting from fits of a two-state exchange model ($\mathrm{A} \rightleftharpoons \mathrm{B}$) to RD data from individual residues vary considerable between residues, rather suggesting that these data may not be well described by a single global two-state exchange process [208] (Fig. 4.4 a, b). Correspondingly, while a majority of RD curves can be reproduced satisfactorily by a global two-state exchange model (*e. g.* with k_{ex} of 724 ± 38 s^{-1} and p_{B} of $4.1 \pm 0.1\%$ at the $\mathrm{N_{TAIL}}$ admixture with 5% PX), several curves, notably those showing large ^{15}N dispersions, are poorly fit by such a model (Fig. 4.4 c, d).

4.3 A three-state binding model for the $\mathrm{N_{TAIL}}$:PX interaction

Given the shortcomings of a global two-state fit, we tested whether $\mathrm{N_{TAIL}}$ RD data could adequately be fit by a model of a single global three-state exchange process ($\mathrm{A} \rightleftharpoons \mathrm{B} \rightleftharpoons \mathrm{C}$). Due to the large parametric space available to three-state exchange models, finding a unique parameter set proved difficult, and different models could be found that resulted in fits of similar quality. We obtained a convergent result by first fitting the $\mathrm{N_{TAIL}}$ data set obtained with 5% PX, which exhibited both good signal-to-noise and a large dynamic

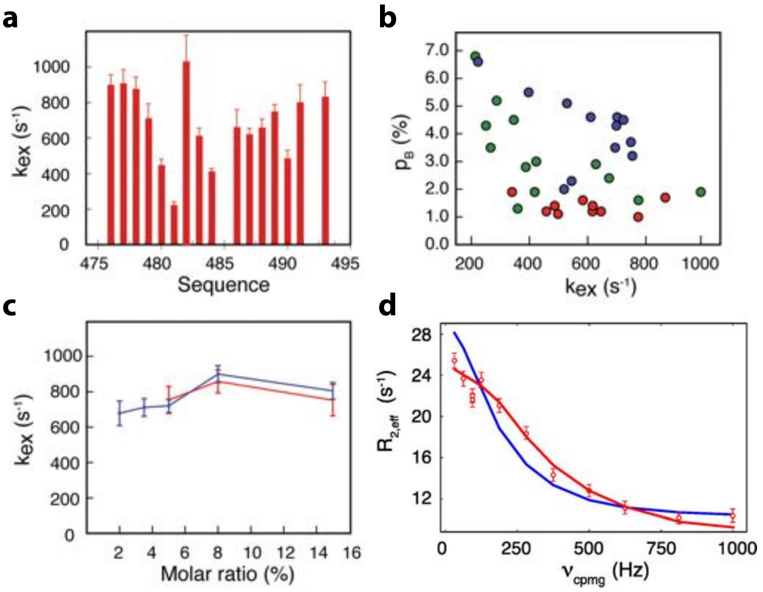

Figure 4.4: Analysis of RD data using two-state models. **(a)** Exchange rates (k_{ex}) determined from $^1H^N$, $^{13}C'$, and ^{15}N RD curves for individual residues in the PX interaction region of N_{TAIL}, fitting admixtures containing 2%, 3.5%, 5%, and 8% PX simultaneously using the Carver-Richards expression for two-state exchange. **(b)** Residue- and admixture-specific exchange rates k_{ex} and bound-state populations p_B for residues in the PX binding site of N_{TAIL}, color-coded by admixture (red 2%, green 3.5%, blue 5% PX), obtained by numerical fits of individual-residue $^1H^N$, $^{13}C'$, and ^{15}N RD data at individual admixtures to a two-state exchange model. **(c)** Dependence of k_{ex} values on molar ratio. Blue: k_{ex} measured for N_{TAIL} with respect to PX:N_{TAIL} molar ratio. k_{ex} values were obtained from global fits, at individual titration mixtures, of a two-state exchange model to N_{TAIL} $^1H^N$, $^{13}C'$, and ^{15}N RD data from all residues exhibiting exchange. The blue curve can be fit using a constant k_{ex} of 771 ± 38 s^{-1}. Red: k_{ex} measured on PX with respect to N_{TAIL}:PX molar ratio. k_{ex} was obtained from global fits of a two-state exchange model to $^1H^N$ and ^{15}N RD data from all residues on PX exhibiting exchange in the presence of N_{TAIL}, but not in its absence. This curve can be fit with a constant value of $k_{ex} = 803 \pm 37$ s^{-1}. **(d)** Improvement in the reproduction of RD data for some sites when using a global three-state model instead of a global two-state model (at individual PX:N_{TAIL} ratios). Shown are experimental ^{15}N RD data (red points) for N_{TAIL} residue 484 at 18.8 T, for the 5% PX:N_{TAIL} admixture. Blue: two-state fit, red: three-state fit.

range of $R_{2,\text{eff}}$ values, and by introducing additional boundary conditions. We demanded that no resultant exchange rate exceed 3000 s^{-1}, a reasonable upper limit for RD processes detectable by CPMG methods, and fixed the sum of the minor state populations ($p_\text{B}+p_\text{C}$) to 5%, the molar percentage of added binding partner PX. This latter condition appeared justified given that the exchange is clearly related to the presence of PX, and that we had measured the K_d of the N_TAIL-PX interaction by isothermal titration calorimetry (ITC) to be 8.4 μM. Based on this information, the observed minor state population should be – within experimental error and at these low titration admixtures – identical to the molar percentage of added binding partner.

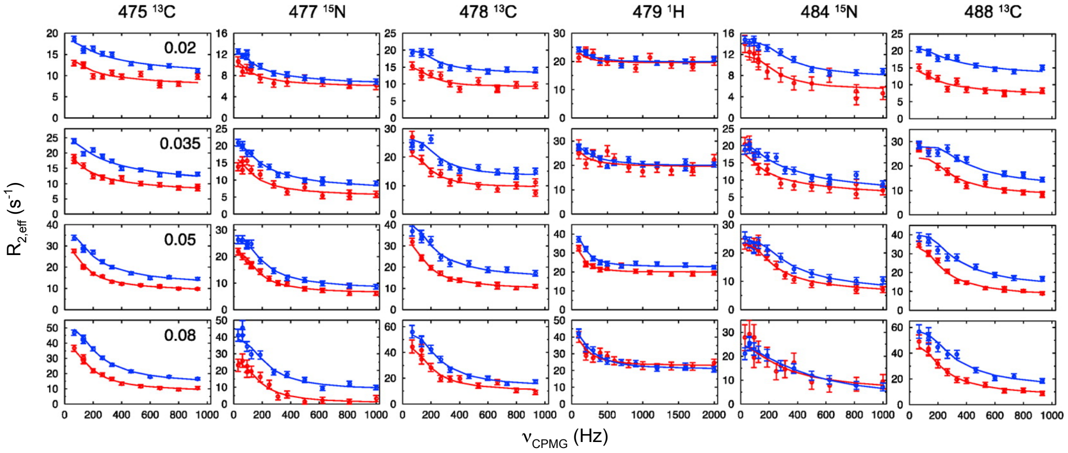

Figure 4.5: Three-state characterization of the N_TAIL:PX interaction from RD. Examples of fits to $^1\text{H}^\text{N}$, $^{13}\text{C}'$, and ^{15}N RD curves from the PX interaction region of N_TAIL at different titration admixtures (shown in different rows; added molar fraction of PX indicated in leftmost column). $^1\text{H}^\text{N}$, $^{13}\text{C}'$, and ^{15}N data from all peptide planes in the PX interaction region of N_TAIL were simultaneously fitted by numerical integration of the Bloch-McConnell equations for three-state exchange, separately for different admixtures. Fixed rates $k_{\text{ex,AB}}$ and $k_{\text{ex,BC}}$ were used, with $k_{\text{ex,AB}}$ varying between 827 and 948 s^{-1} as appropriate for the varying concentrations of free PX in the different admixtures, and $k_{\text{ex,BC}}$ = 2600 s^{-1} constant (see text). Solid lines, fitted curves; circles, data points. Red, 14.1 T; blue, 18.8 T.

The resultant model of a three-state linear exchange has exchange rates of $k_{\text{ex,AB}} = 852 \pm 31$ s^{-1} and $k_{\text{ex,BC}} = 2600 \pm 493$ s^{-1} and excited-state populations of $p_\text{B} = 3.7 \pm 0.1\%$ and $p_\text{C} = 1.3 \pm 0.1\%$ (at the N_TAIL admixture with 5% PX) (Fig. 4.5). Note the similarity of the parameters of the $\text{A} \rightleftharpoons \text{B}$ step of this model with the best fit resulting from a two-state model. Extended grid searches using an upper k_ex cutoff of 4000 s^{-1}, or with $k_{\text{ex,AB}}$ fixed

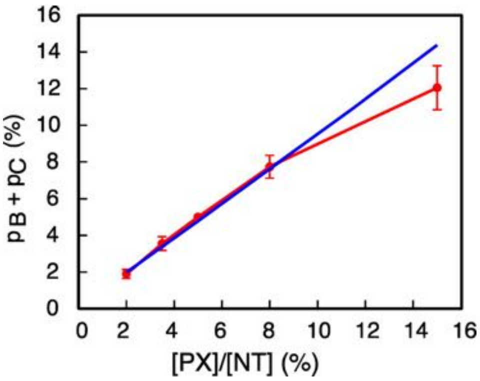

Figure 4.6: Population of the PX-bound forms of $\mathrm{N_{TAIL}}$ for the different PX:$\mathrm{N_{TAIL}}$ admixtures determined from analysis of RD data. Solid red line shows the fitted $\mathrm{p_B} + \mathrm{p_C}$ values from the consensus three-state fit shown in Figure 4.5. Note that, for the 5% data set, $\mathrm{p_B} + \mathrm{p_C}$ was fixed to 5% as described in the text. Blue line indicates the calculated $\mathrm{p_B} + \mathrm{p_C}$ assuming a dissociation constant of 8.4 μM as estimated from ITC measurements.

to 850 $\mathrm{s^{-1}}$, but without restrictions on $k_{\mathrm{ex,BC}}$, p_{B} or p_{C}, confirmed the validity of this three-state model.

Since, in free $\mathrm{N_{TAIL}}$, RD is absent, we judged that the first ($\mathrm{A} \rightleftharpoons \mathrm{B}$) of the two steps of this mechanism, with an exchange rate of 852 ± 31 $\mathrm{s^{-1}}$, corresponds to the bimolecular binding reaction between $\mathrm{N_{TAIL}}$ and PX. Using the concentration of free PX ligand [PX] in the 5% PX admixture of $\mathrm{N_{TAIL}}$, calculated based on the K_d of the interaction of 8.4 μM measured by ITC, the association rate constant k_{on} can be calculated as $k_{\mathrm{on}} = k_{\mathrm{ex}}/([\mathrm{PX}] + K_d)$, yielding a value of 9.7×10^7 $\mathrm{M^{-1}s^{-1}}$. The corresponding dissociation rate constant k_{off} amounts to 811 $\mathrm{s^{-1}}$.

Exchange rates $k_{\mathrm{ex,AB}}$ for the other $\mathrm{N_{TAIL}}$:PX admixtures were calculated based on k_{on} and k_{off} values determined for the 5% PX admixture and the corresponding concentrations of free PX (as $k_{\mathrm{ex,AB}} = k_{\mathrm{on}} \cdot [\mathrm{PX}] + k_{\mathrm{off}}$), yielding values of 827, 839, 879, and 948 $\mathrm{s^{-1}}$ for the 2%, 3.5%, 8%, and 15% PX admixtures, respectively. The rate of the unimolecular second step of the three-state model ($k_{\mathrm{ex,BC}} = 2600 \pm 493$ $\mathrm{s^{-1}}$) was assumed to remain constant. Using this exchange model, dispersion data at all admixtures yield very good fits (with $k_{\mathrm{ex,AB}}$ and $k_{\mathrm{ex,BC}}$ fixed) (Fig. 4.5), significantly improving over two-state fits based on chi-squared statistics ($p \leq 0.01$, see Fig. 4.4 d) at all but the 2% PX admixture ($p = 0.16$), probably due to the low amplitude of RD in the presence of only 2% PX. While $p_{\mathrm{B}} + p_{\mathrm{C}}$ was fixed to 5% at the 5% PX admixture, the three-state fits also result in $p_{\mathrm{B}} + p_{\mathrm{C}}$ values in the range expected from the K_d of the interaction for the other admixtures (Fig. 4.6). The deviation observed for the 15% PX admixture (which is also seen for 2-state fits) may be due to the reduced amount of RD data available at this PX:N_{TAIL} ratio, where a number of peaks are already too broadened to be analyzed quantitatively.

4.4 Binding mechanism and structure of bound N_{TAIL}

Analysis of $^1H^N$, ^{13}C', and ^{15}N chemical shift changes extracted from RD data for the residues in the MoRE of N_{TAIL} yields interesting information on the binding mechanism and the structure of the PX-bound state of N_{TAIL}. The first step of the three-state model of the N_{TAIL}:PX interaction reproduces the best-fitting two-state model not only in terms of k_{ex} and p_{B}, but also the associated ^{13}C' chemical shift changes ($\Delta\omega$) are highly similar (Fig. 4.7 a). ^{13}C' shifts associated with the second step of the three-state model ($\Delta\omega_{\mathrm{AC}}$, measured relative to free-state chemical shifts) are ill-defined (large standard deviations), but reproduce the $\Delta\omega_{\mathrm{AB}}$ pattern for residues with larger dispersion. This indicates that ^{13}C' chemical shift changes in the second step ($\Delta\omega_{\mathrm{BC}}$) are insignificant and that changes in secondary structure, to which ^{13}C' shifts are highly sensitive, occur in the first step. The sign of the ^{13}C' shift changes was established to be positive wherever measurable using established approaches [209], revealing that helical structure is formed or increased during the interaction.

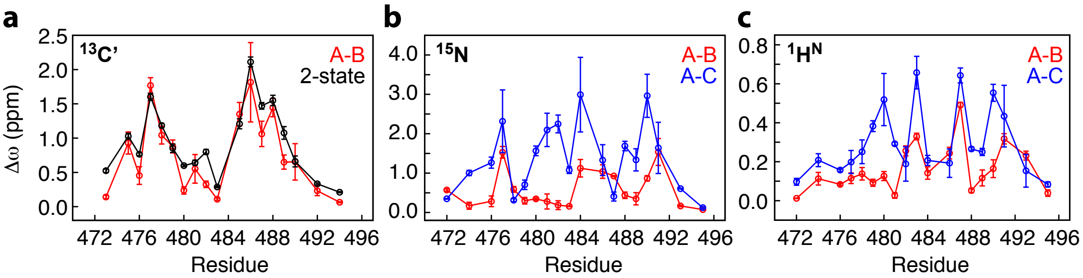

Figure 4.7: Chemical shift changes derived from the consensus three-state exchange model for the N_{TAIL}:PX interaction. **(a)** Comparison of N_{TAIL} ^{13}C' $\Delta\omega$ values for the first step of the global three-state model ($\Delta\omega_{\mathrm{AB}}$, red) with those obtained from a global two-state model (black). Shown are weighted means over all N_{TAIL}:PX admixtures and their standard deviations. **(b, c)** ^{15}N (b) and $^1H^N$ (c) $\Delta\omega_{\mathrm{AB}}$ (red) and $\Delta\omega_{\mathrm{AC}}$ (blue) values in N_{TAIL} obtained from the three-state fit. Weighted means over all admixtures and their standard deviations are shown.

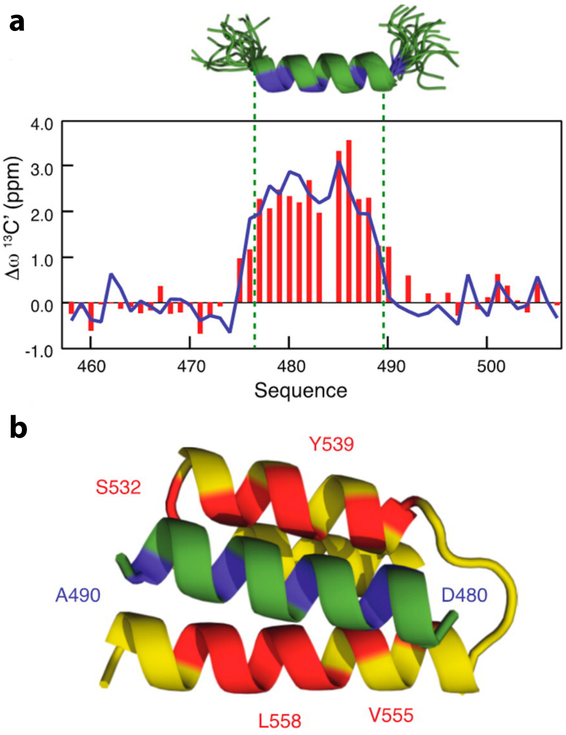

Figure 4.8: Structural analysis of PX-bound N_{TAIL}. **(a)** ^{13}C' secondary chemical shifts of the bound state of N_{TAIL} (red bars, derived by adding $\Delta\omega_{AB}$ from the consensus three-state exchange model to free-state shifts and subtracting random coil shifts from RefDB [210]) and back-calculated secondary chemical shifts from ASTEROIDS minimum ensemble selection (blue line). A single ensemble substate, reporting on helix 476–489 populated to 100%, best reproduces the experimental data for bound N_{TAIL} and is shown in cartoon representation above the plot. Blue residues exhibit $^{1}H^{N}$ $\Delta\omega_{AC}$ values > 0.4 ppm. **(b)** Mapping the binding site of N_{TAIL} with PX. Ribbon representation of N_{TAIL} with sites showing $^{1}H^{N}$ RD-derived shift changes ($\Delta\omega_{AC}$) above 0.4 ppm in blue. Ribbon representation of PX shows residues in red that display significant N_{TAIL}-induced ^{15}N or $^{1}H^{N}$ RD or significant shifts at all admixtures of N_{TAIL}. Numbers show positions of residues on PX (red) and N_{TAIL} (blue) that exhibit RD. The orientation of N_{TAIL} with respect to PX was optimized manually to agree with the position of residues affected by binding.

The second step (B → C), occurring at the faster rate, is associated with larger ^{1}H^{N} and ^{15}N $\Delta\omega$ values (Fig. 4.7 b, c). Especially the ^{1}H^{N} $\Delta\omega_{AC}$ values, exhibiting a pronounced helical periodicity along the sequence (Fig. 4.7 c), appear to map the interaction face of an N$_{TAIL}$ helix with PX. Notably, the rate of this step ($k_{ex,BC} = 2600 \pm 493$ s^{-1}) closely corresponds to that of a known exchange process intrinsic to PX ($k_{ex} = 2860 \pm 160$ s^{-1}) which has been interpreted as a breathing motion of PX helices II and III [211]. Residues of PX affected by N$_{TAIL}$ binding, exhibiting chemical shift changes and/or RD when measured on isotope-labeled PX upon addition of unlabeled N$_{TAIL}$, are distributed across these helices (Fig. 4.8 b) and map out the N$_{TAIL}$ binding site.

The fitted N$_{TAIL}$ ^{13}C' $\Delta\omega_{AB}$ values were added to the ^{13}C' shifts of free N$_{TAIL}$ (ω_{f}) to determine the ^{13}C' chemical shifts in B and C states. To model the bound-state conformation of N$_{TAIL}$, the resultant values were then analyzed using the minimum ensemble ASTEROIDS approach described in ref. [201]. Initially, we assumed a single bound state consisting of an individual helix covering different N$_{TAIL}$ residues; then, we iteratively tested for the presence of more complex equilibria of two or more helices if simpler models did not adequately reproduce the data. Comparison of the experimental ^{13}C' shifts ($\omega_{f} + \Delta\omega_{AB}$) with values predicted from all possible helical ensembles spanning the MoRE reveals that a single helix (residues 476–489), strongly resembling one of the helical states populated in the free-state equilibrium (H2, residues 476–488 [201]), best describes the PX-bound state of N$_{TAIL}$ (Fig. 4.8).

4.5 Discussion

The model of three-state exchange that we found to account best for our RD data reveals a probable trajectory for formation of the N$_{TAIL}$:PX complex (Fig. 4.9). According to this scenario, the interaction proceeds in two steps. Initially, one of the interconverting N$_{TAIL}$ helices known to be present in the free state [201] is stabilized by the interaction with PX, as evidenced by more helical ^{13}C' shifts. ^{1}H^{N} and ^{15}N shift changes are less pronounced in this step, suggesting that the interaction is nonspecific with respect to the PX surface. State B of the $A \rightleftharpoons B \rightleftharpoons C$ equilibrium thus likely corresponds to a dynamic encounter complex. The second, faster step induces large ^{15}N and ^{1}H^{N} shift changes, with the latter reporting on specific binding of one side of the N$_{TAIL}$ helix in the interhelical groove on the surface of PX. Remarkably, the rate associated with this second step corresponds closely to the intrinsic conformational exchange rate observed in the helical groove of PX [211]. It

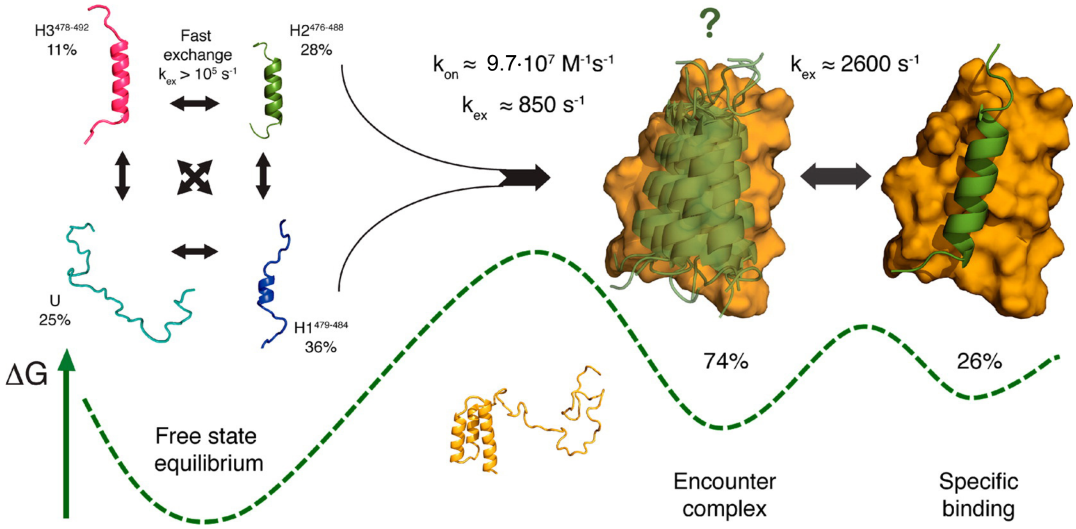
$H3^{478-492}$
11%
Fast
exchange
$k_{ex} > 10^5\ s^{-1}$
$H2^{476-488}$
28%
$k_{on} \approx 9.7 \cdot 10^7\ M^{-1}s^{-1}$
$k_{ex} \approx 850\ s^{-1}$
?
$k_{ex} \approx 2600\ s^{-1}$
U
25%
$H1^{479-484}$
36%
ΔG
74%
26%
Free state
equilibrium
Encounter
complex
Specific
binding

Figure 4.9: Proposed binding mechanism for Sendai virus N_{TAIL} to PX. The underlying conformational equilibrium in the free state, populating three helices (H1, H2, and H3, with populations shown for each [201]) and the unfolded form (U), binds to PX via an initial encounter complex that stabilizes a helix resembling H2 at a rate of 850 s^{-1}. The "fuzzy" nature of the cartoon in the intermediate step indicates that the encounter complex is likely nonspecific and dynamic. Following the encounter, the N_{TAIL} helix formed locks into the PX binding site in the helical groove on the surface of PX at a rate (2600 s^{-1}) coincident with intrinsic motions of the PX helices. A sketch of the free-energy landscape is shown at the bottom, showing that the encounter complex has a higher population than the second more specific complex. The on rate exceeds the diffusion limit and is electrostatically driven.

appears that the initial encounter complex is stabilized at a rate dictated by the intrinsic dynamics of the host protein. Thus, intrinsic dynamics of both binding partners – the fast conformational equilibrium of $\mathrm{N_{TAIL}}$ and a breathing motion of its binding site on PX – regulate their interaction. The presence of two distinct steps in the interaction process and the dynamics within the $\mathrm{N_{TAIL}}$:PX complex may also explain why resonances of $\mathrm{N_{TAIL}}$ remain exchange broadened even in the presence of excess PX. Our work thus constitutes one of the rare experimental characterizations of a “fuzzy complex” [183].

The k_{on} value of 9.7×10^7 $\mathrm{M^{-1}s^{-1}}$ we found for $\mathrm{N_{TAIL}}$:PX binding significantly exceeds the diffusion limit [212] and indicates that electrostatic interactions play a role in initial complex formation. We tested this hypothesis by mutating the negatively charged residues D475 and D478 in the N-terminal part of the $\mathrm{N_{TAIL}}$ interaction region to alanines. The results show a slowing of the effective association rate to 4.4×10^6 $\mathrm{M^{-1}s^{-1}}$, supporting the suggestion that the initial encounter complex is electrostatically driven.

From the experimental data alone, we cannot distinguish whether stabilization of the H2 helix in $\mathrm{N_{TAIL}}$ upon PX binding occurs uniquely through binding of this helical state in a conformational selection-type mechanism or whether the individual $\mathrm{N_{TAIL}}$ states can each form H2 after encountering PX. However, the close similarity of the bound state of $\mathrm{N_{TAIL}}$ with one of the conformers of the free-state equilibrium, as well as the fact that the helical interconversion in free $\mathrm{N_{TAIL}}$ is much faster than the time scale of the PX binding, suggest that conformational selection does play a role in the initial binding of $\mathrm{N_{TAIL}}$ to PX. A recent kinetic study has, on the other hand, found an induced-fit process to best explain the interaction between the closely similar $\mathrm{N_{TAIL}}$ and XD proteins of measles virus [213]. However, it is not clear what process the change in tryptophan fluorescence measured in that study corresponds to exactly at the molecular level. The “locking-in” of $\mathrm{N_{TAIL}}$ on the surface of its binding partner we describe in the SeV $\mathrm{N_{TAIL}}$:PX system may well correspond to the unimolecular induced-fit process detected for measles $\mathrm{N_{TAIL}}$ and XD. It thus seems that in this interaction, conformational selection and induced fit coexist in a mixed multistep process.

Formation of a nonspecific encounter complex, facilitating subsequent localization in the specific binding site, may confer thermodynamic advantages, as has been discussed [190, 214, 215]. In the case of $\mathrm{N_{TAIL}}$, stabilization of the preformed helix may allow native contacts of the final complex to be formed more rapidly, which may be energetically more favorable than complete folding upon binding from the disordered state. In agreement with our observation that helical pre-structuration in the free state of $\mathrm{N_{TAIL}}$ plays a role in binding, a study using NMR and stopped flow on the intrinsically disordered ACTR protein that folds upon binding to its partner NCBD found an acceleration of ligand binding with increasing intrinsic helical content introduced by mutations [216]. On the other hand, a similar study on the disordered PUMA protein indicated that its residual free-state structure has no influence on binding to its partner [217]. However, the free state of PUMA exhibits relatively low helical content (about 20%), and the mutations used did not vary it to a great extent. Conformational selection-type mechanisms may thus play a role in the initial step of an IDP binding to its partner to a degree that corresponds to the amount of prestructuration present in its free-state ensemble. After the initial encounter, further induced-fit type rearrangements within the complex may occur.

This study and comparison to other experimental investigations of kinetics and mechanisms of IDPs binding to their partners thus also highlights the complexity and variability of the mechanisms at play. No individual principle or mechanism (such as conformational selection or induced fit alone) may be able to explain all observations made in different IDP systems, and it is more likely that combinations and mixed mechanisms are employed. In the wake of our study of the $\mathrm{N_{TAIL}}$:PX interaction, we have examined a number of core concepts important in binding of IDPs to their partners, such as conformational selection and induced fit, specificity and promiscuity, fly-casting and pre-structuration, in an extensive review of the relevant literature. This review is included in this work in Appendix A.

Part II

Current work

Chapter 5

Functional dynamics of the protein transporter FhaC in the membrane

5.1 Introduction

Transport of macromolecules across or into membranes is an essential function of the cell. In Gram-negative bacteria, the outer membrane constitutes a major barrier protecting the cell against noxious chemicals such as antibiotics; however, import and export of molecules such as nutrients and virulence factors has to be assured. A wide range of specific transport systems has evolved for this purpose. In particular, for Gram-negative pathogens, protein export is critical to adhere to, invade, or to intoxicate host tissues. One of the systems these bacteria employ for protein secretion is the Two-Partner Secretion (TPS) pathway dedicated to the export of large, elongated β-helical proteins with roles in colonization, biofilm formation, and interbacterial warfare, among others [218]. The two partners of TPS systems are the secreted TpsA proteins and the transmembrane β-barrel TpsB transporters. TpsB proteins are part of the Omp85 superfamily of transporters which mediate protein translocation across or insertion into membranes, comprising notably the BamA insertases that assemble most outer membrane proteins (OMPs) in bacteria [219, 220].

In collaboration with Françoise Jacob-Dubuisson at the Lille Pasteur Institute, I am working on the 61.3 kDa TpsB protein FhaC, which secretes the 230 kDa TpsA protein FHA in the whooping cough agent *Bordetella pertussis*. FHA has adhesin and immunomodulatory functions and is involved in biofilm formation [221]. Françoise Jacob-Dubuisson and coworkers have obtained the crystal structure of FhaC in 2007, which provided the first high-resolution structure of a full-length Omp85 protein (PDB 4QKY [222, 223]). FhaC comprises a 16-stranded transmembrane β barrel preceded by two periplasmic POTRA (polypeptide transport associated) domains (Fig. 5.1 a) which function as the periplasmic receptor of the FHA substrate [224]. An extracellular loop, L6, partially occludes the β barrel and folds back into it, with the arginine residue in a conserved VRGY/F motif forming a salt bridge to the aspartic acid of another conserved motif, F/GxDxG, in β strand 13 of the barrel. L6 and the barrel-proximal POTRA domain are essential for the function of Omp85 proteins [225]. As predicted for most TpsB transporters, FhaC also features an N-terminal helix H1 that crosses the β barrel (Fig. 5.1 a).

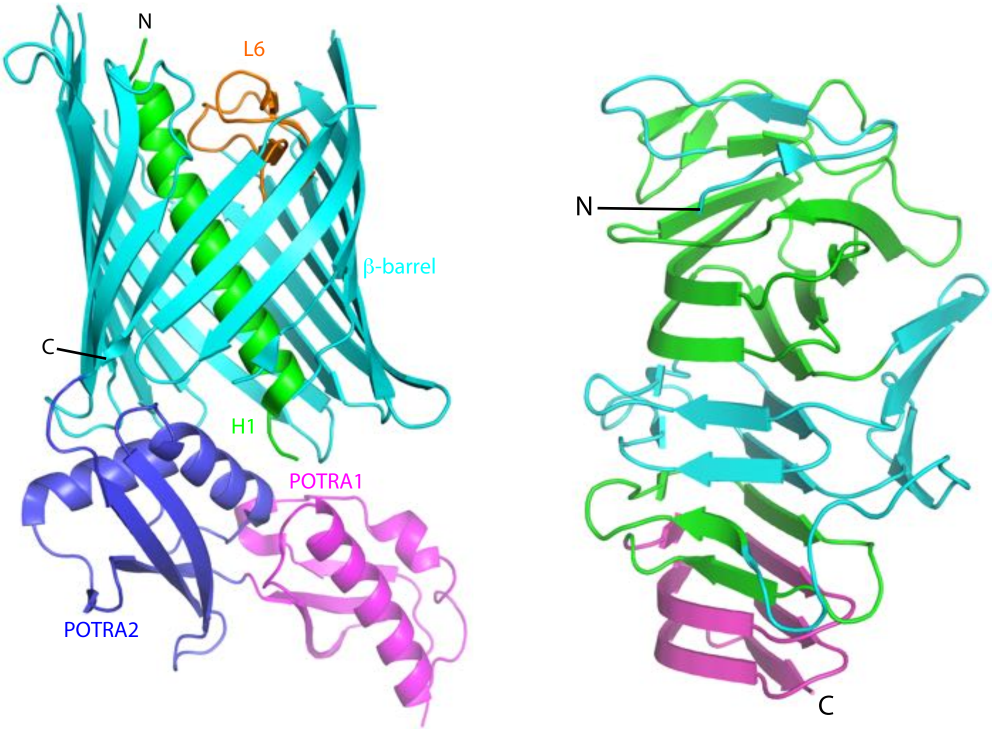

Figure 5.1: Crystal structure of FhaC (left) [222] and Fha30, a 30 kDa N-terminal fragment of FHA (right) [226]. The different structural domains of FhaC, as well as the L6 loop, are highlighted in different colours. The N-terminal helix H1 inside the FhaC barrel is linked to POTRA1 via a 30-residue linker not resolved in the structure. In Fha30, conserved and less conserved regions of the N-terminal TPS domain essential for secretion (residues 1–245) [226] are displayed in green and cyan, respectively. N- and C-termini of the protein chains are indicated.

FHA is recognized by FhaC in an unfolded conformation, is translocated through the barrel and assumes its β-helical fold (Fig. 5.1 b) at the extracellular surface [226, 227]. The exact mechanism of how this is accomplished is however unclear, and its elucidation is at the core of the research project presented in this chapter. First, the driving force of secretion is a matter of debate. Notably, no high-energy, hydrolyzable compounds such as ATP are available in the bacterial periplasm, and the semi-permeable outer membrane cannot sustain a classical electrochemical gradient (although a Donnan potential based on large charged molecules may exist [228]). It is thought that the free energy released by extracellular folding of FHA, at least partially, drives secretion [229]; in addition, the effective irreversibility of the folding, which prevents backtracking of the chain, and charge effects may play a role [230, 231].

Furthermore, the known crystal structure of FhaC most likely represents a closed resting state, since the β barrel is plugged by the L6 loop and the H1 helix, preventing translocation of the FHA substrate. FhaC must thus undergo conformational changes to permit FHA passage. Electron paramagnetic resonance (EPR) experiments on FhaC have revealed that the protein indeed exhibits large-scale dynamics and exists in an equilibrium of different conformations, already in the absence of its substrate. For example, it has been shown that the H1 helix can leave the barrel [232]. Finally, it is an open question whether FhaC simply opens up to allow for FHA passage or whether it actively participates in the transport. The latter is likely the case, since, for example, FhaC residues can be found whose mutation preserves an interaction with FHA, but abolishes its transport [224].

Recent years have seen much progress in the structural biology of β-barrel proteins, with the advent of high-resolution structures of, for example, VDAC [132–134] (see Chapter 3) as well as of the BamA machinery [233–235]. As also indicated by our results discussed in Chapter 3, the original view of β-barrel proteins as being generally particularly stable and rigid has been more and more challenged in the process. Most notably, it has been found that the β-barrels of BamA and the related TamA protein can open up laterally between their first and last β strands, and that, in BamA, lateral opening is required for function [233, 236, 237]. This has led to the "BamA-budding" model of β-barrel insertion into the outer membrane, proposing that nascent outer membrane β-barrel proteins may grow by insertion of β-strands or hairpins into this lateral opening of BamA, forming a hybrid barrel of which the newly generated protein would then "bud off" laterally into the membrane [238].

Based on these findings and the discovery of large-scale dynamics in FhaC [232, 239], our hypothesis is that FhaC dynamics and lateral barrel opening play a role in substrate transport. More precisely, we propose that, after helix H1 leaves the barrel, the hairpin consisting of β strands $\beta 5$ and $\beta 6$ from the second POTRA domain of FhaC (POTRA2) can insert into a gap between the first and last barrel strands created by lateral opening. The

$\beta5$–$\beta6$ hairpin is involved in substrate recognition [224] and has amphipathic properties; thus, it may be envisioned that it temporarily inserts into the FhaC β barrel and hoists the substrate into the barrel lumen. This model may explain how FHA enters the FhaC pore, as well as how directionality of transport is initially established. The proposed mechanism entails that FHA "hitch-hikes" on intrinsic dynamics of FhaC during the transport, and that a structural motif of FhaC exchanges between a soluble and a transmembrane domain. If confirmed, this model would constitute a novel paradigm for protein transport across membranes.

Applying solid-state NMR to FhaC in liposomes, I participate in a multidisciplinary consortium headed by Françoise Jacob-Dubuisson, also involving the groups of Vincent Villeret (X-ray crystallography, Lille), Sarah Cianferani (hydrogen-deuterium exchange mass spectrometry, Strasbourg), and Frank Sobott (ion mobility mass spectrometry, Antwerp / Leeds), aiming to elucidate the FHA transport mechanism of FhaC and minor FhaC conformations that may play a role in it. Specific goals are, among others, a structural description of FhaC open state(s) that allow for passage of FHA and the determination of exchange rates involved in the functional cycle of FhaC. We investigate wild-type (WT) FhaC as well as mutant variants that have been described to alter its open probability, aiming for both structural and dynamical parameters.

5.2 Methodology

To study the 554-residue FhaC protein by solid-state NMR, we have opted for selective $^{13}C^{1}H_3$ labeling of isoleucine (Ile) δ_1 methyl groups in a perdeuterated background. Methyl labeling schemes have been used successfully in solution-state NMR of large proteins where narrow and intense methyl signals can still be obtained despite the unfavorable transverse relaxation properties of large molecules. This is due to the intrinsic rotation of methyl groups and a TROSY effect slowing relaxation of certain methyl coherences which can easily be exploited in a simple HMQC pulse scheme [240]. In solid-state NMR, this effect is not of importance; however, the extensive signal overlap that can be expected for such large proteins makes the use of selective labeling almost a necessity, given typical signal line widths in solid-state NMR spectra. Among selective labeling schemes, methyl labeling offers advantages also useful in the solid state: methyl-bearing amino acids are typically well distributed in hydrophobic cores of proteins, inter-methyl NOE (or, in the solid state, dipolar long-range) contacts usually are structurally informative, and the reduced number of signals yields workable spectra even for very large proteins. In addition, selective methyl labeling can be performed in a straightforward way using appropriately labeled, commercially available precursors (2-ketobutyric acid 4-^{13}C for Ile δ_1 methyls) [240], a protocol already established in our laboratory.

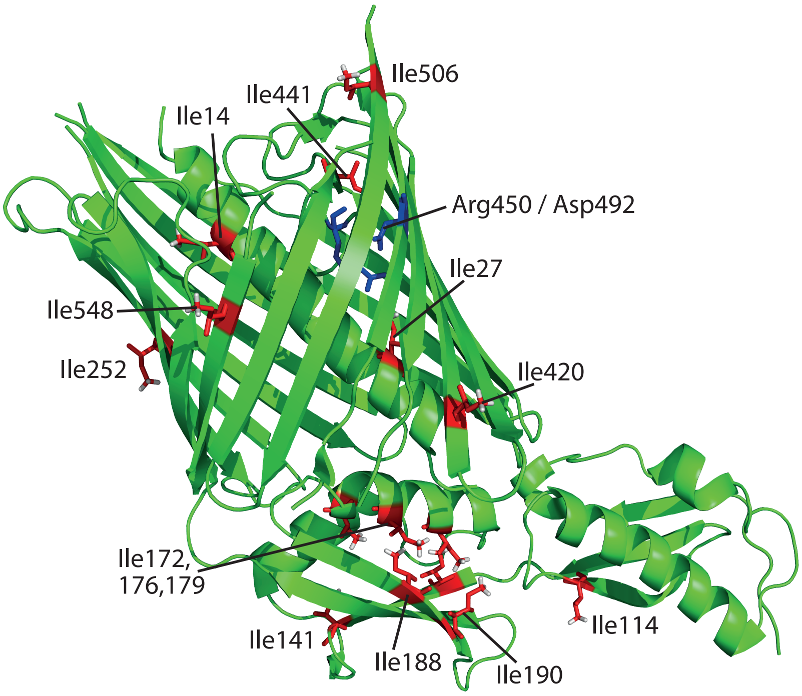

Figure 5.2: FhaC crystal structure (PDB 4QKY [222, 223]) with isoleucine residues labeled and displayed as red sticks. Residues Arg450 and Asp492 forming a conserved salt bridge linking loop L6 and β strand 13 are shown as blue sticks.

While the β barrel of FhaC does not dispose of a hydrophobic core as do globular proteins (the POTRA domains however do), the 15 Ile residues of the protein are nevertheless well distributed across all structural elements and notably in those regions implicated in our model of translocation-related dynamics (2 in the N-terminal helix H1, 1 in POTRA1, 7 in POTRA2 (2 of these in the β5–β6 hairpin), and 5 in the β-barrel, one of which in loop L6 and one in the last β strand) (Fig. 5.2). Ile δ_1 methyl labeling should thus be informative on the conformational transitions of interest here. For example, if the β5–β6 hairpin indeed inserts into the β barrel between strands 1 and 16, through-space contacts between Ile188 and/or Ile190 in the hairpin and Ile548 in β strand 16 may become observable.

We thus expressed WT FhaC and different mutant variants with uniform ^{2}H,^{15}N and selective Ile-δ_1(^{13}C^{1}H$_3$) labeling in *E. coli*. Cloning, expression, purification and reconstitution into *E. coli* polar lipid liposomes, as well as functionality tests by secretion and antibiotic sensitivity assays were performed by Françoise Jacob-Dubuisson as described previously [222, 232, 242]. Lipid to protein ratios used were either 5:1 or 2.5:1 (mass/mass), corresponding to molar ratios of about 400:1 and 200:1, respectively. Samples were packed into 1.3 mm rotors using an ultracentrifugal device (Giotto Biotech). Spectra were recorded on 800 and 950 MHz spectrometers at 50 kHz MAS speed and a sample temperature of about 17°C. 2D ^{1}H-detected CP-based intra-methyl hCH correlation spectra were recorded analogously as described for hNH ("solid HSQC") spectra in [243]. For through-space correlations, an additional ^{1}H-^{1}H mixing time, using 6.4 ms RFDR recoupling [243, 244], was

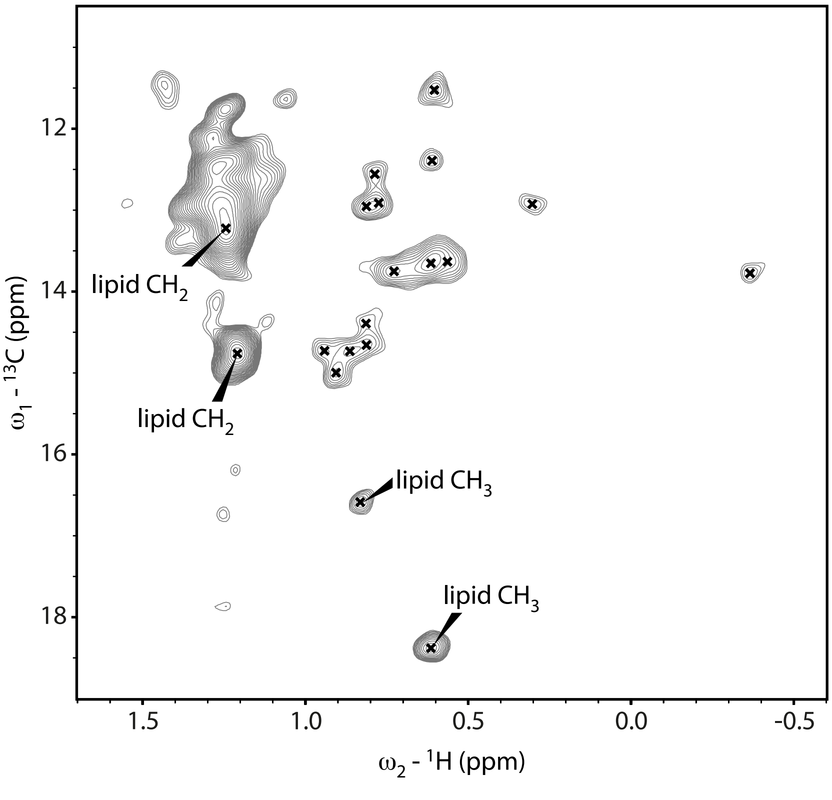

Figure 5.3: hCH dipolar ^{13}C-^{1}H correlation spectrum of WT FhaC in *E. coli* polar lipid liposomes. The general region where isoleucine δ_1 correlations are expected is shown. Lipid signals identified from known lipid chain chemical shifts [241], as well as by comparison of spectra recorded on samples with different lipid to protein ratios, are indicated. Lipid CH$_2$ signals are aliased in the ^{13}C dimension. Putative FhaC Ile δ_1 methyl signals are indicated by unlabeled black crosses.

added before ^{1}H detection, leading to a 2D hChH pulse sequence. To probe for μs time scale dynamics, hCH-based $R_{1\rho}$ experiments with ^{13}C spin-lock field strengths between 1.2 and 10 kHz were recorded as described in [245] for ^{15}N $R_{1\rho}$ experiments.

5.3 Resonance assignments

The "fingerprint" ^{13}C-^{1}H dipolar correlation spectrum of Ile-δ_1(^{13}C^{1}H$_3$)-labeled WT FhaC in liposomes is shown in Figure 5.3. As expected given the high lipid content of the sample, strong lipid peaks are visible; however, isoleucine δ_1 methyl signals are clearly identifiable. Based on peak shapes and intensities, 15 signals were at first tentatively identified (marked by crosses in Fig. 5.3). This corresponds perfectly to the 15 Ile residues of FhaC (however,

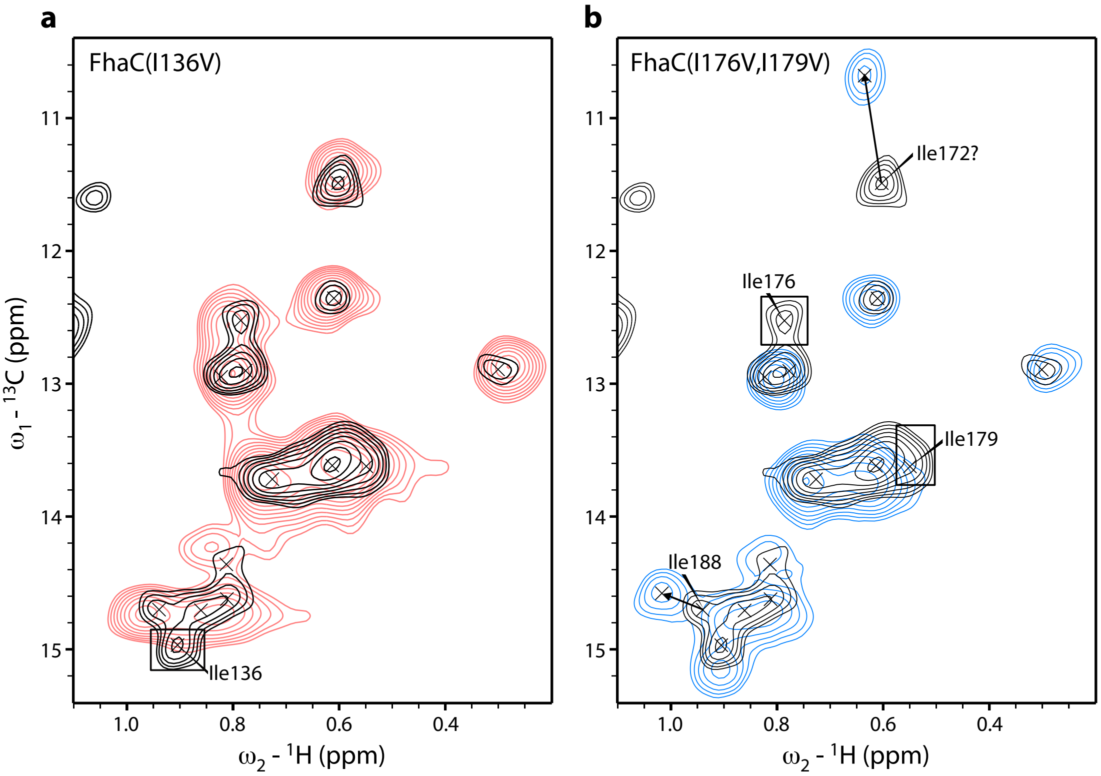

Figure 5.4: Assignment of FhaC Ile residues from mutations. Shown are superpositions of the hCH spectrum of WT FhaC from Figure 5.3 (black, both panels) with the hCH spectrum of FhaC(I136V) (**(a)**, red) and that of FhaC(I176V,I179V) (**(b)**, blue). Vanishing and shifting peaks are indicated by rectangles and arrows, respectively. Labels indicate obtained or confirmed resonance assignments and assignment suggestions.

of course, it cannot be excluded that some signals are, for example, peaks arising from slow exchange and others are broadened out by intermediate exchange or dynamics too fast to yield observable CP signal). The far upfield signal at (13.8 | -0.37) ppm is not always clearly present, but indeed appears to be an Ile signal, possibly affected by aromatic ring currents. It has already been reported before in 1D ^{1}H spectra of FhaC [224]. So far, mutant FhaC variants have confirmed the assumptions made here in terms of the number and position of individual Ile signals contained in overlapping peak groups (see below).

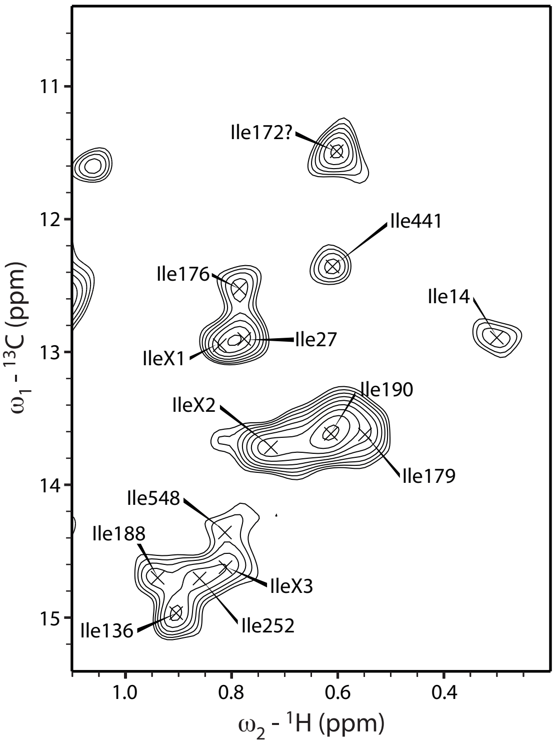

Figure 5.5: Ile δ_1 methyl group assignments of FhaC obtained so far, shown on the WT FhaC hCH spectrum of Figure 5.3. Labels X1, X2, X3 indicate so far unassigned Ile residues.

For assignment of Ile δ_1 methyl signals, Ile-to-Val mutants of FhaC were generated to identify Ile residues via vanishing signals in mutant hCH spectra. All FhaC mutants used were functional as determined by an *in vivo* secretion assay [242]. From four single Ile mutants (I136V, I252V, I441V, I548V), two double mutants (I176V,I179V and I188V,I190V), and a variant in which residues 4 to 26 of the N-terminal helix H1, including Ile14, were deleted (ΔH1), 11 of the 15 Ile residues could so far be assigned. The four single mutants yielded unambiguous assignments via clearly vanishing individual peaks (Fig. 5.4

a). Despite larger changes in their spectra, the two double mutants I176V,I179V and I188V,I190V, together with additional information, allowed to assign the four mutated isoleucines with high confidence and to obtain a suggestion for the assignment of Ile172 in addition (Fig. 5.4 b). For example, the relative placement of Ile176 and Ile179 (Fig. 5.4 b) was obtained from the observation that the peak assigned to Ile179 is more affected in the I188V,I190V mutant, which may be explained by the slightly closer proximity of Ile188 to Ile179 than to Ile176 (4.4 vs. 4.8 Å Cδ_1-Cδ_1 distance in the crystal structure (PDB 4QKY [222, 223])), as well as the observation that the peak assigned to Ile176 is more affected by the ΔH1 mutation and by FHA substrate addition (see below), consistent with the more exposed location of Ile176 [224]. Conversely, Ile188, initially placed relative to Ile190 only because two different chemical shift prediction algorithms [246, 247] suggested more downfield shifts of Ile188 for both ^{13}C and ^{1}H, is more affected in the I176V,I179V mutant (Fig. 5.4 b), confirming its assignment since Ile188 is much closer to both Ile176 and Ile179 in the crystal structure than is Ile190. All assignments obtained so far are shown in Figure 5.5.

5.4 Through-space correlations

To probe inter-methyl distances and potentially identify further resonance assignments or alternative FhaC conformations, we recorded 2D hChH correlation spectra comprising an ^{1}H-^{1}H RFDR mixing period to obtain through-space correlations [243, 244]. While alternative conformations of FhaC (*e. g.* with helix H1 out of the barrel pore) have been shown to be present at equilibrium [232], we sought to interpret any new cross-peak signals not present in intra-methyl hCH spectra in a conservative way, first trying to find short inter-methyl distances in the ground-state FhaC crystal structure (PDB 4QKY [222, 223]) that could explain such signals. We recorded hChH spectra on WT FhaC as well as on a mutant in which residues 4 in H1 and 391 in extracellular loop L5 had been mutated to cysteines (FhaC(4C-391C)). These two cysteines have been shown to be able to form a disulfide bridge, effectively locking H1 in its resting state [232]. Even though the disulfide bridge was only formed to an extent of about 50% in this sample according to gel electrophoresis, we considered this variant as more representative of the closed FhaC state captured in the crystal structure than WT FhaC whose H1 helix can leave the barrel pore in liposomes [232].

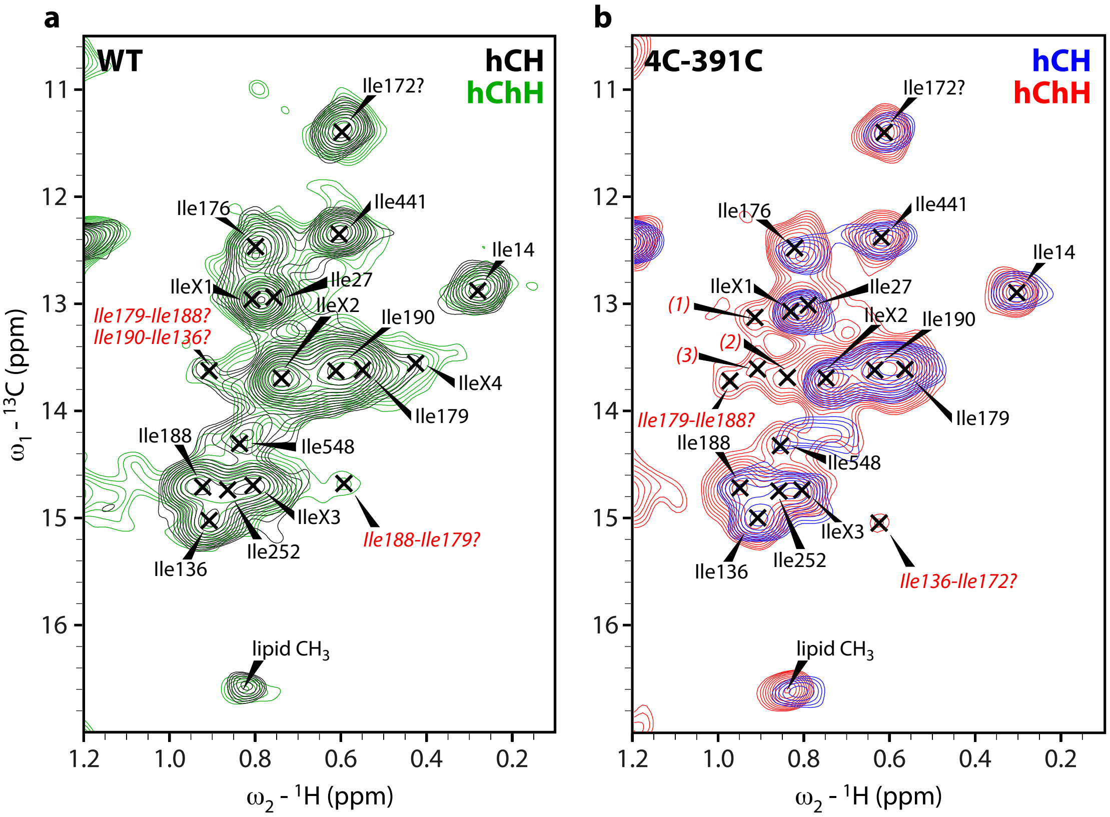

Figure 5.6: hCH (black / blue) intra-methyl and hChH (green / red) through-space correlation spectra of WT FhaC **(a)** and FhaC(4C-391C) **(b)**. Cross-peaks only present in hChH spectra, *i.e.* candidate through-space correlations, and possible assignments are indicated by red labels. See text for details.

Resultant hChH spectra are shown in Figure 5.6. For WT FhaC (Fig. 5.6 a), only one new signal not present in the standard hCH spectrum appears which, while having numerous theoretical assignment possibilities, can be explained by a contact between Ile188 and Ile179 in POTRA2 (4.4 Å Cδ_1-Cδ_1 distance in the crystal structure). Its symmetry-related peak (Ile179–Ile188) or one representing an Ile190–Ile136 contact (8.4 Å Cδ_1-Cδ_1 distance) may also be present, however, spectral intensity at that location is also seen in a hCH spectrum of the same sample. A number of other Ile δ_1 inter-methyl contacts in the crystal structure are in a range that would be expected to yield cross-peaks ($\leq$ 8 Å) given the mixing time used and the high level of deuteration. While some of them would be overlapping with intra-methyl correlations, their general absence is consistent with the assumption that FhaC overall exhibits pronounced dynamics. An additional cross-peak is seen (labeled “IleX4“ in Fig. 5.6 a) for which no corresponding intraresidue peak at its ^{1}H shift of 0.43 ppm exists; this peak also sometimes appears in FhaC variant hCH spectra with high signal-to-noise levels and may thus correspond to a minor peak in slow exchange.

More additional cross-peaks are visible in a hChH spectrum of the FhaC(4C-391C) variant, in agreement with the idea that the 4C-391C disulfide bridge favors a less dynamic FhaC molecule (Fig. 5.6 b). Two of these signals can be explained by the Ile179–Ile188 contact already mentioned and by one between Ile136 and Ile172 (6.3 Å Cδ_1-Cδ_1 distance). Others (labeled (1) to (3) in Fig. 5.6 b) must remain ambiguous at this stage since, for example, no sufficiently short distance exists in the crystal structure between Ile136 and a yet unassigned Ile residue (X1) to explain peak (1), and peak (2), also considering its rather high intensity, may be a correlation with lipid CH$_3$ resonances. Hence, overall, no clear conclusions on additional resonance assignments or alternative FhaC conformations can yet be drawn based on currently available data.

5.5 Open-state mutants and substrate addition

Antibiotic sensitivity assays and electrophysiology have indicated that FhaC variants with a partial H1 deletion (residues 4 to 26, FhaC-ΔH1) or whose conserved Arg450–Asp492 salt bridge is disrupted (FhaC(D492R)) can access more open conformations of the pore [222, 232]. Since the elucidation of open conformation(s) of FhaC is at the heart of this project, we investigated FhaC-ΔH1 and FhaC(D492R) by solid-state NMR. The hCH spectrum of the ΔH1 variant also allowed for assignment of Ile14, absent in this construct, whose resonance vanishes, as well as of Ile27, the first residue after the deletion, whose peak shifts (Fig. 5.7 a).

Interestingly, in FhaC-ΔH1, Ile176 in POTRA2 helix H4, already assigned by Ile-to-Val mutation, appears to vanish as well, and its close neighbor Ile172 broadens and shifts slightly. These two residues are exposed to the hydrophobic groove in POTRA2 involved in substrate recognition which is in contact with the H1–POTRA1 linker region in the absence of substrate [223, 224], which may explain why these residues are affected by partial H1 deletion. Otherwise, it is notable that the effects of two very different FhaC modifications, partial H1 deletion and the D492R mutation, induce similar spectral changes (Fig. 5.7). The D492R mutation, remote from helix H1, nevertheless leads to shifts and broadening in H1 residues; Ile176 in POTRA2 helix H4 is affected in both mutants; and both FhaC

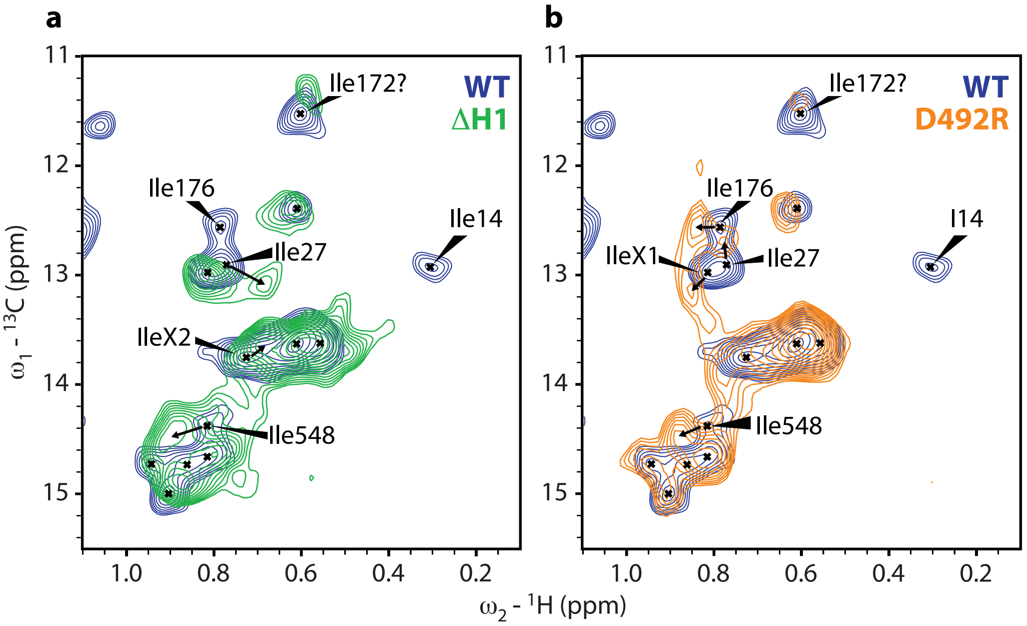

Figure 5.7: Effects of the ΔH1 deletion and the D492R mutation on FhaC. hCH spectrum of WT FhaC (blue, both panels) overlaid with the hCH spectrum of FhaC-ΔH1 (**(a)**, green) and with that of FhaC(D492R) (**(b)**, orange). Affected peaks are labeled; (likely) shift changes are indicated by arrows.

variants exhibit a similar shift of Ile548 in the last C-terminal β strand $\beta 16$. This suggests that both mutations lead to increased mobility of H1 (or what remains of it in FhaC-ΔH1), in agreement with the hypothesized presence of more open FhaC conformations, for which helix H1 should leave the barrel [232]. The shift of Ile548 may indicate a conformational change in or near strand $\beta 16$, as it may occur for barrel opening or hairpin insertion between strands 1 and 16; however, clearly, further experiments are needed to investigate whether this is indeed the case. The Ile548 peak is generally observed to be weak and variable in position, warranting caution in interpreting a shift in structural terms; however, this observation itself indicates that conformational exchange is likely present in or around that residue. So far no or no useful through-space correlation spectra or dynamics experiments could be recorded on ΔH1 and D492R samples due to limited sample stability over time or low signal-to-noise. This will be attempted again on new samples with lower lipid-to-protein ratios to increase sensitivity.

We have also recorded initial experiments adding a variant of FhaC's substrate FHA to FhaC in liposomes. We used a 30 kDa N-terminal fragment of FHA, the smallest

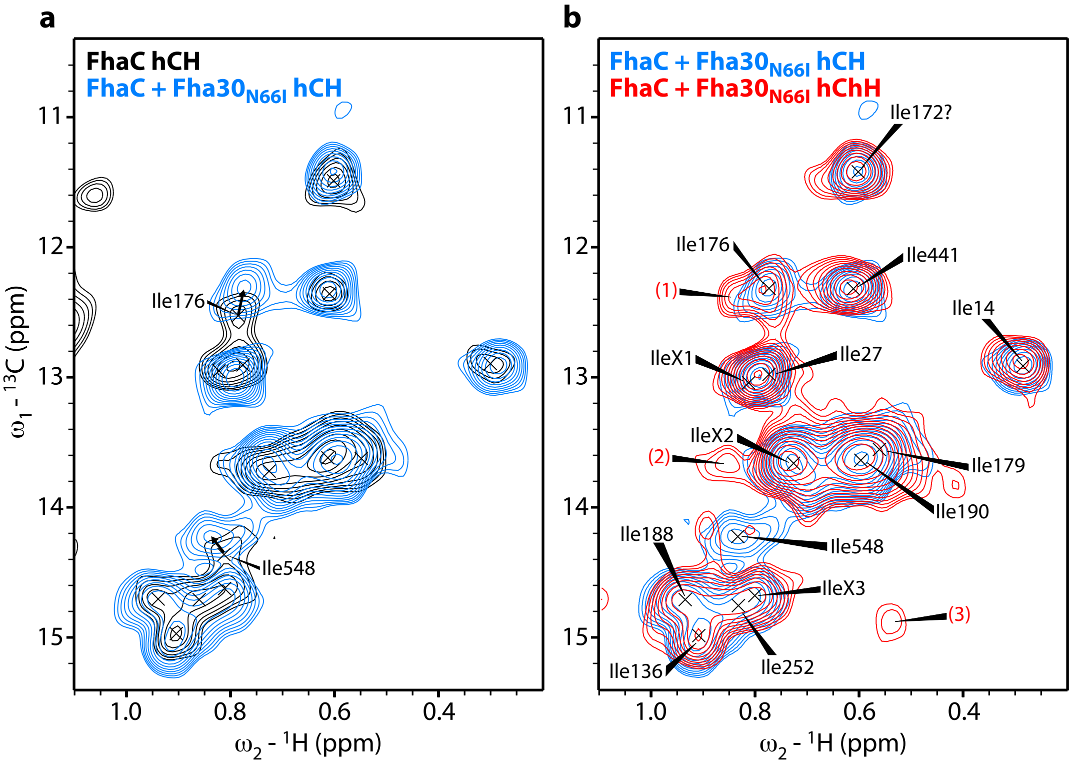

Figure 5.8: Effects of substrate addition to FhaC. hCH spectrum of WT FhaC with Fha30$_{\mathrm{N66I}}$ added in 1:1 molar ratio (blue, both panels) overlaid with the hCH spectrum of WT FhaC alone (**(a)**, black) and with the hChH spectrum of FhaC with Fha30$_{\mathrm{N66I}}$ (**(b)**, red). Peak shifts are indicated in (a); potential through-space correlation signals are labeled (1) to (3) in (b).

secretion-competent FHA truncation [226], bearing an N66I mutation, which favors the unfolded state of FHA and enhances its interaction with FhaC, yet renders it secretion-incompetent [232]. This construct, dubbed Fha30$_{\mathrm{N66I}}$, deuterated and with carbon and nitrogen in natural abundance and solubilized in urea, was added to FhaC in liposomes in a 1:1 molar ratio. The resultant hCH spectrum (Fig. 5.8 a) is surprisingly similar to the WT FhaC spectrum, apart from shifts of residues Ile176 and Ile548, again consistent with the location of Ile176 in the substrate interaction groove of the POTRA2 domain and with possible conformational changes at the interface between first and last β strands of the barrel. Notably, signals from helix H1 (Ile14, Ile27) do not appear to be affected. A hChH through-space correlation spectrum of FhaC with Fha30$_{\mathrm{N66I}}$ (Fig. 5.8 b) exhibits additional cross-peaks in similar locations as discussed above for WT and FhaC(4C-391C) (labeled (2) and (3) in Fig. 5.8 b) and a shoulder next to the Ile176 signal (labeled (1)).

Assuming that the intra-methyl correlation signals in the overlapping spectral regions have the same positions as in FhaC alone, these additional signals may correspond to through-space correlations of POTRA2 residues (Ile176, Ile179, Ile190) with barrel residues (Ile252, Ile548). However, again, this will have to be investigated further. The appearance of cross-peak signals at the positions labeled (2) and (3) in Figure 5.8 b in all hChH spectra discussed so far, but with slightly different positions, casts some doubt on what exactly they correspond to. In addition, while we suggest that parts of POTRA2 may insert into the FhaC β barrel in the course of substrate transport, it is difficult to envision how residues of the POTRA2 helix H4 (Ile176, Ile179) should come into close contact with a barrel residue in β strand 3 (Ile252). More experiments will be needed to elucidate the origin of the spectral changes observed upon substrate addition; in particular, a control experiment for the effects of adding urea alone to FhaC still has to be performed.

5.6 Dynamics by $R_{1\rho}$ relaxation dispersion

In recent years, fast magic-angle spinning, deuteration and ^{1}H detection have enabled the measurement of dynamics parameters previousy inaccessible in solid-state NMR, notably (effective) transverse relaxation rates $R_{2,\mathrm{eff}}$ and their variation with an applied radiofrequency field (relaxation dispersion) [94, 96, 123]. Notably, even for fast MAS and proton dilution, residual coherent ^{1}H-^{1}H dipolar interactions still appear to increase R_2 rates measured by free-precession methods over the values induced by incoherent relaxation and chemical exchange [248]. This problem is much reduced by measuring $R_{1\rho}$ relaxation in the presence of spin-lock pulses and back-calculating $R_{2,\mathrm{eff}}$ using R_1 values measured separately [94, 96, 249]. We have thus recorded a series of ^{13}C $R_{1\rho}$ relaxation dispersion experiments [245] at ^{13}C spin-lock field strengths between 1.2 and 10 kHz, so far on WT FhaC and FhaC(4C-391C) samples with Ile δ_1 methyl labeling, to access microsecond dynamics and minor conformational states of FhaC. Data were analyzed using custom-written scripts as well as the relax software [250] in the framework of Bloch-McConnell theory, using either analytical functions or numerical fits.

Apart from limited signal-to-noise ratios and the consequent need for rather long experiment times, an important limiting factor for quantitative dynamics studies of FhaC is the overlap of many resonance signals even when using the selective Ile δ_1 methyl labeling scheme (Fig. 5.5). For signals which are not fully resolved, extraction of truly residue-specific dynamics data cannot be assured. We have nevertheless opted for analyzing all available data based on signal intensities extracted at the peak positions shown in Figure 5.5, adjusted for variations in peak positions where necessary (residues Ile176, Ile252, and Ile548), despite the possible influence from overlapping signals, to at least approach site-specific dynamics information as closely as possible with the available data.

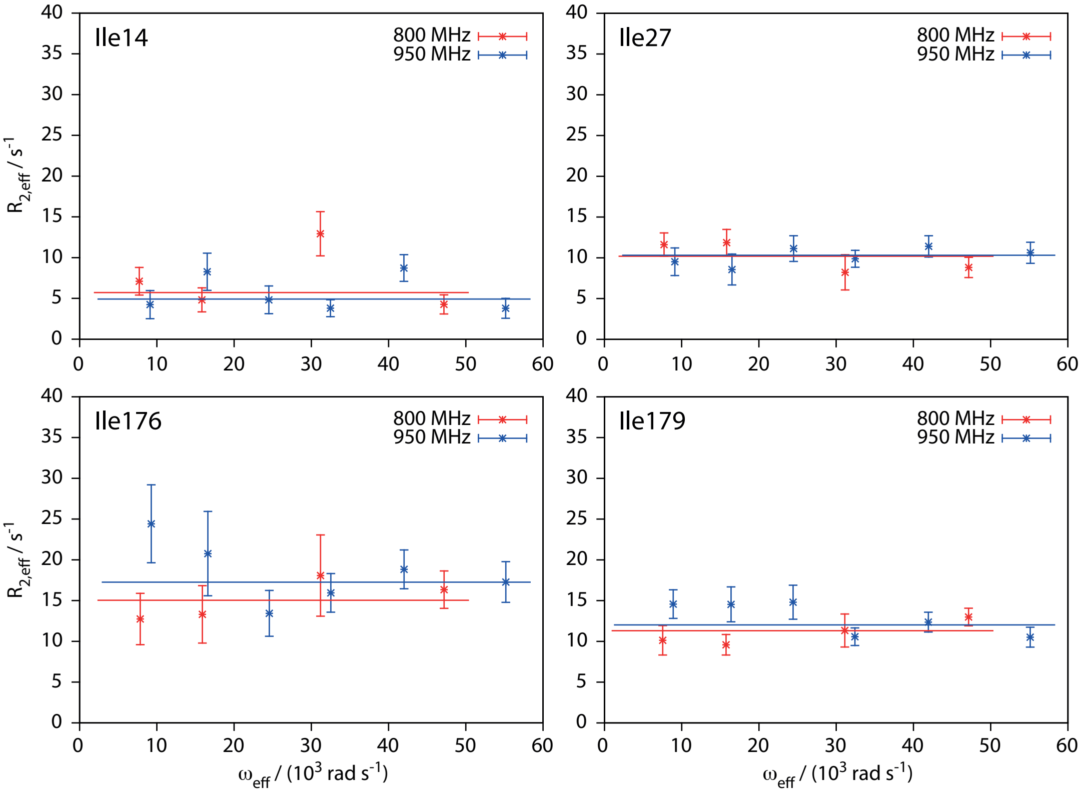

Figure 5.9: ^{13}C $R_{1\rho}$ relaxation dispersion data for δ_1 methyl groups of Ile residues 14, 27, 176, and 179 in WT FhaC. Shown are $R_{2,\mathrm{eff}}$ values, back-calculated from $R_{1\rho}$, as a function of effective rotating-frame spin lock field ω_{eff}, calculated from resonance offset Ω and spin lock field strength ω_1 (in angular frequency units) as $\omega_{\mathrm{eff}} = (\Omega^2 + \omega_1^2)^{1/2}$. Best fits in all cases were obtained by the software relax assuming no exchange ($R_{2,\mathrm{eff}} = \mathrm{const}$). Red, 800 MHz, blue, 950 MHz ^{1}H Larmor frequency.

For WT FhaC, data were recorded at two B_0 field strengths corresponding to 800 and 950 MHz ^{1}H Larmor frequencies. Representative methyl ^{13}C $R_{1\rho}$ relaxation dispersion data for four residues (Ile14 and Ile27 in helix H1, Ile176 and Ile179 in POTRA2 helix H4) are shown in Figure 5.9. In each case, the resultant best fit – judged by Akaike's information criterion (AIC) as implemented in the relax software [250, 251] – was one assuming a constant $R_{2,\mathrm{eff}}$ value without relaxation dispersion. That is, models assuming μs time scale exchange dynamics provided no statistically better fit over the assumption of the absence of such motion. Models assuming chemical exchange were selected only for two residues (Ile441 and Ile548); however, the resultant parameters were clearly unphysical (*e. g.* $k_{\mathrm{ex}} = 0.03\ \mathrm{s}^{-1}$ for Ile441, much too small to be detectable by $R_{1\rho}$ relaxation dispersion, and $\Delta\omega = 720$ ppm for Ile548), and parameter standard deviations exceeded parameter values. The present data thus do not indicate the presence of μs time scale motion accessible to $R_{1\rho}$ relaxation dispersion in FhaC isoleucine sidechains.

For FhaC(4C-391C), a model of fast 2-site exchange [252] was selected for six residues (Ile14, Ile27, Ile179, Ile190, and two unassigned isoleucines) (Fig. 5.10). For the latter

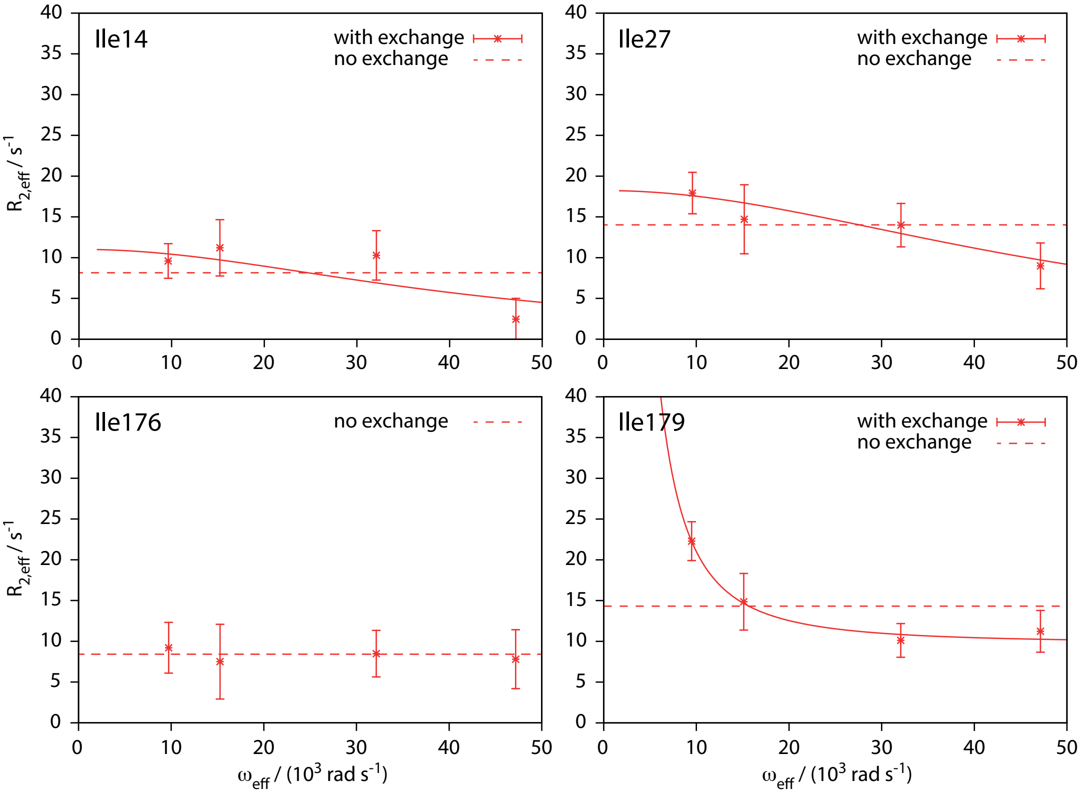

Figure 5.10: ^{13}C R$_{1\rho}$ relaxation dispersion data (R$_{2,\mathrm{eff}}$ vs. ω_{eff} as in Figure 5.9) for δ_1 methyl groups of Ile residues 14, 27, 176, and 179 in FhaC(4C-391C). Best fits obtained by relax assuming exchange (solid lines) are shown where relevant, with $\mathrm{k}_{\mathrm{ex}} = 43,250\ \mathrm{s}^{-1}$ for Ile14 and Ile27 and the (unphysical) k_{ex} of $\sim 10^{-2}\ \mathrm{s}^{-1}$ for Ile179. Best fits assuming no exchange ($\mathrm{R}_{2,\mathrm{eff}} = \mathrm{const}$) are shown for comparison (dashed lines) and for Ile176 for which no exchange was found. All data were recorded at 800 MHz ^{1}H Larmor frequency.

four, no physically reasonable parameters could be obtained ($k_{\mathrm{ex}} < 1\ \mathrm{s}^{-1}$); however, a combined fit of residues Ile14 and Ile27 in helix H1, whose exchange parameters from individual fits were similar, yielded an exchange rate of 43,250 s^{-1}, in the range detectable by $R_{1\rho}$ relaxation dispersion. Helix H1 may thus undergo a concerted motion at this rate; however, this motion is unlikely to be of functional significance for FhaC, since it is not detected in WT FhaC and since H1 is "locked" in FhaC(4C-391C) by a disulfide bridge to the barrel (to the extent of disulfide bridge formation, about 50% in this sample), which would prevent substrate passage through the pore. It may correspond to a fast local motion of H1 around its resting position within the barrel. In general, however, these conclusions were drawn from the limited amount of data – only four spin-lock fields at one B_0 field strength – presently available for FhaC(4C-391C). Additional experiments may clarify whether microsecond dynamics is indeed present in FhaC(4C-391C) and allow for more precise parameter estimates. In particular, the unphysical parameters obtained for Ile179 and Ile190 are likely at least in part due to a lack of data points in the fit, especially at low spin lock fields.

5.7 Outlook

Our work on the FhaC transporter has so far enabled us to assign the resonance signals of 11 of its 15 isoleucine δ_1 methyl groups, which we can now use as probes into structure and function of FhaC. We will finish resonance assignment of the remaining Ile δ_1 methyls via Ile-to-Val mutants. Additional labeling schemes (valine and leucine methyls, amino acid-specific labeling, or uniform (^{2}H,^{15}N,^{13}C) labeling) may be used in the future to extract more extensive information.

We have observed potentially informative through-space correlation signals in spectra of WT FhaC, FhaC(4C-391C), and FhaC with added substrate Fha30$_{\mathrm{N66I}}$. Their origin has so far remained ambiguous and will be further investigated. One strategy will be to reconstitute FhaC in liposomes prepared from deuterated lipids, which we have already purchased, to remove potential cross-peaks of FhaC Ile residues with lipid moieties. In general, only few and weak through-space correlations were seen so far. We will try different pulse sequences for ^{1}H-^{1}H polarization transfer, *e. g.* the recently described BASS-SD approach [253], as well as more classical methods at lower MAS speeds. Possibly, however, the observed lack of through-space correlations is due to the very dynamics of FhaC we are attempting to characterize. Previous studies have already shown that large-scale conformational dynamics are present in FhaC, even at equilibrium and in the absence of substrate [232, 239]. Alternative conformations of FhaC in exchange with the major ground state are likely not populated and/or long-lived enough to give rise to specific identifiable through-space correlation signals. To access minor conformations, apart from relaxation dispersion experiments, we will also use paramagnetic relaxation enhancement (PRE) experiments with paramagnetic spin labels attached to different locations on FhaC, so that even transient long-range interactions should become visible via spectral line broadening [254, 255]. A range of cysteine mutants of FhaC are already available for paramagnetic tag attachment from previous EPR studies [232, 239] and will be used for this purpose.

The FhaC variants investigated that have been described to assume more "open" conformations, FhaC-ΔH1 and FhaC(D492R), exhibit partly similar spectral signatures. Moreover, as in these two mutants, chemical shift changes in residues Ile176 and Ile548 have also been observed upon substrate addition. These observations are suggestive of a common underlying mechanism which we will attempt to elucidate. In particular, we will investigate whether opening of the β barrel between its first and last strands, as suggested by our model, is indeed taking place by, for example, locking the two strands together via a disulfide bridge and testing secretion activity, as well as by recording NMR spectra in the presence of substrate. Evidence from ion mobility mass spectrometry obtained by our collaborators has indicated that a peptide corresponding to the β5-β6 hairpin in POTRA2 can bind to FhaC; we will investigate whether this is indeed the case and, if so, whether it may occur between β strands 1 and 16 in the β barrel.

Based on $R_{1\rho}$ relaxation dispersion experiments conducted so far, no clear evidence for functionally relevant dynamics on the microsecond time scale in FhaC could be obtained. In part, the results are inconclusive due to a low number of data points on dispersion curves and relatively large experimental errors. We will attempt to circumvent these problems by recording more experiments with higher signal-to-noise (longer experiment times), in particular also on the "open" mutants FhaC-ΔH1 and FhaC(D492R) as well as on FhaC in the presence of substrate. We will also apply additional types of experiments to expand the range of motional time scales probed to slower (exchange spectroscopy) and faster time scales (relaxation experiments, measurement of dipolar couplings [95, 98]).

In particular, however, we will more closely investigate the underlying assumptions made so far in the analysis of $R_{1\rho}$ relaxation dispersion in Ile methyl groups. The observation of reasonably flat $R_{2,\mathrm{eff}}$ dispersion curves in a number of residues (as well as in test experiments on ^{2}H,^{15}N,Ile-δ_1(^{13}C^{1}H$_3$)-labeled ubiquitin) does indicate that analysis of these data using the Bloch-McConnell framework is possible. However, on the one hand, for the calculation of $R_{2,\mathrm{eff}}$ values from $R_{1\rho}$ data, methyl R_1 values from monoexponential fits to longitudinal relaxation experiments have been used, while longitudinal relaxation in ^{13}CH$_3$ methyl groups is known to be multiexponential [256, 257]. In solution-state NMR, the difference has been described to be small for more slowly tumbling macromolecules [256], and it is likely to be insignificant here due to the small R_1 contribution at the spin lock fields used; however, this issue merits closer inspection. On the other hand, the spin dynamics of ^{13}CH$_3$ methyl groups in solid-state samples, *i.e.* without global tumbling, under transverse spin-locking fields and magic-angle spinning has so far not

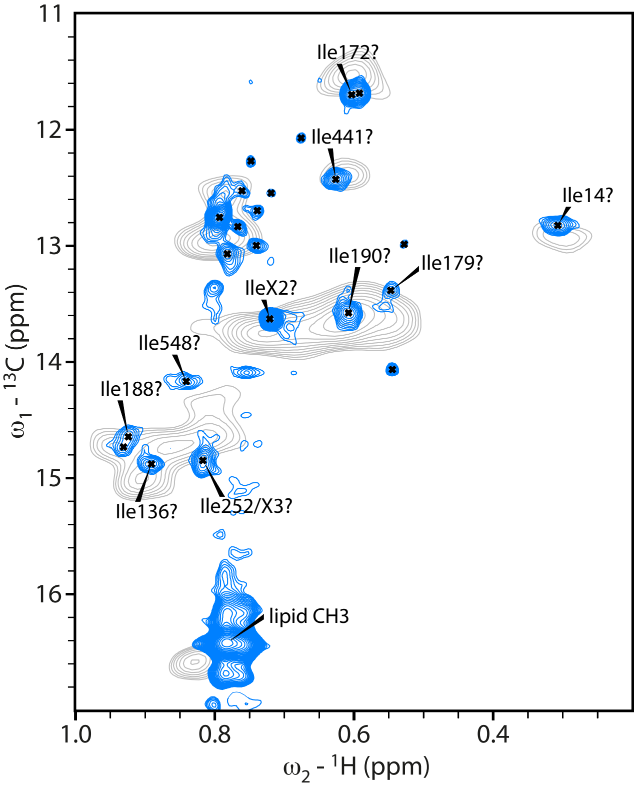

Figure 5.11: ^{13}C-^{1}H HMQC spectrum of ^{2}H,^{15}N,Ile-δ_1(^{13}C^{1}H$_3$)-labeled WT FhaC in DMPC nanodiscs (blue) overlaid with the reference solid-state hCH spectrum of WT FhaC with the same isotope labeling pattern (gray, as in Fig. 5.5). Candidate isoleucine δ_1 methyl signals in the HMQC spectrum (identified by comparison with other spectra of the same sample) are indicated by black crosses. Labels show possible assignments as suggested by peak positions in solid-state spectra (the question marks indicate that these residues were not formally assigned in the solution state).

been investigated in detail. Analysis of the relaxation behavior of methyl groups under these conditions, *e. g.* by numerical simulations [93, 102], is thus warranted before further analysis and interpretation of $R_{1\rho}$ dispersion experiments.

Finally, we have begun to explore solution-state NMR experiments on FhaC reconstituted in nanodiscs [258] as a potential alternative and supplement to solid-state NMR experiments. After considerable effort, Françoise Jacob-Dubuisson has been able to establish a sample preparation protocol that has yielded the first spectra of ^{2}H,^{15}N,Ile-δ_1(^{13}C^{1}H$_3$)-labeled FhaC in dimyristoylphosphocholine (DMPC) nanodiscs (Fig. 5.11). Many peak positions in the HMQC spectrum of the nanodisc sample are similar as in the reference solid-state hCH spectrum, suggesting that assignment transfer may be possible. Several peaks of low intensity are seen that appear to be genuine signals since they are reproduced across different spectra; at least some of these may correspond to minor species of slow exchange processes. Others appear to be artifacts largely due to T_1 noise from the strong lipid CH_3 signal. We will thus use deuterated lipids for a new sample preparation to circumvent this problem.

Of note is how much the signal linewidth in the solid-state spectrum is still larger than that in the solution-state HMQC, despite the use of perdeuteration and fast (50 kHz) magic-angle spinning. This may in part be due to inhomogeneous broadening from conformational heterogeneity in the sample; however, the local environment of FhaC in liposomes and in lipid nanodiscs should be quite similar. It is likely that homogeneous broadening from the large proton network provided by the lipids also contributes to the much larger linewidth in solid-state spectra; consequently, we will also test the effects of using deuterated lipids in the preparation of solid-state liposome samples. In any case, the availability of FhaC samples in nanodiscs opens up the possibility to use the manifold established solution-state experiments to probe dynamics and conformational exchange in methyl-labeled large proteins [257], considerably extending our methodological arsenal to investigate the conformational landscape of FhaC.

Part III

Future plans

Chapter 6

Project: The closed conformation of voltage-gated ion channels by solid-state NMR spectroscopy

6.1 Introduction

In previous chapters, the process of gating, *i.e.* opening and closing the ion conduction pathway, was investigated structurally in two different types of ion channels using solid-state NMR spectroscopy in lipid bilayers. We were notably interested in obtaining information on functionally important channel states whose high-resolution structural characterization had not previously been possible. In KcsA-Kv1.3 (Chapter 1), the previously uncharacterized alternative conformation, the open-inactivated state, could be stabilized in conditions of acidic pH and low (micromolar) potassium concentrations. For VDAC (Chapter 3), important experimental information on its closing process could be obtained; however, the so far elusive closed state itself could not be accessed directly by experiments. Based on the results of our MD simulations, this may be partly due to the dynamic nature of the closed-state conformational ensemble, which may be inaccessible to dipolar-based solid-state NMR experiments. In addition, large-scale conformational transitions that leave the local environment of a given residue largely intact, such as the transition from circular to elliptic barrel states, are difficult to identify from the more local information contained in NMR data.

A key problem, however, is that the unknown closed VDAC conformation is only stable and dominant in the presence of a transmembrane voltage superior to ±30 mV. Experimentally, transmembrane voltages for the study of ion channels have long been applied across cellular or artificial lipid bilayers using microelectrodes in electrophysiology experiments (see for example [260]). However, it has so far not been possible to establish or simulate

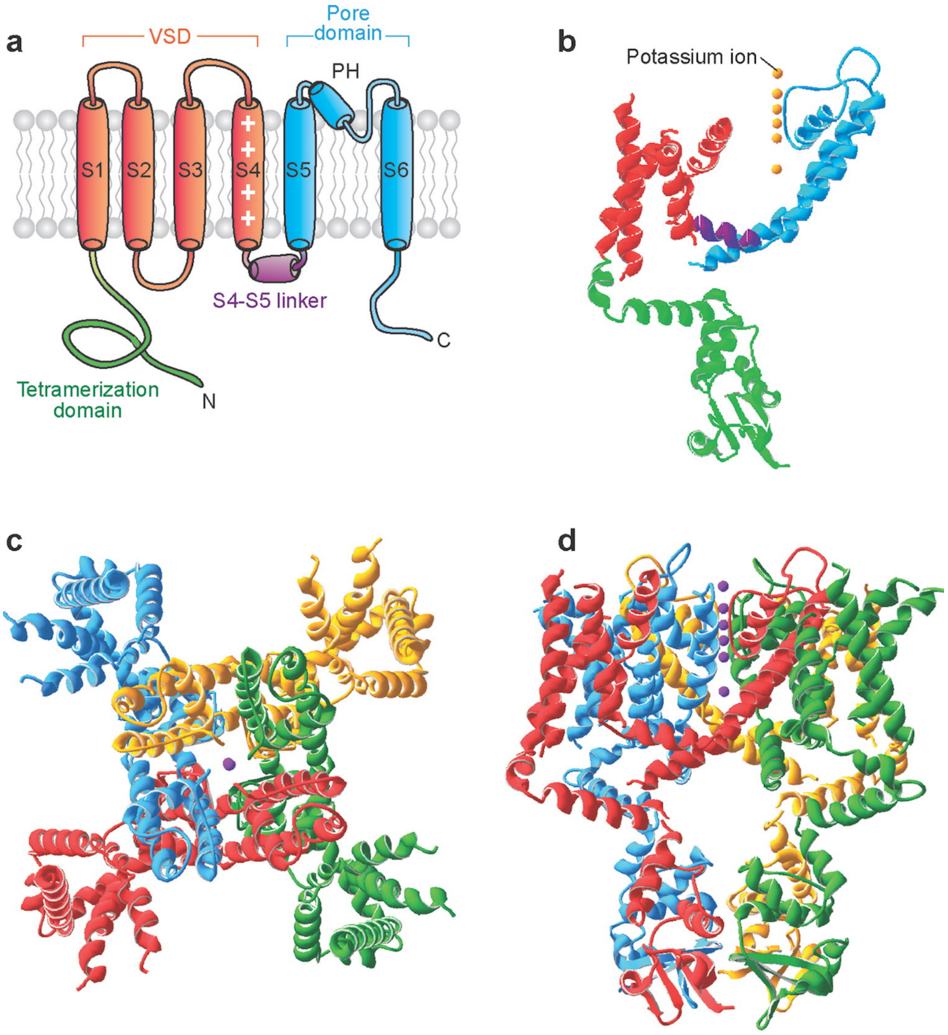
a
VSD
Pore domain
PH
S1
S2
S3
S4
S5
S6
S4-S5 linker
Tetramerization domain
N
C
b
Potassium ion
c
d

Figure 6.1: **(a)** The architecture of a K_v channel subunit. Cylinders are helical segments. The pore domain is shown in blue, the voltage-sensing domain (VSD) in red, the S4-S5 linker in purple, and the N-terminal tetramerization domain in green. **(b)** A single subunit of the Kv1.2 channel [16], color coded as in (a). Potassium ions are colored yellow. **(c, d)** The Kv1.2 tetramer is shown in (c) top view (extracellular side) and (d) side view. Each subunit is shown in a different color. Potassium ions are colored purple. Coordinates from [16]. Figure and legend taken from [259].

a membrane potential in experimental settings used for structural studies. In micelles, bicelles or nanodisc systems used in solution-state NMR, as well as in protein crystals employed in X-ray crystallography, no membrane or isolated membrane compartment is present that could sustain a transmembrane potential. In liposome samples as used in the solid-state NMR studies described in this work, buffer conditions are identical inside and outside of the liposomes. Furthermore, liposomes will not sustain concentration gradients based on small ions on time scales long enough for NMR experiments [261], as also shown by our pH titrations performed on proteoliposomes (Section 1.4). In those experiments, resuspending liposomes in buffers of different pH led to spectral changes that were directly visible in subsequent NMR experiments (usually started on a time scale of one to a few hours after the buffer change) and then remained stable over time, which would not have been expected had the pH change not occurred on the inside of the liposomes as well.

It would however be highly interesting to be able to perform structural biology studies of membrane proteins in the presence of a transmembrane voltage. Not only research on the VDAC channel, but the entire large field of voltage-gated ion channel research would benefit from such a technique. Voltage-gated ion channels (VGICs) are fundamental to electrical signaling in neurons, heart and muscle cells, among others. Voltage-gated sodium ($\mathrm{Na_v}$) channels, for example, initiate action potentials in neurons, while voltage-gated potassium ($\mathrm{K_v}$) channels return the neuronal membrane potential to its resting value [7, 262]. These channels belong to the S4 family of pore-loop channels [9] whose subdomains or subunits each contain 6 transmembrane (TM) helices, the last two of which, with the pore loop in between, form the ion conduction pore, while the first four constitute the voltage-sensing domain (VSD) (Fig. 6.1). Helix 4 (S4) of the VSD contains the gating charges (typically 4 to 7 arginines) that constitute the core of the mobile parts of the voltage sensor [263].

While crystal structures of ion channel pores in open and closed states have been obtained, the voltage sensors in VGIC structures have usually always been found in an activated state [15, 17, 24, 264]. This is expected, since the resting potential of excitable cells is on the order of -100 mV (-70 mV in neurons), and thus, the absence of a transmembrane potential corresponds to a depolarized cell at 0 mV, in which $\mathrm{Na_v}$ and $\mathrm{K_v}$ channels are activated. Much debate has surrounded the exact nature of the movement of VSDs during VGIC (de)activation and their conformation in the resting state. Proposed models range from the transporter model, in which the S4 helix remains nearly static, to the paddle model, in which S4 and the C-terminal part of S3 together undergo a large displacement of 15–20 Å

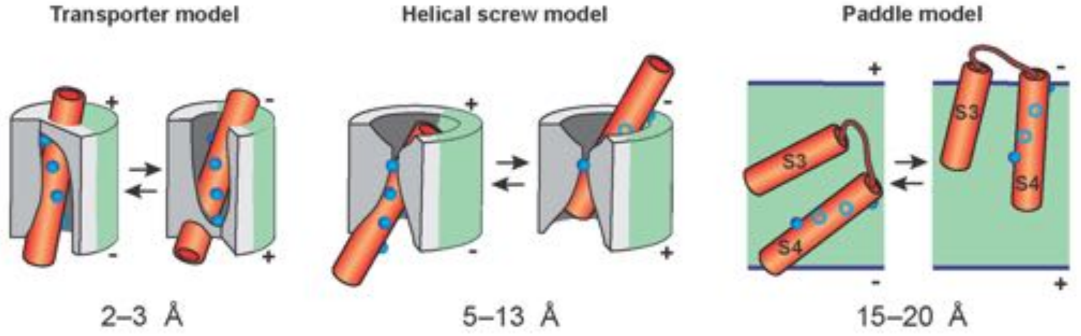

Figure 6.2: Models of voltage sensing. Red cylinders represent the S4 helix unless otherwise indicated. Protein surrounding S4 is colored gray; lipid is colored green. The first four S4 arginines are represented as blue spheres when they are in the foreground; when they are behind the cylinder, they are shown as empty circles. In each model, the S4 resting position is shown on the left, and the activated position on the right. The extent of S4 transmembrane motion involved is reported below each model. Figure and legend adapted from [259].

within the lipid bilayer. In between these, the sliding helix or helical screw models propose that S4 moves more or less linearly on the order of 5 to 10 Å, possibly coupled with a rotation, while being only partially or not at all exposed to lipid [259]. Electrophysiological and biochemical studies as well as modeling have provided constraints on the movement and the resting state(s) of VSDs [11, 263, 265, 266], and initial structures of voltage sensor resting states in an isolated VSD and a two-pore channel have surfaced [267–269]. These data seem to favor the sliding helix / helical screw class of models. However, the VSD resting state in full-length $\mathrm{Na_v}$ and $\mathrm{K_v}$ channels remains elusive, and in the absence of a transmembrane potential, the difficulty remains of identifying which functional state a given structure corresponds to.

I propose here a potential avenue to structurally elucidating ion channel states that require a transmembrane potential, such as the resting state of VGICs and the closed state of VDAC, by directly creating a transmembrane voltage based on a Donnan potential in proteoliposomes for study by solid-state NMR. I will first detail the proposed methodology and then its application to voltage-gated ion channels.

6.2 Methodology

In the presence of an impermeable ion on one side of a membrane permeable to other ionic species present in the solution, a Donnan transmembrane potential is formed based on resultant equilibrium ion concentrations [270, 271]. Such Donnan potentials can be established in liposomes containing ion channels if the liposomes are prepared in the presence of large, impermeable polyanions or polycations such as dextran sulfate or polystyrene sulfonate and then diluted into a buffer without the polyelectrolyte [272]. Alternatively, the polyelectrolyte may be contained in the extraliposomal solution. For the potential to form, at least one ion species in the buffer solution must be able to traverse the liposome membrane. This is already assured when large, nonselective channels such as VDAC or bacterial porins which are permeable to small ions even in “closed” states are studied [272]. If highly selective channels such as voltage-dependent sodium or potassium channels, whose conduction state also changes with transmembrane potential, are to be studied, additional pores will likely have to be introduced into the liposome membrane (such as valinomycin to assure K^+ diffusion). Notably, transmembrane potentials in liposomes may also be generated simply by emulating intra- and extracellular ion concentrations in the buffers within and outside of valinomycin-containing liposomes (high $[K^+]$ inside, high $[Na^+]$ outside) [273]. This may be tested; however, more long-term stability of liposomal membrane potentials may be expected for large polyelectrolytes which should only leak in the case of serious liposome rupture.

It is interesting to note that effects of polyelectrolytes on voltage gating have already been described for the mitochondrial VDAC channel. On the one hand, even symmetric additions of negatively charged dextran sulfate have been shown to induce ultrasteep voltage dependence in VDAC gating in electrophysiological lipid bilayer experiments [274]. This effect can likely be explained by electrostatic interactions of the polyanion with the positively charged N-terminal helix, which according to our model forms the voltage sensor whose movement initiates barrel semi-collapse (Chapter 3). However, in liposome swelling assays, the asymmetric presence of another polyanion has also been shown to affect VDAC open probability in the absence of applied transmembrane voltage [275], which indicates that in those liposomes a Donnan potential may have formed.

Naturally, it has to be tested whether such a liposome preparation indeed succeeds in generating a transmembrane potential. This can be done using potential-selective dyes such as JC-1 (ThermoFisher) which, however, have to be calibrated against known mem-

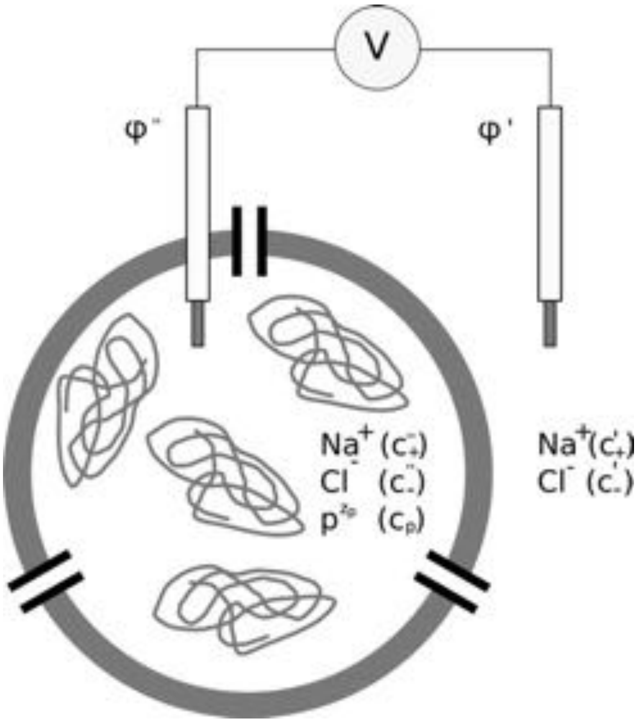

Figure 6.3: Schematic diagram of a liposome with reconstituted ion channels and filled with a polyelectrolyte. Channels permit only small ions such as sodium or chloride to permeate freely. Excess of counterions inside causes a Donnan potential. Figure taken from [272].

brane potentials [273]. On the other hand, a transmembrane potential in liposomes is measurable as a zeta potential via the electrophoretic mobility of the liposomes [272]. For measurement of such zeta potentials, commercial instruments are available from manufacturers such as Malvern or Micromeritics. For proteoliposomes containing the bacterial porin OmpF prepared in 3 mM KCl and 3 mg/ml polystyrene sulfonate and then diluted into 3 mM KCl without polyelectrolyte, zeta potential distributions with peaks in the range of -40 to -50 mV have been generated [272]. Note that the zeta potential is lower than the potential at the surface of the measured particle [276, 277].

Once proteoliposomes containing the ion channel of interest (and potentially additional ionophores to assure permeation of small ions) have been prepared in an asymmetric distribution of a polyelectrolyte, and the presence of a Donnan / zeta potential has been verified, the question will be whether the Donnan potential survives sample preparation for solid-state NMR measurements, *i.e.* sedimentation of liposomes by ultracentrifugation and magic angle spinning at velocities up to 60 kHz (or more). Proteoliposomes have long been used for solid-state NMR and have been observed to provide a stable environment for membrane proteins over long measurement periods (see Chapter 1 and Chapter 3, for example). It has even been shown that proteoliposomes as a whole remain intact during solid-state NMR experiments [278]. However, in that study, small unilamellar vesicles were found to form large multilamellar vesicles under the effect of sample spinning. This may well affect the potentials over the membranes involved. It will have to be examined by (cryo-) electron microscopy (available via access to the BICeL platform in Lille) what effects sample spinning has on the liposomes studied, and it will have to be measured whether they still exhibit measurable zeta potentials when recovered from a solid-state NMR rotor.

6.3 Application to voltage-gated ion channels

I plan to investigate bacterial VGICs whose crystal structures in the activated state are known. This way, overexpression and isotope labeling in *E. coli* should be feasible, and reference to crystal structures will facilitate data analysis. The K^+ channel KvAP from *Aeropyrum pernix* [15] and the Na^+ channel NavAb from *Arcobacter butzleri* [17] are thus prime candidates for this study. I have already obtained a clone of KvAP, and an expression system is available in the laboratory. I will first test its expression, purification and liposome reconstitution without isotope labeling. The NMR and Molecular Interactions group has excellent facilities and expertise in protein expression and purification which will be useful at this stage. In addition, the existing collaboration with renowned membrane protein experts Françoise Jacob-Dubuisson, Vincent Villeret, and Bernard Clantin within the framework of the FhaC project (see Chapter 5) will be invaluable especially for the specific challenges of membrane protein expression, purification, and reconstitution. To assure functional expression of a voltage-gated ion channel, electrophysiology experiments will have to be performed. For this, I will collaborate with Mathias Winterhalter (Jacobs University Bremen, Germany) who also pioneered the preparation of Donnan liposomes using ion channels [272]. Vectoriality of channel insertion into liposomes, important for experiments in the presence of a Donnan potential, has been reported [31, 279]; this will be tested using protease accessibility.

KvAP will then be expressed using (^{13}C,^{15}N) labeling in a protonated or perdeuterated (*i.e.* (^{2}H,^{13}C,^{15}N)) context and its "fingerprint" spectra (^{13}C-^{13}C or ^{1}H-^{15}N correlations, depending on the isotope labeling employed) recorded to evaluate the overall quality of the preparation and which type of isotope labeling to pursue. KvAP is a tetramer of 4 × 295 residues, a considerable size for solid-state NMR studies, but within the range of proteins already studied by this technique [140, 280]. Deuteration and ^{1}H detection at high MAS frequencies are likely the most promising approaches to obtain residue-specific information on KvAP; however, ^{13}C detection may be more appropriate if significant sample heterogeneity is present (as is often the case in studies of amyloid and similar protein fibrils, which to date have usually still been investigated using ^{13}C detection [281–283]).

Should the quality of the solid-state NMR spectra of KvAP turn out to be insufficient, optimization of expression and purification as well as tests of alternative labeling schemes (such as methyl labeling [240, 284], already used in our laboratory for both solution- and solid-state NMR samples, see Chapter 5) will be pursued. A potential problem with KvAP is the dynamic character of its voltage sensors. While, by their nature, voltage sensors have to exhibit a certain mobility, those of KvAP have been suggested to be particularly flexible based on crystal structures obtained in a non-native state [15, 285]. For this reason, in parallel, I will also obtain a clone of NavAb and work on its expression, purification, and reconstitution.

Another route to identifying resonances from the VSDs will be to perform segmental isotope labeling on KvAP or NavAb. Segmental labeling of proteins, using different techniques such as expressed protein ligation or protein splicing, is a very useful technique to reduce crowding in NMR spectra [286]. While its application remains challenging, the modularity of VGICs, which allows the creation of functional chimeras between voltage-sensing and pore domains of different channels [287], lends itself to this technique. Functional KcsA and KvAP channels have already been assembled from peptide segments, even with ligation sites within the pore domain [81], supporting the feasibility of using segmental labeling for KvAP and potentially other channels. The NMR and Molecular Interactions group has an active collaboration with the group of Christian Hackenberger (FMP Berlin, Germany) who is an expert on different techniques of protein ligation. Alternatively, to obtain the KvAP clone, I have been in contact with Francis Valiyaveetil in Portland (USA), who has pioneered channel semisynthesis and ligation studies on KcsA and KvAP; a collaboration on segmental labeling of KvAP may thus be envisioned.

Once both liposomes with a stable Donnan potential and workable spectra of KvAP or NavAb have been obtained, the next step will be to reconstitute the chosen voltage-gated channel into the Donnan liposomes and compare the resultant solid-state NMR spectra with those recorded in the absence of a transmembrane potential. If spectral differences appear, resonance assignment – at least of the regions involved in the spectral changes – will be undertaken by recording appropriate 3D (and possibly 4D) correlation experiments [288]. Obtained ^{13}C resonance assignments will permit analysis of secondary structure [40]. For tertiary structure information, especially proximities of S4 residues to other parts of the protein, through-space correlation spectra will be recorded [243].

6.4 Expected results, potential pitfalls and solutions

It is hoped that, using the approach detailed so far, it will be possible to obtain structural restraints on the positions and movement of VGIC voltage sensors in a lipid membrane in the presence of a defined transmembrane potential. As opposed to previous VGIC structures, this will allow to directly relate the observed structural information to a functional channel state. This should allow to distinguish between the different existing models of voltage sensor function discussed above, which make clear and distinct predictions with regard to the structural parameters that will be measured. Through-space restraints should allow for positioning of the S4 helix relative to its neighbors in activated and resting states, as well as to judge whether the S3 helix remains in place or whether its C-terminal part moves with S4, as postulated by the paddle model [289]. Already from chemical shifts in the VSD and their changes with transmembrane potential, important structural information may be gained, as already shown in Chapter 1. Loop regions whose chemical shifts change may indicate that adjacent helices change their position. Also, in several, but not all VSD structures, 3-10 helix conformation has been observed in parts of the S4 helix, which has been suggested as a mechanism of storing conformational energy to be used for concerted pore opening [11, 17]. S4 secondary structure should be directly observable in the NMR data.

Notably, stable establishment of Donnan potentials in liposomes for solid-state NMR studies would also allow to address the question of the closed state conformation of VDAC experimentally (Chapter 3). This could be exploited in a potential future collaboration with one of the research groups currently working on the VDAC channel. Whether large-scale conformational changes such as barrel semi-collapse indeed occur may also be investigated using EPR spectroscopy, for which the same liposomal preparations could be used. The

EPR research group of Hervé Vezin on site in Lille would be an ideal collaboration partner for this.

Should the unfortunate case arise that *E. coli* expression of (archae)bacterial ion channels does not yield enough protein or spectra of sufficient quality, moving to more complex expression systems may not be an obvious step. Isotope-labeled expression in insect cells or cell-free systems may then nevertheless be an option, given that recent years have seen considerable advances in these technologies [290, 291] and that they are now available by platform access, for example at the ICSN in Gif-sur-Yvette (insect cells) or at the IBS in Grenoble (cell-free expression) via the French Infrastructure for Integrated Structural Biology (FRISBI). In this case, I might envision to directly attempt the expression of an eukaryotic VGIC whose activated-state structure is known, such as Kv1.2 [16].

If attempts to stabilize a transmembrane potential in solid-state NMR liposome samples remain unsuccessful, I will pursue more traditional routes towards stabilizing a resting state of voltage-gated ion channels. Mutations shifting voltage activation to more positive values will be sought, to increase chances of obtaining a resting state in the absence of a transmembrane potential. Different states of voltage sensors have been stabilized using crosslinking experiments in double cysteine mutants [292, 293]; this should also be feasible for a resting state. Disulfide crosslinks should only occur if the corresponding conformation of the VSD is actually visited in the membrane environment; thus, this method would not be expected to stabilize non-native states. In addition, spectroscopic means may offer a glimpse of alternative voltage sensor conformations if they exchange with the visible state – the activated one in the absence of transmembrane potential – on appropriate time scales. CPMG or $R_{1\rho}$ relaxation dispersion experiments as described in Chapters 4 and 5 [123, 245] may offer insight into conformational exchange in voltage sensors and the nature of the exchanging state via its chemical shifts. For example, these techniques may allow conclusions on whether the C-terminal part of the S3 helix (S3B) moves together with S4, as postulated in the paddle model, based on whether or not exchange contributions are found in residues at the S3A–S3B limit.

6.5 Outlook

In summary, I propose an ambitious research project aimed at elucidating the resting state of voltage sensing domains in voltage-gated ion channels. If stable Donnan potentials can successfully be generated in liposome samples for solid-state NMR, it will be possible to extract structural restraints on different channel states, notably the so far largely elusive resting state, in a native-like membrane environment and in the presence of a transmembrane voltage. This would for the first time allow to directly relate structural data to a defined functional state of a voltage-gated ion channel.

Chapter 7

Project: Disordered regions of membrane proteins

7.1 Introduction

In Chapter 4, the phenomenon of intrinsic disorder in proteins was discussed and its function in one specific protein-protein interaction investigated. The existence of functional intrinsically disordered proteins (IDPs) and intrinsically disordered protein regions (IDRs), as well as their roles in important biological processes such as signaling and transcription, have now been widely accepted. So far, the vast majority of studies of protein disorder concerned soluble proteins. However, disorder is also present in membrane proteins, normally in extramembrane regions. A survey found that disordered regions of 30 or more consecutive residues in length are present in 41% of human plasma membrane proteins [294], suggesting that the prevalence of disorder is similar in membrane and soluble proteins [168, 169]. Disorder appears to occur mostly on the cytoplasmic side of membrane proteins [294].

Prominent classes of membrane proteins that exhibit disordered intracellular regions include ion channels, such as voltage-gated potassium channels, but also ligand-gated channels such as the neuronal NMDA receptor important in brain development, learning and memory [295, 296]. Disorder is also present in the large, pharmacologically highly important class of seven-transmembrane-helix G-protein coupled receptors (GPCRs) which are targeted by over 30% of available pharmaceuticals [297]. Their third intracellular loops and intracellular C-terminal regions are typically relatively long (50 residues or more) and disordered [298]. These regions often had to be removed, or even replaced by a folded protein domain, to achieve crystallization [299].

In soluble proteins, disorder is strongly associated with functions such as signalling, scaffolding, and regulation [2, 170, 171]. This also appears to be the case in membrane proteins. For example, a peculiar type of regulation by a disordered region occurs in some voltage-gated potassium ($\mathrm{K_v}$) channels such as the classic *Drosophila Shaker* channel. There, an inactivation peptide situated at the extreme N-terminus of the channel or an accessory β subunit, linked by a disordered region, plugs the ion conduction pore shortly after activation, stopping ion flow. This phenomenon, known as N-type inactivation, regulates action potential frequency [16, 300, 301]. Phosphorylation in intracellular regions of $\mathrm{K_v}$ channels affects current levels and inactivation kinetics [302], and disordered $\mathrm{K_v}$ channel C-terminal tails can interact with scaffold proteins, which underlies channel clustering and synapse assembly [295, 303].

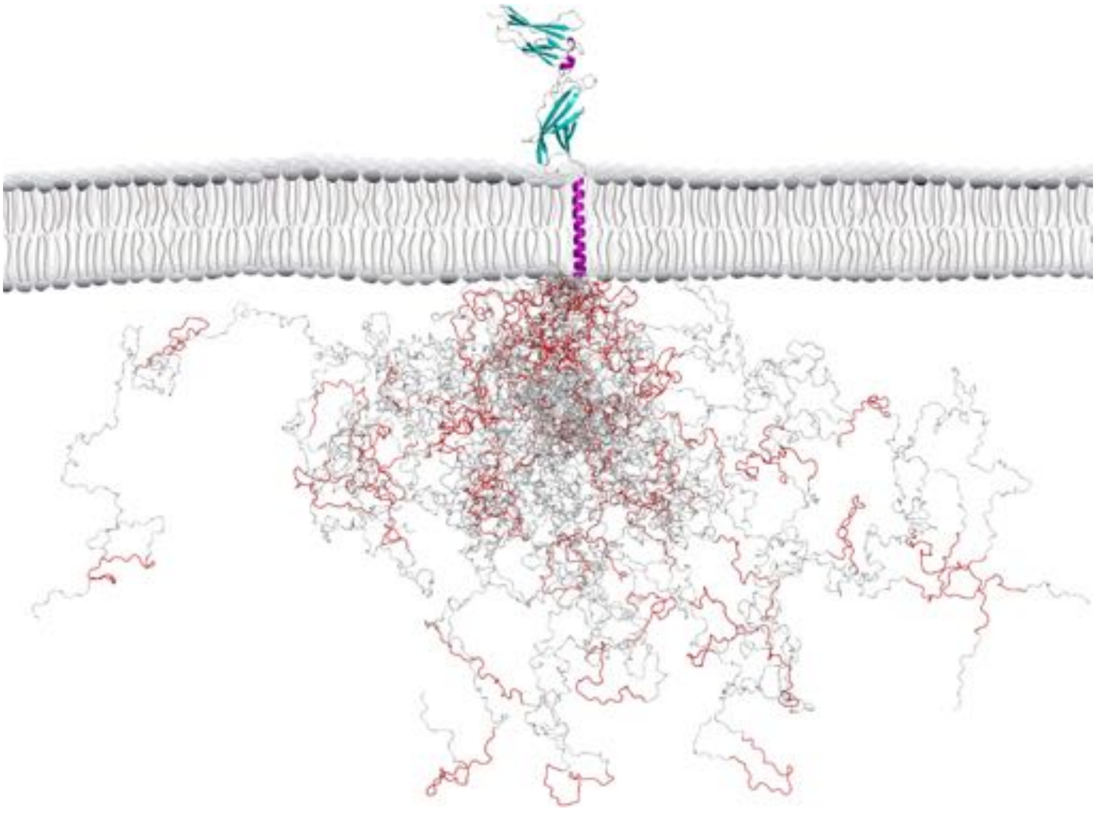

Figure 7.1: Structural model of the human prolactin receptor [304] with folded extracellular domain as determined by crystallography, transmembrane helix as determined by NMR, and intracellular disordered region ensemble-modelled by the flexible-meccano algorithm [305]. Image adapted from [304].

In GPCRs, the long disordered intracellular loop 3 (ICL3) and the C-terminus are substrates of different kinases, affecting downstream signaling and receptor localization. For example, in the β2-adrenergic receptor (β2AR), these regions are substrates of protein kinase A (PKA), and their phosphorylation shifts the preference of β2AR from stimulatory to inhibitory G proteins [306]. PKA, as well as phosphatases, can be linked to the C-terminal region via PKA anchoring proteins (AKAPs) which also tend to be disordered, leading to a dynamic signaling complex [296]. Moreover, phosphorylation by a different class of kinases, the G protein-coupled receptor kinases (GRKs), promotes interaction of GPCRs with β-arrestins, which desensitisizes GPCR signaling by reducing receptor coupling to G proteins and by facilitating receptor internalization; in addition, alternative GPCR signaling through β-arrestin-specific pathways is activated [307]. It has been shown that, depending on the ligand bound, different GRKs establish different phosphorylation patterns in the intracellular disordered regions of β2AR, leading to different functional outcomes [308]. Finally, an intriguing mechanism of regulation implying a disordered region has been described for the NMDA receptor: phosphorylation of its intrinsically disordered intracellular C-terminal domain alleviates inhibition of channel gating by extracellular zinc, and this phenomenon could be reproduced by altering the conformational dynamics of the intracellular region via proline mutations [309].

The manifold ways by which IDRs affect and regulate membrane protein function constitute a vast field of study that so far has not been much exploited from a structural biology point of view. Interest in the subject is increasing [310, 311], and a number of experimental studies have been published recently, investigating notably IDRs of the cystic fibrosis transmembrane conductance regulator (CFTR) [312], the carrier protein Na^+/H^+ exchanger isoform 1 (NHE1) [313], and the prolactin receptor [304]. However, the range of tools developed in recent years to achieve detailed ensemble descriptions of IDPs [195, 196] has not yet been fully exploited for membrane protein IDRs. Hence, I plan to use solution-state NMR and ensemble description methods to investigate conformational sampling and posttranslational modifications in membrane protein IDRs, in order to elucidate their effects on protein-protein interactions mediated by these regions, as well as on conformation and function of the transmembrane regions of the membrane proteins themselves. Especially the latter goal of describing the influence of membrane protein IDRs on transmembrane regions constitutes an exciting project to which solid-state NMR should be able to contribute.

7.2 Systems of study

In general, the systems of interest for this project are voltage-gated ion channels (VGICs), to complement the project described in Chapter 6, as well as GPCRs. Disorder in membrane proteins, as well as in general, is less prevalent in prokaryotes [169], and most regulatory functions of disordered membrane protein regions have been described for eukaryotic proteins. In addition, GPCRs are exclusively eukaryotic. Consequently, this project will deal with eukaryotic proteins. However, distinct disordered subregions of folded proteins such as those of interest here can be usefully studied in isolation in a divide-and-conquer approach [312–314], facilitating also their expression and isotope labeling which can usually be performed in *E. coli*. For expression of full-length proteins, eukaryotic expression systems such as the baculovirus / Sf9 insect cell system, the yeast *Pichia pastoris*, or cell-free expression will likely be necessary. Protocols for isotope labeling of proteins for NMR structural studies in these systems have been described [290, 315–317], and platforms offering these technologies are available via the French Infrastructure for Integrated Structural Biology (FRISBI) at the ICSN in Gif-sur-Yvette (for insect cell expression) and at the IBS in Grenoble (for cell-free expression). For some eukaryotic ion channels, even functional expression in *E. coli* has been reported [273, 318]; this will be tested before moving to eukaryotic expression.

For the longer-term goal of investigating the effects of membrane protein IDRs on transmembrane regions, it will be advantageous to choose proteins whose 3D structure, or that of a homologue, is already known. Among eukaryotic VGICs, obvious candidates would thus be, for example, mammalian homologues of the *Drosophila Shaker* channel such as Kv1.2 [16]. This channel has a 82-residue C-terminal disordered region with several phosphorylation sites, including a conserved motif 30 residues downstream of the last transmembrane helix whose phosphorylation has been described to influence N-type inactivation in this channel family [302]. Among GPCRs, the well-studied β2-adrenergic receptor (β2AR) lends itself to this project. For β2AR, structures in inactive and activated states are available [319–321], as well as NMR resonance assignments for individual sites and in different activation states [322, 323]. Its third ICL and its C-terminal tail encompass 54 and 84 residues, respectively. Finally, the 224-residue C-terminal domain 2 of the 2B subunit of the NMDA receptor, whose conformational sampling has been described to influence channel gating [309], would be a very interesting subject of study on its own. However, given that the NMDA receptor is an obligate heterotetramer of subunits containing between 938 and 1484 residues each (for the human variant), the study of this protein in its entirety by NMR appears presently out of reach.

7.3 Membrane protein IDRs in isolation and in the full-length proteins

The first goal of this project is to express and purify one or more of these membrane protein IDRs and study them in isolation using solution-state NMR spectroscopy. I will focus efforts on Kv1.2 and β2AR IDRs. The choice of a priority – or alternative – system of study will be based on expression levels and spectral quality. After resonance assignment, conformational sampling, secondary structure propensities, and long-range contacts will be investigated by ensemble methods based on chemical shifts, residual dipolar couplings (RDCs) and paramagnetic relaxation enhancements (PREs) [195, 196]. These data will then be recorded again on the chosen IDRs after phosphorylation by their relevant kinases to identify changes in conformational sampling. PKA has been described to phosphorylate IDRs of both *Shaker*-class potassium channels and β2AR as well as other GPCRs [302, 306]. For the β2AR C-terminus, comparison of the structural effects of PKA phosphorylation with those of phosphorylation by GRKs, triggering arrestin signaling and receptor internalization, will be of high interest. The kinases involved can be expressed recombinantly [324] or purchased commercially (*e.g.* from Amgen or Sigma-Aldrich). In the context of the neuronal Tau protein, our laboratory has developed expertise in *in vitro* phosphorylation assays that will be valuable in this context [325, 326]. The interaction of phosphorylated β2AR IDRs with G proteins and β-arrestin will be tested to identify the crucial residues and phosphorylations.

In parallel to studying their IDRs in isolation, isotope-labeled expression and purification of full-length Kv1.2 and β2AR will be attempted to identify if any of these appears promising for the part of this project dealing with the effects of IDRs on transmembrane regions, or whether an entirely different ion channel or GPCR system will have to be sought. Activity tests for purified (unlabeled) protein (based on electrophysiology for Kv1.2 and binding of radiolabeled G protein for β2AR [319]) will be established or performed in collaboration. For studying membrane protein IDRs in the context of the entire protein, on the one hand, scalar coupling-based transfers can be applied to liposomal solid-state samples to select for their mobile extramembrane regions [66, 327]. On the other hand, a suspension of proteoliposomes can be probed by solution-state NMR experiments in which only the

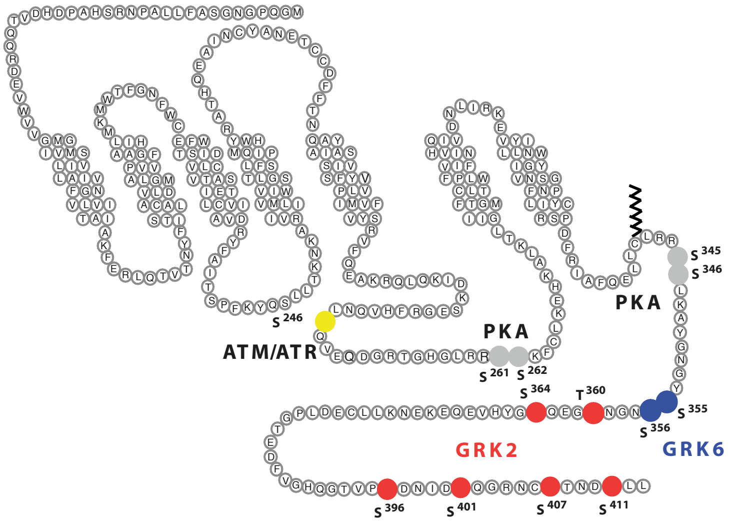

Figure 7.2: Schematic of the β2AR with phosphorylation sites in ICL3 and C-terminus and the corresponding kinases indicated. Figure taken from [308].

highly mobile extramembrane IDRs will be visible, similar as has been shown for the disordered tail of measles virus nucleoprotein in the context of megadalton-size nucleocapsids [314].

For an initial investigation of the conformational sampling of the IDRs in the context of their full-length proteins, uniform ^{15}N labeling, relatively easily accessible also in eukaryotic expression systems, will be used. Given the high sensitivity of ^{15}N and ^{1}H^{N} chemical shifts to their chemical environment, regions of similar or different conformational sampling with respect to the isolated IDRs will directly be visible by comparing their ^{15}N-^{1}H HSQC spectra [314]. As for the isolated IDRs, these experiments will be performed in the absence and presence of phosphorylation, which, in the context of full-length Kv1.2 and β2AR, should be possible before reconstitution into liposomes to ensure accessibility of IDR phosphorylation sites to kinases. For more detailed investigation of conformational propensities, ^{13}C labeling will be used in a second step if ^{15}N-^{1}H HSQC fingerprints differ between the IDRs in isolation and in the full-length proteins. Direct interactions of IDRs with transmembrane regions – or the lipid membrane – will be investigated by looking for resonance intensity changes, as well as by PRE experiments with paramagnetic labels in residues at the transmembrane-cytoplasmic interface. Interaction experiments with G proteins and arrestin will be performed with phosphorylated full-length β2AR to identify the relative contributions of disordered and membrane regions.

7.4 Interplay of membrane protein IDRs and transmembrane regions

To elucidate the effects of IDRs on transmembrane regions, solid-state NMR experiments on liposomal preparations will be used. It will first have to be established which isotope labeling scheme to choose for this part of the project. Uniform ^{13}C,^{15}N labeling with deuteration offers the most information and permits using ^{1}H-detected experiments, which yield higher spectral resolution and require lower amounts of sample. ^{2}H,^{13}C,^{15}N labeling with relatively high efficiency and yield has been described for insect cell expression, however already at rather considerable cost [290, 328, 329]. Alternatively, amino acid type-specific labeling schemes as well as methyl labeling can be achieved in insect cells or yeast [328, 330]; however, several different mutants will very likely have to be used for resonance assignment in the context of specific labeling schemes, also driving up costs and effort. Initial tests and evaluations will therefore be performed based on solid-state ^{1}H-^{15}N HSQC spectra in the context of uniform ^{2}H,^{15}N labeling.

A first question will be whether the presence of IDRs itself affects the transmembrane regions of Kv1.2 and β2AR. Constructs of these proteins with and without their C-terminal IDRs will thus be expressed and their spectra compared, this time selecting for less mobile transmembrane regions using cross polarization-based experiments [327]. Similarly, spectra will be compared with and without IDR phosphorylation by PKA (Kv1.2, β2AR) or GRKs (β2AR). In the case of Kv1.2, for example, this should be informative for effects of IDR phosphorylation on channel gating. In addition, the occurrence of (transient) IDR contacts with residues at the membrane interface will be investigated via PRE experiments, by adding paramagnetic tags to IDR residues.

Should spectral changes in transmembrane regions be observed in these experiments, resonance assignment in the context of the chosen isotope labeling scheme will be undertaken. This step always constitutes a bottleneck of NMR studies that may or may not succeed; however, the availability of crystal structures for Kv1.2 and β2AR suggests that chemical shift prediction algorithms may be usefully employed to obtain suggestions and starting points for the assignment. In addition, for Kv1.2, knowledge on spectral signatures of activation and inactivation gating obtained on bacterial ion channels in previous studies [25] as well as in the parallel project described in Chapter 6 may be helpful to interpret spectral changes. For β2AR, spectra will be recorded in the presence of agonists and antagonists [319, 321] to obtain spectral signatures of activation and inhibition.

In the longer term, I will aim for a structural understanding of how information is transmitted across the membrane and to downstream interaction partners. To obtain mechanistic insight into the interplay of IDRs and transmembrane regions, mutations of residues that have appeared as potential relays in previous experiments will be generated. In the context of β2AR, I will try to elucidate how binding of different ligands (agonists vs. inverse agonists) can lead to different phosphorylation patterns in the IDRs [308] – whether, for example, different parts of the IDRs are recruited to the transmembrane region and protected from phosphorylation, or whether more subtle effects on conformational sampling are at play. One step further, different IDR phosphorylation patterns in β2AR have been shown to induce different conformations in bound β-arrestin [308], which would be another interesting question to investigate structurally; good quality spectra obtained on the related arrestin-1 interacting with rhodopsin indicate that this should be feasible [331]. Finally, the disordered signaling complexes assembled from GPCR intracellular domains, AKAPs and kinases [296] would be a very relevant subject of study for NMR (un)structural biology.

7.5 Outlook

In this project, I aim to elucidate the interplay between transmembrane and intrinsically disordered intracellular regions of membrane proteins. My goal will be to understand how, for example, phosphorylation of an intracellular IDR can affect opening and closing of the transmembrane ion conduction pathway in ion channels, and how different conformations of the transmembrane regions of GPCRs induced by different ligands can lead to different phosphorylation patterns in intracellular IDRs. Using a combination of solution- and solid-state NMR to investigate disordered extramembrane and folded transmembrane regions, and applying ensemble description techniques based on a range of NMR parameters to elucidate conformational sampling of IDRs in different states (isolated or in the full-length protein, free or bound, phosphorylated or not) should allow for a detailed description of this interplay and its determining factors. This should lead to a better understanding of transmembrane signaling by ion channels and GPCRs that also takes into account the disordered regions of these proteins, which are inaccessible to other structural biology techniques.

Part IV

Appendix

List of Symbols and Abbreviations

CP	Cross-polarization
CPMG	Carr-Purcell-Meiboom-Gill
EPR	Electron paramagnetic resonance
GPCR	G-protein coupled receptor
ITC	Isothermal titration calorimetry
MAS	Magic angle spinning
MoRE	Molecular recognition element
OMP	Outer membrane protein
PDB	Protein Data Bank, http://www.rcsb.org/
PDSD	Proton-driven spin diffusion
RD	Relaxation dispersion
ssNMR	Solid-state nuclear magnetic resonance
TM	transmembrane
TPS	Two-partner secretion
VDAC	Voltage-dependent anion channel
VGIC	Voltage-gated ion channel
VSD	Voltage-sensing domain
WT	Wild-type

Appendix A

Binding mechanisms of intrinsically disordered proteins: theory, simulation, and experiment (Mollica et al., Front. Mol. Biosci. 2016)

frontiers
in Molecular Biosciences

REVIEW
published: 09 September 2016
doi: 10.3389/fmolb.2016.00052

Binding Mechanisms of Intrinsically Disordered Proteins: Theory, Simulation, and Experiment

Luca Mollica[1], Luiza M. Bessa[2], Xavier Hanoulle[2], Malene Ringkjøbing Jensen[3], Martin Blackledge[3] and Robert Schneider[2]*

[1] CompuNet, Drug Discovery and Development, Istituto Italiano di Tecnologia, Genova, Italy, [2] NMR & Molecular Interactions, Université de Lille, CNRS, UMR 8576 - UGSF - Unité de Glycobiologie Structurale et Fonctionnelle, Lille, France, [3] Institut de Biologie Structurale, CEA, CNRS, Université Grenoble Alpes, Grenoble, France

In recent years, protein science has been revolutionized by the discovery of intrinsically disordered proteins (IDPs). In contrast to the classical paradigm that a given protein sequence corresponds to a defined structure and an associated function, we now know that proteins can be functional in the absence of a stable three-dimensional structure. In many cases, disordered proteins or protein regions become structured, at least locally, upon interacting with their physiological partners. Many, sometimes conflicting, hypotheses have been put forward regarding the interaction mechanisms of IDPs and the potential advantages of disorder for protein-protein interactions. Whether disorder may increase, as proposed, e.g., in the "fly-casting" hypothesis, or decrease binding rates, increase or decrease binding specificity, or what role pre-formed structure might play in interactions involving IDPs (conformational selection vs. induced fit), are subjects of intense debate. Experimentally, these questions remain difficult to address. Here, we review experimental studies of binding mechanisms of IDPs using NMR spectroscopy and transient kinetic techniques, as well as the underlying theoretical concepts and numerical methods that can be applied to describe these interactions at the atomic level. The available literature suggests that the kinetic and thermodynamic parameters characterizing interactions involving IDPs can vary widely and that there may be no single common mechanism that can explain the different binding modes observed experimentally. Rather, disordered proteins appear to make combined use of features such as pre-formed structure and flexibility, depending on the individual system and the functional context.

Keywords: intrinsically disordered proteins, protein-protein interactions, nuclear magnetic resonance, kinetics, molecular dynamics simulations

OPEN ACCESS

Edited by:
Wei Yang,
State College of Florida,
Manatee–Sarasota, USA

Reviewed by:
Vladimir N. Uversky,
University of South Florida, USA
Ray Luo,
University of California, Irvine, USA
Mikolai Fajer,
UT-Battelle, USA

****Correspondence:***
Robert Schneider
robert.schneider@univ-lille1.fr

Specialty section:
This article was submitted to
Molecular Recognition,
a section of the journal
Frontiers in Molecular Biosciences

Received: *18 July 2016*
Accepted: *24 August 2016*
Published: *09 September 2016*

Citation:
Mollica L, Bessa LM, Hanoulle X, Jensen MR, Blackledge M and Schneider R (2016) Binding Mechanisms of Intrinsically Disordered Proteins: Theory, Simulation, and Experiment. Front. Mol. Biosci. 3:52.
doi: 10.3389/fmolb.2016.00052

INTRODUCTION

The discovery of intrinsically disordered proteins (IDPs) has considerably enhanced our view of protein structure and function. Over the last two decades, it has become accepted that proteins can be functional in the absence of a stable three-dimensional structure (Wright and Dyson, 1999; Dunker et al., 2001, 2002; Tompa, 2002; Dyson and Wright, 2005), and more recently, it has been shown that intrinsic disorder is compatible with the environment inside the cell

© 2017 Tous droits réservés. lilliad.univ-lille.fr

(Bodart et al., 2008; Theillet et al., 2016). Bioinformatic predictions estimate that on the order of 30% of eukaryotic proteins contain disordered regions of sizable length (>=50 residues; Dunker et al., 2000), and the DisProt database of protein disorder (http://www.disprot.org/) now contains entries for 1539 disordered protein regions and 694 entirely disordered proteins (Sickmeier et al., 2007). Their abundance, as well as their implication in disease (Uversky et al., 2008), has sparked considerable interest in IDPs, and a large number of studies have been devoted to the development of experimental and computational approaches in order to understand their conformational behavior and molecular function (Jensen et al., 2014).

IDPs are implicated in a wide range of biological functions, among them notably signal transduction, scaffolding, transcription, cell cycle regulation, or chaperoning (Dunker et al., 2002; Dyson and Wright, 2005). A common theme to these functions are interactions with other proteins or alternatively DNA or small molecules. Given the apparent frequency with which disorder occurs in the aforementioned functional contexts, questions arise as to how IDPs interact with their partners in the absence of well-structured binding sites, which mechanisms they employ to assure specific binding, and in general the advantages intrinsic disorder may have for protein-protein interactions.

In many cases, IDPs do not exhibit fully random statistical coil behavior, but can adopt transiently populated secondary structures and long-range tertiary interactions (Fuxreiter et al., 2004; Salmon et al., 2010). Such structural preorganization has often been found relevant in intermolecular interactions undergone by IDPs. While so-called "fuzzy complexes" of IDPs have been described that retain a high degree of disorder even in the bound state (Tompa and Fuxreiter, 2008), binding of IDPs to physiological partners is often accompanied by a gain in structuration of the binding region, a phenomenon known as "folding upon binding" or "coupled folding and binding" (Dyson and Wright, 2002). How exactly this is accomplished mechanistically has been the subject of intense debate. The discussion has mostly focused on two mechanisms that can be considered as limiting cases, conformational selection (i.e., folding before binding; Karush, 1950; Ma et al., 1999) and induced fit (i.e., folding after binding; Koshland, 1958; **Figure 1**), while more complex mechanisms such as different combinations of these two have also been envisioned (Csermely et al., 2010). In parallel, other, partially related questions have been discussed, such as whether increasing disorder speeds up binding, as proposed in the often-cited "fly-casting" hypothesis (Shoemaker et al., 2000), or conversely, whether increased pre-structuration of IDP binding sites allows for faster binding (Iešmantavičius et al., 2014). Another matter of debate concerns binding affinities and binding specificity achievable in the context of intrinsic disorder, with IDPs often said to accomplish highly specific binding without concomitant high affinity, which may be of advantage in the context of signaling where a once-formed complex needs to dissociate again to switch off the corresponding signal (Tompa, 2002; Zhou, 2012).

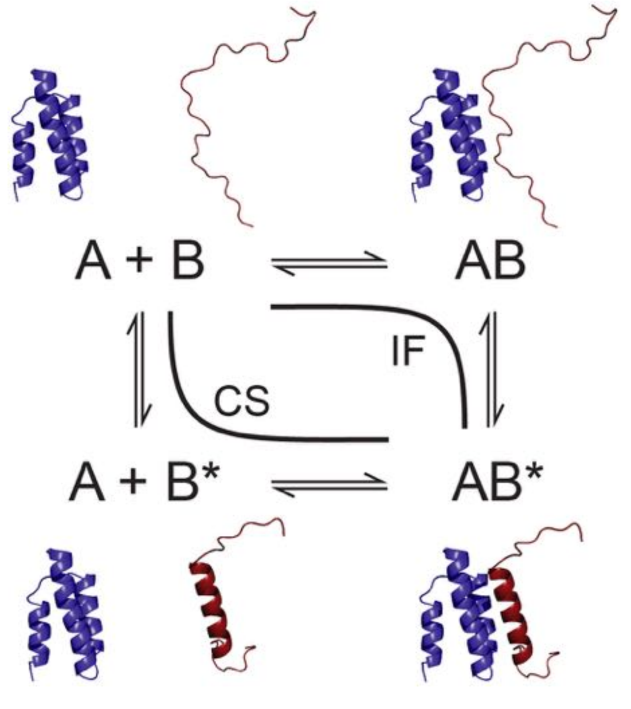

FIGURE 1 | Schematic of conformational selection (CS) and induced fit (IF) as parallel pathways of a bimolecular folding and binding interaction. One of the partners, B, is an IDP that exists in different conformations, unfolded (B) and folded into its final bound state (B*).

Answering these questions is not a trivial task, and especially obtaining detailed mechanistic information on binding interactions, which usually requires the extraction of the rate constants involved, is notoriously difficult. Correspondingly, the number of experimental studies explicitly addressing IDP binding mechanisms is still relatively limited. Nevertheless, recent years have seen a steady increase of research into the details of IDP binding interactions. Two experimental techniques have in particular been used, namely nuclear magnetic resonance (NMR) spectroscopy and non-equilibrium transient kinetic techniques, such as stopped flow or temperature jump experiments (Gianni et al., 2016). Surface plasmon resonance (SPR) measurements also allow for detailed insight into binding kinetics at high temporal resolution, however at the price of immobilization of one of the binding partners, which may affect the interaction in the case of a highly flexible IDP (Schuck and Zhao, 2010). In addition, single-molecule experiments such as fluorescence resonance energy transfer (Gambin et al., 2011) or nanopore translocation (Japrung et al., 2013) have recently gained importance in studying binding reactions. In parallel to these experimental techniques, modeling and computer simulations have increasingly contributed to our understanding of protein interactions at the atomic level, notably also due to the development of various enhanced sampling techniques (Zhou and Bates, 2013; De Vivo et al., 2016). Here, we have chosen to review recent progress in the field based on NMR spectroscopy and transient kinetics experiments, as well as molecular simulations.

METHODOLOGY

Transient Kinetics

Kinetic information on a binding interaction can be obtained from non-equilibrium techniques that either rapidly mix the reactants (e.g., stopped or continuous flow) or perturb a preexisting equilibrium between them, for example by application of a rapid temperature or pressure jump, and then follow the (re-)establishment of equilibrium via a signal whose variation is related to the binding reaction. Usually, optical signals are employed, such as circular dichroism (CD), absorbance, or the fluorescence of a native or introduced aromatic residue, which vary in the course of a folding and/or binding reaction (Bernasconi, 1976; **Figure 2A**). These techniques, originally developed in the context of the study of enzymatic reactions (Eigen and Hammes, 1963), are sensitive to processes occurring on the timescales of microseconds (temperature or pressure jump, continuous flow) to milliseconds and longer (stopped flow) (Gianni et al., 2016). Depending on the relaxation time course of the signal monitored, one or more kinetic time constants (λ or k_{obs}) are obtained from fitting the signal decay. For a simple two-state bimolecular binding reaction with 1:1 stoichiometry

$$\mathrm{A} + \mathrm{B} \underset{k_{\mathrm{off}}}{\overset{k_{\mathrm{on}}}{\rightleftharpoons}} \mathrm{AB} \tag{1}$$

assuming pseudo-first-order conditions for A (i.e., B is present in excess), k_{obs} is given by the sum of the forward and reverse reaction rate constants, $k_{\mathrm{on}}[\mathrm{B}] + k_{\mathrm{off}}$. A multiexponential decay, on the other hand, is direct evidence for a more complex binding mechanism (Kiefhaber et al., 2012; Vogt and Di Cera, 2012). The reaction is then followed over a range of concentrations of the binding partner in excess. Fitting appropriate models to the variation of the observed relaxation rate constant(s) with binding partner concentration allows for the extraction of the underlying reaction rate constants (**Figure 2B**). Notably, even if only one rate constant k_{obs} is experimentally observable, a nonlinear variation of k_{obs} with ligand concentration is evidence for a multistep binding mechanism, and the exact dependence of k_{obs} on concentration gives information on its nature (Tummino and Copeland, 2008; Vogt and Di Cera, 2012). A shortcoming of these methods is that they do not offer site-specific resolution, and the exact nature of the event leading to a change in the observed signal is usually not known.

NMR Spectroscopy

NMR spectroscopy is a sensitive method to investigate binding reactions in proteins and can yield residue-specific information on binding sites, affinities and mechanisms (Zuiderweg, 2002). Typically, binding is monitored by observing the NMR resonances of an isotope- (^{15}N- and/or ^{13}C-) labeled protein in the presence of unlabeled, i.e., NMR-inactive ligand. Ligand binding induces changes in the magnetic environment of spins in the residues involved in the interaction, reflected in changes in the chemical shifts of NMR resonances and/or their line shapes. Importantly, the underlying dynamics of the exchange of a spin between free and bound states affect NMR observables and can be measured using suitable experiments (Mittermaier and Kay, 2009). Thus, although NMR is an equilibrium technique, it can nevertheless provide access to kinetic details of a binding reaction and thereby its mechanism.

How NMR chemical shifts are affected by titrating with increasing amounts of ligand depends on the underlying exchange rate k_{ex} between free and bound state, which, for the simple two-state binding scheme of Equation (1), is equal to the k_{obs} observed in kinetic experiments ($k_{\mathrm{on}}[\mathrm{B}] + k_{\mathrm{off}}$ for the exchange rate relevant if molecule A is observed). In the so-called fast exchange regime, i.e., if k_{ex} is much larger than the chemical shift difference between free- and bound-state signals ($k_{\mathrm{ex}} \gg \Delta\omega$), a single resonance peak is observed for a given spin which moves from the free-state to the bound-state position in the course of the titration. Conversely, for slow exchange ($k_{\mathrm{ex}} \ll \Delta\omega$), the free-state resonances disappear upon titration, while the bound-state signals progressively appear in the spectrum (**Figure 2C**). For intermediate exchange ($k_{\mathrm{ex}} \approx \Delta\omega$), a combination of the two phenomena may be observed, but usually strong broadening or even disappearance of resonance signals occurs (Mittermaier and Kay, 2009). Notably, such titration experiments can already point to the presence of more complex binding mechanisms via, for example, peaks following a curved path (Arai et al., 2012), or combinations of fast- and slow-exchange behavior in individual resonances (Sugase et al., 2007a). Peaks that remain exchange-broadened even in the presence of excess ligand have also been observed in IDP interactions with their partners (Jensen et al., 2011; Schneider et al., 2015), suggesting that the interaction kinetics are characterized by more than two states, for example if the bound state exhibits additional dynamics on the μs–ms timescale.

On the timescales typical for protein-protein binding (μs–ms range), NMR experiments useful for characterizing the exchange underlying such spectral changes are rotating-frame ($R_{1\rho}$; Palmer and Massi, 2006) and Carr-Purcell-Meiboom-Gill (CPMG) relaxation dispersion (Palmer et al., 2001) as well as chemical exchange saturation transfer (CEST) experiments (Vallurupalli et al., 2012). In the context of analyzing IDP binding interactions, especially CPMG relaxation dispersion has been used. This experiment is normally conducted under conditions where either the free or the bound state of the protein under study is dominant and the respective other state(s) spectrally invisible due to its/their low population and preferential exchange broadening. If the exchange between free and bound states occurs on a timescale between about 100 and 2500 s^{-1}, its contribution to the effective transverse relaxation rate $R_{2,\mathrm{eff}}$ (and thus the linewidth) of the visible NMR signals can be quenched by the application of a train of 180° pulses of increasing frequency ν_{CPMG} (Mittermaier and Kay, 2009). Fitting the resultant dependence of $R_{2,\mathrm{eff}}$ on ν_{CPMG} to a model of the underlying exchange yields its exchange rate(s) k_{ex}, the populations of the states involved, and the chemical shift differences between them (**Figure 2D**). Individual rate constants k_{on} and k_{off} may be extracted from k_{ex} by measuring relaxation dispersions at different concentrations or temperatures, or by knowledge of the dissociation constant, K_{d}, of the interaction. In practice, the complexity of systems that can usefully be addressed using this strategy is limited to three exchanging states. NMR

© 2017 Tous droits réservés. lilliad.univ-lille.fr

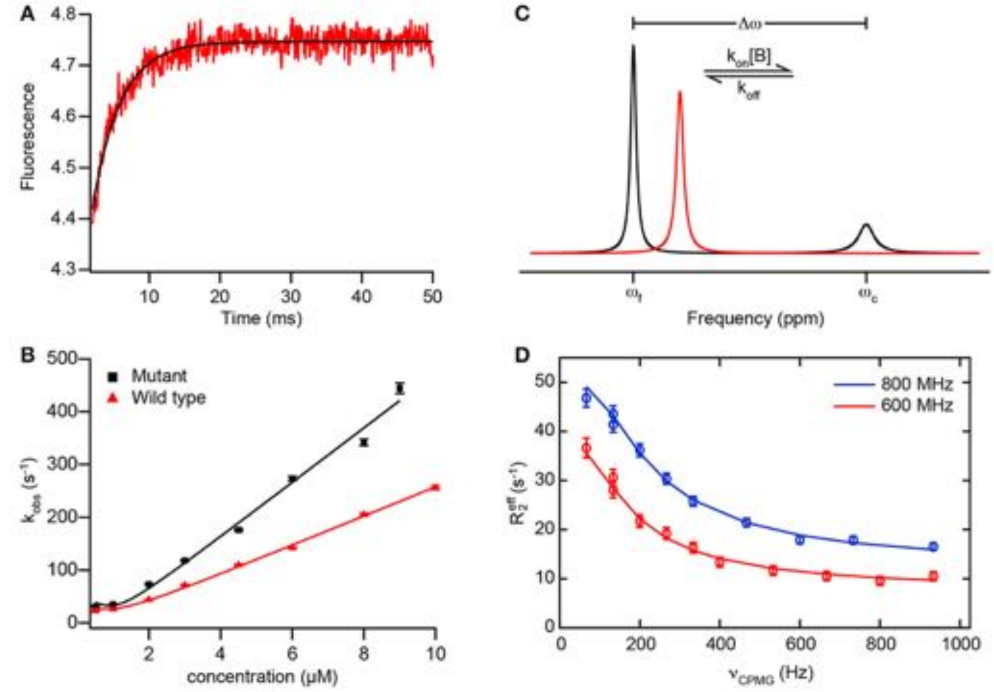

FIGURE 2 | Example data from transient kinetics and NMR to analyze binding mechanisms. (A) Fluorescence trace of a binding reaction measured in a stopped-flow experiment. The fluorescence of an introduced tryptophan residue (W2108) of NCBD(Y2108W) is monitored upon binding of disordered ACTR (see text for details). Red, experimental data; black, fit of an exponential function to obtain k_{obs}. **(B)** Dependence of the rate constant k_{obs} observed in experiments as depicted in **(A)** with varying concentrations of wild-type ACTR (red) and a mutant ACTR variant with increased helix propensity (black). Solid lines are fits using the general equation for reversible association of two molecules (valid also for non-pseudo-first order conditions; Malatesta, 2005). **(A,B)** adapted from Iešmantavičius et al. (2014) with permission of John Wiley & Sons, Inc. **(C)** Schematic 1D NMR spectra of a spin undergoing exchange between two states with different chemical shifts, such as in a reversible binding interaction as in Equation (1). The spin is assumed to be in molecule A, such that the effective association rate constant is given by k_{on}[B]. The free state (chemical shift ω_f) is assumed to be dominant and the complex (chemical shift ω_c) a minor state. Black, spectrum for intermediate to slow exchange ($k_{ex} < \Delta\omega$) with two resolved resonance lines for free and bound state; red, spectrum for intermediate to fast exchange ($k_{ex} > \Delta\omega$) with one averaged resonance signal. In both cases, the effective transverse relaxation rate (and thus the linewidth) of the signals contains a contribution from the exchange, leading to additional line broadening. Note that the minor signal in the black spectrum is preferentially broadened due to its larger exchange contribution k_{off}, which can lead to broadening beyond detection. **(D)** Example data from a CPMG relaxation dispersion experiment measured at two static magnetic fields (red, 600 MHz, blue, 800 MHz ^{1}H Larmor frequency) on the carbonyl ^{13}C of residue 475 in the PX binding site of Sendai virus N$_{TAIL}$ in the presence of 8% (molar) of PX (see text for details; Schneider et al., 2015). Data points show the effective transverse relaxation rate $R_{2,eff}$ of the visible major (free) state signal for different CPMG pulse frequencies ν_{CPMG}. Solid lines are fits to the data using a model of exchange between three states, corresponding to free N$_{TAIL}$, encounter and final complex, allowing for extraction of the rate constants, populations, and chemical shift differences along the interaction trajectory.

signals are broadened by exchange on a similar timescale as the one CPMG experiments are sensitive to (μs–ms); consequently, line broadening may hamper data analysis.

Molecular Simulations

Simulations can, in principle, visualize biomolecular function and interactions in atomic detail and thus allow to elucidate the underlying mechanisms that are often difficult to access from experimental data alone. Recent years have seen a steady increase in both computing power and availability of resources for simulation techniques, from in-house clusters and graphical processing unit- (GPU-) based algorithms to large-scale computing facilities. However, both the models and parameters used as well as the simulation results need to be calibrated against and verified by experimental data to ensure that meaningful results are obtained. IDP systems pose some particular challenges for simulations. Due to their conformational heterogeneity, extensive sampling is required to ensure that the conformational space is adequately covered by the simulation. In addition, compared to their large number of degrees of freedom, experimental data on IDPs is typically sparse, i.e., their characterization is an underdetermined problem and care must be taken, e.g., by cross-validation approaches, to avoid overfitting. Finally, the accuracy of modern force fields for IDP simulations is not well characterized, and standard combinations of force fields and water models primarily developed for folded proteins may not be appropriate for simulations of IDP systems.

Standard molecular dynamics (MD) simulations of IDPs, using all-atom or united-atom representations (the latter with most nonpolar hydrogen atoms "collapsed" into the heavy atom to which they are bound), typically require long simulation times on the microsecond timescale to yield reasonable agreement with experimental data (Lindorff-Larsen et al., 2012). Most commonly, variants of the quantum mechanics-based AMBER or the empirically parametrized CHARMM and GROMOS force fields are used. Some variants have been optimized against NMR parameters, such as AMBER ff99SB-ILDN (Lindorff-Larsen et al., 2010) or CHARMM22* (Best and Hummer, 2009), or improved directly using NMR observables, like AMBER ff99SBNMR1-ILDN, which also contains improved representations of torsion angle potentials (Li and Brüschweiler, 2010). Insufficient solvation of proteins has been observed using current force fields, which is particularly problematic for IDPs (Mercadante et al., 2015). To address this problem, short-range protein-water interactions can be modified in current water models such as TIP3P or SPC known to accurately reproduce the structure of liquid water (Horn et al., 2004; Wang L.-P et al., 2014; Henriques et al., 2015); alternatively, a new water model, TIP4P-D, has been proposed to correct for underestimation of London dispersion interactions (Piana et al., 2015). Extensive simulations on disordered peptides and validation against experimental NMR and small-angle X-ray scattering (SAXS) data have indicated that CHARM22* in conjunction with the TIP4P-D water model reproduces experimental data well, with the notable exception of NMR residual dipolar couplings (RDCs; Rauscher et al., 2015). This shortcoming has been observed for all available force fields and is likely due to the sensitivity of RDCs to both local and long-range structuration. Correspondingly, a bias in current force fields toward overly compact structures—as measured by, e.g., radius of gyration—has been observed (Henriques et al., 2015), which may partly explain why these force fields perform well for compact, folded proteins, but less so for simulations of IDPs where correct reproduction of their flexible and extended nature is essential. The TIP4P-D water model has also been observed to overly destabilize transient secondary structure (Salvi et al., 2016). Efforts have been made to correct for these deficiencies, with the specific aim to better reproduce IDP conformational sampling, for example by corrections to the dihedral potentials of disorder-promoting residues in AMBER ff99SB-ILDN, with some improvement in reproduction of NMR chemical shifts (Wang W. et al., 2014; Ye et al., 2015). Nevertheless, it appears that current force fields and water models are still not calibrated accurately enough to fully capture conformational sampling in IDPs, especially in the presence of transient structure, warranting caution in the interpretation of IDP simulations in terms of underlying mechanisms.

Coupled folding and binding of IDPs to their partners is typically still out of reach of classical MD simulations due to the large number of degrees of freedom as well as the extensive conformational transitions involved. To overcome the sampling limit of classical MD, different approaches can be used. Coarse-grained (CG) simulations reduce the number of degrees of freedom by simplified representations of the molecular system, parametrizing individual amino acids using only one or a few hard spheres (Takada et al., 2015). Compared to all-atom simulations, this yields better agreement of the radius of gyration of IDPs with experiment (Smith et al., 2014). CG simulations are often combined with empirical "Gō-type" potentials to simulate protein-protein binding (Ueda et al., 1978; Karanicolas and Brooks, 2002). Here, terms for non-bonded interactions can be included which favor contacts between those residue pairs that are in contact in a known native structure of the complex investigated (De Sancho and Best, 2012). For protein binding or unfolding, Monte Carlo (MC) simulations have also been used. Here, the properties of the system are computed by repeated random sampling whose outcome is periodically accepted or rejected on the basis of a deterministic principle, i.e., among the conformations of a molecule corresponding to two consecutive steps, the one with minimal energy is chosen (Metropolis criterion; Irbäck and Mohanty, 2006; Staneva et al., 2012).

On the other hand, various enhanced sampling techniques for MD simulations have been proposed. One of the most widely used methods is parallel tempering or replica exchange molecular dynamics (REMD; Okamoto, 2004; Tai, 2004; Ostermeir and Zacharias, 2013). Here, several copies (replicas) of the system are simulated independently and simultaneously at different simulation temperatures. At preset intervals, pairs of replicas are exchanged with a specified transition probability. This allows the system to escape from being trapped in locally stable states at low simulation temperature, while preserving the canonical distribution of sampled states within each replica. Instead of using the simulation temperature as replica co-ordinate (T-REMD), it is also possible to vary the force field or system Hamiltonian across replicas. While improving sampling, REMD is computationally expensive and can become prohibitive for large proteins. An alternative approach known as metadynamics is based on the dynamics performed by a few collective variables of the atomic coordinates (Laio and Parrinello, 2002). In a metadynamics simulation, the system is driven not only by its potential energy, but also by a biasing history-dependent potential constructed as a sum of user-defined Gaussians centered along the trajectory of the collective variables which "fill" the free-energy surface to drive the system away from states that were already visited. Two variants of this technique have mostly been used: well-tempered metadynamics (W-META), a variant that adds an adaptive bias along the trajectory of the collective variables by varying the Gaussian height (Barducci et al., 2008); and bias exchange metadynamics (BE-META), which combines standard metadynamics with the replica exchange approach, allowing for extensive sampling of the free energy landscape (Domene et al., 2015). Recent studies have demonstrated that both BE-META and T-REMD are capable of reproducing secondary structure and lowly populated conformations of disordered peptides (Do et al., 2014; Zerze et al., 2015).

POSSIBLE ADVANTAGES OF INTRINSIC DISORDER

The possible consequences and advantages of intrinsic disorder for protein function and interactions have been extensively discussed (Dunker et al., 2002; Tompa, 2002; Dyson and Wright, 2005; Wright and Dyson, 2015). It appears that the specific qualities of disorder are well suited for the functions in interaction and regulation frequently fulfilled by IDPs. For example, their extended, flexible nature may be advantageous for

© 2017 Tous droits réservés. lilliad.univ-lille.fr

the assembly of complexes due to facile access to the binding sites on an IDP and lack of steric hindrance (Tompa, 2002). Similarly, disordered regions can easily be accessed by modifying enzymes such as kinases, which may be why posttranslational modification sites are also often found in disordered regions (Iakoucheva et al., 2004). At the same time, disordered proteins can form extended binding interfaces that are large compared to their own size, offering the possibility of specific, high-affinity partner recognition (Mészáros et al., 2007; Dogan et al., 2014). On the other hand, their plasticity allows them to bind to different partners, using different or even identical binding sites, a phenomenon known as promiscuity (Tompa et al., 2005; Oldfield et al., 2008). Furthermore, turnover of IDPs in the cell is usually more rapid due to their susceptibility to proteases, which may be of advantage in signaling (Wright and Dyson, 1999; Dyson and Wright, 2005).

Two possible advantages of intrinsic disorder for protein-protein interactions have been put forward and discussed particularly frequently: an increased association rate (k_{on}) due to a "fly-casting" effect (Shoemaker et al., 2000), and an ability to achieve high binding specificity without concomitant high affinity (Zhou, 2012). We will look at these two propositions in more detail in the following sections.

High Association Rates: Fly Casting vs. Pre-formed Structure

The original proposition of the "fly-casting" effect stated that an unfolded protein should be able to form initial interactions with its binding partner already at a greater distance than a folded protein, leading to an increased capture radius and a "reeling in" of the partner to its binding site on the IDP (or vice versa; Shoemaker et al., 2000). This was predicted to lead to an, actually relatively modest, increase in the association rate by a factor of 1.6; however, larger rate enhancements have been suggested for other, more realistic models than were used in the original derivation (Shoemaker et al., 2000; Zhou et al., 2012). Experimentally, very fast association rates around the estimated diffusion limit for folded proteins (up to about 10^9–10^{10} $M^{-1}s^{-1}$) are found surprisingly frequently for IDPs (Sugase et al., 2007b; Arai et al., 2012; Shammas et al., 2013; Dogan et al., 2015; Milles et al., 2015). Association rates exceeding 10^7 $M^{-1}s^{-1}$ are invariably associated with electrostatic attraction (Zhou and Bates, 2013). Indeed, IDPs in general tend to exhibit an elevated net charge (Uversky, 2002), and the vicinities of IDP binding sites have been described to be enriched in complementary charges (Ganguly et al., 2012). However, even if corrections for the effects of electrostatic attraction are applied, k_{on} values in the diffusion-limited range have been found for IDPs (10^5–10^6 $M^{-1}s^{-1}$) (Shammas et al., 2013; Dogan et al., 2015; Milles et al., 2015). This suggests that disorder *per se* may indeed speed up the association process, via fly casting or otherwise. However, the number of kinetic studies of IDP association reactions is still relatively limited, and overall, a wide range of association rate constants has been measured for IDPs, similar to what has been observed for folded proteins (Dogan et al., 2014). Thus, so far it does not seem warranted to claim that IDPs can generally achieve faster association than folded proteins.

Fly casting is difficult to prove or disprove experimentally, largely owing to the difficulty of changing the level of disorder in one of the partners of a binding interaction without affecting other factors as well. Note that the original publication considered a comparison between a completely and a partly folded protein to derive the prediction of a 1.6-fold increase in k_{on}. However, most experimental assessments which can be related to the fly-casting hypothesis have rather involved short binding sites of IDPs exhibiting partial order, such as a transient helix, and modified the propensity to form such structure via mutations or cosolvents. In most of these experiments, stabilizing (secondary) structure was however found to increase association rates, albeit to different extent (Rogers et al., 2013, 2014b; Iešmantavičius et al., 2014; Arai et al., 2015), contradicting the fly-casting hypothesis. The association of the p27 cyclin-dependent kinase (CDK) inhibitor with the cyclin A–Cdk2 complex appears to be an exception; here, stabilizing the linker helix slowed down the time course of inhibition (Bienkiewicz et al., 2002). However, the mutations employed also changed the charge of p27. Moreover, the linker helix makes only few contacts with the cyclin A–Cdk2 complex and likely functions mostly as a spacer between the cyclin A- and Cdk2-binding domains of p27 (Lacy et al., 2004). Investigations of the kinetics of different proteins, with different degrees of disorder, binding to a single target have suggested no influence of pre-formed structure on association rates, or rather kinetic advantages for the more disordered proteins (Shammas et al., 2014; Dogan et al., 2015); however, comparing different proteins with regard to an individual quality is inherently difficult. Thus, while the experimental evidence is not entirely conclusive in this regard, it appears nevertheless that stabilization of the bound-state structure in an IDP prior to interaction leads to faster association rates.

CG simulations with a Gō-like potential of the interaction of the phosphorylated kinase inducible domain (pKID) of the cAMP response element binding protein (CREB) with the KIX domain of the CREB-binding protein (CBP) have also suggested that the kinetic advantage of an increased capture radius would be offset by the slower translational diffusion of a disordered protein (Huang and Liu, 2009). This likely only applies to large-scale changes in disorder, and thus diffusion coefficient, envisioned in the original fly-casting hypothesis; stabilization of a transient helix in the binding site of an IDP was not observed to have an effect on its diffusion (Iešmantavičius et al., 2014). However, based on these simulations, another mechanism was proposed by which disorder could speed up protein-protein association, namely a reduction of the free-energy barrier between initial and final complex due to facilitated folding after initial binding (i.e., induced fit, see also below), or equivalently, an increase in the number of collisions leading to productive binding (Huang and Liu, 2009). The expected increase in k_{on} from this effect is again rather modest, a factor of 2.5 (Huang and Liu, 2009). Similarly, in Gō model simulations on the interaction of the C-TAD domain of hypoxia-inducible factor-1α (HIF1α) to the TAZ1 domain of CBP, the observed association rate approached the fast experimental one only if the model allowed for non-native contacts to occur, leading to a broad distribution of encounter complexes productive for binding (De Sancho and Best, 2012). Electrostatic interactions appear to play a crucial role in this process by reducing the redissociation rate after initial encounter, as well as by increasing the probability of native-like topologies in the collision complexes (Ganguly et al., 2013). A facilitated transition between initial and final complex bears some resemblance to a fly-casting mechanism, albeit without an effect of a larger capture radius. Notably, rather than increasing association rates beyond those achievable by ordered proteins, this effect of disorder seems to avoid the orientational restraints and steric hindrance that would result if IDPs had to rigidly dock their binding partners, at least in those cases where the binding interface is more complex and extended (Zhou et al., 2012). In the aforementioned case of p27 binding to the cyclin A–Cdk2 complex, it was noted that, due to steric clashes, p27 could not bind if it were rigid in its bound conformation; this would explain the requirement for a flexible linker helix found experimentally (Bienkiewicz et al., 2002; Zhou et al., 2012). One could thus argue that the flexibility of IDPs counterbalances the negative effects on association rates that their often extended binding interfaces would otherwise have, globally leading to a similar range of association rates as found in folded proteins (Dogan et al., 2014).

Regardless of the effects of pre-formed structure on kinetics, stabilization of bound-state secondary structure has always been observed to increase affinity and lead to corresponding changes in downstream functional responses of IDPs (Parker et al., 1998, 1999; Petros et al., 2000; Rogers et al., 2014b). For example, stabilizing the transient helix with which the transactivation domain (TAD) of the tumor suppressor p53 binds to the repressor oncoprotein MDM2 leads to stronger binding and concomitant effects on target gene expression and cell cycle regulation (Zondlo et al., 2006; Li et al., 2010; Borcherds et al., 2014). In the disordered domain D2 of hepatitis C virus (HCV) protein NS5A, a short structural motif dubbed the PW turn was identified whose disruption abolished HCV replication and affected interaction with the host protein cyclophilin A (Dujardin et al., 2015). These and other examples underline the importance of pre-formed structure in IDP binding and indicate that it typically has a functional role.

Affinity and Specificity

It has been suggested that the loss of conformational entropy of IDPs associated with folding upon binding results in an overall unfavorable entropic contribution to binding, thereby uncoupling binding strength from specificity, i.e., allowing for highly specific binding without high affinity (Tompa, 2002; Fuxreiter et al., 2004; Dyson and Wright, 2005; Zhou, 2012). This has been cited as an example of enthalpy-entropy compensation (Fuxreiter et al., 2004) and as an advantage in the context of signaling, where interactions have to be reversible to assure that a signal can be switched off again. However, it is not entirely clear how disorder can uncouple specificity and affinity, since the two are intimately linked by definition. Thermodynamic specificity, in essence, consists in differences in (relative) affinity to multiple possible targets and therefore also depends on the availability and concentration of binding partners (Zondlo et al., 2006). Thus, an interaction of weak or moderate affinity may well be highly specific, however only as long as any possible competing interaction exhibits even weaker affinity (or the concentrations of other binding partners are sufficiently low). Also, in principle, if a binding interaction is accompanied by a large unfavorable entropy change, and if enthalpy-entropy compensation is at play, the result should not be an overall low affinity of the complex, but rather a concomitant large favorable enthalpic contribution, as has been noted in the context of folding upon binding in protein-DNA interactions (Spolar and Record, 1994). Finally, IDPs also engage in promiscuous interactions with different binding partners, even via identical binding sites as in the case of the C-terminal regulatory region of p53 (Oldfield et al., 2008), possibly leading to different functional responses (moonlighting; Tompa et al., 2005). It is not clear how intrinsic disorder would be able to both assure high binding specificity and still permit promiscuous interactions.

In fact, the reduction in entropy associated with folding upon binding of an IDP does not generally entail an overall unfavorable entropic contribution to binding. First, pre-formed structure corresponding to the bound conformation, as well as disordered segments not directly involved in the binding, reduce the entropy penalty of folding upon binding (Fuxreiter et al., 2004), as is the case for so-called "fuzzy complexes" that retain dynamics even within the binding regions (Mittag et al., 2008; Tompa and Fuxreiter, 2008). But even for IDP complexes reaching a stable bound conformation, the gain in solvent entropy from the release of solvation water molecules can be considerable, especially given that IDPs tend to form comparatively large, extended binding interfaces with pronounced hydrophobic character (Dyson and Wright, 2005; Mészáros et al., 2007; Ganguly et al., 2012; Dogan et al., 2014). The overall entropy of folding and binding of an IDP to its partner may thus well be favorable, as, for example, in the case of the interaction of the disordered transactivation domain of the transcriptional activator c-Myb with the KIX domain of CBP (Parker et al., 1999). Notably, the formation of a large hydrophobic interface typically also leads to a favorable binding enthalpy, which can compensate for unfavorable entropic contributions, as seen for example in the interaction of the disordered activation domain of the activator for thyroid hormone and retinoid receptors (ACTR) with the nuclear coactivator binding domain (NCBD) of CBP (Demarest et al., 2002).

Overall, as is the case for association rates, IDP interactions exhibit a wide range of affinities, including very high ones, as do folded proteins (Dogan et al., 2014). Notably, nanomolar dissociation constants have been found even for IDP complexes involved in signaling, such as ACTR–NCBD (Demarest et al., 2002), p27–cyclin A–Cdk2 (Lacy et al., 2004), or the complex between disordered PUMA and folded Mcl-1 from the mammalian Bcl-2 family of apoptosis regulators (Rogers et al., 2014b). How the signal associated with the formation of such complexes is switched off again, given their high affinity, is not clear. However, other, competing interactions of comparable affinity may be involved. As mentioned, specificity essentially corresponds to relative affinity and thus depends on the context in which a particular complex exists. In any case, intrinsic disorder does not seem to generally lead to low-affinity and/or high-specificity complexes.

CONFORMATIONAL SELECTION, INDUCED FIT AND BEYOND

Distinguishing Conformational Selection and Induced Fit

The discussion about the mechanisms used by IDPs to bind to their partners has often been framed in the context of a supposed dichotomy of conformational selection vs. induced fit (**Figure 1**), while more recent results tend to suggest that IDP binding mechanisms may be more complex, exhibiting various mixed, intermediate mechanisms, or a coexistence of these two limiting cases (Espinoza-Fonseca, 2009; Csermely et al., 2010). Conformational selection, in a strict sense, implies that the bound-state conformation of an IDP preexists in its free state and that exclusively this conformation is binding competent. Induced fit in the context of IDPs, on the other hand, entails that binding occurs in a more or less unfolded state and that conformational rearrangements to the final bound state take place in a unimolecular reaction within the complex. Evidence for both mechanisms has been found in binding of various IDPs to their partners, sometimes even for a single IDP (Gianni et al., 2012; Arai et al., 2015), but conclusive proof of one or the other is usually difficult and may not reflect the true complexity of the underlying binding mechanism.

As mentioned, a necessary condition for a conformational selection mechanism is that molecules assuming the bound conformation preexist in the free state ensemble of the IDP. NMR and MD studies have often found evidence for such pre-formed conformers closely resembling the bound state, for IDPs as well as for folded proteins, suggesting that conformational selection plays a role in their binding (Lange et al., 2008; Boehr et al., 2009; Kjaergaard et al., 2010; Jensen et al., 2011; Krieger et al., 2014). However, pre-formed bound-state structure *per se* is not evidence for a conformational selection mechanism, since its existence does not prove its (exclusive) implication in binding (Dogan and Jemth, 2014). Such evidence normally requires kinetic measurements of the reaction rate constants over a range of concentrations of at least one of the binding partners. However, in many cases, multistep reactions such as folding before or after binding do not become directly evident as, for example, multiexponential relaxation in non-equilibrium experiments or evident three-state behavior in NMR relaxation dispersion data.

For transient kinetics experiments, even if only a single k_{obs} is observable experimentally, a multistep reaction can nevertheless become apparent if k_{obs} varies nonlinearly with the concentration of the binding partner. In that case, a k_{obs} increasing or decreasing hyperbolically with concentration has often been taken as evidence for an induced fit or conformational selection mechanism, respectively (Tummino and Copeland, 2008). However, this is only valid under the so-called rapid equilibrium assumption, where binding is assumed to be fast relative to the folding step (Vogt and Di Cera, 2012). This assumption is not necessarily justified, especially in the context of IDPs forming short elements of secondary structure, which can occur on a sub-μs timescale (Eaton et al., 1997). Consequently, it has been shown that, while a k_{obs} decreasing with binding partner concentration can only be explained by conformational selection, a hyperbolic increase in k_{obs}, as is often observed experimentally, can actually be accounted for by both induced fit and conformational selection mechanisms, leading to the suggestion that binding by conformational selection may be much more widespread than previously thought (Vogt and Di Cera, 2012, 2013). Recently, it has been pointed out that a distinction between the two binding mechanisms may be made in kinetic experiments by varying the concentrations of both reaction partners in separate experiments (Gianni et al., 2014). Induced fit yields a hyperbolically increasing k_{obs} in both cases. Conformational selection, on the other hand, results in a linear k_{obs} variation if the concentration of the species undergoing conformational change is varied, while hyperbolic behavior (increasing or decreasing k_{obs}) is retained for variation of the concentration of the other partner. In practice, it may however be difficult to obtain data for a wide enough range of protein concentrations to draw clear mechanistic conclusions. Alternatively, binding kinetics may be studied at different temperatures or with different ligands; however, the latter method assumes that only the microscopic rate constants, not the basic mechanism, would change for different ligands (Vogt and Di Cera, 2012).

Conundrums in Experimental Data

Kinetic data that can satisfactorily be explained by conformational selection or induced fit alone have been described in the literature, often for enzymes binding to their substrates (Kirschner et al., 1966; Wong et al., 1991; Kim et al., 2007; Johnson, 2008). Frequently, however, NMR or non-equilibrium kinetics measurements of IDP binding interactions give no direct indications of multistep mechanisms at all, with NMR relaxation dispersion data being well fit by two-state models and k_{obs} from rapid mixing or temperature jump experiments varying linearly with ligand concentration (Shammas et al., 2013; Rogers et al., 2014b; Arai et al., 2015). Nevertheless, since both folding and binding take place, the underlying mechanism should be more complex than two-state. One of the processes involved may simply be too fast to be observed or be associated with too small a change in measurement parameters (fluorescence or NMR chemical shift, for example). Indeed, apparent two-state behavior is frequently observed in IDPs with simple bound topologies such as a single stretch of helix. In these cases, information on the binding mechanism and the role of pre-formed structure is often sought by modifying secondary structure content via mutation or by adding (secondary) structure stabilizing compounds such as trifluoroethanol (TFE; Gianni et al., 2012; Rogers et al., 2014b).

As discussed above, stabilizing the—in most studies, helical—bound-state secondary structure in IDPs has always been observed to stabilize the complexes with their binding partners, i.e., to increase affinity, while the effect of increased secondary structure on the on rate k_{on} of IDP binding is more ambiguous

(Bienkiewicz et al., 2002; Gianni et al., 2012; Iešmantavičius et al., 2014; Rogers et al., 2014b; Arai et al., 2015). Nevertheless, in a majority of cases, k_{on} increases with increasing content of bound-state-like secondary structure within IDP binding sites, although to different extents. This behavior would be expected in a conformational selection scenario; increasing the population of the binding-competent conformer should lead to faster association. However, an increase in k_{on} strictly is only evidence for a reduced free energy of the rate-limiting transition state of the reaction with respect to the free state. This rate-limiting step may well correspond to folding occurring after initial binding; in that case, binding would be accelerated by the increased propensity of the binding site for the bound-state structure, rather than by increased availability of an obligatory pre-folded conformation (Iešmantavičius et al., 2014). Conversely, the observed complex stabilization by increased free-state secondary structure content has typically been traced to a reduction in the off rate (k_{off}), i.e., a lower free energy of the final bound state with respect to the rate-limiting transition state (Gianni et al., 2012; Rogers et al., 2014a,b). Such an effect is normally interpreted as folding after binding, i.e., an induced fit mechanism. Again, however, this depends on where on the reaction coordinate the transition state occurs; it may correspond to a rate-limiting folding step that precedes binding. However, for binding reactions, it seems reasonable to assume that the transition state is already a complexed state; especially the formation of short segments of helical secondary structure in the free state of an IDP is unlikely to account for the rate-limiting step of a folding and binding interaction. Thus, if (de)stabilization of bound-state secondary structure affects k_{off}, a contribution of an induced-fit mechanism to the binding can be assumed.

Similar to Φ value analysis that relates activation free energy to equilibrium free energy of binding (Fersht and Sato, 2004), information on the transition state of a folding and binding reaction can be obtained from how K_{d} varies with k_{on} or k_{off} for a series of modifying conditions (such as mutations or addition of TFE or denaturant; Prakash, 2011). If, for a given molecular system, a Brønsted plot of $\log(k_{\mathrm{on}})$ or $\log(k_{\mathrm{off}})$ against $\log(K_{\mathrm{d}})$ is linear (i.e., gives a linear free-energy relationship, LFER), the position of the transition state on the reaction coordinate can be estimated from the slope of the plot. A large negative slope (approaching -1) in a plot of $\log(k_{\mathrm{on}})$ against $\log(K_{\mathrm{d}})$ indicates a "late" transition state with the property investigated by the modifications (such as secondary structure or tertiary contacts) largely formed, analogously to large values in Φ value analysis. Note that the results of such studies depend on the type of modification made to the system investigated. For example, for the interaction of the transcription factor c-Myb with the KIX domain of CBP, it has been postulated, based on kinetic binding studies in varying TFE concentrations, that c-Myb is largely unstructured in the transition state (Gianni et al., 2012). However, based on mutagenesis, it was concluded that the transition state exhibits a high degree (about 89%) of native order (Giri et al., 2013). It is difficult to envision how, in the transition state, the KIX binding region of c-Myb could be mostly unfolded and nevertheless undergo such a large percentage of interactions characteristic of the final bound complex, where it is present in a helical conformation (Zor et al., 2004). However, the mutations used were not chosen to perturb a specific quality such as secondary structure or hydrophobic interactions, and they were situated both within and outside of the binding interface, making their relative effects on folding and binding difficult to estimate. In the BH3 motif of disordered PUMA that binds as a helix to Mcl-1, secondary structure content was more specifically targeted by mutating residues outside of the binding interface to proline or glycine (Rogers et al., 2014a,b). Here, a modest effect on k_{on} (variation over one order of magnitude) was observed, but a much stronger one (up to 1000-fold) on k_{off}, again interpreted as evidence for an early transition state and binding of PUMA in a mostly disordered conformation (Rogers et al., 2014a,b). These results indeed show that no particular part of the bound-state secondary structure of PUMA is strictly required for its binding. However, the free state of PUMA has been observed to exhibit only about 20% overall helicity; a transition state with little secondary structure is thus not yet evidence against conformational selection. Since the mutations employed did not vary helical content to a great extent, a small effect on k_{on} is perhaps not surprising. Also, some mutations introduced charge changes, and proline mutations are strongly disruptive to hydrogen bonding and may introduce additional complications via *cis-trans* isomerization.

In a study on the folding and binding of ACTR to the NCBD domain of CBP, helical secondary structure in free ACTR was targeted by carefully designed mutations to non-interface residues, explicitly excluding mutations to proline or involving changes in charge (Iešmantavičius et al., 2014). Resultant effects on helicity were monitored using both CD and NMR spectroscopy, and binding kinetics of the mutants to NCBD were measured by stopped-flow fluorimetry. Here, a clear correlation of free- state helical content, which varied in the range of 20–70% in the different mutants, with both k_{on} and k_{off}, which both varied 2- to 2.5-fold, was found. The plot of $\log(k_{\mathrm{on}})$ vs. $\log(K_{\mathrm{d}})$ resulted in a slope of -0.47, while in an earlier study, mutations affecting the hydrophobic binding interface yielded an average Φ value of 0.14 (Dogan et al., 2013). This has been interpreted as a transition state in which crucial hydrophobic intermolecular interactions are only formed to 14%, but with the ACTR binding region already 47% helical (Iešmantavičius et al., 2014), indicating a mixed mechanism in which partly pre-formed conformers of ACTR bind and fold further to their final bound conformation within the complex. A reanalysis of the mutagenesis data performed in (Giri et al., 2013) in terms of the effect of the different mutations on helical secondary structure content also indicated that helicity is in fact correlated with k_{on} in the interaction of c-Myb with KIX (Arai et al., 2015).

Mixed Multistep Mechanisms: A Potential Solution

Clearly, the different effects of mutations and cosolvents on folding and binding processes are often difficult to separate. However, an emerging consensus from this type of experiment seems to be that induced fit always has a role in the systems investigated, but that mixed mechanisms seem to be at play, as seen from the finding that pre-formed secondary structure affects on rates and is reflected in the degree of structuration of the transition state. It has already been noted that IDP binding mechanisms may be more complex than either conformational selection or induced fit, and that various combinations or intermediates of these two extremes need to be considered (Espinoza-Fonseca, 2009; Csermely et al., 2010). In particular, conformational selection and induced fit may coexist, with relative flux through the two pathways being determined by substrate concentration as well as the relative populations of the different forms of the protein undergoing a conformational change (Hammes et al., 2009). Reaction steps respectively exhibiting characteristics of conformational selection and induced fit may also occur sequentially in a multistep reaction (Espinoza-Fonseca, 2009; Csermely et al., 2010). Such complex behavior with parallel multistep pathways has been invoked in a detailed study for the folding and pyrophosphate binding of the *Bacillus subtilis* RNase P protein subunit (Daniels et al., 2014). Here, it was suggested that fast folding kinetics and low ligand concentrations favor conformational selection pathways, while slow folding and increasing ligand concentrations shift the balance toward induced fit pathways. With three conformational substates and two substrate binding sites, the system investigated in this study exhibits particular complexity; nevertheless, increasing evidence suggests that other IDPs may employ similar combinations of pathways and individual interaction steps in their interactions with binding partners.

As mentioned, an acceleration of binding by increased secondary structure content may reflect a rate-limiting folding step occurring after binding. However, there are indications for a role of partial conformational selection in such cases. As discussed above, very high, diffusion-limited association rates are recurrently found in interactions of IDPs with their partners, notably in the aforementioned PUMA–Mcl-1, cMyb–KIX, and ACTR–NCBD systems (Dogan et al., 2012; Rogers et al., 2013; Shammas et al., 2013). This is often cited as evidence for induced-fit type binding, since the requirement of a conformational selection mechanism for a pre-folded, possibly lowly populated, conformation should be incompatible with diffusion-limited association, where each encounter of the binding partners should lead to productive binding. However, it seems difficult to delineate the diffusion limit for disordered proteins, and even for induced-fit type binding, an energy barrier for folding after binding may remain that slows down the overall association (Rogers et al., 2013), likely in a similar way as conformational selection would. Most notably, however, the involvement of pre-formed structure in diffusion-limited interactions very likely depends on the degree of prestructuration of a particular molecule. For IDPs whose binding sites display a high content of secondary structure resembling the bound state, such as c-Myb(284–315) (70%; Arai et al., 2015) or the disordered C-terminal N_{TAIL} region of the nucleoprotein from Sendai virus (up to 75%; Jensen et al., 2008), it would likely be a pure induced-fit mechanism that would hamper fast association, given the prevalence of pre-formed conformers. It thus seems likely that, as described by Oas and coworkers for RNase P folding and binding (Daniels et al., 2014), highly populated, fast-folding pre-formed structure would preferentially participate in binding, at least if the partner protein is not present in excess.

After initial binding of pre-folded conformers, further folding may still occur within the complex. Such behavior is likely when secondary structure is significantly populated in the free state of an IDP, but is extended further in the final bound state, as seen for example in binding of the N-terminal region of the vesicular stomatitis virus (VSV) phosphoprotein P to the nucleoprotein N. Residues 25–31 of P form a transient helix populated up to 35% in the free state (Leyrat et al., 2012); in the N^0P complex, P is helical in residues 17–31 (Leyrat et al., 2011). Similarly, in the transactivation domain of p53, residues 22–25 have been observed to populate helical secondary structure (Wells et al., 2008), while the crystal structure of the complex between this motif and the MDM2 oncoprotein features a helix in residues 19–25 (Kussie et al., 1996). Alternatively, the docking regions D1, D2, and D3 of the regulatory region of the mitogen-activated protein kinase (MAPK) kinase MKK7 all bind to the MAPK JNK1 in extended or polyproline conformation, despite sampling different regions of Ramachandran space in the free state (helical, polyproline, or random coil, respectively; Kragelj et al., 2015). For these interactions, an induced fit step appears obligatory since the bound-state conformation is not populated in the free ensemble, at least not to a measurable extent. Induced fit also certainly plays a role in the intriguing cases of individual disordered motifs binding to different partners in different conformations, as has been observed for residues 374–388 of the C-terminal regulatory region of p53 which bind to the proteins S100ββ, sirtuin, CBP, and cyclin A2 in helix, sheet, or different coil conformations, respectively (Oldfield et al., 2008). Induced fit has indeed been observed in an MD study of the interaction of S100ββ with p53 and another disordered partner, the TRTK-12 fragment from the protein CapZ. Here, MD simulations were complemented with Monte Carlo calculations for improved sampling of the binding process. Despite their differing sequences and bound-state structures, both peptides were observed to employ similar induced-fit binding mechanisms via non-native encounter complexes formed in the periphery of the S100ββ binding pocket. Nevertheless, helical structure similar to the bound state was observed in simulations of the free peptides (Staneva et al., 2012). Gō-type coarse-grained simulations of other IDP interactions such as those of PUMA with Mcl-1 or HIF1α, p53, and ACTR with their cognate domains of CBP (TAZ1, TAZ2, and NCBD, respectively) have also found important induced fit contributions to the binding mechanisms, involving a broad range of encounter complexes. Here, significant folding typically occurred only after formation of at least 20% of native intermolecular contacts (De Sancho and Best, 2012; Ganguly et al., 2013; Rogers et al., 2014a).

NMR studies of IDP folding and binding support the notion of complex multistep interactions with different contributions of conformational selection and induced fit. A seminal study of Wright and coworkers on the interaction of the pKID domain of CREB with the KIX domain of CBP suggested a model of exchange between four states, namely the free proteins, a transient, nonspecific encounter complex, a partially folded intermediate, and the final complex (Sugase et al., 2007a). The latter three states were inferred from fits to relaxation dispersion data measured on the complex, while the initial step of formation of an encounter complex was indicated by resonance signals of free pKID shifting in fast exchange during titration experiments. Encounter complex and intermediate were found to be only partially structured, clearly showing that this interaction proceeds largely via an induced-fit mechanism. A different result was obtained for the binding to KIX of c-Myb, whose primary binding site on KIX is the same as for pKID. Here, NMR relaxation dispersion data were consistent with an effective two-state mechanism (Arai et al., 2015), as was the case for stopped-flow and temperature-jump kinetic experiments (Gianni et al., 2012; Giri et al., 2013; Shammas et al., 2013). Based on the latter, an induced-fit mechanism was postulated (Gianni et al., 2012; Giri et al., 2013). However, recent coarse-grained as well as all-atom simulations of this interaction found no unique pathway for binding and indicated that c-Myb conformations with widely varying helical content can bind to KIX with similar probabilities (Ithuralde et al., 2016). In addition, in the transient kinetics experiments, a shorter c-Myb construct exhibiting relatively low helical content in the free state (around 30%) was used (Shammas et al., 2013). NMR data on the longer c-Myb (284–315) construct, on the other hand, rather indicated a fast free-state folding equilibrium. The large (70%) helical content in this construct, the effect on k_{on} of mutations affecting secondary structure, and the apparent high degree of structure in the transition state underline a role of conformational selection in this interaction (Giri et al., 2013; Arai et al., 2015). The differences apparent in the binding of pKID and c-Myb to KIX were related to their different roles in transcriptional activation, where largely unfolded KID requires induction by phosphorylation for high-affinity interaction with KIX, while the more helically preconfigured c-Myb acts as constitutive activator (Zor et al., 2002; Arai et al., 2015).

The previously mentioned case of the interaction of the ACTR activation domain with the NCBD domain of CBP has also been investigated by both non-equilibrium kinetics and NMR experiments, as well as Gō-type CG simulations. Here, an additional complication arises from the fact that both domains are disordered in their free states, however to different degrees. NCBD has been described as a molten globule (Kjaergaard et al., 2010), while ACTR is fully disordered with transient helical elements (Iešmantavičius et al., 2013). Both proteins thus undergo a coupled folding and binding reaction that has been described as mutual synergistic folding (Demarest et al., 2002). Free NCBD largely populates a conformation resembling its ACTR-bound state (Kjaergaard et al., 2010), while the H1 helix found in NCBD-bound ACTR is partly pre-formed in free ACTR to a population of 38% (Iešmantavičius et al., 2013). Transient kinetics experiments, as well as simulations, have suggested a multistep, largely induced-fit, binding mechanism (Dogan et al., 2012; Ganguly et al., 2013). However, as discussed above, the effects of mutations on binding kinetics have also indicated a partly helical transition state with few native tertiary interactions (Dogan et al., 2013) and a clear influence of helicity on association rate (Iešmantavičius et al., 2014). It thus seems likely that the pre-folded conformers present in the free-state ensembles of both ACTR and NCBD play a role in the initial binding step. For example, as has been suggested, the interaction may be initiated by a pre-formed first helix of ACTR making weak native-like contacts with the first helix of NCBD (Dogan et al., 2013). Such a mechanism is supported by the respective timescales of folding and binding observed in this system. NMR line shapes indicate that formation of the (fluid) tertiary structure of NCBD occurs on a timescale of $10^4\ \mathrm{s}^{-1}$, with transient helix formation in ACTR likely even faster (Eaton et al., 1997; Jensen et al., 2008), while the rate of complex formation is on the order of $500\,\mathrm{s}^{-1}$ or slower (Iešmantavičius et al., 2014). Pre-formed binding competent conformers of both proteins would thus be readily available for complex formation.

In another study relevant to the subject, we have investigated the interaction between disordered $\mathrm{N_{TAIL}}$ and the PX domain of the phosphoprotein from Sendai virus (SeV) using relaxation dispersion NMR experiments. The data were best explained by a three-state model in which one of the preexisting conformers of the highly helical free-state ensemble is initially stabilized in a nonspecific encounter complex with PX, as evidenced by the dominance of ^{13}C backbone chemical shift modulations during the first step of the interaction. From a helical periodicity in ^{15}N and ^{1}H shifts that dominate the second step, we concluded that this $\mathrm{N_{TAIL}}$ helix then locks into its final bound position in a hydrophobic interhelical groove of PX, at a rate coincident with intrinsic motion of that groove (Schneider et al., 2015; **Figure 3**). The first step of this model thus comprises both folding and binding which could not be resolved kinetically. However, the bound conformation is—with one residue difference—nearly identical to one of the helical conformers populated to 28% in the free state. In addition, the molar fractions of PX used ($<=15\%$) were below the population of that helical conformer, and the formation of helices in free $\mathrm{N_{TAIL}}$ is much faster—above $10^5\ \mathrm{s}^{-1}$ from NMR data, in agreement with known helix folding rates (Eaton et al., 1997)—than the on rate, below 140 s^{-1} under the conditions measured. It can thus be assumed that, in these conditions, enough pre-folded $\mathrm{N_{TAIL}}$ conformers resembling the bound state will always be available for a conformational-selection type interaction in the first step of binding.

Interestingly, a temperature-jump kinetic study on the closely related $\mathrm{N_{TAIL}}$-XD system from measles virus (MeV) has also found complex kinetics with at least two steps, but has come to the opposite conclusion that the interaction is characterized by a global induced-fit mechanism (Dosnon et al., 2015). This study used the kinetic test in which the concentrations of both binding partners are varied in separate experiments (Gianni et al., 2014) and found a hyperbolic dependence of the observed rate constant k_{obs} in both cases, in agreement with an induced-fit interaction. The sequence homology between the corresponding proteins in the two viruses is rather low (about 20% identity), so the mechanisms involved in binding may well be different. However, it is unlikely that even the temperature jump technique, appropriate for fast reactions, is sensitive to the very fast rate of helix formation and interconversion in the free $\mathrm{N_{TAIL}}$ proteins of both viruses (Eaton et al., 1997; Jensen et al., 2008, 2011). The curvature observed in the variation of k_{obs} with the concentrations of both $\mathrm{N_{TAIL}}$ and XD from

© 2017 Tous droits réservés. lilliad.univ-lille.fr

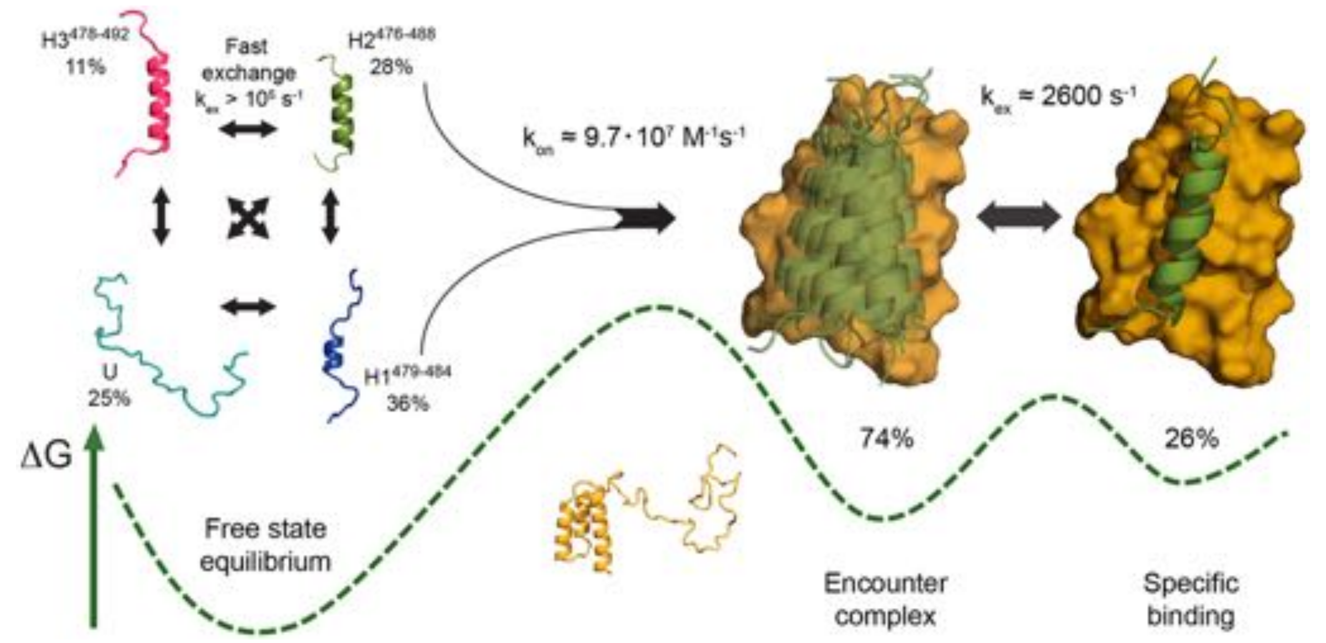

FIGURE 3 | Schematic of the mechanism of folding and binding of disordered Sendai virus N_{TAIL} to its partner PX, as proposed based on NMR relaxation dispersion data (Schneider et al., 2015), as an example of a multistep coupled folding and binding reaction with elements of both conformational selection and induced fit. The PX binding site of free N_{TAIL} populates three defined helical conformers (H1–H3) in rapid exchange with a fully unfolded state (U) **(left)**. Interaction with PX stabilizes an N_{TAIL} conformer closely resembling H2 (green) in a nonspecific encounter complex on the surface of PX (yellow), likely involving conformational selection of H2 under the experimental conditions employed **(center)**. This N_{TAIL} conformer then locks into its final bound state in an interhelical groove of PX at a rate coincident with an intrinsic breathing motion of PX, a rearrangement step corresponding to induced fit **(right)**. A sketch of the free energy landscape is shown at the bottom, indicating the higher population of encounter complex compared to final complex deduced from experimental data. Adapted with permission from Schneider et al. (2015). Copyright 2015 American Chemical Society.

MeV confirms that a conformational change occurs within the complex between the two proteins. However, it is unknown what the observed change in tryptophan fluorescence corresponds to exactly at the molecular level. A "locking-in" of a pre-formed helical N_{TAIL} conformer on the surface of its binding partner, as inferred from NMR data on the SeV system, may also explain the unimolecular process detected in the temperature jump fluorimetry experiments on the MeV proteins. Thus, it appears likely that, in these two systems as well, conformational selection- and induced fit-type processes coexist in a sequential manner. The site-specific resolution offered by NMR spectroscopy clearly allows for additional detailed insight into the molecular processes underlying the measured kinetic parameters in these cases.

The MeV N_{TAIL}-XD interaction has also been investigated by molecular simulations. Free N_{TAIL} was simulated using REMD, while simulation of the binding process either employed a hybrid potential, incorporating structural information on the bound state as attractive potential terms (Wang et al., 2013), or a combination of replica exchange and metadynamics (Han et al., 2016). Both studies reached similar conclusions about a sequential combination of conformational selection and induced fit in this system, in agreement with the experimental studies mentioned above. However, the composition of the simulated free-state ensemble in the study by Wang et al. differed somewhat from that of an ensemble based on experimental data (Jensen and Blackledge, 2014). In particular, experimental NMR RDCs were less well reproduced by the REMD ensemble, likely due to the prevalence of kinked helical conformers in the latter. The free-state ensemble described by Han et al. is similarly enriched in such structures, suggesting it is subject to the same issues regarding reproduction of experimental data. This observation underlines that current force fields still encounter problems in simulating the conformational sampling of IDPs in their isolated state, especially when transient structure is present. Consequently, caution should also be exercised in drawing conclusions on interaction mechanisms from molecular simulations.

A Synthetic View of IDP Folding and Binding

Overall, it appears that most coupled folding and binding reactions exhibited by IDPs are considerably more complex than could easily be described by either conformational selection or induced fit models. It has long been realized that these two mechanisms, while useful concepts and appropriate for the characterization of a range of known binding interactions, as well as individual reaction steps, are very likely too reductionist to describe the complexity of most biomolecular interactions entirely. The two limiting cases of flexible protein binding mechanisms seem to coexist not only as parallel pathways with

© 2017 Tous droits réservés. lilliad.univ-lille.fr

flux-dependent relative importance (Hammes et al., 2009), but also sequentially in the multistep folding and binding reactions that are often found for IDPs. The picture that emerges from the studies discussed here is that conformational selection may play a role in the initial step of an IDP binding to its partner to a degree that corresponds to the amount of prestructuration present in its free-state ensemble. After the initial encounter, further induced-fit type rearrangements within the complex seem to occur nearly universally, from diffusion of a fully formed bound-state IDP conformation on the surface of its partner, as in the SeV N_{TAIL}–PX interaction (Schneider et al., 2015), to further folding of more complex structures, as apparent in, for example, the pKID–KIX or ACTR–NCBD interactions (Sugase et al., 2007a; Dogan et al., 2012).

Notably, the more complex a conformation adopted by an IDP in a complex, the more induced fit is likely to play a dominant role. While a single helix, given appropriate sequence composition such as N-capping residues (Richardson and Richardson, 1988; Doig et al., 1997; Jensen et al., 2008), can form easily and quickly, more complex topologies such as the three-helix fold of ACTR in complex with NCBD are unlikely to contribute significantly to initial binding in a folded form. Especially in the absence of a stable hydrophobic core, their spontaneous formation appears exceedingly unlikely; in addition, the steric hindrance of binding of such a pre-formed conformation to its partner would be considerable. In case of pure conformational selection, dramatically reduced association rates would be expected (Zhou et al., 2012). Rather, IDPs seem to achieve fast association by their ability to form complex bound topologies and extended binding interfaces rapidly by virtue of their flexibility, once the binding partner presents a template for their induced folding beyond a pre-formed folded "nucleus." Coupled folding and binding of IDPs thus seems well described by the proposed "dock-and-coalesce" mechanism (Zhou et al., 2012) which, in terms classically used to describe protein folding, corresponds more to sequential structure formation as in diffusion-collision models (Karplus and Weaver, 1994), rather than nucleation-condensation mechanisms with concerted formation of secondary and tertiary structure (Itzhaki et al., 1995). Nevertheless, the variability observed in IDP binding mechanisms warrants caution in any such generalization.

In a broader sense, the observation that conformational selection and induced fit may be combined within a single pathway in a binding interaction suggests that the generic term "coupled folding and binding," often employed to leave open the question about whether binding precedes folding or vice versa, may actually be a quite accurate description of more complex interactions of IDPs with their partners. It has been stated that concurrent folding and binding would be extremely improbable since, already individually, folding and binding are low frequency stochastic events whose simultaneous occurrence would thus be even more rare (Hammes et al., 2009). However, this assumes that folding and binding are instantaneous, purely random events occurring on a static energy landscape, which is likely not the case. In particular, it has to be kept in mind that the energy landscape of interacting molecules changes while they approach each other. This has been underlined by a recent all-atom MD study of the interaction of a folded protein, ubiquitin, with a short ubiquitin-interacting motif (UIM) peptide sequence (Long and Brüschweiler, 2011). Already at nanometer distance to the ligand, largely due to long-range electrostatic effects, it was found that the energy landscape of ubiquitin began to change, more and more favoring a preexisting energy well containing conformers similar to the bound state. It was pointed out that this interaction is well described by induced fit when considering the average structure of ubiquitin at any given protein-ligand distance; however, when considering the entire ensemble of ubiquitin conformations present at each point of the approach, conformational selection on a changing energy landscape is a more appropriate characterization. The overall mechanism was thus described as a "superposition" of conformational selection and induced fit (Long and Brüschweiler, 2011). Such a description may be well suited to explain the complex kinetics of folding and binding observed experimentally in IDPs, whose highly dynamic nature makes the need of ensemble descriptions even more evident (Jensen et al., 2014). Indeed, the term "conformational funneling" that we introduced in the context of the SeV N_{TAIL}-PX interaction is conceptually very similar (Schneider et al., 2015; Gianni et al., 2016). This approach would also allow to transcend the likely too simplistic view of mutually exclusive, strictly sequential or strictly parallel conformational selection or induced fit pathways.

Beyond Structure: Fuzzy Complexes

While so far we have mostly discussed IDP binding interactions that involve individual binding sites and lead to well-defined complexes, the repertoire of binding mechanisms available to IDPs has been found to be much larger than that. So-called "fuzzy complexes" can retain considerable dynamics in the bound state (Tompa and Fuxreiter, 2008). In fact, the complex between N_{TAIL} and PX in Sendai virus discussed above already provides one example, with the nonspecific initial complex of N_{TAIL} diffusing on the surface of PX actually being more populated than the final bound state (Schneider et al., 2015). This dynamic behavior has also been used as an explanation for the persistent line broadening observed in NMR spectra of this complex, even in presence of excess ligand. The disordered cyclin-dependent kinase inhibitor Sic1 has been found to interact with a single binding site on its receptor Cdc4 via multiple phosphorylated suboptimal binding sites that engage the partner in rapid exchange and only become transiently ordered upon interaction (Mittag et al., 2008). The requirement for each site to be phosphorylated for interaction, as well as the rapid equilibrium of several Sic1 sites exchanging on a single receptor binding site, leads to global high-affinity binding and a finely tunable, sensitive response of this interaction to Sic1 phosphorylation. An even more extreme example of dynamic binding is found in the interaction of phenylalanine-glycine-(FG-) rich nucleoporins (FG-Nups) with nuclear transport receptors (NTRs) during their transit through the nuclear pore complex. A recent detailed investigation of the interaction of the NTR importin β with a PxFG-rich domain of the FG-Nup Nup153 has demonstrated extremely rapid, concurrent binding of minimalistic Nup153 motifs (in principle, individual phenylalanine side chains) to importin β, while the overall disordered nature of Nup153 remained unperturbed, to the extent that backbone ^{13}C chemical shifts remain oblivious to the interactions mediated by their aromatic sidechain moieties (Milles et al., 2015). The unique properties of this multivalent interaction have been proposed to be at the core of rapid nuclear transport. Dynamic complexes of IDPs and multisite interactions thus seem to provide important advantages for rapid, yet sensitive and selective molecular recognition, with the avoidance of a large entropy loss upon binding likely being one of them. The hypothesis that an IDP interaction could be dynamic to such an extent that NMR spectra remain completely unaffected, as put forward for the dimerization of the T-cell receptor zeta subunit (Sigalov et al., 2007), has however not been confirmed by further experiments (Nourse and Mittag, 2014), suggesting that even "fuzzy complexes" are characterized by a transient local gain in structure within binding sites.

CONCLUDING REMARKS

IDPs often seem to escape concepts that attempt to unify and generalize their behavior. While some phenomena, such as fast association rates or moderate affinities, are found recurrently in IDP interactions, they are not generally associated with disorder, and IDPs appear to employ various combinations of conformational selection and induced fit mechanisms of binding, making use of both pre-formed structured elements and structural adaptation after binding. However, it should not be expected that IDPs are a homogeneous class of proteins; their mechanistic repertoire is large, as is the range of functions they are involved in. In that sense, IDPs should probably be regarded as less fundamentally different from folded proteins than they appear at first glance; after all, they are governed by the same fundamental laws of kinetics and thermodynamics. In recent years, techniques such as transient kinetics, NMR spectroscopy, and molecular simulations have considerably increased our knowledge about the mechanisms employed by IDPs to fulfill their functions. In particular, it has become increasingly evident that combining the results gained using these different techniques allows for additional mechanistic insight not easily obtained from the individual approaches alone. Further research in this exciting field should allow us to gain a more representative picture on what may or may not distinguish disorder from order in protein function.

AUTHOR CONTRIBUTIONS

All authors participated in writing of the manuscript and approved of its final version.

ACKNOWLEDGMENTS

We are grateful to Magnus Kjærgaard for providing **Figures 2A,B**.

REFERENCES

Arai, M., Ferreon, J. C., and Wright, P. E. (2012). Quantitative analysis of multisite protein-ligand interactions by NMR: binding of intrinsically disordered p53 transactivation subdomains with the TAZ2 domain of CBP. *J. Am. Chem. Soc.* 134, 3792–3803. doi: 10.1021/ja209936u

Arai, M., Sugase, K., Dyson, H. J., and Wright, P. E. (2015). Conformational propensities of intrinsically disordered proteins influence the mechanism of binding and folding. *Proc. Natl. Acad. Sci. U.S.A.* 112, 9614–9619. doi: 10.1073/pnas.1512799112

Barducci, A., Bussi, G., and Parrinello, M. (2008). Well-tempered metadynamics: a smoothly converging and tunable free-energy method. *Phys. Rev. Lett.* 100:20603. doi: 10.1103/PhysRevLett.100.020603

Bernasconi, C. F. (1976). *Relaxation Kinetics*. New York, NY: Academic Press.

Best, R. B., and Hummer, G. (2009). Optimized molecular dynamics force fields applied to the helix-coil transition of polypeptides. *J. Phys. Chem. B* 113, 9004–9015. doi: 10.1021/jp901540t

Bienkiewicz, E. A., Adkins, J. N., and Lumb, K. J. (2002). Functional consequences of preorganized helical structure in the intrinsically disordered cell-cycle inhibitor p27(Kip1). *Biochemistry* 41, 752–759. doi: 10.1021/bi015763t

Bodart, J.-F., Wieruszeski, J.-M., Amniai, L., Leroy, A., Landrieu, I., Rousseau-Lescuyer, A., et al. (2008). NMR observation of Tau in Xenopus oocytes. *J. Magn. Reson.* 192, 252–257. doi: 10.1016/j.jmr.2008.03.006

Boehr, D. D., Nussinov, R., and Wright, P. E. (2009). The role of dynamic conformational ensembles in biomolecular recognition. *Nat. Chem. Biol.* 5, 789–796. doi: 10.1038/nchembio.232

Borcherds, W., Theillet, F.-X., Katzer, A., Finzel, A., Mishall, K. M., Powell, A. T., et al. (2014). Disorder and residual helicity alter p53-Mdm2 binding affinity and signaling in cells. *Nat. Chem. Biol.* 10, 1000–1002. doi: 10.1038/nchembio.1668

Csermely, P., Palotai, R., and Nussinov, R. (2010). Induced fit, conformational selection and independent dynamic segments: an extended view of binding events. *Trends Biochem. Sci.* 35, 539–546. doi: 10.1016/j.tibs.2010.04.009

Daniels, K. G., Tonthat, N. K., McClure, D. R., Chang, Y.-C., Liu, X., Schumacher, M. A., et al. (2014). Ligand concentration regulates the pathways of coupled protein folding and binding. *J. Am. Chem. Soc.* 136, 822–825. doi: 10.1021/ja4086726

Demarest, S. J., Martinez-Yamout, M., Chung, J., Chen, H., Xu, W., Dyson, H. J., et al. (2002). Mutual synergistic folding in recruitment of CBP/p300 by p160 nuclear receptor coactivators. *Nature* 415, 549–553. doi: 10.1038/415549a

De Sancho, D., and Best, R. B. (2012). Modulation of an IDP binding mechanism and rates by helix propensity and non-native interactions: association of HIF1α with CBP. *Mol. Biosyst.* 8, 256–267. doi: 10.1039/C1MB05252G

De Vivo, M., Masetti, M., Bottegoni, G., and Cavalli, A. (2016). Role of molecular dynamics and related methods in drug discovery. *J. Med. Chem.* 59, 4035–4061. doi: 10.1021/acs.jmedchem.5b01684

Do, T. N., Choy, W.-Y., and Karttunen, M. (2014). Accelerating the conformational sampling of intrinsically disordered proteins. *J. Chem. Theory Comput.* 10, 5081–5094. doi: 10.1021/ct5004803

Dogan, J., Gianni, S., and Jemth, P. (2014). The binding mechanisms of intrinsically disordered proteins. *Phys. Chem. Chem. Phys.* 16, 6323–6331. doi: 10.1039/C3CP54226B

Dogan, J., and Jemth, P. (2014). Only kinetics can prove conformational selection. *Biophys. J.* 107, 1997–1998. doi: 10.1016/j.bpj.2014.08.037

Dogan, J., Jonasson, J., Andersson, E., and Jemth, P. (2015). Binding rate constants reveal distinct features of disordered protein domains. *Biochemistry* 54, 4741–4750. doi: 10.1021/acs.biochem.5b00520

Dogan, J., Mu, X., Engström, Å., and Jemth, P. (2013). The transition state structure for coupled binding and folding of disordered protein domains. *Sci. Rep.* 3:2076. doi: 10.1038/srep02076

© 2017 Tous droits réservés. lilliad.univ-lille.fr

Dogan, J., Schmidt, T., Mu, X., Engström, Å., and Jemth, P. (2012). Fast association and slow transitions in the interaction between two intrinsically disordered protein domains. *J. Biol. Chem.* 287, 34316–34324. doi: 10.1074/jbc.M112.399436

Doig, A. J., MacArthur, M. W., Stapley, B. J., and Thornton, J. M. (1997). Structures of N-termini of helices in proteins. *Protein Sci.* 6, 147–155. doi: 10.1002/pro.5560060117

Domene, C., Barbini, P., and Furini, S. (2015). Bias-exchange metadynamics simulations: an efficient strategy for the analysis of conduction and selectivity in ion channels. *J. Chem. Theory Comput.* 11, 1896–1906. doi: 10.1021/ct501053x

Dosnon, M., Bonetti, D., Morrone, A., Erales, J., di Silvio, E., Longhi, S., et al. (2015). Demonstration of a folding after binding mechanism in the recognition between the measles virus NTAIL and X domains. *ACS Chem. Biol.* 10, 795–802. doi: 10.1021/cb5008579

Dujardin, M., Madan, V., Montserret, R., Ahuja, P., Huvent, I., Launay, H., et al. (2015). A proline-tryptophan turn in the intrinsically disordered domain 2 of NS5A protein is essential for Hepatitis C virus RNA replication. *J. Biol. Chem.* 290, 19104–19120. doi: 10.1074/jbc.M115.644419

Dunker, A. K., Brown, C. J., Lawson, J. D., Iakoucheva, L. M., and Obradoviæ, Z. (2002). Intrinsic disorder and protein function. *Biochemistry* 41, 6573–6582. doi: 10.1021/bi012159+

Dunker, A. K., Lawson, J. D., Brown, C. J., Williams, R. M., Romero, P., Oh, J. S., et al. (2001). Intrinsically disordered protein. *J. Mol. Graph. Model.* 19, 26–59. doi: 10.1016/S1093-3263(00)00138-8

Dunker, A. K., Obradovic, Z., Romero, P., Garner, E. C., and Brown, C. J. (2000). Intrinsic protein disorder in complete genomes. *Genome Inform. Ser. Workshop Genome Inform.* 11, 161–171. Available online at: http://www.dabi.temple.edu/~zoran/papers/dunker00.pdf

Dyson, H. J., and Wright, P. E. (2002). Coupling of folding and binding for unstructured proteins. *Curr. Opin. Struct. Biol.* 12, 54–60. doi: 10.1016/S0959-440X(02)00289-0

Dyson, H. J., and Wright, P. E. (2005). Intrinsically unstructured proteins and their functions. *Nat. Rev. Mol. Cell Biol.* 6, 197–208. doi: 10.1038/nrm1589

Eaton, W. A., Muñoz, V., Thompson, P. A., Chan, C. K., and Hofrichter, J. (1997). Submillisecond kinetics of protein folding. *Curr. Opin. Struct. Biol.* 7, 10–14.

Eigen, M., and Hammes, G. G. (1963). "Elementary steps in enzyme reactions (as studied by relaxation spectrometry)," in *Advances in Enzymology - and Related Areas of Molecular Biology*, ed F. F. Nord (Hoboken, NJ), 1–38. Available online at: http://doi.wiley.com/10.1002/9780470122709.ch1 (Accessed June 23, 2016).

Espinoza-Fonseca, L. M. (2009). Reconciling binding mechanisms of intrinsically disordered proteins. *Biochem. Biophys. Res. Commun.* 382, 479–482. doi: 10.1016/j.bbrc.2009.02.151

Fersht, A. R., and Sato, S. (2004). Phi-value analysis and the nature of protein-folding transition states. *Proc. Natl. Acad. Sci. U.S.A.* 101, 7976–7981. doi: 10.1073/pnas.0402684101

Fuxreiter, M., Simon, I., Friedrich, P., and Tompa, P. (2004). Preformed structural elements feature in partner recognition by intrinsically unstructured proteins. *J. Mol. Biol.* 338, 1015–1026. doi: 10.1016/j.jmb.2004.03.017

Gambin, Y., VanDelinder, V., Ferreon, A. C. M., Lemke, E. A., Groisman, A., and Deniz, A. A. (2011). Visualizing a one-way protein encounter complex by ultrafast single-molecule mixing. *Nat. Methods* 8, 239–241. doi: 10.1038/nmeth.1568

Ganguly, D., Otieno, S., Waddell, B., Iconaru, L., Kriwacki, R. W., and Chen, J. (2012). Electrostatically accelerated coupled binding and folding of intrinsically disordered proteins. *J. Mol. Biol.* 422, 674–684. doi: 10.1016/j.jmb.2012.06.019

Ganguly, D., Zhang, W., and Chen, J. (2013). Electrostatically accelerated encounter and folding for facile recognition of intrinsically disordered proteins. *PLoS Comput. Biol.* 9:e1003363. doi: 10.1371/journal.pcbi.1003363

Gianni, S., Dogan, J., and Jemth, P. (2014). Distinguishing induced fit from conformational selection. *Biophys. Chem.* 189, 33–39. doi: 10.1016/j.bpc.2014.03.003

Gianni, S., Dogan, J., and Jemth, P. (2016). Coupled binding and folding of intrinsically disordered proteins: what can we learn from kinetics? *Curr. Opin. Struct. Biol.* 36, 18–24. doi: 10.1016/j.sbi.2015.11.012

Gianni, S., Morrone, A., Giri, R., and Brunori, M. (2012). A folding-after-binding mechanism describes the recognition between the transactivation domain of c-Myb and the KIX domain of the CREB-binding protein. *Biochem. Biophys. Res. Commun.* 428, 205–209. doi: 10.1016/j.bbrc.2012.09.112

Giri, R., Morrone, A., Toto, A., Brunori, M., and Gianni, S. (2013). Structure of the transition state for the binding of c-Myb and KIX highlights an unexpected order for a disordered system. *Proc. Natl. Acad. Sci. U.S.A.* 110, 14942–14947. doi: 10.1073/pnas.1307337110

Hammes, G. G., Chang, Y.-C., and Oas, T. G. (2009). Conformational selection or induced fit: a flux description of reaction mechanism. *Proc. Natl. Acad. Sci. U.S.A.* 106, 13737–13741. doi: 10.1073/pnas.0907195106

Han, M., Xu, J., Ren, Y., and Li, J. (2016). Simulation of coupled folding and binding of an intrinsically disordered protein in explicit solvent with metadynamics. *J. Mol. Graph. Model.* 68, 114–127. doi: 10.1016/j.jmgm.2016.06.015

Henriques, J., Cragnell, C., and Skepö, M. (2015). Molecular dynamics simulations of intrinsically disordered proteins: force field evaluation and comparison with experiment. *J. Chem. Theory Comput.* 11, 3420–3431. doi: 10.1021/ct501178z

Horn, H. W., Swope, W. C., Pitera, J. W., Madura, J. D., Dick, T. J., Hura, G. L., et al. (2004). Development of an improved four-site water model for biomolecular simulations: TIP4P-Ew. *J. Chem. Phys.* 120, 9665–9678. doi: 10.1063/1.1683075

Huang, Y., and Liu, Z. (2009). Kinetic advantage of intrinsically disordered proteins in coupled folding-binding process: a critical assessment of the "fly-casting" mechanism. *J. Mol. Biol.* 393, 1143–1159. doi: 10.1016/j.jmb.2009.09.010

Iakoucheva, L. M., Radivojac, P., Brown, C. J., O'Connor, T. R., Sikes, J. G., Obradovic, Z., et al. (2004). The importance of intrinsic disorder for protein phosphorylation. *Nucleic Acids Res.* 32, 1037–1049. doi: 10.1093/nar/gkh253

Iešmantavičius, V., Dogan, J., Jemth, P., Teilum, K., and Kjaergaard, M. (2014). Helical propensity in an intrinsically disordered protein accelerates ligand binding. *Angew. Chem. Int. Ed. Engl.* 53, 1548–1551. doi: 10.1002/anie.201307712

Iešmantavičius, V., Jensen, M. R., Ozenne, V., Blackledge, M., Poulsen, F. M., and Kjaergaard, M. (2013). Modulation of the intrinsic helix propensity of an intrinsically disordered protein reveals long-range helix-helix interactions. *J. Am. Chem. Soc.* 135, 10155–10163. doi: 10.1021/ja4045532

Irbäck, A., and Mohanty, S. (2006). PROFASI: a monte carlo simulation package for protein folding and aggregation. *J. Comput. Chem.* 27, 1548–1555. doi: 10.1002/jcc.20452

Ithuralde, R. E., Roitberg, A. E., and Turjanski, A. G. (2016). Structured and unstructured binding of an intrinsically disordered protein as revealed by atomistic simulations. *J. Am. Chem. Soc.* 138, 8742–8751. doi: 10.1021/jacs.6b02016

Itzhaki, L. S., Otzen, D. E., and Fersht, A. R. (1995). The structure of the transition state for folding of chymotrypsin inhibitor 2 analysed by protein engineering methods: evidence for a nucleation-condensation mechanism for protein folding. *J. Mol. Biol.* 254, 260–288. doi: 10.1006/jmbi.1995.0616

Japrung, D., Dogan, J., Freedman, K. J., Nadzeyka, A., Bauerdick, S., Albrecht, T., et al. (2013). Single-molecule studies of intrinsically disordered proteins using solid-state nanopores. *Anal. Chem.* 85, 2449–2456. doi: 10.1021/ac3035025

Jensen, M. R., and Blackledge, M. (2014). Testing the validity of ensemble descriptions of intrinsically disordered proteins. *Proc. Natl. Acad. Sci. U.S.A.* 111, E1557–E1558. doi: 10.1073/pnas.1323876111

Jensen, M. R., Communie, G., Ribeiro, E. A., Martinez, N., Desfosses, A., Salmon, L., et al. (2011). Intrinsic disorder in measles virus nucleocapsids. *Proc. Natl. Acad. Sci. U.S.A.* 108, 9839–9844. doi: 10.1073/pnas.1103270108

Jensen, M. R., Houben, K., Lescop, E., Blanchard, L., Ruigrok, R. W. H., and Blackledge, M. (2008). Quantitative conformational analysis of partially folded proteins from residual dipolar couplings: application to the molecular recognition element of Sendai virus nucleoprotein. *J. Am. Chem. Soc.* 130, 8055–8061. doi: 10.1021/ja801332d

Jensen, M. R., Zweckstetter, M., Huang, J., and Blackledge, M. (2014). Exploring free-energy landscapes of intrinsically disordered proteins at atomic resolution using NMR spectroscopy. *Chem. Rev.* 114, 6632–6660. doi: 10.1021/cr400688u

Johnson, K. A. (2008). Role of induced fit in enzyme specificity: a molecular forward/reverse switch. *J. Biol. Chem.* 283, 26297–26301. doi: 10.1074/jbc.R800034200

Karanicolas, J., and Brooks, C. L. (2002). The origins of asymmetry in the folding transition states of protein L and protein G. *Protein Sci.* 11, 2351–2361. doi: 10.1110/ps.0205402

Karplus, M., and Weaver, D. L. (1994). Protein folding dynamics: the diffusion-collision model and experimental data. *Protein Sci.* 3, 650–668. doi: 10.1002/pro.5560030413

© 2017 Tous droits réservés. lilliad.univ-lille.fr

Karush, F. (1950). Heterogeneity of the binding sites of bovine serum albumin. *J. Am. Chem. Soc.* 72, 2705–2713. doi: 10.1021/ja01162a099

Kiefhaber, T., Bachmann, A., and Jensen, K. S. (2012). Dynamics and mechanisms of coupled protein folding and binding reactions. *Curr. Opin. Struct. Biol.* 22, 21–29. doi: 10.1016/j.sbi.2011.09.010

Kim, Y. B., Kalinowski, S. S., and Marcinkeviciene, J. (2007). A pre-steady state analysis of ligand binding to human glucokinase: evidence for a preexisting equilibrium. *Biochemistry* 46, 1423–1431. doi: 10.1021/bi0617308

Kirschner, K., Eigen, M., Bittman, R., and Voigt, B. (1966). The binding of nicotinamide-adenine dinucleotide to yeast d-glyceraldehyde-3-phosphate dehydrogenase: temperature-jump relaxation studies on the mechanism of an allosteric enzyme. *Proc. Natl. Acad. Sci. U.S.A.* 56, 1661–1667. doi: 10.1073/pnas.56.6.1661

Kjaergaard, M., Teilum, K., and Poulsen, F. M. (2010). Conformational selection in the molten globule state of the nuclear coactivator binding domain of CBP. *Proc. Natl. Acad. Sci. U.S.A.* 107, 12535–12540. doi: 10.1073/pnas.1001693107

Koshland, D. E. (1958). Application of a theory of enzyme specificity to protein synthesis. *Proc. Natl. Acad. Sci. U.S.A.* 44, 98–104. doi: 10.1073/pnas.44.2.98

Kragelj, J., Palencia, A., Nanao, M. H., Maurin, D., Bouvignies, G., Blackledge, M., et al. (2015). Structure and dynamics of the MKK7-JNK signaling complex. *Proc. Natl. Acad. Sci. U.S.A.* 112, 3409–3414. doi: 10.1073/pnas.1419528112

Krieger, J. M., Fusco, G., Lewitzky, M., Simister, P. C., Marchant, J., Camilloni, C., et al. (2014). Conformational recognition of an intrinsically disordered protein. *Biophys. J.* 106, 1771–1779. doi: 10.1016/j.bpj.2014.03.004

Kussie, P. H., Gorina, S., Marechal, V., Elenbaas, B., Moreau, J., Levine, A. J., et al. (1996). Structure of the MDM2 oncoprotein bound to the p53 tumor suppressor transactivation domain. *Science* 274, 948–953. doi: 10.1126/science.274.5289.948

Lacy, E. R., Filippov, I., Lewis, W. S., Otieno, S., Xiao, L., Weiss, S., et al. (2004). p27 binds cyclin-CDK complexes through a sequential mechanism involving binding-induced protein folding. *Nat. Struct. Mol. Biol.* 11, 358–364. doi: 10.1038/nsmb746

Laio, A., and Parrinello, M. (2002). Escaping free-energy minima. *Proc. Natl. Acad. Sci. U.S.A.* 99, 12562–12566. doi: 10.1073/pnas.202427399

Lange, O. F., Lakomek, N.-A., Farès, C., Schröder, G. F., Walter, K. F. A., Becker, S., et al. (2008). Recognition dynamics up to microseconds revealed from an RDC-derived ubiquitin ensemble in solution. *Science* 320, 1471–1475. doi: 10.1126/science.1157092

Leyrat, C., Schneider, R., Ribeiro, E. A. Jr., Yabukarski, F., Yao, M., Gérard, F. C. A., et al. (2012). Ensemble structure of the modular and flexible full-length vesicular stomatitis virus phosphoprotein. *J. Mol. Biol.* 423, 182–197. doi: 10.1016/j.jmb.2012.07.003

Leyrat, C., Yabukarski, F., Tarbouriech, N., Ribeiro, E. A., Jensen, M. R., Blackledge, M., et al. (2011). Structure of the vesicular stomatitis virus N^0-P complex. *PLoS Pathog.* 7:e1002248. doi: 10.1371/journal.ppat.1002248

Li, C., Pazgier, M., Li, C., Yuan, W., Liu, M., Wei, G., et al. (2010). Systematic mutational analysis of peptide inhibition of the p53-MDM2/MDMX interactions. *J. Mol. Biol.* 398, 200–213. doi: 10.1016/j.jmb.2010.03.005

Li, D.-W., and Brüschweiler, R. (2010). NMR-based protein potentials. *Angew. Chem. Int. Ed. Engl.* 49, 6778–6780. doi: 10.1002/anie.201001898

Lindorff-Larsen, K., Piana, S., Palmo, K., Maragakis, P., Klepeis, J. L., Dror, R. O., et al. (2010). Improved side-chain torsion potentials for the Amber ff99SB protein force field. *Proteins* 78, 1950–1958. doi: 10.1002/prot.22711

Lindorff-Larsen, K., Trbovic, N., Maragakis, P., Piana, S., and Shaw, D. E. (2012). Structure and dynamics of an unfolded protein examined by molecular dynamics simulation. *J. Am. Chem. Soc.* 134, 3787–3791. doi: 10.1021/ja209931w

Long, D., and Brüschweiler, R. (2011). *In silico* elucidation of the recognition dynamics of ubiquitin. *PLoS Comput. Biol.* 7:e1002035. doi: 10.1371/journal.pcbi.1002035

Ma, B., Kumar, S., Tsai, C. J., and Nussinov, R. (1999). Folding funnels and binding mechanisms. *Protein Eng.* 12, 713–720. doi: 10.1093/protein/12.9.713

Malatesta, F. (2005). The study of bimolecular reactions under non-pseudo-first order conditions. *Biophys. Chem.* 116, 251–256. doi: 10.1016/j.bpc.2005.04.006

Mercadante, D., Milles, S., Fuertes, G., Svergun, D. I., Lemke, E. A., and Gräter, F. (2015). Kirkwood-buff approach rescues overcollapse of a disordered protein in canonical protein force fields. *J. Phys. Chem. B* 119, 7975–7984. doi: 10.1021/acs.jpcb.5b03440

Mészáros, B., Tompa, P., Simon, I., and Dosztányi, Z. (2007). Molecular principles of the interactions of disordered proteins. *J. Mol. Biol.* 372, 549–561. doi: 10.1016/j.jmb.2007.07.004

Milles, S., Mercadante, D., Aramburu, I. V., Jensen, M. R., Banterle, N., Koehler, C., et al. (2015). Plasticity of an ultrafast interaction between nucleoporins and nuclear transport receptors. *Cell* 163, 734–745. doi: 10.1016/j.cell.2015.09.047

Mittag, T., Orlicky, S., Choy, W.-Y., Tang, X., Lin, H., Sicheri, F., et al. (2008). Dynamic equilibrium engagement of a polyvalent ligand with a single-site receptor. *Proc. Natl. Acad. Sci. U.S.A.* 105, 17772–17777. doi: 10.1073/pnas.0809222105

Mittermaier, A. K., and Kay, L. E. (2009). Observing biological dynamics at atomic resolution using NMR. *Trends Biochem. Sci.* 34, 601–611. doi: 10.1016/j.tibs.2009.07.004

Nourse, A., and Mittag, T. (2014). The cytoplasmic domain of the T-cell receptor zeta subunit does not form disordered dimers. *J. Mol. Biol.* 426, 62–70. doi: 10.1016/j.jmb.2013.09.036

Okamoto, Y. (2004). Generalized-ensemble algorithms: enhanced sampling techniques for Monte Carlo and molecular dynamics simulations. *J. Mol. Graph. Model.* 22, 425–439. doi: 10.1016/j.jmgm.2003.12.009

Oldfield, C. J., Meng, J., Yang, J. Y., Yang, M. Q., Uversky, V. N., and Dunker, A. K. (2008). Flexible nets: disorder and induced fit in the associations of p53 and 14-3-3 with their partners. *BMC Genomics* 9(Suppl. 1):S1. doi: 10.1186/1471-2164-9-S1-S1

Ostermeir, K., and Zacharias, M. (2013). Advanced replica-exchange sampling to study the flexibility and plasticity of peptides and proteins. *Biochim. Biophys. Acta* 1834, 847–853. doi: 10.1016/j.bbapap.2012.12.016

Palmer, A. G., Kroenke, C. D., and Loria, J. P. (2001). Nuclear magnetic resonance methods for quantifying microsecond-to-millisecond motions in biological macromolecules. *Methods Enzymol.* 339, 204–238. doi: 10.1016/S0076-6879(01)39315-1

Palmer, A. G., and Massi, F. (2006). Characterization of the dynamics of biomacromolecules using rotating-frame spin relaxation NMR spectroscopy. *Chem. Rev.* 106, 1700–1719. doi: 10.1021/cr0404287

Parker, D., Jhala, U. S., Radhakrishnan, I., Yaffe, M. B., Reyes, C., Shulman, A. I., et al. (1998). Analysis of an activator:coactivator complex reveals an essential role for secondary structure in transcriptional activation. *Mol. Cell* 2, 353–359. doi: 10.1016/S1097-2765(00)80279-8

Parker, D., Rivera, M., Zor, T., Henrion-Caude, A., Radhakrishnan, I., Kumar, A., et al. (1999). Role of secondary structure in discrimination between constitutive and inducible activators. *Mol. Cell. Biol.* 19, 5601–5607. doi: 10.1128/MCB.19.8.5601

Petros, A. M., Nettesheim, D. G., Wang, Y., Olejniczak, E. T., Meadows, R. P., Mack, J., et al. (2000). Rationale for Bcl-xL/Bad peptide complex formation from structure, mutagenesis, and biophysical studies. *Protein Sci.* 9, 2528–2534. doi: 10.1017/S096183680000331X

Piana, S., Donchev, A. G., Robustelli, P., and Shaw, D. E. (2015). Water dispersion interactions strongly influence simulated structural properties of disordered protein states. *J. Phys. Chem. B* 119, 5113–5123. doi: 10.1021/jp508971m

Prakash, M. K. (2011). Insights on the role of (dis)order from protein-protein interaction linear free-energy relationships. *J. Am. Chem. Soc.* 133, 9976–9979. doi: 10.1021/ja201500z

Rauscher, S., Gapsys, V., Gajda, M. J., Zweckstetter, M., de Groot, B. L., and Grubmüller, H. (2015). Structural ensembles of intrinsically disordered proteins depend strongly on force field: a comparison to experiment. *J. Chem. Theory Comput.* 11, 5513–5524. doi: 10.1021/acs.jctc.5b00736

Richardson, J. S., and Richardson, D. C. (1988). Amino acid preferences for specific locations at the ends of alpha helices. *Science* 240, 1648–1652. doi: 10.1126/science.3381086

Rogers, J. M., Oleinikovas, V., Shammas, S. L., Wong, C. T., De Sancho, D., Baker, C. M., et al. (2014a). Interplay between partner and ligand facilitates the folding and binding of an intrinsically disordered protein. *Proc. Natl. Acad. Sci. U.S.A.* 111, 15420–15425. doi: 10.1073/pnas.1409122111

Rogers, J. M., Steward, A., and Clarke, J. (2013). Folding and binding of an intrinsically disordered protein: fast, but not "diffusion-limited." *J. Am. Chem. Soc.* 135, 1415–1422. doi: 10.1021/ja309527h

Rogers, J. M., Wong, C. T., and Clarke, J. (2014b). Coupled folding and binding of the disordered protein PUMA does not require particular residual structure. *J. Am. Chem. Soc.* 136, 5197–5200. doi: 10.1021/ja4125065

© 2017 Tous droits réservés. lilliad.univ-lille.fr

Salmon, L., Nodet, G., Ozenne, V., Yin, G., Jensen, M. R., Zweckstetter, M., et al. (2010). NMR characterization of long-range order in intrinsically disordered proteins. *J. Am. Chem. Soc.* 132, 8407–8418. doi: 10.1021/ja101645g

Salvi, N., Abyzov, A., and Blackledge, M. (2016). Multi-timescale dynamics in intrinsically disordered proteins from NMR relaxation and molecular simulation. *J. Phys. Chem. Lett.* 7, 2483–2489. doi: 10.1021/acs.jpclett.6b00885

Schneider, R., Maurin, D., Communie, G., Kragelj, J., Hansen, D. F., Ruigrok, R. W. H., et al. (2015). Visualizing the molecular recognition trajectory of an intrinsically disordered protein using multinuclear relaxation dispersion NMR. *J. Am. Chem. Soc.* 137, 1220–1229. doi: 10.1021/ja511066q

Schuck, P., and Zhao, H. (2010). The role of mass transport limitation and surface heterogeneity in the biophysical characterization of macromolecular binding processes by SPR biosensing. *Methods Mol. Biol.* 627, 15–54. doi: 10.1007/978-1-60761-670-2_2

Shammas, S. L., Travis, A. J., and Clarke, J. (2013). Remarkably fast coupled folding and binding of the intrinsically disordered transactivation domain of cMyb to CBP KIX. *J. Phys. Chem. B* 117, 13346–13356. doi: 10.1021/jp404267e

Shammas, S. L., Travis, A. J., and Clarke, J. (2014). Allostery within a transcription coactivator is predominantly mediated through dissociation rate constants. *Proc. Natl. Acad. Sci. U.S.A.* 111, 12055–12060. doi: 10.1073/pnas.1405815111

Shoemaker, B. A., Portman, J. J., and Wolynes, P. G. (2000). Speeding molecular recognition by using the folding funnel: the fly-casting mechanism. *Proc. Natl. Acad. Sci. U.S.A.* 97, 8868–8873. doi: 10.1073/pnas.160259697

Sickmeier, M., Hamilton, J. A., LeGall, T., Vacic, V., Cortese, M. S., Tantos, A., et al. (2007). DisProt: the database of disordered proteins. *Nucleic Acids Res.* 35, D786–D793. doi: 10.1093/nar/gkl893

Sigalov, A. B., Zhuravleva, A. V., and Orekhov, V. Y. (2007). Binding of intrinsically disordered proteins is not necessarily accompanied by a structural transition to a folded form. *Biochimie* 89, 419–421. doi: 10.1016/j.biochi.2006.11.003

Smith, W. W., Ho, P.-Y., and O'Hern, C. S. (2014). Calibrated langevin-dynamics simulations of intrinsically disordered proteins. *Phys. Rev. E Stat. Nonlin. Soft Matter. Phys.* 90:42709. doi: 10.1103/PhysRevE.90.042709

Spolar, R. S., and Record, M. T. (1994). Coupling of local folding to site-specific binding of proteins to DNA. *Science* 263, 777–784. doi: 10.1126/science.8303294

Staneva, I., Huang, Y., Liu, Z., and Wallin, S. (2012). Binding of two intrinsically disordered peptides to a multi-specific protein: a combined Monte Carlo and molecular dynamics study. *PLoS Comput. Biol.* 8:e1002682. doi: 10.1371/journal.pcbi.1002682

Sugase, K., Dyson, H. J., and Wright, P. E. (2007a). Mechanism of coupled folding and binding of an intrinsically disordered protein. *Nature* 447, 1021–1025. doi: 10.1038/nature05858

Sugase, K., Lansing, J. C., Dyson, H. J., and Wright, P. E. (2007b). Tailoring relaxation dispersion experiments for fast-associating protein complexes. *J. Am. Chem. Soc.* 129, 13406–13407. doi: 10.1021/ja0762238

Tai, K. (2004). Conformational sampling for the impatient. *Biophys. Chem.* 107, 213–220. doi: 10.1016/j.bpc.2003.09.010

Takada, S., Kanada, R., Tan, C., Terakawa, T., Li, W., and Kenzaki, H. (2015). Modeling structural dynamics of biomolecular complexes by coarse-grained molecular simulations. *Acc. Chem. Res.* 48, 3026–3035. doi: 10.1021/acs.accounts.5b00338

Theillet, F.-X., Binolfi, A., Bekei, B., Martorana, A., Rose, H. M., Stuiver, M., et al. (2016). Structural disorder of monomeric α-synuclein persists in mammalian cells. *Nature* 530, 45–50. doi: 10.1038/nature16531

Tompa, P. (2002). Intrinsically unstructured proteins. *Trends Biochem. Sci.* 27, 527–533. doi: 10.1016/S0968-0004(02)02169-2

Tompa, P., and Fuxreiter, M. (2008). Fuzzy complexes: polymorphism and structural disorder in protein-protein interactions. *Trends Biochem. Sci.* 33, 2–8. doi: 10.1016/j.tibs.2007.10.003

Tompa, P., Szász, C., and Buday, L. (2005). Structural disorder throws new light on moonlighting. *Trends Biochem. Sci.* 30, 484–489. doi: 10.1016/j.tibs.2005.07.008

Tummino, P. J., and Copeland, R. A. (2008). Residence time of receptor-ligand complexes and its effect on biological function. *Biochemistry* 47, 5481–5492. doi: 10.1021/bi8002023

Ueda, Y., Taketomi, H., and Gō, N. (1978). Studies on protein folding, unfolding, and fluctuations by computer simulation. II. A. Three-dimensional lattice model of lysozyme. *Biopolymers* 17, 1531–1548. doi: 10.1002/bip.1978.360170612

Uversky, V. N. (2002). Natively unfolded proteins: a point where biology waits for physics. *Protein Sci.* 11, 739–756. doi: 10.1110/ps.4210102

Uversky, V. N., Oldfield, C. J., and Dunker, A. K. (2008). Intrinsically disordered proteins in human diseases: introducing the D2 concept. *Annu. Rev. Biophys.* 37, 215–246. doi: 10.1146/annurev.biophys.37.032807.125924

Vallurupalli, P., Bouvignies, G., and Kay, L. E. (2012). Studying "invisible" excited protein states in slow exchange with a major state conformation. *J. Am. Chem. Soc.* 134, 8148–8161. doi: 10.1021/ja3001419

Vogt, A. D., and Di Cera, E. (2012). Conformational selection or induced fit? A critical appraisal of the kinetic mechanism. *Biochemistry* 51, 5894–5902. doi: 10.1021/bi3006913

Vogt, A. D., and Di Cera, E. (2013). Conformational selection is a dominant mechanism of ligand binding. *Biochemistry* 52, 5723–5729. doi: 10.1021/bi400929b

Wang, L.-P., Martinez, T. J., and Pande, V. S. (2014). Building force fields: an automatic, systematic, and reproducible approach. *J. Phys. Chem. Lett.* 5, 1885–1891. doi: 10.1021/jz500737m

Wang, W., Ye, W., Jiang, C., Luo, R., and Chen, H.-F. (2014). New force field on modeling intrinsically disordered proteins. *Chem. Biol. Drug Des.* 84, 253–269. doi: 10.1111/cbdd.12314

Wang, Y., Chu, X., Longhi, S., Roche, P., Han, W., Wang, E., et al. (2013). Multiscaled exploration of coupled folding and binding of an intrinsically disordered molecular recognition element in measles virus nucleoprotein. *Proc. Natl. Acad. Sci. U.S.A.* 110, E3743–E3752. doi: 10.1073/pnas.1308381110

Wells, M., Tidow, H., Rutherford, T. J., Markwick, P., Jensen, M. R., Mylonas, E., et al. (2008). Structure of tumor suppressor p53 and its intrinsically disordered N-terminal transactivation domain. *Proc. Natl. Acad. Sci. U.S.A.* 105, 5762–5767. doi: 10.1073/pnas.0801353105

Wong, I., Patel, S. S., and Johnson, K. A. (1991). An induced-fit kinetic mechanism for DNA replication fidelity: direct measurement by single-turnover kinetics. *Biochemistry* 30, 526–537. doi: 10.1021/bi00216a030

Wright, P. E., and Dyson, H. J. (1999). Intrinsically unstructured proteins: re-assessing the protein structure-function paradigm. *J. Mol. Biol.* 293, 321–331. doi: 10.1006/jmbi.1999.3110

Wright, P. E., and Dyson, H. J. (2015). Intrinsically disordered proteins in cellular signalling and regulation. *Nat. Rev. Mol. Cell Biol.* 16, 18–29. doi: 10.1038/nrm3920

Ye, W., Ji, D., Wang, W., Luo, R., and Chen, H.-F. (2015). Test and evaluation of ff99IDPs force field for intrinsically disordered proteins. *J. Chem. Inf. Model.* 55, 1021–1029. doi: 10.1021/acs.jcim.5b00043

Zerze, G. H., Miller, C. M., Granata, D., and Mittal, J. (2015). Free energy surface of an intrinsically disordered protein: comparison between temperature replica exchange molecular dynamics and bias-exchange metadynamics. *J. Chem. Theory Comput.* 11, 2776–2782. doi: 10.1021/acs.jctc.5b00047

Zhou, H.-X. (2012). Intrinsic disorder: signaling via highly specific but short-lived association. *Trends Biochem. Sci.* 37, 43–48. doi: 10.1016/j.tibs.2011.11.002

Zhou, H.-X., and Bates, P. A. (2013). Modeling protein association mechanisms and kinetics. *Curr. Opin. Struct. Biol.* 23, 887–893. doi: 10.1016/j.sbi.2013.06.014

Zhou, H.-X., Pang, X., and Lu, C. (2012). Rate constants and mechanisms of intrinsically disordered proteins binding to structured targets. *Phys. Chem. Chem. Phys.* 14, 10466–10476. doi: 10.1039/c2cp41196b

Zondlo, S. C., Lee, A. E., and Zondlo, N. J. (2006). Determinants of specificity of MDM2 for the activation domains of p53 and p65: proline27 disrupts the MDM2-binding motif of p53. *Biochemistry* 45, 11945–11957. doi: 10.1021/bi060309g

© 2017 Tous droits réservés. lilliad.univ-lille.fr

Zor, T., De Guzman, R. N., Dyson, H. J., and Wright, P. E. (2004). Solution structure of the KIX domain of CBP bound to the transactivation domain of c-Myb. *J. Mol. Biol.* 337, 521–534. doi: 10.1016/j.jmb.2004.01.038

Zor, T., Mayr, B. M., Dyson, H. J., Montminy, M. R., and Wright, P. E. (2002). Roles of phosphorylation and helix propensity in the binding of the KIX domain of CREB-binding protein by constitutive (c-Myb) and inducible (CREB) activators. *J. Biol. Chem.* 277, 42241–42248. doi: 10.1074/jbc.M207361200

Zuiderweg, E. R. P. (2002). Mapping protein-protein interactions in solution by NMR spectroscopy. *Biochemistry* 41, 1–7. doi: 10.1021/bi011870b

Conflict of Interest Statement: The authors declare that the research was conducted in the absence of any commercial or financial relationships that could be construed as a potential conflict of interest.

Copyright © 2016 Mollica, Bessa, Hanoulle, Jensen, Blackledge and Schneider. This is an open-access article distributed under the terms of the Creative Commons Attribution License (CC BY). The use, distribution or reproduction in other forums is permitted, provided the original author(s) or licensor are credited and that the original publication in this journal is cited, in accordance with accepted academic practice. No use, distribution or reproduction is permitted which does not comply with these terms.

Bibliography

[1] J. D. Watson and F. H. Crick. Molecular structure of nucleic acids; a structure for deoxyribose nucleic acid. *Nature*, 171(4356):737–738, Apr 1953. DOI 10.1038/171737a0.

[2] H. J. Dyson and P. E. Wright. Intrinsically unstructured proteins and their functions. *Nat. Rev. Mol. Cell Biol.*, 6(3):197–208, Mar 2005. DOI 10.1038/nrm1589.

[3] Y. Ito and P. Selenko. Cellular structural biology. *Curr. Opin. Struct. Biol.*, 20(5):640–648, Oct 2010. DOI 10.1016/j.sbi.2010.07.006.

[4] Anthony K. Mittermaier and Lewis E. Kay. Observing biological dynamics at atomic resolution using NMR. *Trends Biochem Sci*, 34(12):601–611, Dec 2009. DOI 10.1016/j.tibs.2009.07.004.

[5] S. Granier and B. Kobilka. A new era of GPCR structural and chemical biology. *Nat. Chem. Biol.*, 8:670–673, July 2012. DOI 10.1038/nchembio.1025.

[6] E. Nogales. The development of cryo-EM into a mainstream structural biology technique. *Nat. Methods*, 13:24–27, January 2016.

[7] B. Hille. *Ionic Channels of Excitable Membranes.* Sinauer Associates Inc., Sunderland, MA, 3rd edition, 2001.

[8] F. M. Ashcroft. *Ion channels and disease.* Academic Press, 1999.

[9] F. M. Ashcroft. From molecule to malady. *Nature*, 440:440–447, March 2006. DOI 10.1038/nature04707.

[10] H. T. Kurata and D. Fedida. A structural interpretation of voltage-gated potassium channel inactivation. *Prog. Biophys. Mol. Biol.*, 92(2):185–208, Oct 2006. DOI 10.1016/j.pbiomolbio.2005.10.001.

[11] W. A. Catterall, G. Wisedchaisri, and N. Zheng. The chemical basis for electrical signaling. *Nat. Chem. Biol.*, 13:455–463, April 2017. ISSN 1552-4469. DOI 10.1038/nchembio.2353.

[12] G. Yellen. The moving parts of voltage-gated ion channels. *Q. Rev. Biophys.*, 31(3):239–295, Aug 1998. DOI 10.1017/S0033583598003448.

[13] D. A. Doyle, J. Morais Cabral, R. A. Pfuetzner, A. Kuo, J. M. Gulbis, S. L. Cohen, B. T. Chait, and R. MacKinnon. The structure of the potassium channel: molecular basis of K^+

conduction and selectivity. *Science*, 280(5360):69–77, Apr 1998. DOI 10.1126/science.280.5360.69.

[14] Y. Jiang, A. Lee, J. Chen, M. Cadene, B. T. Chait, and R. MacKinnon. Crystal structure and mechanism of a calcium-gated potassium channel. *Nature*, 417:515–522, May 2002. DOI 10.1038/417515a.

[15] Y. Jiang, A. Lee, J. Chen, V. Ruta, M. Cadene, B. T. Chait, and R. MacKinnon. X-ray structure of a voltage-dependent K^+ channel. *Nature*, 423(6935):33–41, May 2003. DOI 10.1038/nature01580.

[16] S. B. Long, E. B. Campbell, and R. Mackinnon. Crystal structure of a mammalian voltage-dependent Shaker family K^+ channel. *Science*, 309(5736):897–903, Aug 2005. DOI 10.1126/science.1116269.

[17] J. Payandeh, T. Scheuer, N. Zheng, and W. A. Catterall. The crystal structure of a voltage-gated sodium channel. *Nature*, 475:353–358, July 2011. DOI 10.1038/nature10238.

[18] M. Liao, E. Cao, D. Julius, and Y. Cheng. Structure of the TRPV1 ion channel determined by electron cryo-microscopy. *Nature*, 504:107–112, December 2013. DOI 10.1038/nature12822.

[19] J. Wu, Z. Yan, Z. Li, C. Yan, S. Lu, M. Dong, and N. Yan. Structure of the voltage-gated calcium channel CaV1.1 complex. *Science*, 350:aad2395, December 2015. DOI 10.1126/science.aad2395.

[20] W. Wang and R. MacKinnon. Cryo-EM structure of the open human ether-à-go-go-related K(+) channel hERG. *Cell*, 169:422–430, April 2017. DOI 10.1016/j.cell.2017.03.048.

[21] C.-H. Lee and R. MacKinnon. Structures of the human HCN1 hyperpolarization-activated channel. *Cell*, 168:111–120, January 2017. DOI 10.1016/j.cell.2016.12.023.

[22] W. A. Catterall. From ionic currents to molecular mechanisms: the structure and function of voltage-gated sodium channels. *Neuron*, 26:13–25, April 2000. DOI 10.1016/S0896-6273(00)81133-2.

[23] M. Zhou, J. H. Morais-Cabral, S. Mann, and R. MacKinnon. Potassium channel receptor site for the inactivation gate and quaternary amine inhibitors. *Nature*, 411:657–661, June 2001. DOI 10.1038/35079500.

[24] Y. Zhou, J. H. Morais-Cabral, A. Kaufman, and R. MacKinnon. Chemistry of ion coordination and hydration revealed by a K^+ channel-Fab complex at 2.0 Å resolution. *Nature*, 414(6859):43–48, Nov 2001. DOI 10.1038/35102009.

[25] C. Ader, R. Schneider, S. Hornig, P. Velisetty, E. M. Wilson, A. Lange, K. Giller, I. Ohmert, M.-F. Martin-Eauclaire, D. Trauner, S. Becker, O. Pongs, and M. Baldus. A structural link between inactivation and block of a K^+ channel. *Nat. Struct. Mol. Biol.*, 15(6):605–612, Jun 2008. DOI 10.1038/nsmb.1430.

[26] A. Lange, K. Giller, S. Hornig, M.-F. Martin-Eauclaire, O. Pongs, S. Becker, and M. Baldus. Toxin-induced conformational changes in a potassium channel revealed by solid-state NMR. *Nature*, 440(7086):959–962, Apr 2006. DOI 10.1038/nature04649.

[27] H. Schrempf, O. Schmidt, R. Kümmerlen, S. Hinnah, D. Müller, M. Betzler, T. Steinkamp, and R. Wagner. A prokaryotic potassium ion channel with two predicted transmembrane segments from Streptomyces lividans. *EMBO J.*, 14(21):5170–5178, Nov 1995. DOI 10.1002/j.1460-2075.1995.tb00201.x.

[28] C. Legros, V. Pollmann, H. G. Knaus, A. M. Farrell, H. Darbon, P. E. Bougis, M. F. Martin-Eauclaire, and O. Pongs. Generating a high affinity scorpion toxin receptor in KcsA-Kv1.3 chimeric potassium channels. *J. Biol. Chem.*, 275(22):16918–16924, Jun 2000. DOI 10.1074/jbc.275.22.16918.

[29] C. Legros, C. Schulze, M. L. Garcia, P. E. Bougis, M.-F. Martin-Eauclaire, and O. Pongs. Engineering-specific pharmacological binding sites for peptidyl inhibitors of potassium channels into KcsA. *Biochemistry*, 41(51):15369–15375, Dec 2002. DOI 10.1021/bi026264a.

[30] M. LeMasurier, L. Heginbotham, and C. Miller. KcsA: it's a potassium channel. *J. Gen. Physiol.*, 118(3):303–314, Sep 2001. DOI 10.1085/jgp.118.3.303.

[31] L. G. Cuello, J. G. Romero, D. M. Cortes, and E. Perozo. pH-dependent gating in the Streptomyces lividans K^+ channel. *Biochemistry*, 37(10):3229–3236, Mar 1998. DOI 10.1021/bi972997x.

[32] J. F. Cordero-Morales, L. G. Cuello, Y. Zhao, V. Jogini, D. M. Cortes, B. Roux, and E. Perozo. Molecular determinants of gating at the potassium-channel selectivity filter. *Nat. Struct. Mol. Biol.*, 13(4):311–318, Apr 2006. DOI 10.1038/nsmb1069.

[33] R. Schneider, C. Ader, A. Lange, K. Giller, S. Hornig, O. Pongs, S. Becker, and M. Baldus. Solid-state NMR spectroscopy applied to a chimeric potassium channel in lipid bilayers. *J. Am. Chem. Soc.*, 130(23):7427–7435, Jun 2008. DOI 10.1021/ja800190c.

[34] Christian Ader, Robert Schneider, Sönke Hornig, Phanindra Velisetty, Vitya Vardanyan, Karin Giller, Iris Ohmert, Stefan Becker, Olaf Pongs, and Marc Baldus. Coupling of activation and inactivation gate in a K^+-channel: potassium and ligand sensitivity. *EMBO J*, 28 (18):2825–2834, Sep 2009. DOI 10.1038/emboj.2009.218.

[35] G. W. Vuister, S. J. Kim, C. Wu, and A. Bax. 2D and 3D NMR study of phenylalanine residues in proteins by reverse isotopic labeling. *J. Am. Chem. Soc.*, 116(20):9206–9210, Oct 1994. DOI 10.1021/ja00099a041.

[36] H. Heise, W. Hoyer, S. Becker, O. C. Andronesi, D. Riedel, and M. Baldus. Molecular-level secondary structure, polymorphism, and dynamics of full-length alpha-synuclein fibrils studied by solid-state NMR. *Proc. Natl. Ac. Sci. USA*, 102(44):15871–15876, Nov 2005. DOI 10.1073/pnas.0506109102.

[37] A. Pines, M. G. Gibby, and J. S. Waugh. Proton-enhanced nuclear induction spectroscopy. a method for high resolution NMR of dilute spins in solids. *J. Chem. Phys.*, 56(4):1776–1777, 1972. DOI 10.1063/1.1677439.

[38] M. Baldus. Correlation experiments for assignment and structure elucidation of immobilized polypeptides under magic angle spinning. *Progr. NMR Spectr.*, 41(1–2):1–47, Sep 2002. DOI 10.1016/S0079-6565(02)00007-9.

[39] D. S. Wishart and B. D. Sykes. Chemical shifts as a tool for structure determination. *Meth. Enzymol.*, 239:363–392, 1994. DOI 10.1016/S0076-6879(94)39014-2.

[40] S. Luca, D. V. Filippov, J. H. van Boom, H. Oschkinat, H. J. M. de Groot, and M. Baldus. Secondary chemical shifts in immobilized peptides and proteins: A qualitative basis for structure refinement under Magic Angle Spinning. *J. Biomol. NMR*, 20(4):325–331, Aug 2001. DOI 10.1023/A:1011278317489.

[41] D. M. Cortes, L. G. Cuello, and E. Perozo. Molecular architecture of full-length KcsA: role of cytoplasmic domains in ion permeation and activation gating. *J. Gen. Physiol.*, 117(2): 165–180, Feb 2001. DOI 10.1085/jgp.117.2.165.

[42] J. H. Chill, J. M. Louis, C. Miller, and A. Bax. NMR study of the tetrameric KcsA potassium channel in detergent micelles. *Prot. Sci.*, 15(4):684–698, Apr 2006. DOI 10.1110/ps.051954706.

[43] K. A. Baker, C. Tzitzilonis, W. Kwiatkowski, S. Choe, and R. Riek. Conformational dynamics of the KcsA potassium channel governs gating properties. *Nat. Struct. Mol. Biol.*, 14(11): 1089–1095, Nov 2007. DOI 10.1038/nsmb1311.

[44] V. P. T. Pau, Y. Zhu, Z. Yuchi, Q. Q. Hoang, and D. S. C. Yang. Characterization of the C-terminal domain of a potassium channel from Streptomyces lividans (KcsA). *J. Biol. Chem.*, 282(40):29163–29169, Oct 2007. DOI 10.1074/jbc.M703277200.

[45] K. Takeuchi, H. Takahashi, S. Kawano, and I. Shimada. Identification and characterization of the slowly exchanging pH-dependent conformational rearrangement in KcsA. *J. Biol. Chem.*, 282(20):15179–15186, May 2007. DOI 10.1074/jbc.M608264200.

[46] S. Neal, A. M. Nip, H. Y. Zhang, and D. S. Wishart. Rapid and accurate calculation of protein H-1, C-13 and N-15 chemical shifts. *J. Biomol. NMR*, 26(3):215–240, Jul 2003. DOI 10.1023/A:1023812930288.

[47] S. Uysal, V. Vásquez, V. Tereshko, K. Esaki, F. A. Fellouse, S. S. Sidhu, S. Koide, E. Perozo, and A. Kossiakoff. Crystal structure of full-length KcsA in its closed conformation. *Proc. Natl. Ac. Sci. USA*, 106:6644–6649, April 2009. DOI 10.1073/pnas.0810663106.

[48] S. Y. Noskov, S. Bernèche, and B. Roux. Control of ion selectivity in potassium channels by electrostatic and dynamic properties of carbonyl ligands. *Nature*, 431(7010):830–834, Oct 2004. DOI 10.1038/nature02943.

[49] F. Bezanilla and C. M. Armstrong. Negative conductance caused by entry of sodium and cesium ions into the potassium channels of squid axons. *J. Gen. Phys.*, 60:588–608, November 1972. DOI 10.1085/jgp.60.5.588.

[50] L. Heginbotham, M. LeMasurier, L. Kolmakova-Partensky, and C. Miller. Single Streptomyces lividans K^+ channels: functional asymmetries and sidedness of proton activation. *J. Gen. Physiol.*, 114(4):551–560, Oct 1999. DOI 10.1085/jgp.114.4.551.

[51] Y. Jiang, A. Lee, J. Chen, M. Cadene, B. T. Chait, and R. MacKinnon. The open pore conformation of potassium channels. *Nature*, 417(6888):523–526, May 2002. DOI 10.1038/417523a.

[52] S. Bernèche and B. Roux. A gate in the selectivity filter of potassium channels. *Structure*, 13(4):591–600, Apr 2005. DOI 10.1016/j.str.2004.12.019.

[53] J. F. Cordero-Morales, V. Jogini, A. Lewis, V. Vásquez, D. M. Cortes, B. Roux, and E. Perozo. Molecular driving forces determining potassium channel slow inactivation. *Nat. Struct. Mol. Biol.*, 14(11):1062–1069, Nov 2007. DOI 10.1038/nsmb1309.

[54] A. Lange, S. Luca, and M. Baldus. Structural constraints from proton-mediated rare-spin correlation spectroscopy in rotating solids. *J. Am. Chem. Soc.*, 124(33):9704–9705, Aug 2002. DOI 10.1021/ja026691b.

[55] A. T. Brunger, P. D. Adams, G. M. Clore, W. L. DeLano, P. Gros, R. W. Grosse-Kunstleve, J. S. Jiang, J. Kuszewski, M. Nilges, N. S. Pannu, R. J. Read, L. M. Rice, T. Simonson, and G. L. Warren. Crystallography & NMR system: A new software suite for macromolecular structure determination. *Acta Cryst. D*, 54:905–921, Sep 1998. DOI 10.1107/S0907444998003254.

[56] A. L. Morris, M. W. MacArthur, E. G. Hutchinson, and J. M. Thornton. Stereochemical quality of protein structure coordinates. *Proteins*, 12(4):345–364, Apr 1992. DOI 1002/prot.340120407.

[57] M. J. Lenaeus, M. Vamvouka, P. J. Focia, and A. Gross. Structural basis of TEA blockade in a model potassium channel. *Nat. Struct. Mol. Biol.*, 12(5):454–459, May 2005. DOI 10.1038/nsmb929.

[58] S. W. Lockless, M. Zhou, and R. MacKinnon. Structural and thermodynamic properties of selective ion binding in a K^+ channel. *PLoS Biol.*, 5(5):e121, May 2007. DOI 10.1371/journal.pbio.0050121.

[59] S. N. Gradl, J. P. Felix, E. Y. Isacoff, M. L. Garcia, and D. Trauner. Protein surface recognition by rational design: nanomolar ligands for potassium channels. *J. Am. Chem. Soc.*, 125(42):12668–12669, Oct 2003. DOI 10.1021/ja036155z.

[60] G. Panyi and C. Deutsch. Cross talk between activation and slow inactivation gates of Shaker potassium channels. *J. Gen. Physiol.*, 128(5):547–559, Nov 2006. DOI 10.1085/jgp.200609644.

[61] T. Baukrowitz and G. Yellen. Modulation of K^+ current by frequency and external $[K^+]$: a tale of two inactivation mechanisms. *Neuron*, 15(4):951–960, Oct 1995. DOI 10.1016/0896-6273(95)90185-X.

[62] T. Baukrowitz and G. Yellen. Use-dependent blockers and exit rate of the last ion from the multi-ion pore of a K^+ channel. *Science*, 271(5249):653–656, Feb 1996. DOI 10.1126/science.271.5249.653.

[63] G. Panyi and C. Deutsch. Probing the cavity of the slow inactivated conformation of Shaker potassium channels. *J. Gen. Physiol.*, 129(5):403–418, May 2007. DOI 10.1085/jgp.200709758.

[64] C. Ader, R. Schneider, K. Seidel, M. Etzkorn, S. Becker, and M. Baldus. Structural rearrangements of membrane proteins probed by water-edited solid-state NMR spectroscopy. *J. Am. Chem. Soc.*, 131(1):170–176, Jan 2009. DOI 10.1021/ja806306e.

[65] K. K. Kumashiro, K. Schmidt-Rohr, O. J. Murphy, K. L. Ouellette, W. A. Cramer, and L. K. Thompson. A novel tool for probing membrane protein structure: Solid-state NMR with proton spin diffusion and X-nucleus detection. *J. Am. Chem. Soc.*, 120(20):5043–5051, May 1998. DOI 10.1021/ja972655e.

[66] M. Etzkorn, S. Martell, O. C. Andronesi, K. Seidel, M. Engelhard, and M. Baldus. Secondary structure, dynamics, and topology of a seven-helix receptor in native membranes, studied by solid-state NMR spectroscopy. *Angew. Chem. Int. Ed. Engl.*, 46(3):459–462, 2007. DOI 10.1002/anie.200602139.

[67] P. Keim, R. A. Vigna, J. S. Morrow, R. C. Marshall, and F. R. Gurd. Carbon 13 nuclear magnetic resonance of pentapeptides of glycine containing central residues of serine, threonine, aspartic and glutamic acids, asparagine, and glutamine. *J. Biol. Chem.*, 248(22):7811–7818, Nov 1973.

[68] Z. T. Gu and A. McDermott. Chemical shielding anisotropy of protonated and deprotonated carboxylates in amino-acids. *J. Am. Chem. Soc.*, 115(10):4282–4285, 1993. DOI 10.1021/ja00063a051.

[69] A. N. Thompson, D. J. Posson, P. V. Parsa, and C. M. Nimigean. Molecular mechanism of pH sensing in KcsA potassium channels. *Proc. Natl. Ac. Sci. USA*, 105(19):6900–6905, May 2008. DOI 10.1073/pnas.0800873105.

[70] M. P. Bhate and A. E. McDermott. Protonation state of E71 in KcsA and its role for channel collapse and inactivation. *Proc. Natl. Ac. Sci. USA*, 109:15265–15270, September 2012. DOI 10.1073/pnas.1211900109.

[71] J. F. Cordero-Morales, L. G. Cuello, and E. Perozo. Voltage-dependent gating at the KcsA selectivity filter. *Nat. Struct. Mol. Biol.*, 13(4):319–322, Apr 2006. DOI 10.1038/nsmb1070.

[72] R. S. Hurst, M. J. Roux, L. Toro, and E. Stefani. External barium influences the gating charge movement of Shaker potassium channels. *Biophys. J.*, 72(1):77–84, Jan 1997. DOI 10.1016/S0006-3495(97)78648-X.

[73] U. Zachariae, R. Schneider, P. Velisetty, A. Lange, D. Seeliger, S. J. Wacker, Y. Karimi-Nejad, G. Vriend, S. Becker, O. Pongs, M. Baldus, and B. L. de Groot. The molecular mechanism of toxin-induced conformational changes in a potassium channel: relation to C-type inactivation. *Structure*, 16(5):747–754, May 2008. DOI 10.1016/j.str.2008.01.018.

[74] M. P. Bhate, B. J. Wylie, L. Tian, and A. E. McDermott. Conformational dynamics in the selectivity filter of KcsA in response to potassium ion concentration. *J. Mol. Biol.*, 401: 155–166, August 2010. DOI 10.1016/j.jmb.2010.06.031.

[75] B. J. Wylie, M. P. Bhate, and A. E. McDermott. Transmembrane allosteric coupling of the gates in a potassium channel. *Proc. Natl. Ac. Sci. USA*, 111:185–190, January 2014. DOI 10.1073/pnas.1319577110.

[76] Y. Xu, M. P. Bhate, and A. E. McDermott. Transmembrane allosteric energetics characterization for strong coupling between proton and potassium ion binding in the KcsA channel. *Proc. Natl. Ac. Sci. USA*, 114:8788–8793, August 2017. DOI 10.1073/pnas.1701330114.

[77] S. Imai, M. Osawa, K. Takeuchi, and I. Shimada. Structural basis underlying the dual gate properties of KcsA. *Proc. Natl. Ac. Sci. USA*, 107:6216–6221, April 2010. DOI 10.1073/pnas.0911270107.

[78] L. G. Cuello, V. Jogini, D. M. Cortes, A. C. Pan, D. G. Gagnon, O. Dalmas, J. F. Cordero-Morales, S. Chakrapani, B. Roux, and E. Perozo. Structural basis for the coupling between activation and inactivation gates in K(+) channels. *Nature*, 466:272–275, July 2010. DOI 10.1038/nature09136.

[79] L. G. Cuello, V. Jogini, D. M. Cortes, and E. Perozo. Structural mechanism of C-type inactivation in K(+) channels. *Nature*, 466:203–208, July 2010. DOI 10.1038/nature09153.

[80] S. Uysal, L. G. Cuello, D. M. Cortes, S. Koide, A. A. Kossiakoff, and E. Perozo. Mechanism of activation gating in the full-length KcsA K+ channel. *Proc. Natl. Ac. Sci. USA*, 108: 11896–11899, July 2011. DOI 10.1073/pnas.1105112108.

[81] P. K. Devaraneni, A. G. Komarov, C. A. Costantino, J. J. Devereaux, K. Matulef, and F. I. Valiyaveetil. Semisynthetic K+ channels show that the constricted conformation of the selectivity filter is not the C-type inactivated state. *Proc. Natl. Ac. Sci. USA*, 110: 15698–15703, September 2013. DOI 10.1073/pnas.1308699110.

[82] T. Hoshi and C. M. Armstrong. C-type inactivation of voltage-gated K+ channels: pore constriction or dilation? *J. Gen. Physiol.*, 141:151–160, February 2013. DOI 10.1085/jgp.201210888.

[83] J. Li, J. Ostmeyer, E. Boulanger, H. Rui, E. Perozo, and B. Roux. Chemical substitutions in the selectivity filter of potassium channels do not rule out constricted-like conformations for C-type inactivation. *Proc. Natl. Ac. Sci. USA*, 114(42):11145–11150, October 2017. DOI 10.1073/pnas.1706983114.

[84] R. Schneider, K. Seidel, M. Etzkorn, A. Lange, S. Becker, and M. Baldus. Probing molecular motion by double-quantum (^{13}C,^{13}C) solid-state NMR spectroscopy: application to ubiquitin. *J. Am. Chem. Soc.*, 132(1):223–233, Jan 2010. DOI 10.1021/ja906283h.

[85] A. G. Palmer. NMR characterization of the dynamics of biomacromolecules. *Chem. Rev.*, 104(8):3623–3640, Aug 2004. DOI 10.1021/cr030413t.

[86] K. K. Frederick, M. S. Marlow, K. G. Valentine, and A. J. Wand. Conformational entropy in molecular recognition by proteins. *Nature*, 448:325–329, July 2007. DOI 10.1038/nature05959.

[87] S.-R. Tzeng and C. G. Kalodimos. Protein activity regulation by conformational entropy. *Nature*, 488:236–240, August 2012. DOI 10.1038/nature11271.

[88] A. G Palmer. Chemical exchange in biomacromolecules: past, present, and future. *J. Magn. Reson.*, 241:3–17, April 2014. DOI 10.1016/j.jmr.2014.01.008.

[89] E. Z. Eisenmesser, O. Millet, W. Labeikovsky, D. M. Korzhnev, M. Wolf-Watz, D. A. Bosco, J. J. Skalicky, L. E. Kay, and D. Kern. Intrinsic dynamics of an enzyme underlies catalysis. *Nature*, 438:117–121, November 2005. DOI 10.1038/nature04105.

[90] P. Neudecker, P. Robustelli, A. Cavalli, P. Walsh, P. Lundström, A. Zarrine-Afsar, S. Sharpe, M. Vendruscolo, and L. E. Kay. Structure of an intermediate state in protein folding and aggregation. *Science*, 336:362–366, April 2012. DOI 10.1126/science.1214203.

[91] M. Blackledge. Recent progress in the study of biomolecular structure and dynamics in solution from residual dipolar couplings. *Progr. NMR Spectr.*, 46(1):23–61, 2005. DOI 10.1016/j.pnmrs.2004.11.002.

[92] N. A. Lakomek, T. Carlomagno, S. Becker, C. Griesinger, and J. Meiler. A thorough dynamic interpretation of residual dipolar couplings in ubiquitin. *J. Biomol. NMR*, 34:101–115, February 2006. DOI 10.1007/s10858-005-5686-0.

[93] P. Schanda and M. Ernst. Studying dynamics by magic-angle spinning solid-state NMR spectroscopy: Principles and applications to biomolecules. *Progr. NMR Spectr.*, 96:1–46, August 2016. DOI 10.1016/j.pnmrs.2016.02.001.

[94] J. R. Lewandowski, H. J. Sass, S. Grzesiek, M. Blackledge, and L. Emsley. Site-specific measurement of slow motions in proteins. *J. Am. Chem. Soc.*, 133:16762–16765, October 2011. DOI 10.1021/ja206815h.

[95] J. D. Haller and P. Schanda. Amplitudes and time scales of picosecond-to-microsecond motion in proteins studied by solid-state NMR: a critical evaluation of experimental approaches and application to crystalline ubiquitin. *J. Biomol. NMR*, 57:263–280, November 2013. DOI 10.1007/s10858-013-9787-x.

[96] J. R. Lewandowski. Advances in solid-state relaxation methodology for probing site-specific protein dynamics. *Acc. Chem. Res.*, 46:2018–2027, September 2013. DOI 10.1021/ar300334g.

[97] J. L. Lorieau and A. E. McDermott. Conformational flexibility of a microcrystalline globular protein: order parameters by solid-state NMR spectroscopy. *J. Am. Chem. Soc.*, 128(35): 11505–11512, Sep 2006. DOI 10.1021/ja062443u.

[98] P. Schanda, B. H. Meier, and M. Ernst. Quantitative analysis of protein backbone dynamics in microcrystalline ubiquitin by solid-state NMR spectroscopy. *J. Am. Chem. Soc.*, 132: 15957–15967, November 2010. DOI 10.1021/ja100726a.

[99] K. Seidel, M. Etzkorn, L. Sonnenberg, C. Griesinger, A. Sebald, and M. Baldus. Studying molecular 3D structure and dynamics by high-resolution solid-state NMR: Application to L-tyrosine-ethylester. *J. Phys. Chem. A*, 109(11):2436–2442, Mar 2005. DOI 10.1021/jp045605m.

[100] X. Helluy and A. Sebald. Structure and dynamic properties of solid L-tyrosine-ethylester as seen by C-13 MAS NMR. *J. Phys. Chem. B*, 107(14):3290–3296, Apr 2003. DOI 10.1021/jp0277210.

[101] M. Hohwy, C. M. Rienstra, C. P. Jaroniec, and R. G. Griffin. Fivefold symmetric homonuclear dipolar recoupling in rotating solids: Application to double quantum spectroscopy. *J. Chem. Phys.*, 110(16):7983–7992, Apr 1999. DOI 10.1063/1.478702.

[102] S. A. Smith, T. O. Levante, B. H. Meier, and R. R. Ernst. Computer simulations in magnetic resonance. An object-oriented programming approach. *J. Magn. Reson. A*, 106(1):75–105, Jan 1994. DOI 10.1006/jmra.1994.1008.

[103] J. D. van Beek. matNMR: a flexible toolbox for processing, analyzing and visualizing magnetic resonance data in Matlab. *J. Magn. Reson.*, 187(1):19–26, Jul 2007. DOI 10.1016/j.jmr.2007.03.017. URL `http://matnmr.sourceforge.net/`.

[104] R. W. Martin and K. W. Zilm. Preparation of protein nanocrystals and their characterization by solid state NMR. *J. Magn. Reson.*, 165(1):162–174, Nov 2003. DOI 10.1016/S1090-7807(03)00253-2.

[105] A. Böckmann, A. Lange, A. Galinier, S. Luca, N. Giraud, M. Juy, H. Heise, R. Montserret, F. Penin, and M. Baldus. Solid state NMR sequential resonance assignments and conformational analysis of the 2x10.4 kDa dimeric form of the Bacillus subtilis protein Crh. *J. Biomol. NMR*, 27(4):323–339, Dec 2003. DOI 10.1023/A:1025820611009.

[106] K. Seidel, M. Etzkorn, H. Heise, S. Becker, and M. Baldus. High-resolution solid-state NMR studies on uniformly [^{13}C,^{15}N]-labeled ubiquitin. *ChemBioChem*, 6(9):1638–1647, Sep 2005. DOI 10.1002/cbic.200500085.

[107] A. Hershko and A. Ciechanover. The ubiquitin system. *Annu. Rev. Biochem.*, 67:425–479, 1998. DOI 10.1146/annurev.biochem.67.1.425.

[108] C. M. Pickart and M. J. Eddins. Ubiquitin: structures, functions, mechanisms. *Biochim. Biophys. Acta*, 1695(1-3):55–72, Nov 2004. DOI 10.1016/j.bbamcr.2004.09.019.

[109] N. Tjandra, S. E. Feller, R. W. Pastor, and A. Bax. Rotational diffusion anisotropy of human ubiquitin from N-15 NMR relaxation. *J. Am. Chem. Soc.*, 117(50):12562–12566, Dec 1995. DOI 10.1021/ja00155a020.

[110] G. Cornilescu, J. L. Marquardt, M. Ottiger, and A. Bax. Validation of protein structure from anisotropic carbonyl chemical shifts in a dilute liquid crystalline phase. *J. Am. Chem. Soc.*, 120(27):6836–6837, Jul 1998. DOI 10.1021/ja9812610.

[111] S. G. Zech, A. J. Wand, and A. E. McDermott. Protein structure determination by high-resolution solid-state NMR spectroscopy: application to microcrystalline ubiquitin. *J. Am. Chem. Soc.*, 127(24):8618–8626, Jun 2005. DOI 10.1021/ja0503128.

[112] S. Vijay-Kumar, C. E. Bugg, and W. J. Cook. Structure of ubiquitin refined at 1.8 Å resolution. *J. Mol. Biol.*, 194(3):531–544, Apr 1987. DOI 10.1016/0022-2836(87)90679-6.

[113] J. Kuszewski, C. D. Schwieters, D. S. Garrett, R. A. Byrd, N. Tjandra, and G. M. Clore. Completely automated, highly error-tolerant macromolecular structure determination from multidimensional nuclear Overhauser enhancement spectra and chemical shift assignments. *J. Am. Chem. Soc.*, 126(20):6258–6273, May 2004. DOI 10.1021/ja049786h.

[114] C. D. Schwieters, J. J. Kuszewski, and G. M. Clore. Using Xplor-NIH for NMR molecular structure determination. *Progr. NMR Spectr.*, 48(1):47–62, 2006. DOI 10.1016/j.pnmrs.2005.10.001.

[115] C. D. Schwieters, J. J. Kuszewski, N. Tjandra, and G. M. Clore. The Xplor-NIH NMR molecular structure determination package. *J. Magn. Reson.*, 160(1):65–73, Jan 2003. DOI 10.1016/S1090-7807(02)00014-9.

[116] G. Cornilescu, F. Delaglio, and A. Bax. Protein backbone angle restraints from searching a database for chemical shift and sequence homology. *J. Biomol. NMR*, 13(3):289–302, Mar 1999. DOI 10.1023/A:1008392405740.

[117] A. Loquet, B. Bardiaux, C. Gardiennet, C. Blanchet, M. Baldus, M. Nilges, T. Malliavin, and A. Böckmann. 3D structure determination of the Crh protein from highly ambiguous solid-state NMR restraints. *J. Am. Chem. Soc.*, 130(11):3579–3589, Mar 2008. DOI 10.1021/ja078014t.

[118] R. Koradi, M. Billeter, and K. Wüthrich. MOLMOL: A program for display and analysis of macromolecular structures. *J. Mol. Graph.*, 14(1):51, Feb 1996. DOI 10.1016/0263-7855(96)00009-4.

[119] W. L. DeLano. The PyMOL Molecular Graphics System. DeLano Scientific, Palo Alto, CA, USA, 2002. URL `http://www.pymol.org`.

[120] A. Majumdar and R. Ghose. Probing slow backbone dynamics in proteins using TROSY-based experiments to detect cross-correlated time-modulation of isotropic chemical shifts. *J. Biomol. NMR*, 28(3):213–227, 2004. DOI 10.1023/B:JNMR.0000013705.98136.99.

[121] F. Massi, M. J. Grey, and A. G. Palmer. Microsecond timescale backbone conformational dynamics in ubiquitin studied with NMR R-1p relaxation experiments. *Prot. Sci.*, 14(3): 735–742, 2005. DOI 10.1110/ps.041139505.

[122] O. F. Lange, N.-A. Lakomek, C. Farès, G. F. Schröder, K. F. A. Walter, S. Becker, J. Meiler, H. Grubmüller, C. Griesinger, and B. L. de Groot. Recognition dynamics up to microseconds revealed from an RDC-derived ubiquitin ensemble in solution. *Science*, 320(5882):1471–1475, Jun 2008. DOI 10.1126/science.1157092.

[123] M. Tollinger, A. C. Sivertsen, B. H. Meier, M. Ernst, and P. Schanda. Site-resolved measurement of microsecond-to-millisecond conformational-exchange processes in proteins by solid-state NMR spectroscopy. *J. Am. Chem. Soc.*, 134:14800–14807, September 2012. ISSN 1520-5126. DOI 10.1021/ja303591y.

[124] K. Y. Huang, G. A. Amodeo, L. Tong, and A. McDermott. The structure of human ubiquitin in 2-methyl-2,4-pentanediol: a new conformational switch. *Prot. Sci.*, 20:630–639, March 2011. DOI 10.1002/pro.584.

[125] R. Benz. Permeation of hydrophilic solutes through mitochondrial outer membranes: review on mitochondrial porins. *Biochim. Biophys. Acta*, 1197:167–196, June 1994. DOI 10.1016/0304-4157(94)90004-3.

[126] M. Colombini. VDAC: the channel at the interface between mitochondria and the cytosol. *Mol. Cell. Biochem.*, 256-257:107–115, 2004. DOI 10.1023/B:MCBI.0000009862.17396.8d.

[127] V. Shoshan-Barmatz, N. Keinan, and H. Zaid. Uncovering the role of VDAC in the regulation of cell life and death. *J. Bioenerg. Biomembr.*, 40:183–191, June 2008. DOI 10.1007/s10863-008-9147-9.

[128] V. Shoshan-Barmatz, V. De Pinto, M. Zweckstetter, Z. Raviv, N. Keinan, and N. Arbel. VDAC, a multi-functional mitochondrial protein regulating cell life and death. *Mol. Aspects Med.*, 31:227–285, June 2010. DOI 10.1016/j.mam.2010.03.002.

[129] S. J. Schein, M. Colombini, and A. Finkelstein. Reconstitution in planar lipid bilayers of a voltage-dependent anion-selective channel obtained from paramecium mitochondria. *J. Membr. Biol.*, 30:99–120, December 1976. DOI 10.1007/BF01869662.

[130] V. De Pinto, S. Reina, F. Guarino, and A. Messina. Structure of the voltage dependent anion channel: state of the art. *J. Bioenerg. Biomembr.*, 40:139–147, June 2008. DOI 10.1007/s10863-008-9140-3.

[131] J. Song, C. Midson, E. Blachly-Dyson, M. Forte, and M. Colombini. The topology of VDAC as probed by biotin modification. *J. Biol. Chem.*, 273:24406–24413, September 1998. DOI 10.1074/jbc.273.38.24406.

[132] S. Hiller, R. G. Garces, T. J. Malia, V. Y. Orekhov, M. Colombini, and G. Wagner. Solution structure of the integral human membrane protein VDAC-1 in detergent micelles. *Science*, 321(5893):1206–1210, Aug 2008. DOI 10.1126/science.1161302.

[133] M. Bayrhuber, T. Meins, M. Habeck, S. Becker, K. Giller, S. Villinger, C. Vonrhein, C. Griesinger, M. Zweckstetter, and K. Zeth. Structure of the human voltage-dependent anion channel. *Proc. Natl. Ac. Sci. USA*, 105(40):15370–15375, Oct 2008. DOI 10.1073/pnas.0808115105.

[134] R. Ujwal, D. Cascio, J.-P. Colletier, S. Faham, J. Zhang, L. Toro, P. Ping, and J. Abramson. The crystal structure of mouse VDAC1 at 2.3 Å resolution reveals mechanistic insights into metabolite gating. *Proc. Natl. Ac. Sci. USA*, 105(46):17742–17747, Nov 2008. DOI 10.1073/pnas.0809634105.

[135] M. Colombini. Voltage gating in the mitochondrial channel, VDAC. *J. Membr. Biol.*, 111: 103–111, October 1989. DOI 10.1007/BF01871775.

[136] T. K. Rostovtseva, W. Tan, and M. Colombini. On the role of VDAC in apoptosis: fact and fiction. *J. Bioenerg. Biomembr.*, 37:129–142, June 2005. DOI 10.1007/s10863-005-6566-8.

[137] S. Abu-Hamad, N. Arbel, D. Calo, L. Arzoine, A. Israelson, N. Keinan, R. Ben-Romano, O. Friedman, and V. Shoshan-Barmatz. The VDAC1 N-terminus is essential both for apoptosis and the protective effect of anti-apoptotic proteins. *J. Cell Sci.*, 122:1906–1916, June 2009. DOI 10.1242/jcs.040188.

[138] L. Thomas, E. Blachly-Dyson, M. Colombini, and M. Forte. Mapping of residues forming the voltage sensor of the voltage-dependent anion-selective channel. *Proc. Natl. Ac. Sci. USA*, 90:5446–5449, June 1993.

[139] J. Song, C. Midson, E. Blachly-Dyson, M. Forte, and M. Colombini. The sensor regions of VDAC are translocated from within the membrane to the surface during the gating processes. *Biophys. J.*, 74:2926–2944, June 1998. DOI 10.1016/S0006-3495(98)78000-2.

[140] R. Schneider, M. Etzkorn, K. Giller, V. Daebel, J. Eisfeld, M. Zweckstetter, C. Griesinger, S. Becker, and A. Lange. The native conformation of the human VDAC1 N terminus. *Angew. Chem. Int. Ed.*, 49(10):1882–1885, Mar 2010. DOI 10.1002/anie.200906241.

[141] U. Zachariae, R. Schneider, R. Briones, Z. Gattin, J.-P. Demers, K. Giller, E. Maier, M. Zweckstetter, C. Griesinger, S. Becker, R. Benz, B. L. de Groot, and A. Lange. β-barrel mobility underlies closure of the voltage-dependent anion channel. *Structure*, 20(9): 1540–1549, Sep 2012. DOI 10.1016/j.str.2012.06.015.

[142] H. Engelhardt, T. Meins, M. Poynor, V. Adams, S. Nussberger, W. Welte, and K. Zeth. High-level expression, refolding and probing the natural fold of the human voltage-dependent anion channel isoforms I and II. *J. Membr. Biol.*, 216:93–105, April 2007. DOI 10.1007/s00232-007-9038-8.

[143] R. Verel, M. Ernst, and B. H. Meier. Adiabatic dipolar recoupling in solid-state NMR: the DREAM scheme. *J. Magn. Reson.*, 150:81–99, May 2001. DOI 10.1006/jmre.2001.2310.

[144] B. Popp, D. A. Court, R. Benz, W. Neupert, and R. Lill. The role of the N and C termini of recombinant Neurospora mitochondrial porin in channel formation and voltage-dependent gating. *J. Biol. Chem.*, 271:13593–13599, June 1996. DOI 10.1074/jbc.271.23.13593.

[145] D. A. Koppel, K. W. Kinnally, P. Masters, M. Forte, E. Blachly-Dyson, and C. A. Mannella. Bacterial expression and characterization of the mitochondrial outer membrane channel. Effects of n-terminal modifications. *J. Biol. Chem.*, 273:13794–13800, May 1998. DOI 10.1074/jbc.273.22.13794.

[146] J. Zimmerberg and V. A. Parsegian. Polymer inaccessible volume changes during opening and closing of a voltage-dependent ionic channel. *Nature*, 323:36–39, 1986. DOI 10.1038/323036a0.

[147] S. Peng, E. Blachly-Dyson, M. Forte, and M. Colombini. Large scale rearrangement of protein domains is associated with voltage gating of the VDAC channel. *Biophys. J.*, 62:123–31, April 1992. DOI 10.1016/S0006-3495(92)81799-X.

[148] Om P. Choudhary, Rachna Ujwal, William Kowallis, Rob Coalson, Jeff Abramson, and Michael Grabe. The electrostatics of vdac: implications for selectivity and gating. *J Mol Biol*, 396(3):580–592, Feb 2010. DOI 10.1016/j.jmb.2009.12.006.

[149] C. A. Mannella. Minireview: on the structure and gating mechanism of the mitochondrial channel, VDAC. *J. Bioenerg. Biomembr.*, 29:525–531, December 1997. DOI 10.1023/A:1022489832594.

[150] T. K. Rostovtseva, N. Kazemi, M. Weinrich, and S. M. Bezrukov. Voltage gating of VDAC is regulated by nonlamellar lipids of mitochondrial membranes. *J. Biol. Chem.*, 281:37496–37506, December 2006. DOI 10.1074/jbc.M602548200.

[151] S. Villinger, R. Briones, K. Giller, U. Zachariae, A. Lange, B. L. de Groot, C. Griesinger, S. Becker, and M. Zweckstetter. Functional dynamics in the voltage-dependent anion channel. *Proc. Natl. Ac. Sci. USA*, 107:22546–22551, December 2010. DOI 10.1073/pnas.1012310108.

[152] G. Runke, E. Maier, W. A. T. Summers, D. C. Bay, R. Benz, and D. A. Court. Deletion variants of Neurospora mitochondrial porin: electrophysiological and spectroscopic analysis. *Biophys. J.*, 90:3155–3164, May 2006. DOI 10.1529/biophysj.105.072520.

[153] B. Martinac, M. Buechner, A. H. Delcour, J. Adler, and C. Kung. Pressure-sensitive ion channel in Escherichia coli. *Proc. Natl. Ac. Sci. USA*, 84:2297–2301, April 1987.

[154] S. Sukharev. Purification of the small mechanosensitive channel of Escherichia coli (MscS): the subunit structure, conduction, and gating characteristics in liposomes. *Biophys. J.*, 83:290–298, July 2002. DOI 10.1016/S0006-3495(02)75169-2.

[155] C. Kutzner, H. Grubmüller, B. L. de Groot, and U. Zachariae. Computational electrophysiology: the molecular dynamics of ion channel permeation and selectivity in atomistic detail. *Biophys. J.*, 101:809–817, August 2011. DOI 10.1016/j.bpj.2011.06.010.

[156] V. De Pinto, G. Prezioso, F. Thinnes, T. A. Link, and F. Palmieri. Peptide-specific antibodies and proteases as probes of the transmembrane topology of the bovine heart mitochondrial porin. *Biochemistry*, 30:10191–10200, October 1991. DOI 10.1021/bi00106a017.

[157] X. W. Guo, P. R. Smith, B. Cognon, D. D'Arcangelis, E. Dolginova, and C. A. Mannella. Molecular design of the voltage-dependent, anion-selective channel in the mitochondrial outer membrane. *J. Struct. Biol.*, 114:41–59, 1995. DOI 10.1006/jsbi.1995.1004.

[158] S. Geula, D. Ben-Hail, and V. Shoshan-Barmatz. Structure-based analysis of VDAC1: N-terminus location, translocation, channel gating and association with anti-apoptotic proteins. *Biochem. J.*, 444:475–485, June 2012. DOI 10.1042/BJ20112079.

[159] M. Colombini. The published 3D structure of the VDAC channel: native or not? *Trends Biochem. Sci.*, 34:382–389, August 2009. DOI 10.1016/j.tibs.2009.05.001.

[160] S. Hiller, J. Abramson, C. Mannella, G. Wagner, and K. Zeth. The 3D structures of VDAC represent a native conformation. *Trends Biochem. Sci.*, 35:514–521, September 2010. DOI 10.1016/j.tibs.2010.03.005.

[161] Oscar Teijido, Rachna Ujwal, Carl-Olof Hillerdal, Lisen Kullman, Tatiana K. Rostovtseva, and Jeff Abramson. Affixing n-terminal α-helix to the wall of the voltage-dependent anion channel does not prevent its voltage gating. *J Biol Chem*, 287(14):11437–11445, Mar 2012. DOI 10.1074/jbc.M111.314229.

[162] B. Mertins, G. Psakis, W. Grosse, K. C. Back, A. Salisowski, P. Reiss, U. Koert, and L.-O. Essen. Flexibility of the N-terminal mVDAC1 segment controls the channel's gating behavior. *PLoS ONE*, 7:e47938, 2012. DOI 10.1371/journal.pone.0047938.

[163] R. Schneider, D. Maurin, G. Communie, J. Kragelj, D. F. Hansen, R. W. H. Ruigrok, M. Ringkjøbing Jensen, and M. Blackledge. Visualizing the molecular recognition trajectory of an intrinsically disordered protein using multinuclear relaxation dispersion NMR. *J. Am. Chem. Soc.*, 137(3):1220–1229, Jan 2015. DOI 10.1021/ja511066q.

[164] A. K. Dunker, J. D. Lawson, C. J. Brown, R. M. Williams, P. Romero, J. S. Oh, C. J. Oldfield, A. M. Campen, C. M. Ratliff, K. W. Hipps, J. Ausio, M. S. Nissen, R. Reeves, C. Kang, C. R. Kissinger, R. W. Bailey, M. D. Griswold, W. Chiu, E. C. Garner, and Z. Obradovic. Intrinsically disordered protein. *J. Mol. Graph. Model.*, 19:26–59, 2001. DOI 10.1016/S1093-3263(00)00138-8.

[165] R. S. Spolar and M. T. Record. Coupling of local folding to site-specific binding of proteins to DNA. *Science*, 263:777–784, February 1994. DOI 10.1126/science.8303294.

[166] R. W. Kriwacki, L. Hengst, L. Tennant, S. I. Reed, and P. E. Wright. Structural studies of p21Waf1/Cip1/Sdi1 in the free and Cdk2-bound state: conformational disorder mediates binding diversity. *Proc. Natl. Ac. Sci. USA*, 93:11504–11509, October 1996.

[167] P. E. Wright and H. J. Dyson. Intrinsically unstructured proteins: re-assessing the protein structure-function paradigm. *J. Mol. Biol.*, 293:321–331, October 1999. DOI 10.1006/jmbi.1999.3110.

[168] A. K. Dunker, Z. Obradovic, P. Romero, E. C. Garner, and C. J. Brown. Intrinsic protein disorder in complete genomes. *Genome informatics. Workshop on Genome Informatics*, 11:161–171, 2000. URL `http://www.dabi.temple.edu/~zoran/papers/dunker00.pdf`.

[169] B. Xue, A. K. Dunker, and V. N. Uversky. Orderly order in protein intrinsic disorder distribution: disorder in 3500 proteomes from viruses and the three domains of life. *J. Biomol. Struct. Dyn.*, 30:137–149, 2012. DOI 10.1080/07391102.2012.675145.

[170] A. K. Dunker, C. J. Brown, J. D. Lawson, L. M. Iakoucheva, and Z. Obradovic. Intrinsic disorder and protein function. *Biochemistry*, 41(21):6573–6582, May 2002. DOI 10.1021/bi012159+.

[171] P. E. Wright and H. J. Dyson. Intrinsically disordered proteins in cellular signalling and regulation. *Nat. Rev. Mol. Cell. Biol.*, 16:18–29, January 2015. ISSN 1471-0080. DOI 10.1038/nrm3920.

[172] A. Molliex, J. Temirov, J. Lee, M. Coughlin, A. P. Kanagaraj, H. J. Kim, T. Mittag, and J. P. Taylor. Phase separation by low complexity domains promotes stress granule assembly and drives pathological fibrillization. *Cell*, 163:123–133, September 2015. DOI 10.1016/j.cell.2015.09.015.

[173] V. N. Uversky. Protein intrinsic disorder-based liquid-liquid phase transitions in biological systems: Complex coacervates and membrane-less organelles. *Adv. Colloid Interface Sci.*, 239:97–114, January 2017. DOI 10.1016/j.cis.2016.05.012.

[174] S. Chakrabortee, J. S. Byers, S. Jones, D. M. Garcia, B. Bhullar, A. Chang, R. She, L. Lee, B. Fremin, S. Lindquist, and D. F. Jarosz. Intrinsically disordered proteins drive emergence and inheritance of biological traits. *Cell*, 167:369–381.e12, October 2016. DOI 10.1016/j.cell.2016.09.017.

[175] T. C. Boothby, H. Tapia, A. H. Brozena, S. Piszkiewicz, A. E. Smith, I. Giovannini, L. Rebecchi, G. J. Pielak, D. Koshland, and B. Goldstein. Tardigrades use intrinsically disordered proteins to survive desiccation. *Mol. Cell*, 65:975–984.e5, March 2017. DOI 10.1016/j.molcel.2017.02.018.

[176] S. Milles, D. Mercadante, I. V. Aramburu, M. Ringkjøbing Jensen, N. Banterle, C. Koehler, S. Tyagi, J. Clarke, S. L. Shammas, M. Blackledge, F. Gräter, and E. A. Lemke. Plasticity of an ultrafast interaction between nucleoporins and nuclear transport receptors. *Cell*, 163: 734–745, October 2015. DOI 10.1016/j.cell.2015.09.047.

[177] V. N. Uversky, C. J. Oldfield, and A. K. Dunker. Intrinsically disordered proteins in human diseases: introducing the D2 concept. *Annu. Rev. Biophys.*, 37:215–246, 2008. DOI 10.1146/annurev.biophys.37.032807.125924.

[178] N. Krishnan, D. Koveal, D. H. Miller, B. Xue, S. D. Akshinthala, J. Kragelj, M. Ringkjøbing Jensen, C.-M. Gauss, R. Page, M. Blackledge, S. K. Muthuswamy, W. Peti, and N. K. Tonks. Targeting the disordered C terminus of PTP1B with an allosteric inhibitor. *Nat. Chem. Biol.*, 10:558–566, July 2014. DOI 10.1038/nchembio.1528.

[179] J. L. Neira, J. Bintz, M. Arruebo, B. Rizzuti, T. Bonacci, S. Vega, A. Lanas, A. Velázquez-Campoy, J. L. Iovanna, and O. Abián. Identification of a drug targeting an intrinsically disordered protein involved in pancreatic adenocarcinoma. *Sci. Rep.*, 7:39732, January 2017. DOI 10.1038/srep39732.

[180] R. A. V. Morales, C. A. MacRaild, J. Seow, B. Krishnarjuna, N. Drinkwater, R. Rouet, R. F. Anders, D. Christ, S. McGowan, and R. S. Norton. Structural basis for epitope masking and strain specificity of a conserved epitope in an intrinsically disordered malaria vaccine candidate. *Sci. Rep.*, 5:10103, May 2015. DOI 10.1038/srep10103.

[181] M. Fuxreiter, I. Simon, P. Friedrich, and P. Tompa. Preformed structural elements feature in partner recognition by intrinsically unstructured proteins. *J. Mol. Biol.*, 338:1015–1026, May 2004. DOI 10.1016/j.jmb.2004.03.017.

[182] L. Salmon, G. Nodet, V. Ozenne, G. Yin, M. Ringkjøbing Jensen, M. Zweckstetter, and M. Blackledge. NMR characterization of long-range order in intrinsically disordered proteins. *J. Am. Chem. Soc.*, 132:8407–8418, June 2010. DOI 10.1021/ja101645g.

[183] P. Tompa and M. Fuxreiter. Fuzzy complexes: polymorphism and structural disorder in protein-protein interactions. *Trends Biochem. Sci.*, 33:2–8, January 2008. DOI 10.1016/j.tibs.2007.10.003.

[184] K. Van Roey, T. J. Gibson, and N. E. Davey. Motif switches: decision-making in cell regulation. *Curr. Opin. Struct. Biol.*, 22:378–385, June 2012. DOI 10.1016/j.sbi.2012.03.004.

[185] P. Tompa, N. E. Davey, T. J. Gibson, and M. M. Babu. A million peptide motifs for the molecular biologist. *Mol. Cell*, 55:161–169, July 2014. DOI 10.1016/j.molcel.2014.05.032.

[186] H. J. Dyson and P. E. Wright. Coupling of folding and binding for unstructured proteins. *Curr. Opin. Struct. Biol.*, 12:54–60, February 2002. DOI 10.1016/S0959-440X(02)00289-0.

[187] F. Karush. Heterogeneity of the binding sites of bovine serum albumin. *J. Am. Chem. Soc.*, 72(6):2705–2713, 1950. DOI 10.1021/ja01162a099.

[188] B. Ma, S. Kumar, C. J. Tsai, and R. Nussinov. Folding funnels and binding mechanisms. *Protein Eng.*, 12:713–720, September 1999. DOI 10.1093/protein/12.9.713.

[189] D. E. Koshland. Application of a theory of enzyme specificity to protein synthesis. *Proc. Natl. Ac. Sci. USA*, 44:98–104, February 1958.

[190] P. Csermely, R. Palotai, and R. Nussinov. Induced fit, conformational selection and independent dynamic segments: an extended view of binding events. *Trends Biochem. Sci.*, 35:539–546, October 2010. DOI 10.1016/j.tibs.2010.04.009.

[191] H.-X. Zhou. Intrinsic disorder: signaling via highly specific but short-lived association. *Trends Biochem. Sci.*, 37:43–48, February 2012. DOI 10.1016/j.tibs.2011.11.002.

[192] P. Tompa, C. Szász, and L. Buday. Structural disorder throws new light on moonlighting. *Trends Biochem. Sci.*, 30:484–489, September 2005. DOI 10.1016/j.tibs.2005.07.008.

[193] P. Tompa. Unstructural biology coming of age. *Curr. Opin. Struct. Biol.*, 21:419–425, June 2011. DOI 10.1016/j.sbi.2011.03.012.

[194] A. K. Dunker and C. J. Oldfield. Back to the future: Nuclear magnetic resonance and bioinformatics studies on intrinsically disordered proteins. *Adv. Exp. Med. Biol.*, 870:1–34, 2015. DOI 10.1007/978-3-319-20164-1_1.

[195] R. Schneider, J.-R. Huang, M. Yao, G. Communie, V. Ozenne, L. Mollica, L. Salmon, M. Ringkjøbing Jensen, and M. Blackledge. Towards a robust description of intrinsic protein disorder using nuclear magnetic resonance spectroscopy. *Mol BioSyst*, 8(1):58–68, Jan 2012. DOI 10.1039/c1mb05291h.

[196] M. Ringkjøbing Jensen, M. Zweckstetter, J.-R. Huang, and M. Blackledge. Exploring free-energy landscapes of intrinsically disordered proteins at atomic resolution using NMR spectroscopy. *Chem. Rev.*, 114:6632–6660, July 2014. DOI 10.1021/cr400688u.

[197] V. Ozenne, R. Schneider, M. Yao, J.-R. Huang, L. Salmon, M. Zweckstetter, M. Ringkjøbing Jensen, and M. Blackledge. Mapping the potential energy landscape of intrinsically disordered proteins at amino acid resolution. *J. Am. Chem. Soc.*, 134(36): 15138–15148, Sep 2012. DOI 10.1021/ja306905s.

[198] A. J. Baldwin and L. E. Kay. NMR spectroscopy brings invisible protein states into focus. *Nat. Chem. Biol.*, 5:808–814, November 2009. DOI 10.1038/nchembio.238.

[199] K. Sugase, H. J. Dyson, and P. E. Wright. Mechanism of coupled folding and binding of an intrinsically disordered protein. *Nature*, 447:1021–1025, June 2007. ISSN 1476-4687. DOI 10.1038/nature05858.

[200] J. Curran, H. Homann, C. Buchholz, S. Rochat, W. Neubert, and D. Kolakofsky. The hypervariable C-terminal tail of the Sendai paramyxovirus nucleocapsid protein is required for template function but not for RNA encapsidation. *J. Virol.*, 67:4358–4364, July 1993.

[201] M. Ringkjøbing Jensen, K. Houben, E. Lescop, L. Blanchard, R. W. H. Ruigrok, and M. Blackledge. Quantitative conformational analysis of partially folded proteins from residual dipolar couplings: application to the molecular recognition element of Sendai virus nucleoprotein. *J. Am. Chem. Soc.*, 130(25):8055–8061, Jun 2008. DOI 10.1021/ja801332d.

[202] D. F. Hansen, P. Vallurupalli, and L. E. Kay. An improved 15N relaxation dispersion experiment for the measurement of millisecond time-scale dynamics in proteins. *J. Phys. Chem. B*, 112:5898–5904, May 2008. DOI 10.1021/jp074793o.

[203] P. Lundström, D. F. Hansen, and L. E. Kay. Measurement of carbonyl chemical shifts of excited protein states by relaxation dispersion NMR spectroscopy: comparison between uniformly and selectively (13)C labeled samples. *J. Biomol. NMR*, 42:35–47, September 2008. DOI 10.1007/s10858-008-9260-4.

[204] R. Ishima and D. A. Torchia. Extending the range of amide proton relaxation dispersion experiments in proteins using a constant-time relaxation-compensated CPMG approach. *J. Biomol. NMR*, 25:243–248, March 2003. DOI 10.1023/A:1022851228405.

[205] D. F. Hansen, P. Vallurupalli, P. Lundström, P. Neudecker, and L. E. Kay. Probing chemical shifts of invisible states of proteins with relaxation dispersion NMR spectroscopy: how well can we do? *J. Am. Chem. Soc.*, 130:2667–2675, February 2008. DOI 10.1021/ja078337p.

[206] D. M. Korzhnev, P. Neudecker, A. Mittermaier, V. Y. Orekhov, and L. E. Kay. Multiple-site exchange in proteins studied with a suite of six NMR relaxation dispersion experiments: an application to the folding of a Fyn SH3 domain mutant. *J. Am. Chem. Soc.*, 127:15602–15611, November 2005. DOI 10.1021/ja054550e.

[207] J. P. Carver and R. E. Richards. A general two-site solution for the chemical exchange produced dependence of T_2 upon the carr-Purcell pulse separation. *J. Magn. Reson.*, 6: 89–105, 1972. DOI 10.1016/0022-2364(72)90090-X.

[208] D. M. Korzhnev, X. Salvatella, M. Vendruscolo, A. A. Di Nardo, A. R. Davidson, C. M. Dobson, and L. E. Kay. Low-populated folding intermediates of Fyn SH3 characterized by relaxation dispersion NMR. *Nature*, 430:586–590, July 2004. DOI 10.1038/nature02655.

[209] N. R. Skrynnikov, F. W. Dahlquist, and L. E. Kay. Reconstructing NMR spectra of "invisible" excited protein states using HSQC and HMQC experiments. *J. Am. Chem. Soc.*, 124: 12352–12360, October 2002. DOI 10.1021/ja0207089.

[210] H. Zhang, S. Neal, and D. S. Wishart. RefDB: a database of uniformly referenced protein chemical shifts. *J. Biomol. NMR*, 25(3):173–195, Mar 2003. DOI 10.1023/A:1022836027055.

[211] K. Houben, L. Blanchard, M. Blackledge, and D. Marion. Intrinsic dynamics of the partly unstructured PX domain from the Sendai virus RNA polymerase cofactor P. *Biohpys. J.*, 93:2830–2844, October 2007. DOI 10.1529/biophysj.107.108829.

[212] M. Kjaergaard, K. Teilum, and F. M. Poulsen. Conformational selection in the molten globule state of the nuclear coactivator binding domain of CBP. *Proc. Natl. Ac. Sci. USA*, 107:12535–12540, July 2010. DOI 10.1073/pnas.1001693107.

[213] M. Dosnon, D. Bonetti, A. Morrone, J. Erales, E. di Silvio, S. Longhi, and S. Gianni. Demonstration of a folding after binding mechanism in the recognition between the measles virus NTAIL and X domains. *ACS Chem. Biol.*, 10:795–802, March 2015. DOI 10.1021/cb5008579.

[214] T. Kiefhaber, A. Bachmann, and K. S. Jensen. Dynamics and mechanisms of coupled protein folding and binding reactions. *Curr. Opin. Struct. Biol.*, 22:21–29, February 2012. DOI 10.1016/j.sbi.2011.09.010.

[215] B. A. Shoemaker, J. J. Portman, and P. G. Wolynes. Speeding molecular recognition by using the folding funnel: the fly-casting mechanism. *Proc. Natl. Ac. Sci. USA*, 97:8868–8873, August 2000. DOI 10.1073/pnas.160259697.

[216] V. Iešmantavičius, J. Dogan, P. Jemth, K. Teilum, and M. Kjaergaard. Helical propensity in an intrinsically disordered protein accelerates ligand binding. *Angew. Chem. Int. Ed.*, 53: 1548–1551, February 2014. DOI 10.1002/anie.201307712.

[217] J. M. Rogers, C. T. Wong, and J. Clarke. Coupled folding and binding of the disordered protein PUMA does not require particular residual structure. *J. Am. Chem. Soc.*, 136: 5197–5200, April 2014. DOI 10.1021/ja4125065.

[218] F. Jacob-Dubuisson, J. Guérin, S. Baelen, and B. Clantin. Two-partner secretion: as simple as it sounds? *Res. Microbiol.*, 164:583–595, 2013. DOI 10.1016/j.resmic.2013.03.009.

[219] E Heinz and T. Lithgow. A comprehensive analysis of the Omp85/TpsB protein superfamily structural diversity, taxonomic occurrence, and evolution. *Front. Microbiol.*, 5:370, 2014. DOI 10.3389/fmicb.2014.00370.

[220] D. P. Ricci and T. J. Silhavy. The Bam machine: a molecular cooper. *Biochim. Biophys. Acta*, 1818:1067–1084, April 2012. DOI 10.1016/j.bbamem.2011.08.020.

[221] J. A. Melvin, E. V. Scheller, J. F. Miller, and P. A. Cotter. Bordetella pertussis pathogenesis: current and future challenges. *Nat. Rev. Microbiol.*, 12:274–288, April 2014. DOI 10.1038/nrmicro3235.

[222] B. Clantin, A.-S. Delattre, P. Rucktooa, N. Saint, A. C. Méli, C. Locht, F. Jacob-Dubuisson, and V. Villeret. Structure of the membrane protein FhaC: a member of the Omp85-TpsB transporter superfamily. *Science*, 317:957–961, August 2007. ISSN 1095-9203. DOI 10.1126/science.1143860.

[223] T. Maier, B. Clantin, F. Gruss, F. Dewitte, A.-S. Delattre, F. Jacob-Dubuisson, S. Hiller, and V. Villeret. Conserved Omp85 lid-lock structure and substrate recognition in FhaC. *Nat. Commun.*, 6:7452, June 2015. DOI 10.1038/ncomms8452.

[224] A.-S. Delattre, N. Saint, B. Clantin, E. Willery, G. Lippens, C. Locht, V. Villeret, and F. Jacob-Dubuisson. Substrate recognition by the POTRA domains of TpsB transporter FhaC. *Mol. Microbiol.*, 81:99–112, July 2011. DOI 10.1111/j.1365-2958.2011.07680.x.

[225] A.-S. Delattre, B. Clantin, N. Saint, C. Locht, V. Villeret, and F. Jacob-Dubuisson. Functional importance of a conserved sequence motif in FhaC, a prototypic member of the TpsB/Omp85 superfamily. *FEBS J.*, 277:4755–4765, November 2010. DOI 10.1111/j.1742-4658.2010.07881.x.

[226] B. Clantin, H. Hodak, E. Willery, C. Locht, F. Jacob-Dubuisson, and V. Villeret. The crystal structure of filamentous hemagglutinin secretion domain and its implications for the two-partner secretion pathway. *Proc. Natl. Ac. Sci. USA*, 101:6194–6199, April 2004. DOI 10.1073/pnas.0400291101.

[227] C. Baud, J. Guérin, E. Petit, E. Lesne, E. Dupré, C. Locht, and F. Jacob-Dubuisson. Translocation path of a substrate protein through its Omp85 transporter. *Nat. Comm.*, 5:5271, October 2014. DOI 10.1038/ncomms6271.

[228] K. Sen, J. Hellman, and H. Nikaido. Porin channels in intact cells of Escherichia coli are not affected by Donnan potentials across the outer membrane. *J. Biol. Chem.*, 263:1182–1187, January 1988.

[229] F. Jacob-Dubuisson, R. Fernandez, and L. Coutte. Protein secretion through autotransporter and two-partner pathways. *Biochim. Biophys. Acta*, 1694:235–257, November 2004. DOI 10.1016/j.bbamcr.2004.03.008.

[230] J. H. Peterson, P. Tian, R. Ieva, N. Dautin, and H. D. Bernstein. Secretion of a bacterial virulence factor is driven by the folding of a C-terminal segment. *Proc. Natl. Ac. Sci. USA*, 107:17739–17744, October 2010. DOI 10.1073/pnas.1009491107.

[231] W. Kang'ethe and H. D. Bernstein. Charge-dependent secretion of an intrinsically disordered protein via the autotransporter pathway. *Proc. Natl. Ac. Sci. USA*, 110:E4246–E4255, November 2013. DOI 10.1073/pnas.1310345110.

[232] J. Guérin, C. Baud, N. Touati, N. Saint, E. Willery, C. Locht, H. Vezin, and F. Jacob-Dubuisson. Conformational dynamics of protein transporter FhaC: large-scale motions of plug helix. *Mol. Mic.*, 92:1164–1176, June 2014. ISSN 1365-2958. DOI 10.1111/mmi.12585.

[233] N. Noinaj, A. J. Kuszak, J. C. Gumbart, P. Lukacik, H. Chang, N. C. Easley, T. Lithgow, and S. K. Buchanan. Structural insight into the biogenesis of β-barrel membrane proteins. *Nature*, 501:385–390, September 2013. DOI 10.1038/nature12521.

[234] J. Bakelar, S. K. Buchanan, and N. Noinaj. The structure of the β-barrel assembly machinery complex. *Science*, 351:180–186, January 2016. DOI 10.1126/science.aad3460.

[235] Y. Gu, H. Li, H. Dong, Y. Zeng, Z. Zhang, N. G. Paterson, P. J. Stansfeld, Z. Wang, Y. Zhang, W. Wang, and C. Dong. Structural basis of outer membrane protein insertion by the BAM complex. *Nature*, 531:64–69, March 2016. DOI 10.1038/nature17199.

[236] F. Gruss, F. Zähringer, R. P. Jakob, B. M. Burmann, S. Hiller, and T. Maier. The structural basis of autotransporter translocation by TamA. *Nat. Struct. Mol. Biol.*, 20:1318–1320, November 2013. DOI 10.1038/nsmb.2689.

[237] N. Noinaj, A. J. Kuszak, C. Balusek, J. C. Gumbart, and S. K. Buchanan. Lateral opening and exit pore formation are required for BamA function. *Structure*, 22:1055–1062, July 2014. DOI 10.1016/j.str.2014.05.008.

[238] N. Noinaj, S. E. Rollauer, and S. K. Buchanan. The β-barrel membrane protein insertase machinery from Gram-negative bacteria. *Curr. Opin. Struct. Biol.*, 31:35–42, April 2015. DOI 10.1016/j.sbi.2015.02.012.

[239] J. Guérin, N. Saint, C. Baud, A. C. Meli, E. Etienne, C. Locht, H. Vezin, and F. Jacob-Dubuisson. Dynamic interplay of membrane-proximal POTRA domain and conserved loop L6 in Omp85 transporter FhaC. *Mol. Microbiol.*, 98:490–501, October 2015. DOI 10.1111/mmi.13137.

[240] A. M. Ruschak and L. E. Kay. Methyl groups as probes of supra-molecular structure, dynamics and function. *J. Biomol. NMR*, 46:75–87, January 2010. DOI 10.1007/s10858-009-9376-1.

[241] C. W. Lee and R. G. Griffin. Two-dimensional 1H/13C heteronuclear chemical shift correlation spectroscopy of lipid bilayers. *Biophys. J.*, 55:355–358, February 1989. DOI 10.1016/S0006-3495(89)82812-7.

[242] A. C. Méli, H. Hodak, B. Clantin, C. Locht, G. Molle, F. Jacob-Dubuisson, and N. Saint. Channel properties of TpsB transporter FhaC point to two functional domains with a C-terminal protein-conducting pore. *J. Biol. Chem.*, 281:158–166, January 2006. DOI 10.1074/jbc.M508524200.

[243] Michael J. Knight, Amy L. Webber, Andrew J. Pell, Paul Guerry, Emeline Barbet-Massin, Ivano Bertini, Isabella C. Felli, Leonardo Gonnelli, Roberta Pierattelli, Lyndon Emsley, Anne Lesage, Torsten Herrmann, and Guido Pintacuda. Fast resonance assignment and fold determination of human superoxide dismutase by high-resolution proton-detected solid-state MAS NMR spectroscopy. *Angew. Chem. Int. Ed. Engl.*, 50(49):11697–11701, Dec 2011. DOI 10.1002/anie.201106340.

[244] A. E. Bennett, J. H. Ok, R. G. Griffin, and S. Vega. Chemical-Shift Correlation Spectroscopy in Rotating Solids - Radio Frequency-Driven Dipolar Recoupling and Longitudinal Exchange. *J. Chem. Phys.*, 96(11):8624–8627, Jun 1992. DOI 10.1063/1.462267.

[245] P. Ma, J. D. Haller, J. Zajakala, P. Macek, A. C. Sivertsen, D. Willbold, J. Boisbouvier, and P. Schanda. Probing transient conformational states of proteins by solid-state R(1ρ) relaxation-dispersion NMR spectroscopy. *Angew. Chem. Int. Ed.*, 53:4312–4317, April 2014. ISSN 1521-3773. DOI 10.1002/anie.201311275.

[246] B. Han, Y. Liu, S. W. Ginzinger, and D. S. Wishart. SHIFTX2: significantly improved protein chemical shift prediction. *J. Biomol. NMR*, 50:43–57, May 2011. DOI 10.1007/s10858-011-9478-4.

[247] A. B. Sahakyan, W. F. Vranken, A. Cavalli, and M. Vendruscolo. Structure-based prediction of methyl chemical shifts in proteins. *J. Biomol. NMR*, 50:331–346, August 2011. DOI 10.1007/s10858-011-9524-2.

[248] J. R. Lewandowski, J.-N. Dumez, Ü. Akbey, S. Lange, L. Emsley, and H. Oschkinat. Enhanced resolution and coherence lifetimes in the solid-state NMR spectroscopy of perdeuterated proteins under ultrafast magic-angle spinning. *J. Phys. Chem. Lett.*, 2(17):2205–2211, 2011. DOI 10.1021/jz200844n.

[249] A. G. Palmer and F. Massi. Characterization of the dynamics of biomacromolecules using rotating-frame spin relaxation NMR spectroscopy. *Chem. Rev.*, 106:1700–1719, May 2006. DOI 10.1021/cr0404287.

[250] S. Morin, T. E. Linnet, M. Lescanne, P. Schanda, G. S. Thompson, M. Tollinger, K. Teilum, S. Gagné, D. Marion, C. Griesinger, M. Blackledge, and E. J. d'Auvergne. relax: the analysis of biomolecular kinetics and thermodynamics using NMR relaxation dispersion data. *Bioinformatics*, 30:2219–2220, August 2014. DOI 10.1093/bioinformatics/btu166.

[251] E. J. d'Auvergne and P. R. Gooley. The use of model selection in the model-free analysis of protein dynamics. *J. Biomol. NMR*, 25:25–39, January 2003. DOI 10.1023/A:1021902006114.

[252] D. G. Davis, M. E. Perlman, and R. E. London. Direct measurements of the dissociation-rate constant for inhibitor-enzyme complexes via the T1ρ and T2 (CPMG) methods. *J. Magn. Reson.*, 104(3):266–275, 1994. DOI 10.1006/jmrb.1994.1084.

[253] M. G. Jain, D. Lalli, J. Stanek, C. Gowda, S. Prakash, T. S. Schwarzer, T. Schubeis, K. Castiglione, L. B. Andreas, P. K. Madhu, G. Pintacuda, and V. Agarwal. Selective (1)H-(1)H distance restraints in fully protonated proteins by very fast magic-angle spinning solid-state NMR. *J. Phys. Chem. Lett.*, 8:2399–2405, June 2017. DOI 10.1021/acs.jpclett.7b00983.

[254] P. S. Nadaud, J. J. Helmus, N. Höfer, and C. P. Jaroniec. Long-range structural restraints in spin-labeled proteins probed by solid-state nuclear magnetic resonance spectroscopy. *J. Am. Chem. Soc.*, 129:7502–7503, June 2007. DOI 10.1021/ja072349t.

[255] G. M. Clore. Practical aspects of paramagnetic relaxation enhancement in biological macromolecules. *Meth. Enzymol.*, 564:485–497, 2015. DOI 10.1016/bs.mie.2015.06.032.

[256] L. E. Kay and D. A. Torchia. The effects of dipolar cross correlation on 13C methyl-carbon T1, T2, and NOE measurements in macromolecules. *J. Magn. Reson.*, 95(3):536–547, 1991. DOI 10.1016/0022-2364(91)90167-R.

[257] D. Sheppard, R. Sprangers, and V. Tugarinov. Experimental approaches for NMR studies of side-chain dynamics in high-molecular-weight proteins. *Prog. Nucl. Magn. Reson. Spectrosc.*, 56:1–45, January 2010. DOI 10.1016/j.pnmrs.2009.07.004.

[258] T. K. Ritchie, Y. V. Grinkova, T. H. Bayburt, I. G. Denisov, J. K. Zolnerciks, W. M. Atkins, and S. G. Sligar. Chapter 11 - Reconstitution of membrane proteins in phospholipid bilayer nanodiscs. *Meth. Enzymol.*, 464:211–231, 2009. DOI 10.1016/S0076-6879(09)64011-8.

[259] F. Tombola, M. M. Pathak, and E. Y. Isacoff. How does voltage open an ion channel? *Annu. Rev. Cell Dev. Biol.*, 22:23–52, 2006. DOI 10.1146/annurev.cellbio.21.020404.145837.

[260] J. D. Lippiat, editor. *Potassium Channels. Methods and Protocols*, volume 491 of *Methods in Molecular Biology.* Humana Press, 2009. DOI 10.1007/978-1-59745-526-8.

[261] D. W. Deamer and J. W. Nichols. Proton-hydroxide permeability of liposomes. *Proc. Natl. Ac. Sci. USA*, 80:165–168, January 1983.

[262] A. L. Hodgkin and A. F. Huxley. A quantitative description of membrane current and its application to conduction and excitation in nerve. *J. Physiol.*, 117:500–544, August 1952. DOI 10.1113/jphysiol.1952.sp004764.

[263] W. A. Catterall. Ion channel voltage sensors: structure, function, and pathophysiology. *Neuron*, 67:915–928, September 2010. DOI 10.1016/j.neuron.2010.08.021.

[264] S. B. Long, X. Tao, E. B. Campbell, and R. MacKinnon. Atomic structure of a voltage-dependent K^+ channel in a lipid membrane-like environment. *Nature*, 450(7168):376–382, Nov 2007. DOI 10.1038/nature06265.

© 2017 Tous droits réservés. lilliad.univ-lille.fr

[265] K. J. Swartz. Sensing voltage across lipid membranes. *Nature*, 456:891–897, December 2008. DOI 10.1038/nature07620.

[266] E. Vargas, V. Yarov-Yarovoy, F. Khalili-Araghi, W. A. Catterall, M. L. Klein, M. Tarek, E. Lindahl, K. Schulten, E. Perozo, F. Bezanilla, and B. Roux. An emerging consensus on voltage-dependent gating from computational modeling and molecular dynamics simulations. *J. Gen. Physiol.*, 140:587–594, December 2012. DOI 10.1085/jgp.201210873.

[267] Q. Li, S. Wanderling, M. Paduch, D. Medovoy, A. Singharoy, R. McGreevy, C. A. Villalba-Galea, R. E. Hulse, B. Roux, K. Schulten, A. Kossiakoff, and E. Perozo. Structural mechanism of voltage-dependent gating in an isolated voltage-sensing domain. *Nat. Struct. Mol. Biol.*, 21:244–252, March 2014. DOI 10.1038/nsmb.2768.

[268] J. Guo, W. Zeng, Q. Chen, C. Lee, L. Chen, Y. Yang, C. Cang, D. Ren, and Y. Jiang. Structure of the voltage-gated two-pore channel TPC1 from Arabidopsis thaliana. *Nature*, 531:196–201, March 2016. DOI 10.1038/nature16446.

[269] A. F. Kintzer and R. M. Stroud. Structure, inhibition and regulation of two-pore channel TPC1 from Arabidopsis thaliana. *Nature*, 531:258–262, March 2016. DOI 10.1038/nature17194.

[270] F. G. Donnan. Theorie der Membrangleichgewichte und Membranpotentiale bei Vorhandensein von nicht dialysierenden Elektrolyten. Ein Beitrag zur physikalisch-chemischen Physiologie. *Zeitschrift für Elektrochemie und angewandte physikalische Chemie*, 17(14):572–581, 1911. URL `http://onlinelibrary.wiley.com/doi/10.1002/bbpc.19110171405/abstract`.

[271] C. R. Cantor and P. R. Schimmel. *Biophysical chemistry*, volume 3. Freeman and Company, New York, 1980.

[272] M. Lindemann and M. Winterhalter. Membrane channels as a tool to control nanoreactors. *IEEE Proc. Nanobiotechnol.*, 153:107–111, August 2006. DOI 10.1049/ip-nbt:20050027.

[273] B. Chanda and M. K. Mathew. Functional reconstitution of bacterially expressed human potassium channels in proteoliposomes: membrane potential measurements with JC-1 to assay ion channel activity. *Biochim. Biophys. Acta*, 1416:92–100, January 1999. DOI 10.1016/S0005-2736(98)00217-X.

[274] P. S. Mangan and M. Colombini. Ultrasteep voltage dependence in a membrane channel. *Proc. Natl. Ac. Sci. USA*, 84:4896–4900, July 1987.

[275] M. Colombini, C. L. Yeung, J. Tung, and T. König. The mitochondrial outer membrane channel, VDAC, is regulated by a synthetic polyanion. *Biochim. Biophys. Acta*, 905:279–286, December 1987. DOI 10.1016/0005-2736(87)90456-1.

[276] M. Kaszuba, J. Corbett, F. M. Watson, and A. Jones. High-concentration zeta potential measurements using light-scattering techniques. *Phil. Trans. R. Soc. A*, 368:4439–4451, September 2010. DOI 10.1098/rsta.2010.0175.

[277] S. Bhattacharjee. DLS and zeta potential - what they are and what they are not? *J. Control. Release*, 235:337–351, August 2016. DOI 10.1016/j.jconrel.2016.06.017.

[278] M. P. Bhate, B. J. Wylie, A. Thompson, L. Tian, C. Nimigean, and A. E. McDermott. Preparation of uniformly isotope labeled KcsA for solid state NMR: expression, purification, reconstitution into liposomes and functional assay. *Prot. Expr. Purif.*, 91:119–124, October 2013. DOI 10.1016/j.pep.2013.07.013.

[279] S. Aimon, J. Manzi, D. Schmidt, J. A. Poveda Larrosa, P. Bassereau, and G. E. S. Toombes. Functional reconstitution of a voltage-gated potassium channel in giant unilamellar vesicles. *PloS ONE*, 6:e25529, 2011. DOI 10.1371/journal.pone.0025529.

[280] L. Shi, I. Kawamura, K.-H. Jung, L. S. Brown, and V. Ladizhansky. Conformation of a seven-helical transmembrane photosensor in the lipid environment. *Angew. Chem. Int. Ed.*, 50:1302–1305, February 2011. DOI 10.1002/anie.201004422.

[281] M. D. Tuttle, G. Comellas, A. J. Nieuwkoop, D. J. Covell, D. A. Berthold, K. D. Kloepper, J. M. Courtney, J. K. Kim, A. M. Barclay, A. Kendall, W. Wan, G. Stubbs, C. D. Schwieters, V. M. Y. Lee, J. M. George, and C. M. Rienstra. Solid-state NMR structure of a pathogenic fibril of full-length human α-synuclein. *Nat. Struct. Mol. Biol.*, 23:409–415, May 2016. DOI 10.1038/nsmb.3194.

[282] M. A. Wälti, F. Ravotti, H. Arai, C. G. Glabe, J. S. Wall, A. Böckmann, P. Güntert, B. H. Meier, and R. Riek. Atomic-resolution structure of a disease-relevant Aβ(1-42) amyloid fibril. *Proc. Natl. Ac. Sci. USA*, 113:E4976–E4984, August 2016. DOI 10.1073/pnas.1600749113.

[283] T. Theint, P. S. Nadaud, D. Aucoin, J. J. Helmus, S. P. Pondaven, K. Surewicz, W. K. Surewicz, and C. P. Jaroniec. Species-dependent structural polymorphism of Y145Stop prion protein amyloid revealed by solid-state NMR spectroscopy. *Nat. Comm.*, 8:753, September 2017. DOI 10.1038/s41467-017-00794-z.

[284] H. K. Fasshuber, J.-P. Demers, V. Chevelkov, K. Giller, S. Becker, and A. Lange. Specific 13C labeling of leucine, valine and isoleucine methyl groups for unambiguous detection of long-range restraints in protein solid-state NMR studies. *J. Magn. Reson.*, 252:10–19, March 2015. DOI 10.1016/j.jmr.2014.12.013.

[285] S.-Y. Lee, A. Lee, J. Chen, and R. MacKinnon. Structure of the KvAP voltage-dependent K+ channel and its dependence on the lipid membrane. *Proc. Natl. Ac. Sci. USA*, 102: 15441–15446, October 2005. DOI 10.1073/pnas.0507651102.

[286] Gerrit Volkmann and Hideo Iwaï. Protein trans-splicing and its use in structural biology: opportunities and limitations. *Mol Biosyst*, 6(11):2110–2121, Nov 2010. DOI 10.1039/c0mb00034e.

[287] A. A. Alabi, M. I. Bahamonde, H. J. Jung, J. I. Kim, and K. J. Swartz. Portability of paddle motif function and pharmacology in voltage sensors. *Nature*, 450:370–375, November 2007. DOI 10.1038/nature06266.

[288] E. Barbet-Massin, A. J. Pell, J. S. Retel, L. B. Andreas, K. Jaudzems, W. T. Franks, A. J. Nieuwkoop, M. Hiller, V. Higman, P. Guerry, A. Bertarello, M. J. Knight, M. Felletti, T. Le Marchand, S. Kotelovica, I. Akopjana, K. Tars, M. Stoppini, V. Bellotti, M. Bolognesi, S. Ricagno, J. J. Chou, R. G. Griffin, H. Oschkinat, A. Lesage, L. Emsley, T. Herrmann, and G. Pintacuda. Rapid proton-detected NMR assignment for proteins with fast magic angle spinning. *J. Am. Chem. Soc.*, 136:12489–12497, September 2014. DOI 10.1021/ja507382j.

[289] Y. Jiang, V. Ruta, J. Chen, A. Lee, and R. MacKinnon. The principle of gating charge movement in a voltage-dependent K^+ channel. *Nature*, 423(6935):42–48, May 2003. DOI 10.1038/nature01581.

[290] A. Sitarska, L. Skora, J. Klopp, S. Roest, C. Fernández, B. Shrestha, and A. D. Gossert. Affordable uniform isotope labeling with (2)H, (13)C and (15)N in insect cells. *J. Biomol. NMR*, 62:191–197, June 2015. DOI 10.1007/s10858-015-9935-6.

[291] R. Linser, V. Gelev, F. Hagn, H. Arthanari, S. G. Hyberts, and G: Wagner. Selective methyl labeling of eukaryotic membrane proteins using cell-free expression. *J. Am. Chem. Soc.*, 136: 11308–11310, August 2014. DOI 10.1021/ja504791j.

[292] P. G. DeCaen, V. Yarov-Yarovoy, E. M. Sharp, T. Scheuer, and W. A. Catterall. Sequential formation of ion pairs during activation of a sodium channel voltage sensor. *Proc. Natl. Ac. Sci. USA*, 106:22498–22503, December 2009. DOI 10.1073/pnas.0912307106.

[293] P. G. DeCaen, V. Yarov-Yarovoy, Y. Zhao, T. Scheuer, and W. A. Catterall. Disulfide locking a sodium channel voltage sensor reveals ion pair formation during activation. *Proc. Natl. Ac. Sci. USA*, 105:15142–15147, September 2008. DOI 10.1073/pnas.0806486105.

[294] Y. Minezaki, K. Homma, and K. Nishikawa. Intrinsically disordered regions of human plasma membrane proteins preferentially occur in the cytoplasmic segment. *J. Mol. Biol.*, 368:902–913, May 2007. DOI 10.1016/j.jmb.2007.02.033.

[295] E. Magidovich, S. J. Fleishman, and O. Yifrach. Intrinsically disordered C-terminal segments of voltage-activated potassium channels: a possible fishing rod-like mechanism for channel binding to scaffold proteins. *Bioinformatics*, 22:1546–1550, July 2006. DOI 10.1093/bioinformatics/btl137.

[296] M. Kjaergaard and B. B. Kragelund. Functions of intrinsic disorder in transmembrane proteins. *Cell. Mol. Life Sci.*, 74(17):3205–3224, September 2017. DOI 10.1007/s00018-017-2562-5.

[297] A. L. Hopkins and C. R. Groom. The druggable genome. *Nat. Rev. Drug Discov.*, 1:727–730, September 2002. DOI 10.1038/nrd892.

[298] A. J. Venkatakrishnan, T. Flock, D. E. Prado, M. E. Oates, J. Gough, and M. Madan Babu. Structured and disordered facets of the GPCR fold. *Curr. Opin. Struct. Biol.*, 27:129–137, August 2014. DOI 10.1016/j.sbi.2014.08.002.

[299] D. M. Rosenbaum, S. G. F. Rasmussen, and B. K. Kobilka. The structure and function of G-protein-coupled receptors. *Nature*, 459:356–363, May 2009. DOI 10.1038/nature08144.

[300] W. N. Zagotta, T. Hoshi, and R. W. Aldrich. Restoration of inactivation in mutants of Shaker potassium channels by a peptide derived from ShB. *Science*, 250:568–571, October 1990. DOI 10.1126/science.2122520.

[301] M. K. Schott, C. Antz, R. Frank, J. P. Ruppersberg, and H. R. Kalbitzer. Structure of the inactivating gate from the Shaker voltage gated K^+ channel analyzed by NMR spectroscopy. *Eur. Biophys. J.*, 27:99–104, 1998. DOI 10.1007/s002490050115.

[302] E. A. Jonas and L. K. Kaczmarek. Regulation of potassium channels by protein kinases. *Curr. Opin. Neurobiol.*, 6:318–323, June 1996. DOI 10.1016/S0959-4388(96)80114-0.

[303] E. Magidovich, I. Orr, D. Fass, U. Abdu, and O. Yifrach. Intrinsic disorder in the C-terminal domain of the Shaker voltage-activated K^+ channel modulates its interaction with scaffold proteins. *Proc. Natl. Ac. Sci. USA*, 104:13022–13027, August 2007. DOI 10.1073/pnas.0704059104.

[304] K. Bugge, E. Papaleo, G. W. Haxholm, J. T. S. Hopper, C. V. Robinson, J. G. Olsen, K. Lindorff-Larsen, and B. B. Kragelund. A combined computational and structural model of the full-length human prolactin receptor. *Nat. Comm.*, 7:11578, May 2016. DOI 10.1038/ncomms11578.

[305] V. Ozenne, F. Bauer, L. Salmon, J.-R. Huang, M. Ringkjøbing Jensen, S. Segard, P. Bernadó, C. Charavay, and M. Blackledge. Flexible-meccano: a tool for the generation of explicit ensemble descriptions of intrinsically disordered proteins and their associated experimental observables. *Bioinformatics*, 28:1463–1470, June 2012. DOI 10.1093/bioinformatics/bts172.

[306] R. J. Lefkowitz. G protein-coupled receptors. III. New roles for receptor kinases and beta-arrestins in receptor signaling and desensitization. *J. Biol. Chem.*, 273:18677–18680, July 1998. DOI 10.1074/jbc.273.30.18677.

[307] S. K. Shenoy and R. J. Lefkowitz. Seven-transmembrane receptor signaling through beta-arrestin. *Sci. Signal.*, 2005:cm10, November 2005. DOI 10.1126/stke.2005/308/cm10.

[308] K. N. Nobles, K. Xiao, S. Ahn, A. K. Shukla, C. M. Lam, S. Rajagopal, R. T. Strachan, T.-Y. Huang, E. A. Bressler, M. R. Hara, S. K. Shenoy, S. P. Gygi, and R. J. Lefkowitz. Distinct phosphorylation sites on the $\beta(2)$-adrenergic receptor establish a barcode that encodes differential functions of β-arrestin. *Sci. Signal.*, 4:ra51, August 2011. DOI 10.1126/scisignal.2001707.

[309] U. B. Choi, R. Kazi, N. Stenzoski, L. P. Wollmuth, V. N. Uversky, and M. E. Bowen. Modulating the intrinsic disorder in the cytoplasmic domain alters the biological activity of the N-methyl-D-aspartate-sensitive glutamate receptor. *J. Biol. Chem.*, 288:22506–22515, August 2013. DOI 10.1074/jbc.M113.477810.

[310] J. Bürgi, B. Xue, V. N. Uversky, and F. G. van der Goot. Intrinsic disorder in transmembrane proteins: Roles in signaling and topology prediction. *PLoS ONE*, 11:e0158594, 2016. DOI 10.1371/journal.pone.0158594.

[311] B. Xue, L. Li, S. O. Meroueh, V. N. Uversky, and A. K. Dunker. Analysis of structured and intrinsically disordered regions of transmembrane proteins. *Mol. BioSyst.*, 5:1688–1702, December 2009. ISSN 1742-2051. DOI 10.1039/B905913J.

[312] Z. Bozoky, M. Krzeminski, R. Muhandiram, J. R. Birtley, A. Al-Zahrani, P. J. Thomas, R. A. Frizzell, R. C. Ford, and J. D. Forman-Kay. Regulatory R region of the CFTR chloride channel is a dynamic integrator of phospho-dependent intra- and intermolecular interactions. *Proc. Natl. Ac. Sci. USA*, 110:E4427–E4436, November 2013. DOI 10.1073/pnas.1315104110.

[313] A.-B. Nørholm, R. Hendus-Altenburger, G. Bjerre, M. Kjaergaard, S. F. Pedersen, and B. B. Kragelund. The intracellular distal tail of the Na+/H+ exchanger NHE1 is intrinsically disordered: implications for NHE1 trafficking. *Biochemistry*, 50:3469–3480, May 2011. DOI 10.1021/bi1019989.

[314] M. Ringkjøbing Jensen, G. Communie, E. A. Ribeiro, Jr, N. Martinez, A. Desfosses, L. Salmon, L. Mollica, F. Gabel, M. Jamin, S. Longhi, R. W. H. Ruigrok, and M. Blackledge. Intrinsic disorder in measles virus nucleocapsids. *Proc. Natl. Ac. Sci. USA*, 108(24): 9839–9844, Jun 2011. DOI 10.1073/pnas.1103270108.

[315] Y. Fan, S. Emami, R. Munro, V. Ladizhansky, and L. S. Brown. Isotope labeling of eukaryotic membrane proteins in yeast for solid-state NMR. *Meth. Enzymol.*, 565:193–212, 2015. DOI 10.1016/bs.mie.2015.05.010.

[316] P. J. Focke, C. Hein, B. Hoffmann, K. Matulef, F. Bernhard, V. Dötsch, and F. I. Valiyaveetil. Combining in vitro folding with cell free protein synthesis for membrane protein expression. *Biochemistry*, 55:4212–4219, August 2016. DOI 10.1021/acs.biochem.6b00488.

[317] M.-L. Fogeron, A. Badillo, F. Penin, and A. Böckmann. Wheat germ cell-free overexpression for the production of membrane proteins. *Meth. Mol. Biol.*, 1635:91–108, 2017. DOI 10.1007/978-1-4939-7151-0_5.

[318] N. Uozumi, T. Nakamura, J. I. Schroeder, and S. Muto. Determination of transmembrane topology of an inward-rectifying potassium channel from Arabidopsis thaliana based on functional expression in Escherichia coli. *Proc. Natl. Ac. Sci. USA*, 95:9773–9778, August 1998. DOI 10.1073/pnas.95.17.9773.

[319] S. G. F. Rasmussen, H.-J. Choi, D. M. Rosenbaum, T. S. Kobilka, F. S. Thian, P. C. Edwards, M. Burghammer, V. R. P. Ratnala, R. Sanishvili, R. F. Fischetti, G. F. X. Schertler, W. I. Weis, and B. K. Kobilka. Crystal structure of the human beta2 adrenergic G-protein-coupled receptor. *Nature*, 450(7168):383–387, Nov 2007. DOI 10.1038/nature06325.

[320] S. G. F. Rasmussen, H.-J. Choi, J. J. Fung, E. Pardon, P. Casarosa, P. S. Chae, B. T. Devree, D. M. Rosenbaum, F. S. Thian, T. S. Kobilka, A. Schnapp, I. Konetzki, R. K. Sunahara, S. H. Gellman, A. Pautsch, J. Steyaert, W. I. Weis, and B. K. Kobilka. Structure of a nanobody-stabilized active state of the $\beta(2)$ adrenoceptor. *Nature*, 469:175–180, January 2011. DOI 10.1038/nature09648.

[321] S. G. F. Rasmussen, B. T. DeVree, Y. Zou, A. C. Kruse, K. Y. Chung, T. S. Kobilka, F. S. Thian, P. S. Chae, E. Pardon, D. Calinski, J. M. Mathiesen, S. T. A. Shah, J. A. Lyons, M. Caffrey, S. H. Gellman, J. Steyaert, G. Skiniotis, W. I. Weis, R. K. Sunahara, and B. K. Kobilka. Crystal structure of the $\beta2$ adrenergic receptor-Gs protein complex. *Nature*, 477: 549–555, July 2011. DOI 10.1038/nature10361.

[322] Y. Kofuku, T. Ueda, J. Okude, Y. Shiraishi, K. Kondo, M. Maeda, H. Tsujishita, and I. Shimada. Efficacy of the $\beta2$-adrenergic receptor is determined by conformational equilibrium in the transmembrane region. *Nat. Commun.*, 3:1045, 2012. DOI 10.1038/ncomms2046.

[323] R. Nygaard, Y. Zou, R. O. Dror, T. J. Mildorf, D. H. Arlow, A. Manglik, A. C. Pan, C. W. Liu, J. J. Fung, M. P. Bokoch, F. S. Thian, T. S. Kobilka, D. E. Shaw, L. Mueller, R. S. Prosser, and B. K. Kobilka. The dynamic process of $\beta(2)$-adrenergic receptor activation. *Cell*, 152:532–542, January 2013. DOI 10.1016/j.cell.2013.01.008.

[324] R. Sterne-Marr, A. I. Baillargeon, K. R. Michalski, and J. J. G. Tesmer. Expression, purification, and analysis of G-protein-coupled receptor kinases. *Meth. Enzymol.*, 521:347–366, 2013. DOI 10.1016/B978-0-12-391862-8.00019-3.

[325] C. Despres, C. Byrne, H. Qi, F.-X. Cantrelle, I. Huvent, B. Chambraud, E.-E. Baulieu, Y. Jacquot, I. Landrieu, G. Lippens, and C. Smet-Nocca. Identification of the tau phosphorylation pattern that drives its aggregation. *Proc. Natl. Ac. Sci. USA*, 114:9080–9085, August 2017. DOI 10.1073/pnas.1708448114.

[326] H. Qi, C. Despres, S. Prabakaran, F.-X. Cantrelle, B. Chambraud, J. Gunawardena, G. Lippens, C. Smet-Nocca, and I. Landrieu. The study of posttranslational modifications of tau protein by nuclear magnetic resonance spectroscopy: Phosphorylation of tau protein by ERK2 recombinant kinase and rat brain extract, and acetylation by recombinant creb-binding protein. *Meth. Mol. Biol.*, 1523:179–213, 2017. DOI 10.1007/978-1-4939-6598-4_11.

[327] O. C. Andronesi, S. Becker, K. Seidel, H. Heise, H. S. Young, and M. Baldus. Determination of membrane protein structure and dynamics by magic-angle-spinning solid-state NMR spectroscopy. *J. Am. Chem. Soc.*, 127(37):12965–12974, Sep 2005. DOI 10.1021/ja0530164.

[328] L. Skora, B. Shrestha, and A. D. Gossert. Isotope labeling of proteins in insect cells. *Meth. Enzymol.*, 565:245–288, 2015. DOI 10.1016/bs.mie.2015.05.013.

[329] C. Opitz, S. Isogai, and S. Grzesiek. An economic approach to efficient isotope labeling in insect cells using homemade 15N-, 13C- and 2H-labeled yeast extracts. *J. Biomol. NMR*, 62: 373–385, July 2015. DOI 10.1007/s10858-015-9954-3.

[330] L. Clark, J. A. Zahm, R. Ali, M. Kukula, L. Bian, S. M. Patrie, K. H. Gardner, M. K. Rosen, and D. M. Rosenbaum. Methyl labeling and TROSY NMR spectroscopy of proteins expressed in the eukaryote Pichia pastoris. *J. Biomol. NMR*, 62:239–245, July 2015. DOI 10.1007/s10858-015-9939-2.

[331] T. Zhuang, Q. Chen, M.-K. Cho, S. A. Vishnivetskiy, T. M. Iverson, V. V. Gurevich, and C. R. Sanders. Involvement of distinct arrestin-1 elements in binding to different functional

forms of rhodopsin. *Proc. Natl. Ac. Sci. USA*, 110:942–947, January 2013. DOI 10.1073/pnas.1215176110.